Computational Thermodynamics and Its Applications

Zi-Kui Liu

Abstract

Thermodynamics is a science concerning the state of a system, whether it is stable, metastable or unstable, when interacting with the surroundings. In this overview, fundamentals of thermodynamics are briefly reviewed through the integration of first and second laws of thermodynamics for open and nonequilibrium systems to demonstrate that the reversible equilibrium and irreversible nonequilibrium thermodynamics can be integrated to enhance the power and utilities of thermodynamics. The recent progresses in computational thermodynamics, the remaining challenges, and potential impacts in broad scientific fields are discussed. It is shown that computational thermodynamics enables the modeling of thermodynamics of a state as a function of both external and internal variables and enables quantitative calculations of a broad range of properties of a multicomponent system in terms of first and second derivatives of energy, including not only equilibrium states when there are no driving forces for any internal processes and but also non-equilibrium states with driving forces for internal processes. Consequently, external constraints such as fixed strain and internal degree of freedoms such as ordering and defects can be described in a coherent framework and applied to materials design. Furthermore, two important but largely overlooked aspects in thermodynamics will be discussed, i.e. the rigorous application of statistical thermodynamics with the probability of configurations and their contributions to system properties, and the applications of second derivatives of energy with respect to either two extensive variables or two potentials or a mixture of them in terms of understanding and predicting emergent behaviors, critical phenomena, kinetic coefficients, and mechanical properties.

1. Introduction

Thermodynamics is a science concerning the state of a system, whether it is stable, metastable or unstable, when interacting with its surroundings. The interactions can involve exchanges of any combinations of heat, work, and mass between the system and the surroundings, defined by the boundary conditions. The typical work includes contributions from the external mechanic, electric and magnetic fields. The first law of thermodynamics describes those interactions, stating that the net change of energy of the surroundings must be balanced by the opposite change of the internal energy of the system. While the second law of thermodynamics governs the evolution of the state inside the system under given interactions between the system and the surroundings. The second law of thermodynamics declares that any internal processes, when occurred spontaneously, i.e. irreversibly as commonly named, must result in a positive entropy production. The combination of the first and second laws of thermodynamics was first derived by Gibbs,[1] and he called it the fundamental thermodynamic equation, [2] which inspired Maxwell to construct a model of its surface.[1] The combined law of thermodynamics represents the integration of the external and internal variables of a system and self-evidently includes both equilibrium and nonequilibrium states of a system,[3] though Gibbs focused on applications of the combined law to equilibrium states in his work. [1,2]

Through a series of seminal publications, Gibbs [1] developed the foundation for the equilibrium of heterogeneous substances through geometrical representation of thermodynamic properties including tie-lines, tie-triangles, definition of chemical potentials, and criteria of equilibrium and stability. The introduction of functions that are now called enthalpy, Helmholtz energy, and Gibbs energy has enabled the theoretical and experimental applications of thermodynamics with

various boundary conditions between systems and surroundings. Since Gibbs focused on equilibrium, the nonequilibrium aspect of thermodynamics was developed into a separate branch, i.e. irreversible thermodynamics that concerns with transport processes and with the rates of chemical reactions.[4–8]

In this overview, the fundamentals of thermodynamics are reviewed, and computational methodologies are discussed in terms of models and input data and tools for modeling. The applications of computational thermodynamics are presented for calculations of phase equilibria and phase diagrams, modeling of internal degree of freedoms in terms of defects, predictions of physical properties in terms of derivatives of energy, kinetic coefficients in terms of energy landscape, and design of materials.

2. Fundamentals of thermodynamics

2.1. Combined first and second law of thermodynamics

The first law of thermodynamics for an open system, whether in an equilibrium or nonequilibrium state, can be written as follows [9]

$$dU = dQ + dW + \sum U_i dN_i \qquad \textbf{Eq. 1}$$

where dU is the change of the internal energy of the system, dQ and dN_i are the heat and the amount of component i added (positive) or removed from the system (negative), respectively, and dW is the amount of any types of work that the system receives from (positive values) or release to (negative values) the surroundings, and U_i is the partial internal energy of component i in the surroundings when $dN_i > 0$ or in the system when $dN_i < 0$. For a system in equilibrium with its surroundings, the U_i is the same in both the surroundings and system. The advantage to

start the first law for an open system is that the chemical potential of a component is naturally introduced as shown below.[9] U_i can be represented by the internal energy of the system as follows

$$U_i = \left[\frac{\partial U}{\partial N_i}\right]_{dQ=0,dW=0,N_{j\neq i}} \quad \textbf{Eq. 2}$$

The second law of thermodynamics is introduced by defining the entropy change of an open system, dS, as follows [9,10]

$$dS = \frac{dQ}{T} + \sum S_i dN_i + d_{ip}S \quad \textbf{Eq. 3}$$

where T is the temperature, S_i the partial molar entropy of component *i* in the surroundings ($dN_i > 0$) or in the system ($dN_i < 0$), and $d_{ip}S$ the entropy production due to spontaneous internal processes (*IP*) in the system. The first two terms on the right-hand side of Eq. 3 concern the interactions between the surroundings and the system, while the third term represents what happens inside the system. Consequently, the right-hand side of Eq. 3 contains both the external and internal contributions. The second law of thermodynamics dictates that any spontaneous *IPs* must result in positive entropy production, i.e. $d_{ip}S > 0$.

Combining Eq. 1 and Eq. 3 gives the combined law of thermodynamics. As in most books on thermodynamics, the work due to the hydrostatic pressure, $-PdV$, is considered, and the combined law of thermodynamics is written as follows

$$dU = TdS - PdV + \sum \mu_i dN_i - Td_{ip}S = \sum Y^a dX^a - Td_{ip}S \quad \textbf{Eq. 4}$$

where P and V are pressure and volume, respectively, and μ_i is the chemical potential of component i in the surroundings ($dN_i > 0$) or in the system ($dN_i < 0$), defined as follows

$$\mu_i = U_i - TS_i \qquad \textbf{Eq. 5}$$

The differential form of μ_i will be discussed later when $d_{ip}S$ is defined.

In the last part of Eq. 4, Y^a denotes the potentials, i.e., T, $-P$ and μ_i, and X^a denotes the molar quantities or extensive quantities, i.e., S, V and N_i.[3,9] Y^a and X^a form a conjugate pair of variables. It should be emphasized that both dV and dN_i in Eq. 4 refer to the changes that the surroundings imposes on the system, while dS further contains the contributions from *IPs* inside the system as shown by Eq. 3. The works due to elastic/plastic/magnetic/electric fields can be added when needed, and they will be briefly discussed later in this section.[11–15]

It is worth noting that Gibbs [1] derived the combined law for a closed system at equilibrium (see Eqs. 11 and 12 on page 63 in ref. [1]), i.e.

$$dU = TdS - PdV \qquad \textbf{Eq. 6}$$

and then introduced the chemical potential by considering the exchange of mass between the system and the surroundings. This approach is commonly used in the literature, e.g. Eqs. 1.49 and 3.1 in the book by Hillert[3] though the amount of matter was introduced in Eq. 1.7, but not individual components. From the above derivations, it can be seen that it is important to start the first law for an open system, Eq. 1, and introduce the entropy change of the system with all contributions, Eq. 3, so that the chemical potential is defined naturally by Eq. 5.[9,10] Hopefully, this procedure can help to enhance the clarity and significance on the definition of chemical potential and that the entropy includes the production by internal processes when the system is not at equilibrium. The latter is important when thermodynamics is applied to nonequilibrium states as shown in the latter part of this paper.

When a system is at equilibrium, the second law stipulates that there are no *IPs* that can produce entropy, i.e., $Td_{ip}S = 0$. Eq. 4 thus reduces to

$$dU = TdS - PdV + \sum \mu_i dN_i = \sum Y^a dX^a \qquad \textbf{Eq. 7}$$

with X^a as the independent variables of the internal energy, called nature variables of internal energy as they are defined naturally by the combined law, i.e. $U(X^a)$, and all the potentials are also the function of X^a, i.e., $Y^i(X^a)$. This is the equation in the work by Gibbs [1] and in most textbooks on thermodynamics. It needs to be emphasized again that Eq. 7 is for systems at equilibrium ***only***, and the internal variables depend on the external variables.

2.2. Non-equilibrium systems and internal variables

For a system not at equilibrium, there are possible spontaneous *IPs* that can result in entropy production in the system. For the sake of simplicity, let us consider one *IP* in the system at the moment, and discussions with more *IP*s can be found in the literature.[3,9] For one IP, an internal variable, ξ, is introduced to define the internal state, and the entropy production due to the change of the internal variable in terms of the Taylor expansion to the third order is written as follows [9]

$$Td_{ip}S = Dd\xi - \frac{1}{2}D_2(d\xi)^2 + \frac{1}{6}D_3(d\xi)^3 \qquad \textbf{Eq. 8}$$

where D is the driving force for the *IP*, $d\xi$ the change of the internal variable that represents the *IP's* progress, and D_2 and D_3 are related to the stability and criticality of the *IP*.[10] It is evident that there are two possibilities for equilibrium, i.e. $D \leq 0$ which will make $d\xi = 0$ at the same time, or $D > 0$ and $d\xi = 0$. The former is called full equilibrium or simply equilibrium, and the

latter is referred as constrained equilibrium or frozen in equilibrium in which some *IPs* with $D > 0$ are prohibited to take place.[3] $D = 0$ denotes a smooth equilibrium of which the driving force, and ξ can be evaluated by the first derivative as shown below.[3]

The combined law of thermodynamics, Eq. 4, can be re-written as follows:

$$dU = \sum Y^a dX^a - Dd\xi + \frac{1}{2}D_2(d\xi)^2 - \frac{1}{6}D_3(d\xi)^3 \qquad \textbf{Eq. 9}$$

The internal energy and all properties are a function of both X^a and ξ, i.e. $U(X^a, \xi)$, $Y^i(X^a, \xi)$, and $D_j(X^a, \xi)$, with ξ as an independent variable for nonequilibrium states. An equilibrium state is reached by solving the value of internal variable ξ so that

$$D = \left[\frac{\partial U}{\partial \xi}\right]_{X^a} = 0 \qquad \textbf{Eq. 10}$$

At equilibrium with $D = 0$, ξ is thus no longer an independent variable and becomes a variable dependent on X^a. Consequently, the internal energy, $U(X^a)$, reaches its extreme with all X^a kept constant, i.e. no exchange of X^a between the system and the surroundings, and all the potentials, Y^a, are homogeneous in the system.[3,9]

The stability of an equilibrium state is determined by the sign of D_2 written as

$$D_2 = \left[\frac{\partial^2 U}{\partial \xi^2}\right]_{X^a} = \left[\frac{\partial^2 U}{\partial (X^b)^2}\right]_{X^a} = \left[\frac{\partial Y^b}{\partial X^b}\right]_{X^a} \qquad \textbf{Eq. 11}$$

when the transfer of X^b between two places in the system is considered. The equilibrium state is stable when $D_2 > 0$ and unstable when $D_2 < 0$. At $D_2 = 0$, the system is at the limit of stability. Furthermore, when $D = D_2 = D_3 = 0$, the system reaches a critical point between the homogenous and inhomogeneous states. It is to be noted that we have not differentiated the

stable vs metastable equilibrium states so far because they are determined by relative values of U at various states with their signs of D_2 being positive.

The potentials, Y^a, are defined by the first derivatives of internal energy to X^a with all other extensive variables and ξ kept constant. Particularly the chemical potential is defined as[3,9]

$$\mu_i = \left[\frac{\partial U}{\partial N_i}\right]_{S,V,N_{j\neq i},\xi} \qquad \textbf{Eq. 12}$$

Both Eq. 2 and Eq. 12 are the partial derivative of internal enery with respec to component i, but with different variables kept constant. Eq. 2 represented an adiabatic system, while Eq. 12 is for a system with constant entropy defined by Eq. 3, both with no work exchage and close to all components except the component i with the surroundings. From Eq. 3, one can see that since $S_i > 0$, dQ is not zero and has the opposite sign of dN_i for an equilibrium system with $d_{ip}S = 0$. Therefore, the system represented by Eq. 12 must exchange heat with the surroundings, and the amount of heat exchanged can be calculated from Eq. 3 as follows with $dS = 0$,

$$dQ = TS_i dN_i \qquad \textbf{Eq. 13}$$

It is evident that the system represented by Eq. 12 under constant entropy is different from the adiabatic system represented by Eq. 2, resulting in Eq. 2 and Eq. 12 differing by TS_i.

It should be emphasized that for nonequilbrium states with $D > 0$ for some *IP*s, ξ is an independent variable, and S includes the contribution from internal entropy production. Since entropy and volume can not be controled easily in experiments, several new energy functions are defined through Lagrange transformation, such as enthaly, Helhomtz energy, and Gibbs

energy.[1,3] The form of the combined law of thermodynamics in terms of the most widely used Gibbs energy, $G = U - TS + PV$, is written as

$$dG = -SdT + VdP + \sum \mu_i dN_i - Dd\xi + \frac{1}{2}D_2(d\xi)^2 - \frac{1}{6}D_3(d\xi)^3 \quad \textbf{Eq. 14}$$

The nature variables of Gibbs energy are T, P, N_i, and ξ, i.e., $G(T, P, N_i, \xi)$, and the chemical potential of a component is defined as

$$\mu_i = \left[\frac{\partial G}{\partial N_i}\right]_{T,P,N_{j\neq i},\xi} \quad \textbf{Eq. 15}$$

The differences in the expressions for chemical potential in Eq. 12 and Eq. 15 originate from how the system interacts with the surroundings, i.e. an isentropic, isovolumetric system vs an isothermal, isobaric system, both open to component i only. At equilibrium with $D = 0$, the Gibbs energy is minimized for an isothermal, isobaric, and closed system, resulting in the homogeneou chemical potential for each component in the system. The previous discussions on instability and criticality in terms of D, D_2, and D_3 apply the same here. The Gibbs energy is widely used because its natural variables, T, P, and N_i, are the variables usually controlled in experiments.

Eq. 15 becomes more complicated when the Gibbs energy is normalized to per mole of atoms, i.e. $G_m = G/\sum N_k$, where G_m is a function of mole fractions defined as $x_i = N_i/\sum N_k$. While all N_i:s are independent, but x_i:s are not due to $\sum x_i = 1$. Consequently, Eq. 15 becomes [3]

$$\mu_i = G_m + \left[\frac{\partial G_m}{\partial x_i}\right]_{T,P,x_{j\neq i},\xi} - \sum x_k \left[\frac{\partial G_m}{\partial x_k}\right]_{T,P,x_{j\neq k},\xi} \quad \textbf{Eq. 16}$$

It is important to note that the derivatives in Eq. 16 is taken under the condition that all x_i:s are treated as independent variables. Alternatively, one can use $x_1 = 1 - \sum_{i=2}^{c} x_i$ to remove the mole fraction of component 1 from Eq. 16 so the rest mole fractions are independent variables.[3]

2.3. Equilibrium systems and secondary derivatives of free energy

Based on the above discussion, it is evident that the reason that thermodynamics is commonly considered for applications to equilibrium systems only is that the internal variable, ξ, becomes a dependent variable for an equilibrium state. The value of ξ is obtained by the minimization of Gibbs energy of the system, thus removed from Eq. 14, which results in the Gibbs energy as a function of T, P, and N_i. This is the following combined law of thermodynamics in almost all textbooks on thermodynamics, applicable to systems ***at equilibrium only***

$$dG = -SdT + VdP + \sum \mu_i dN_i \qquad \textbf{Eq. 17}$$

In addition to molar Gibbs energy and mole fraction, G_m and x_i, one can also introduce molar entropy, S_m, molar volume, V_m, and their partial quantities, S_i and V_i by Eq. 16.[3] In the rest of the paper, the molar quantities and extensive variables are sometime used interchangeably. The key to make use the complete thermodynamics, covering both equilibrium and nonequilibrium states of a system, is to include internal variables as independent variables of the Gibbs energy so D, D_2, and D_3 can be evaluated to study stability, instability, and criticality of the system. It is worth noting that, in complex nonequilibrium systems, there can be multiple *IPs* and many interactions between IPs,[10] resulting in the formation of dissipative structures,[16] which will not be discussed in details in the present paper, but briefly mentioned in Sections 5.3 and 5.6.

The combined law of thermodynamics with elastic, electric, and magnetic fields can be written as follows for an equilibrium system[9]

$$dU = TdS - V\sum \sigma_{ij} d\epsilon_{kl} - V\sum E_j dD_j - V\sum \mathcal{H}_j dB_j + \sum \mu_i dN_i = \sum Y^a dX^a \qquad \textbf{Eq. 18}$$

where $i, j, k, l = 1,2,3$, V is the volume, σ_{ij} and ε_{kl} are the components of stress and strain, E_i and D_i are the components of electric field and electric displacement, $\mathcal{H}_i$ and B_i are the components of magnetic field and magnetic induction. It is to be reminded that by convention Y^a represents T, $-\sigma_{ij}$, $-E_j$, and $-\mathcal{H}_j$. The negative sign is that the decrease of the system volume increases the internal energy of the system as the system receives energy from the surroundings, the same as in the case of pressure shown in Eq. 4. It is noted that the positive sign is also used in the literature depending on the definition of strain, magnetic induction and electric displacement.[13] The first partial derivatives of internal energy with respect to its natural variables give its conjugate variables. The second partial derivatives with respect to the same natural variable result in a set of physical properties which must be positive for a stable system based on the stability condition represented by Eq. 11. The second partial derivatives with respect to a different natural variable denote many other physical properties, though their sign is not pre-determined by the combined law of thermodynamics, but some constraints can be derived, which will be discussed in a separate paper.

In typical experiments, most potentials are controlled except chemical potentials, which is the reason that Gibbs energy with temperature and pressure as natural variables is widely used.

Consequently, one may define a new free energy and its combined law of thermodynamics from Eq. 18 as follows

$$\Phi = U - TS + V\sum \sigma_{ij}\epsilon_{kl} + V\sum E_j D_j + V\sum \mathcal{H}_j B_j \qquad \textbf{Eq. 19}$$

$$d\Phi = -SdT + V\sum \epsilon_{kl} d\sigma_{ij} + V\sum D_j dE_j + V\sum B_j d\mathcal{H}_j + \sum \mu_i dN_i \qquad \textbf{Eq. 20}$$

Table 1 lists various physical properties derived from the derivatives of the conjugate variables (first column) with respect to the natural variables (first row) of Φ. These properties are related to the second derivatives of Φ with respect to its natural variables from ref. [9] The last column and last row are newly added in the present paper and will be discussed in next paragraph. The table is symmetric due to the Maxwell relations with the negative sign for all entropy derivatives in the present sign convention of Eq. 18 and Eq. 20. The diagonal quantities, including those in tensors that can be further expanded with more quantities such as those shown in Eq. 54, are well known physical quantities and all positive for a stable system and approach zero at the limit of stability as shown by Eq. 11. The off-diagonal terms, including those in tensors, are first derivatives of two non-conjugate variables, i.e. the second derivatives of Φ with respect to two different natural variables, and give another set of physical properties. These properties represented by the off-diagonal terms are not prescribed to be positive from the combined law of thermodynamics and thus can become negative under certain conditions such as thermal expansion discussed in Section 5.3.[9,17]

It is interesting to see that the piezocaloric effect is the same as thermal expansion and can be negative too.[18,19] Under hydrostatic pressure, it is $\left(-\frac{\partial S}{\partial P}\right)$ and does not have a dedicated name

in the literature. It is related to heat transport under pressure and equals to thermal expansion. It is assigned the term "*compress heat*" in the present paper because increasing pressure reduces the entropy of a system with positive thermal expansion, thus releasing heat to the surroundings. It is interesting to note that the entropy increases with the increase of pressure for a system with negative thermal expansion as discussed in Section 5.3.1, connecting the volume that is easier to measure experimentally with the entropy that is easier to predict based on statistical mechanics.

The quantities in the last row and last column with their tentative names assigned in italic are worth further discussions. They are the second derivatives of free energy with respect to one extensive variable and one potential, while other quantities in the Table are with respect to two potentials, and it is hard to find any discussion of them in the literature. These quantities are related to the transport properties and discussed in Section 5.5. It shows that the chemical potential to temperature derivative is related to the partial entropy. This inspired us to consider the Seebeck coefficient, which represents the potency of electron migration under temperature gradient and equals to partial entropy of electrons (see the details discussed in Section 5.5.2). By the same token, one can define other transport properties in terms of the derivative of chemical potential of a species, including electrons, as follows

$$\frac{\partial \mu_i}{\partial Y^a} = \frac{\partial^2 \Phi(Y^a, N_i)}{\partial Y^a \partial N_i} = \frac{\partial X^a}{\partial N_i} = X^a_{N_i} \qquad \textbf{Eq. 21}$$

where $X^a_{N_i}$ denotes the partial molar quantity of X^a. It is worth noting that Eq. 21 provides a significant and important approach for predicting transport properties as briefly discussed in Section 5.5.3 and can be generalized as follows

$$\frac{\partial Y^b}{\partial Y^a} = \frac{\partial^2 \varphi(Y^a, X^b)}{\partial Y^a \partial X^b} = \frac{\partial X^a}{\partial X^b} \qquad \textbf{Eq. 22}$$

where the free energy, $\varphi(Y^a, X^b)$, has Y^a and X^b as its natural variables with other natural variables being either potentials or molar quantities depending on experimental conditions.

Table 1. Physical quantities related to the first directives of conjugate variables (first column) to natural variables (first row) of Φ, symmetric due to the Maxwell relations with the negative sign for all entropy derivatives [9,17]

	T, **temperature**	σ_{kl}, **stress**	E_k, **electric field**	$\mathcal{H}_k$, **magnetic field**	N_k, **moles**
S, **entropy**	$\frac{C}{T}$, heat capacity	α_{kl}, piezocaloric effect	p_k, electrocaloric effect	m_k, magnetocaloric effect	$\frac{\partial S}{\partial N_k} = S_{N_k}$, partial entropy
ε_{ij}, **strain**	α_{ij}, thermal expansion	s_{ijkl}, elastic compliance	a_{ijk}, converse piezoelectricity	q_{ijk}, piezomagnetic moduli	$\frac{\partial \varepsilon_{ij}}{\partial N_k}$, *partial strain*
D_i, **electric displacement**	p_i, pyroelectric coefficients	a_{ikl}, piezoelectric moduli	k_{ik}, permittivity	b_{ik}, magnetoelectric coefficient	$\frac{\partial D_i}{\partial N_k}$, *partial electric displacement*
B_i, **magnetic induction**	m_i, pyromagnetic coefficient	q_{ikl}, piezomagnetic moduli	b_{ik}, magnetoelectric coefficient	μ_{ik}, permeability	$\frac{\partial B_i}{\partial N_k}$, *partial magnetic induction*
μ_k, **chemical potential**	$\frac{\partial \mu_i}{\partial T}$, *thermal transport*	$\frac{\partial \mu_i}{\partial \sigma_{kl}}$, *stress transport*	$\frac{\partial \mu_i}{\partial E_k}$, *electric migration*	$\frac{\partial \mu_i}{\partial H_k}$, *magnetic migration*	$\frac{\partial \mu_i}{\partial N_k}$, thermodynamic factor

2.4. Phases and configurations

2.4.1. Definition of phases, Gibbs-Duhem equation, and Gibbs phase rule

The discipline of materials science and engineering primarily concerns microstructures in materials which are composed of individual phases, defects in individual phases, and interfaces between phases and grains, which can all be considered as internal variables. The internal

variables of a phase include the lattice structures in terms of lattice configuration and atomic configurations in terms of lattice site occupancies by atoms which further includes the spin structures in terms of magnetic and polar configurations and the atomic short- and long-range ordering, and defects such as vacancy, dislocations, twins, and stacking faults. Each set of internal variables defines a specific configuration, and the statistical combinations of all configurations define what are usually referred to as a phase.

Considering a homogeneous system at *equilibrium*, i.e., a classical definition of a phase when all internal variables are dependent variables, the integration of Eq. 7 in combination with the definition of Gibbs energy gives

$$G = U - TS + PV = \sum \mu_i N_i \qquad \textbf{Eq. 23}$$

In a space composed of $U,\ S,\ V$, and N_i, a phase can be defined by a hyper surface with all the independent variables being extensive variables. The partial or directional derivatives of U to $S,$ V, and N_i give the potentials of $T, -P$, and μ_i, respectively, resulting in that all phases at equilibrium with each other have the same partial derivatives, i.e. the directional slopes of the hyper surface. While in a space composed of $G,\ T, -P$, and N_i, the partial derivatives of G are a mixture of extensive variables and potentials, i.e. $S,\ V$, and μ_i, resulting in that the equal Gibbs energy for phases at equilibrium with respect to the potential axes of T and $-P$, while the same partial derivatives of Gibbs energy with respect to the axes of extensive variable, N_i, which does make the equilibrium construction more complicated.[20]

What happens if all the extensive variables are replaced by their conjugate potentials in the combined law of thermodynamics? By differentiating Eq. 23, i.e.

$$dG = \sum(\mu_i dN_i + N_i d\mu_i) \qquad \textbf{Eq. 24}$$

It is worth mentioning that the differential of chemical potential, $d\mu_i$, is because μ_i is a function of all the natural variables of G even though μ_i is not independent variables of G. Combining Eq. 17 and Eq. 24, one obtains the Gibbs-Duhem equation at *equilibrium* as follows

$$-SdT - Vd(-P) - \sum N_i d\mu_i = 0 \qquad \textbf{Eq. 25}$$

This equation implies that the changes of all potentials in a phase at *equilibrium* are not independent. Consequently, a phase can be defined by a hyper surface in the space composed of potentials only, $T, -P$, and μ_i, and Eq. 25 depicts that the hyper surface is *concave* with all partial derivatives of the hyper surface being negative, i.e.

$$\left[\frac{\partial Y^b}{\partial Y^a}\right]_{Y^c} = -\frac{X^a}{X^b} < 0 \qquad \textbf{Eq. 26}$$

It should be emphasized that Eq. 26 is different from Eq. 21 and Eq. 22, as they represent different characteristic functions with different natural variables, Φ_1 and Φ_2, as follows

$$d\Phi_1(X^a, Y^b, Y^c) = Y^a dX^a - X^b dY^b - \sum X^c dY^c \qquad \textbf{Eq. 27}$$

$$d\Phi_2(Y^a, Y^b, Y^c) = d[\Phi_1(X^a, Y^b, Y^c) - X^a Y^a] = -X^a dY^a - X^b dY^b - \sum X^c dY^c = 0 \qquad \textbf{Eq. 28}$$

where $\Phi_1\left(X^a, Y^b, Y^c\right)$ is for Eq. 21 with $X^a = N_i$, and $\Phi_2\left(Y^a, Y^b, Y^c\right) = constant$ for Eq. 26. Furthermore, Eq. 21 and Eq. 22 can be used for non-equilibrium systems with ξ being independent variables and $d\xi = 0$, while Eq. 26 is for systems at *equilibrium* only with ξ being dependent variables and $D = 0$.

A two-phase equilibrium is reached when two hyper surfaces in the space composed of only potentials intercept each other so each potential has the same value in both phases, resulting in a hyper line, and so on. This exercise results in the Gibbs phase rule as follows

$$v = c + 2 - p \qquad \textbf{Eq. 29}$$

where v is the number of *potentials* that can be changed *independently* without changing the number of phases in equilibrium, denoted by p, in a system with c independent components. The number "2" denote T and P and will change if more potentials are added such as electric and magnetic fields.

2.4.2. Introduction of configurations and configurational entropy

The definition of phase in the above discussion becomes somewhat ambiguous when the system is near a critical point which is a zero-dimension point in the space composed of *potentials* (see discussions in Section 2.2). A critical point separates a macroscopically homogenous single phase on one side and a macroscopically inhomogeneous mixture of multiple phases on the other side. When the system shifts *infinitesimally* away from the critical point to either side of the critical point, one can imagine that all phases must be very similar to each other and are formed from the same set of *configurations* or *building blocks* but with slightly different amount of each configuration.[21,22] The entropy due to the mixture of those configurations in the phase based on statistical mechanics by Gibbs[23] can be written as follows [10,23]

$$S^{conf} = -k_B \sum_{k=1}^{m} p^k ln p^k \qquad \textbf{Eq. 30}$$

$$p^k = \frac{Z^k}{Z} = \frac{Z^k}{\sum Z^j} \qquad \textbf{Eq. 31}$$

where k_B is the Boltzmann constant, p^k and Z^k are the probability and partition function of configuration k, respectively, and Z is the partition function of the phase, i.e. the summation of the partition function of all configurations. Both equations can be written in the integration form when the distribution is continuous. The superscript for configurations is used here to differentiate the subscript for components. We called this approach "partition function" approach in our previous publications.[10,24–27] The total entropy of the phase is thus

$$S = \sum p^k S^k + S^{conf} = \sum p^k (S^k - k_B ln p^k) \qquad \textbf{Eq. 32}$$

where S^k is the entropy of configuration k, which is composed of sub-configurations such as thermal electrons and phonons computed in the similar fashion as Eq. 30.[28,29] From the energy point of view, one of the unique configurations must have the lowest energy though potentially with multiplicity or degeneracy based on certain criterion such symmetry or energy, designated as the ground configuration, g, with a partition function of Z^g, and Eq. 31 can thus be re-written as

$$p^g = \frac{1}{1 + \sum_{j \neq g} Z^j / Z^g} \qquad \textbf{Eq. 33}$$

$$p^k = \frac{Z^k / Z^g}{1 + \sum_{j \neq g} Z^j / Z^g} = Z^k \frac{p^g}{Z^g} \qquad \textbf{Eq. 34}$$

In the classic view of a phase with all $p^k / p^g = Z^k / Z^g \approx 0$, the phase is practically composed of the ground configuration only with $p^g \approx 1$, and $S^{conf} = 0$. The other extreme is that all configurations have the same probability, i.e. all degenerated, and are in equilibrium with each other, i.e. $Z^k / Z^g = 1/\Omega$, with Ω being the number of the degenerated configuration, and the probability of each configuration is the inverse of Ω, which results in the following well known form of configurational entropy

$$p^k = \frac{1}{\Omega} \quad \textbf{Eq. 35}$$

$$S^{conf} = k_B ln\Omega \quad \textbf{Eq. 36}$$

The most common example is an ideal solution used in all textbooks. In an ideal solution, each atomic configuration is assumed to have the same energy and symmetry and thus the same probability, resulting in the following ideal configurational entropy in per mole of atoms

$$S^{conf} = -R\sum x_i ln x_i \quad \textbf{Eq. 37}$$

where $x_i = N_i / \sum N_k$ is the mole fraction of independent component i, and R the gas constant.

3. Thermodynamic modeling

To make use of thermodynamics efficiently for multicomponent systems, the analytical mathematical models of Gibbs energy as a function of its natural variables, i.e. $G(T, P, N_i, \xi)$, are needed. The most commonly used modeling approach in thermodynamics is the CALPHAD method, which stands for CALculation of PHAse Diagram pioneered by Kaufman. [30,31] In the CALPHAD method,[32,33] the Gibbs energy of each phase, typically defined by its lattice structure and/or atomic long-range ordering, is modeled in the space of its natural variables, T, $-P$, N_i, and ξ. The usual internal variables are the spin configuration and atomic short- and/or long-range ordering. The commonly used mathematical model for solid solution phases in the CALPHAD community is based on the compound energy formalism (CEF) built on the sublattices of a lattice structure in terms of its Wyckoff positions.[34,35]

3.1. Phases with one sublattice and third law of thermodynamics

For solution phases with one type of Wyckoff position, the molar Gibbs energy of phase α, G_m^α, is written as

$$G_m^\alpha = \sum x_i^\alpha {}^oG_i^\alpha + RT \sum x_i^\alpha ln x_i^\alpha + {}^{ex}G_m^\alpha \quad \textbf{Eq. 38}$$

$${}^oG_i^\alpha = {}^oH_i^\alpha - T{}^oS_i^\alpha \quad \textbf{Eq. 39}$$

where ${}^oG_i^\alpha$, ${}^oH_i^\alpha$, and ${}^oS_i^\alpha$ are the Gibbs energy, enthalpy, and entropy of pure component i in the structure of phase α, respectively, and ${}^{ex}G_m^\alpha$ the non-ideal, excess Gibbs energy of mixing. The commonly used reference state for each component is the enthalpy of the component in its stable structure at room temperature and one atmospheric pressure and the entropy at 0K as follows:

$${}^oH_i^{SER}(298\ K, 1atm) = 0 \quad \textbf{Eq. 40}$$

which is called the stable element reference (SER) state. The reference state of entropy is given by the third law of thermodynamics, i.e. the entropy of the element equals to zero at 0K

$${}^oS_i(0K, 1atm) = 0 \quad \textbf{Eq. 41}$$

Several models for ${}^{ex}G_m^\alpha$ are available in the literature [32,33] with one commonly used being the Muggianu extension[36] of the Redlich-Kister formalism[37] (MRK) due to its symmetrical characteristics when applied to multicomponent systems as follows

$${}^{ex}G_m^\alpha = \sum_{i<j} x_i^\alpha x_j^\alpha \sum_k {}^kL_{i,j}^\alpha \left(x_i^\alpha - x_j^\alpha\right)^k + \sum_{i<j<l} x_i^\alpha x_j^\alpha x_l^\alpha L_{i,j,l}^\alpha \quad \textbf{Eq. 42}$$

where ${}^kL_{i,j}^\alpha$ is the k^{th} order of binary interaction parameters between components i and j, which can be temperature dependent, and $L_{i,j,l}^\alpha$ the ternary interaction parameter among components i, j, and l, which can be both temperature and composition dependent. For solution phases with strong short-range ordering, the quasichemical model[38] describes the entropy of mixing more

accurately by considering the differences in various bonding energies, while the associate model[39] assumes the explicit formation of various complex species. Both the bond probability and the amounts of associates in the above models are all part of internal variables, ξ.

One significant issue in Eq. 38 is when the pure component i is not stable in the structure of phase α, and ${}^{o}G_i^{\alpha}$ is thus not known or difficult to obtain from experiments. Kaufman[40] examined this and introduced the concept of "lattice stability" to represent the energy difference between the stable and non-stable structures of pure component i and estimated their values through various extrapolation schemes.[41] For example, the Gibbs energy of W in the fcc structure is written as

$$ {}^{o}G_W^{fcc} = {}^{o}G_W^{bcc} + \Delta^{o}G_W^{fcc-bcc} \qquad \textbf{Eq. 43} $$

where $\Delta^{o}G_W^{fcc-bcc}$ is termed as "lattice stability". The concept of the lattice stability formed the foundation of the CALPHAD modeling.[31] Theoretical predictions of lattice stability have been pursued along the way with significant progresses made in recent years,[41–47] and further improvements may be made using the concept of configurations discussed above for the instability of non-ground structures of pure elements.[44]

3.2. Phases with more than one sublattices

For solid phases with multiple sets of Wyckoff positions or interstitial sites, each set can be treated as one sublattice in the CEF modeling approach, such as $(Fe, Cr)_3C$ with one sublattice for Fe and Cr and another sublattice for C. The internal variables are defined by the mole fractions in each sublattice, called site fraction, i.e., y_i^t for the mole fraction of component i in

sublattice t with $\sum_i y_i^t = 1$. The mole fraction of component i in the phase is computed as follows

$$x_i = \sum\nolimits_t a^t y_i^t \,/ \sum\nolimits_t a^t \qquad \textbf{Eq. 44}$$

where a^t is the number of sites of the sublattice t. The corresponding ideal entropy of mixing in per mole of formula (mf) with $\sum_t a^t$ mole of components, i.e. Eq. 37, becomes

$$S_{mf}^{conf} = -R \sum\nolimits_t a^t \sum\nolimits_i y_i^t ln(y_i^t) \qquad \textbf{Eq. 45}$$

The Gibbs energy of such a phase is written as follows

$$G_{mf}^{\alpha} = \sum_{em} \left(\prod_t y_i^t \, {}^{o}G_{em}^{\alpha} \right) + RT \sum_t a^t \sum_i y_i^t ln y_i^t + {}^{ex}G_{mf}^{\alpha} \qquad \textbf{Eq. 46}$$

$$\begin{aligned} {}^{ex}G_{mf} = {} & \sum\nolimits_t \prod\nolimits_{l,s\neq t} y_l^s \sum_{i<j} \sum\nolimits_j y_i^t y_j^t L_{i,j:l}^t + \sum\nolimits_t \prod\nolimits_{l,s\neq t} y_l^s \sum\nolimits_{i<j} \sum\nolimits_{j<k} \sum\nolimits_k y_i^t y_j^t y_k^t L_{i,j,k:l}^t \\ & + \sum\nolimits_t \prod\nolimits_{l,s\neq (t,u)} y_l^s \sum\nolimits_{i<j} \sum\nolimits_{j<k} \sum\nolimits_k y_i^t y_j^t y_m^u y_n^u L_{i,j:m,n:l}^{t,u} \end{aligned} \qquad \textbf{Eq. 47}$$

where ${}^{o}G_{em}^{\alpha}$ is the Gibbs energy of an *endmember* (em) with only one component in each sublattice such as Fe_3C and Cr_3C in $(Fe,Cr)_3C$, playing the same role as the pure element in Eq. 38; $L_{i,j:l}^t$ represents the binary interaction between components *i* and *j* in sublattice *t* with other sublattices containing only one component each, denoted by l; $L_{i,j,k:l}^t$ the ternary interaction among components *i*, *j* and *k* in sublattice *t* with other sublattices containing only one component each, denoted by l; and $L_{i,j:m,n:l}^{t,u}$ the reciprocal interaction among components *i* and *j* in sublattice *t* and components *m* and *n* in sublattice *u* with other sublattices containing only one component each, denoted by l, which is used to describe short-ranging ordering among components *i*, *j*, *m*, and *n* between the two sublattices, noting that *m* and *n* can be the same components as *i* and *j* for an ordering-disordering transition.[48] The sublattice model has also

been used to model ionic phases including both ionic liquid and solid phases with the additional constraints on charge neutrality.[49–53]

3.3. Phases with magnetic polarization

The CALPHAD model of the magnetic Gibbs energy was based on the work by Inden[54,55] and revised by Hillert and Jarl[56] for ferromagnetic materials as a function of temperature with the second-order magnetic transition temperature and magnetic moments as a function of composition. This model was extended by Hertzman and Sundman[57] to the systems with ferromagnetism (FM) on one side and antiferromagnetism (AFM) on the other side such as the Fe-Cr system, which was further revised by Chen and Sundman[58] and Xiong *et al.*[59] The latest revision of the magnetic model is shown in the following equations

$$G_m^{mag} = RTg(\tau)ln(1+\beta) \quad \textbf{Eq. 48}$$

where β is the magnetic moment of the phase, $\tau = T/T_c$ with T_c being the critical temperature, i.e. Curie temperature for FM to paramagnetic (PM) transition and Neel temperature for AFM to PM transition, and $g(\tau)$ a function describing the discontinuity of heat capacity above and below T_C as follows for phases with one sublattice model

$$T_c = \sum x_i {}^0T_{C,i} + {}^{ex}T_c \quad \textbf{Eq. 49}$$

$$1+\beta = \prod (\beta_i + 1)^{x_i} \quad \textbf{Eq. 50}$$

$$\beta_i = x_i {}^0\beta_i + \sum x_j {}^0\beta_{ij} + {}^{ex}\beta_i \quad \textbf{Eq. 51}$$

$$g(\tau) = \begin{cases} 0, & \tau \le 0 \\ 1 - \frac{1}{D}\left[0.38438376\frac{\tau^{-1}}{p} + 0.63570895\left(\frac{1}{p}-1\right)\left(\frac{\tau^3}{6} + \frac{\tau^9}{135} + \frac{\tau^{15}}{600} + \frac{\tau^{21}}{1617}\right)\right], & 0 < \tau \le 1 \\ -\frac{1}{D}\left(\frac{1}{21}\tau^{-7} + \frac{1}{630}\tau^{-21} + \frac{1}{2975}\tau^{-35} + \frac{1}{8232}\tau^{-49}\right), & \tau > 1 \end{cases} \quad \textbf{Eq. 52}$$

$$D = 0.33471979 + 0.49649686\left(\frac{1}{p} - 1\right) \quad \textbf{Eq. 53}$$

where ${}^{0}T_{C,i}$ and ${}^{0}\beta_i$ are the critical temperature and magnetic moment of pure i, ${}^{ex}T_C$ and ${}^{ex}\beta_i$ represent the non-ideal interaction which can be modeled using the MKS formalism by Eq. 42, ${}^{0}\beta_{ij}$ is the magnetic moment of i in pure j, p is the fraction of the total disordering enthalpy absorbed above the critical temperature, given as 0.28 for fcc and hcp metals and 0.40 for bcc metals, respectively. In the model by Hillert and Jarl[56], the MKS model was directly applied to β, which resulted in some challenges in modeling of systems where two elements have different magnetic ordering such as FM for Fe and AFM for Cr in the Fe-Cr system.[57,58] Xiong *et al*.[59] further proposed Eq. 50 and two separate equations for AFM and FM in the form of Eq. 49, and at the same time pointed out the limitation of the revised model when a system experiences a transition between AFM and FM states as a function of temperature.[60,61] Therefore, more works are needed in further improving the magnetic model in the CALPHAD approach.

As expected, theoretic prediction of Gibbs energy of a magnetic phase as a function of temperature has progressed, including the quantum Heisenberg model within many-body theory using the mean-field and random-phase approximation,[62–64] our recent approach based on statistical mixture of distinct magnetic spin configurations with the entropy shown by Eq. 32, [25–27,65,66] and the cluster expansions and Monte Carlo simulations in terms of both atomic disordering and magnetic spin disordering have also demonstrated its potential applicability to binary and ternary systems.[67–69] The theoretic predictions serve as input data for CALPHAD modeling presented above.[70]

3.4. Phases with electric polarization

Phases with electric polarization are dominated by ferrielectric materials with $PbTiO_3$ being one prototype which is a cubic perovskite structure at high temperatures and transitions to a tetragonal perovskite structure with ferroelectricity at 760 K through a second order phase transition.[71–74] Their thermodynamic modeling is largely based on the work by Cross and co-workers led by Haun [75–77] in terms of phenomenological Landau-Ginsburg-Devonshire formalism [78] with the internal variables including ferroelectric and antiferroelectric polarizations and oxygen octahedral tilt angel plus strain in a sixth-order polynomial.[79] The unpolarized and unstrained crystal, which is the stable structure at high temperature, is used as the reference state, and the crystal symmetry is often taken into account to remove some terms, e.g. with odd terms for a phase being centrosymmetrical.[76] The Landau coefficients of common ferroelectric phases were compiled by Chen.[80] One of the drawback using the unpolarized and unstrained crystal stable at high temperatures is that this crystal is unstable at zero K, and its properties cannot be predicted theoretically due to the instability as discussed in Section 5.3.

Since the strain is considered as the independent variable, Helmholtz energy is modeled instead of Gibbs energy with the following equation[80]

$$F(\varepsilon, P) = \frac{1}{2}\alpha_{ij}P_iP_j + \frac{1}{3}\beta_{ijk}P_iP_jP_k + \frac{1}{4}\gamma_{ijkl}P_iP_jP_kP_l + \frac{1}{5}\delta_{ijklm}P_iP_jP_kP_lP_m + \frac{1}{6}\omega_{ijklmn}P_iP_jP_kP_lP_mP_n + \frac{1}{2}c_{ijkl}\varepsilon_{ij}\varepsilon_{kl} - a_{ijk}\varepsilon_{ij}P_k - \frac{1}{2}q_{ijkl}\varepsilon_{ij}P_kP_l + \cdots, \quad \textbf{Eq. 54}$$

where P_i:s are the electric polarizations in various directions, α_{ij}, β_{ijk}, γ_{ijkl}, δ_{ijklm}, and ω_{ijklmn} are the phenomenological Landau coefficients, and c_{ijkl}, a_{ijk}, and q_{ijkl} are the elastic, piezoelectric, and electrostrictive constant tensors (see Table 1 except q_{ijkl} involving the third derivative of the

free energy as shown below), respectively. The Landau coefficients can be modeled as a function of compositions[81] and in principle also as a function of temperature and are related to the derivatives of the free energy. For example, from Eq. 54, it seems that the following relation exists among the coefficients[13]

$$q_{ijkl} = -\frac{\partial \alpha_{kl}}{\partial \sigma_{ij}} = -\frac{\partial^3 \Phi}{\partial \sigma_{ij} \partial E_k \partial E_l} \qquad \textbf{Eq. 55}$$

In comparison with the modeling of magnetic polarization in Section 3.3, it is evident to see that coefficients and the tensors need to be modeled as a function of temperatures and compositions as it was done for elastic tensors.[82] Their modeling remains future opportunities for the CALPHAD community to develop such modeling approaches. Furthermore, since the energy differences between various configurations are relatively small, the author anticipates that the modeling of configurations can play significant roles for ferroelectric materials.[74] Theoretical prediction based on the ferroelectric effective Hamiltonian can also provide finite-temperature thermodynamic properties through Monte Carlo simulations.[83–87]

3.5. Polymer solutions

A polymer molecule consists of the same repeating units of one or more monomers such as a DNA (Deoxyribonucleic acid), which can be an atom or a small molecule. The number of repeating units can be as large as 10^4–10^5 with variable molecular mass. Gibbs energy functions of polymers with a single molecular mass can be treated similarly as in previous sections. The mixtures of different polymer molecules are often called polymer blends or polymer solutions when one of them has only one or a few repeating units, which will all be called polymer

solutions here. There are three typical architectures of polymerization: a linear chain, a branched chain, and a cross-linked polymer. Nearly all polymers are mixtures of molecules with a different degree of polymerization, i.e. repeating units, with a molecular mass distribution, complicating the modeling of their thermodynamic properties because of the dependence of properties on molecular mass.

The ideal entropy of mixing in a polymer solution is quite different from that of atomically random solutions because the monomers in a polymer molecule are connected to each other and cannot move freely. One common approach to calculate the ideal entropy of a polymer solution is to evoke a lattice model and assume that one monomer occupies a lattice site with a fixed volume. The number of translational states of a single molecule is equal to the number of lattice sites available. The ideal mixing entropy of a solution in per mole of lattice sites can be written as[9]

$$S_m = -R\sum_i \frac{\phi_i}{m_i} ln\phi_i \qquad \textbf{Eq. 56}$$

where m_i and ϕ_i are the number of lattice sites per molecule i and the volume fraction of molecule i in the solution, respectively.

Gibbs energy of a multicomponent random polymer solution can be written as

$$G_m = \sum \frac{\phi_i}{m_i} {}^0G_{im} + RT\left(\sum \frac{\phi_i}{m_i} ln\phi_i + \sum \phi_i\phi_j\chi_{ij}\right) \qquad \textbf{Eq. 57}$$

where ${}^0G_{im}$ is the Gibbs energy of molecular i per mole of lattice site, and χ_{ij} the unitless interaction parameter between molecule i and j. Eq. 57 is similar to the Flory–Huggins solution equations.[88,89]

More thermodynamic modeling approaches for liquid-liquid and liquid-vapor equilibria nonelectrolyte including polymer solutions were developed almost in parallel with the CALPHAD method, with the UNIversal QUAsiChemical (UNIQUAC) model [90] being one of the major models. The UNIQUAC model generalizes the Guggenheim's quasi-chemical analysis through introduction of the local area fraction as the primary concentration variable and can reduce to several well-known equations with well-defined simplifying assumptions, including the Wilson [91] and Non-Random Two-Liquid (NRTL) [92] models. In the UNIQUAC model, the effects of molecular size and shape are introduced through structural parameters obtained from pure-component data and the use of Staverman's combinatorial entropy [93], which extends the Flory-Huggins model discussed above to include molecules containing rings and crosslinks.

Different from the CALPHAD method, the UNIQUAC approach models the expression of the molar excess Gibbs energy with the activity coefficient analytically derived from the partial derivative of total excess Gibbs energy with respect to the component, which is prone to errors. Recently, Li et al. [94] re-cast the UNIQUAC model in the CALPHAD framework and implemented it in OpenCalphad,[95] aiming for better equilibrium calculations than existing computational implementations of the UNIQUAC model in the literature and the exchange of ideas and experiences between the CALPHAD and UNIQUAC communities.[95,96] The

UNIQUAC model is represented in the CALPHAD nomenclature with combinatorial, ${}^{cmb}G_m$, and residual, ${}^{res}G_m$, contributions as follows

$$G_m = \sum x_i \, ({}^0G_i + RTlnx_i) + {}^{cmb}G_m + {}^{res}G_m \quad \textbf{Eq. 58}$$

$${}^{cmb}G_m = RT \sum x_i \, ln\frac{\Phi_i}{x_i} + \frac{z}{2}\sum x_i \, q_i ln\frac{\theta_i}{\Phi_i} \quad \textbf{Eq. 59}$$

$${}^{res}G_m = -RT \sum x_i \, q_i ln\rho_i \quad \textbf{Eq. 60}$$

$$\Phi_i = \frac{r_i x_i}{\sum r_j \, x_j} \quad \textbf{Eq. 61}$$

$$\theta_i = \frac{q_i x_i}{\sum q_j \, x_j} \quad \textbf{Eq. 62}$$

$$\rho_i = \sum \theta_j \tau_{ji} \quad \textbf{Eq. 63}$$

$$\tau_{ji} = exp\left(-\frac{w_{ji}}{T}\right) \quad \textbf{Eq. 64}$$

where q_i and x_i are a surface-area and a volume parameter of constituent i, respectively, z is the average number of nearest neighbors of a constituent, always assumed to be 10, and $w_{ji} \neq w_{ij}$ are the model parameters.

Calculations of thermodynamic properties and phase diagrams for binary, ternary, and quaternary systems among water, 2,2,4-trimethylpentane, acetonitrile, aniline, benzene, methylcyclopentane, n-heptane, n-hexane, and n-octane. Furthermore, the evaluation of model parameters of the acetonitrile-benzene-n-heptane ternary system is demonstrated and compared with the modeling and experimental results in the literature. It was found that the parameters in the acetonitrile-benzene and the benzene-n-heptane binary systems are substantially different from those in the literature, with the new modeling showing similar agreement on activity coefficients, but better agreement on excess enthalpies when compared with experimental data.

It is anticipated that the new modeling capability will enhance the modeling of multicomponent polymer solutions.

3.6. Phases with defects

Defects play significant roles in determining the properties of materials. Defects in a phase include vacancy, dislocation, twin, and stacking fault, and defects between phases include grain boundary and phase interfaces. For materials with small sizes, surface can be important and may be considered as a defect due to the structure and property differences from those of the bulk. It is important to realize that the defects alter both lattice and atomic configurations through lattice distortions and elemental redistributions such as segregations. As defects can form a range of configurations, the "partition function" approach discussed in Section 2.4.2 can be used to calculate their probability of various metastable configurations in the phase.

The formation of defects usually requires additional energy as a penalty, but at the same time increases the entropy of the phase by introducing disorder to stabilize the defects. The competition between formation energy, entropy, and segregation can sometimes result in thermodynamically stable configurations of defects in a phase or even become a separate phase by itself such as the long period structure order (LPSO) in Mg alloys (see further discussion in Section 3.6.3). This competition can be described by three contributions: the amounts of defects, dn_D, segregation to the defects, dn_i, and configurational entropy due to the defects with the combined law under constant P and N_i as follows

$$dG = \sum\nolimits_{conf} p^{conf} \left\{ G_D dn_D + \sum (\mu_i^D - \mu_i^I) dn_i \right\} - S_D^{conf} dT \qquad \textbf{Eq. 65}$$

where the summation with *conf* is for various defect configurations with probability of p^{conf}, G_D is the Gibbs energy of formation per defect, μ_i^D and μ_i^I are the chemical potentials of component i at the defect and in the interior away from the defects, all for one configuration, and S_D^{conf} the configurational entropy by Eq. 30 for various defect configurations, respectively. When $\mu_i^D \neq \mu_i^I$, the component i will segregate or de-segregate to the defect to reduce the energy of the system. Eq. 65 was first formulated for the thermodynamics of nanograins for a given defect configuration, i.e. grain structure without S_D^{conf}, which illustrates that nanograins can be thermodynamically stable when the two internal processes are coupled to give $dG = 0$.[97] It is plausible that the same approach can be applied to stabilized other defects through segregations due to the strong binding energy between elements and defects such as oxygen and vacancy.[98,99] Some common defects are discussed in following sections.

3.6.1. Vacancy

Modeling of vacancy is not only important to thermodynamics, but also essential to kinetics of vacancy-mediated diffusion.[100] In the CALPHAD modeling, the vacancy is treated as a non-conserved component in the compound energy formalism as shown in Eq. 38 and Eq. 46, in which the Gibbs energy of vacancy, ${}^oG_{Va}$, needs to be defined first before the interaction parameters with other components are evaluated. It is evident that the amount of vacancy is not controlled from the surroundings, but internally determined by the system, thus an internal variable, ξ. Furthermore, vacancies can group to form divacancy and trivacancy clusters, resulting in more internal variables. Therefore, the amounts of vacancy and vacancy clusters are internal variables of the system, n_D in Eq. 65.

Various values were suggested in the literature for ${}^{o}G_{Va}$. The most intuitive one is zero [101–104], since the vacancy-endmember is "nothing". Other choices include $RTln10$ [105] and $30T$ J/mol. [33,106,107] A more recent work [108] analyzed previous results and found that the behavior of the model is very sensitive to the value of ${}^{o}G_{va}$ through numerical simulations. When ${}^{o}G_{Va}$ is zero or negative, there is no equilibrium state at the vacancy-lean side. When ${}^{o}G_{Va}$ is positive but below a critical value, there are multiple equilibrium states. When ${}^{o}G_{Va}$ exceeds this critical value, there is one unique solution associated with the equilibrium vacancy concentration. Based on these observations, it was concluded that ${}^{o}G_{Va}$ should be larger than a critical value, $(ln2 - 1/2)RT$, to ensure a unique equilibrium state. Moreover, it was often mentioned that ${}^{o}G_{Va}$ is just a formal parameter without any physical meaning. Another work [107] also noticed the problems caused by a zero or negative ${}^{o}G_{Va}$. In practice this problem is solved with part of the Gibbs energy of formation of vacancies in a unary system coupled with the interaction parameter.[109]

We presented a physical model to enable a unified thermodynamic treatment of the vacancy-bearing solid and the gas, i.e. the vapor of the solid, for CALPHAD modeling.[110] The model parameters are related to quantities that can be calculated by first-principles or measured experimentally. Since the formation of vacancy has significant impact on volume, the pressure effect must be considered in the Gibbs energy model by defining ${}^{o}G_{Va}$ as

$${}^{o}G_{Va} = {}^{o}G_{Va,P=0} + PV_{Va} \qquad \textbf{Eq. 66}$$

where P is the pressure, V_{Va} the molar volume of the vacancy, and ${}^{o}G_{Va,P=0}$ the Gibbs energy of vacancy at P=0 and ${}^{o}G_{Va,P=0} = 0$. Here the pressure effect is ignored for the solid element

without vacancies, since its volume changes little. The pressure effect is considered for the vacancy-endmember, making its molar Gibbs energy non-zero. The reason is that although a vacancy has nothing inside, it occupies certain amount of volume, subject to energy penalties from pressure.

For a one-component system with vacancy, the sublattice model is (A, Va), and the Gibbs energy in one mole of component A is written as

$$G_m = \frac{G}{y_A} = G_A + \frac{1-y_A}{y_A} PV_{Va} + RTlny_A + RT\frac{1-y_A}{y_A} ln(1-y_A) + (1-y_A)L \qquad \textbf{Eq. 67}$$

where y_A is the site fraction of component A, equal to $y_A = 1 - y_{Va}$ with y_{Va} being the site fraction of vacancy, G_A the Gibbs energy of component A without vacancy, and L the MRK interaction parameter between A and vacancy. Either y_A or y_{Va} can be considered as the internal variable, ξ. The equilibrium states are found by solving the following equation at a constant temperature

$$\frac{\partial G_m}{\partial y_A} = -\frac{PV_{Va}}{{y_A}^2} - \frac{RT}{{y_A}^2} ln(1-y_A) - L + (1-y_A)\frac{\partial L}{\partial y_A} = 0 \qquad \textbf{Eq. 68}$$

It is shown that there are two solutions from the above equation: one is the solid, and the other is the ideal gas.[110] It is evident that when these two solutions give the same G_m in terms of one mole of component A, the solid phase with vacancy and the gas phase, both with one mole of atoms, are in equilibrium with each other, i.e.

$$G_m^{gas} = G_m^{solid} \qquad \textbf{Eq. 69}$$

Solving Eq. 68 and Eq. 69, one obtains the values of the two unknows, y_A^{gas} and y_A^{solid}, depending on the values of V_{Va} and L along with its derivative. The pressure thus obtained represents the vapor pressure of the solid in terms of the ideal gas law as follows

$$P^{vapor} = y_A^{gas} RT/V_{Va} \qquad \textbf{Eq. 70}$$

P^{vapor} and y_A^{solid} are two well defined physical quantities that can be measured experimentally, but not y_A^{gas}. Eq. 70 shows that y_A^{gas} is a function of V_{Va} for given P^{vapor} and T. It is also evident that V_{Va} and L jointly determine the value of y_A^{solid} as shown by Eq. 68 and discussed in [109].

As in the spirit of CALPHAD modeling, to make the thermodynamic models of different elements consistent, a universal value for V_{Va} is needed, and the interaction parameters can then be evaluated. We suggested to use $V_{Va} = 10^{-7} m^3/mol$ for mono-vacancy, since the molar volumes of most elements are around this value.[110] Furthermore, the vacancy model denoted by Eq. 67 and Eq. 68 not only presents a physics-based approach, but also treats the solid and its vapor in one formula and demonstrates that vacancy is an equilibrium feature of the system. It is worth mentioning that the sum of partial pressures of all components equals to the system's total pressure when there are no other gaseous species in the system, which will be further discussed with applications involving the gas phase in Section 5.4.5.

In addition to mono-vacancy, vacancy clusters can also be treated similarly. Furthermore, in systems with more than one component, the interactions between vacancy and different components are important, resulting in the formation of vacancy/component clusters and redistribution of components in the phase similar to short-range ordering mentioned above.

When all these clusters exist, their energetics result in different probabilities for them to exist in the phase, and the "partition function" approach discussed in Section 2.4.2 can thus be used with the internal configurations represented by various clusters so their respective statistical probabilities can be evaluated. Both vacancies and vacancy clusters can be the equilibrium features of a phase with the driving force, i.e. Eq. 10, for their changes being zero.

3.6.2. Dislocation

While the energetics of vacancy and clusters of vacancies and vacancy/components are modeled using the CALPHAD approach, the energetics of dislocations have not been modeled in the same framework in the literature due to the complexity of dislocations in a phase. The central question is to define the internal variables to describe the configurations involving dislocations and develop models to represent the Gibbs energies of configurations, while the configurational entropy among various configurations and total entropy can be evaluated in terms of Eq. 30 and Eq. 32 discussed before.

While thermodynamics of dislocations has always been part of discussion on dislocations,[111–113] it was Langer, Bouchbinder, and Lookman (LBL) who emphasized the importance to explicitly take the internal variables into consideration of thermodynamics of dislocations.[114] One key internal variable is the population of dislocations by a single, averaged, area density ρ, which can be replaced by a set of densities for different types of dislocations and different orientations. In LBL thermodynamic model, the internal degrees of freedom of a solid-like material can be separated into two weakly interacting subsystems: (1) configurational subsystem defined by the mechanically stable positions of the constituent atoms and (2) kinetic-vibrational subsystem

defined by the momenta and the displacements of the atoms at small distances away from their stable positions, each with its own "effective temperature", defined as

$$\chi = \frac{\partial U_C}{\partial S_C} \qquad \textbf{Eq. 71}$$

where U_C is the energy of any configuration of dislocations with the entropy, S_C, defined by the number of such configurations in any energy intervals. The rate at which inelastic external work is being done by the stress is introduced in their thermodynamic analysis in terms of plastic strain rate, plus a new equation for the dependence of the dislocation density on external strain. Consequently, an equation for the hardening rate was derived with dislocation density as the internal variable and a set of physical parameters including the magnitude of the Burgers vector, lattice parameter, formation energy of dislocation, and elastic constants.

The concept of "effective temperature" in various forms similar to Eq. 71 has been used in the literature extensively, particularly in the field of astronomy.[115,116] As shown by Bouchbinder and Langer[117], its essence is to separate various entropy contributions to the energy of the system, and it thus should not affect the fundamentals of thermodynamics discussed in this paper. It can be seen from the work by Langer, Bouchbinder, and Lookman,[114] the only internal variable is the dislocation density with the external variables being the strain and strain rate. In a one-component system, one can thus formulate the energetics of a system as follows

$$G_A^D = {}^oG_A + \Delta H_A^D - T\Delta S_A^D \qquad \textbf{Eq. 72}$$

where ΔH_A^D and ΔS_A^D are the enthalpy and entropy of formation of dislocation as a function of T, $-P$, N_i and ρ_l where ρ_l is the dislocation density for the type l dislocation.

In the spirit of the CALPHAD approach (see Eq. 42), one may be tempted to write the general form for a one-component system as follows

$$\Delta G_A^D = \Delta H_A^D - T\Delta S_A^D = \sum\nolimits_l \rho_l L_l^D + \sum\nolimits_{l,m} \rho_l \rho_m L_{l,m}^D \qquad \textbf{Eq. 73}$$

where $L_l^D = \Delta H_l^D - T\Delta S_l^D$ is the model parameter related to the enthalpy and entropy of formation of type l dislocation which includes the elastic energy associated with its formation, and $L_{l,m}^D$ denotes the interaction parameter between the same or different types of dislocations in terms of both elastic deformation and dislocation multi-junctions.[118,119] Higher order interaction parameters can be added. Both L_l^D and $L_{l,m}^D$ can be the functions of temperature, strain, and strain rate and can be modeled in the framework discussed by Langer, Bouchbinder, and Lookman,[114] with inputs from first-principles calculations and experiments.[120] Their dependences on dislocation density can be modeled in terms of the MRK formalism shown in Eq. 42 with the compositions replaced by dislocation densities. At the same time, the pressure needs to be replaced by stresses as the natural variables of Gibbs energy.

In multicomponent systems, there are additional internal variables to describe the redistribution of components between dislocations and the matrix because the interaction parameters are composition dependent, see Eq. 65. This redistribution can result in the formation of clusters around dislocations that reduces the energy of the system, such as the Cottrell atmosphere.[111,121–123] These interactions and the formation of clusters can also be modeled using the MRK formalism discussed in Section 3.1 though diffusion of component at low temperatures could be too slow to reach equilibrium except for interstitial elements. The different configurations of dislocations and clusters with different energetics and thus their statistical probability of

existence in the phase can be treated by the "partition function" approach discussed in Section 2.4.2 with S_D^{conf} in Eq. 65.

3.6.3. Twin boundary and stacking fault

The CALPHAD modeling of twin boundaries and stacking faults are not available in the literature. The internal variable of a twin boundary or a stacking fault can be the area of the twin boundary or stacking fault in a given volume of the phase. The Gibbs energy can have the similar form as Eq. 73 for pure components and the MRK formalism discussed in Section 3.1 for interactions between elements and defects in multicomponent materials.

Even though twin boundaries and stacking faults are both planar defects in a phase, they are significant different as a twin boundary only changes the crystal orientation, while a stacking fault changes the crystal structure, usually between fcc and hcp crystal structures. As a matter of fact, the alternating configurations can result in the formation of new LPSO structures, [124–128] which may thus be called "*defect phases*" in contrast to "*defected phases*" or "*defects in phases*" because the periodic arrangements of stacking faults result in different long-range lattice structures. The divisions among "*defects in phases*", "*defected phases*", or "*defect phases*", can be fuzzy when the defect configurations change their stability from unstable to metastable or even stable due to the interactions among themselves and multicomponents. A defect phase with long-range ordering can be modeled as a regular phase as shown in Sections 3.1 and 3.4 such as the LPSO phases in Mg alloys.[128,129]

3.6.4. Grain boundary, surface, and phase interface

As an interface between two grains of the same phase, the contribution of grain boundary to the energy of the system is usually represented by the first term in Eq. 65, i.e.

$$dG = \gamma_0 dA \qquad \textbf{Eq. 74}$$

where γ_0 is the grain boundary energy as a function of its five degrees of freedom, and A the grain boundary area. It is evident from this equation that the decrease of grain boundary area reduces the free energy of a polycrystal material until it becomes single crystal without grain boundary.

Even though the segregation of components to grain boundary has been known for a long time, γ_0 in Eq. 74 is usually assumed to be a constant and independent of segregation. It was until relatively recent that the reduction of grain boundary energy is considered, partially related to the development of nanograined materials where the composition in the grain boundary is closely related to the overall composition, resulting in the grain boundary energy as a function of grain boundary composition.[97,130–133] There are thus two independent internal variables, ξ: the grain size represented by the grain boundary area and the grain boundary composition. Applying Eq. 65 to grain boundary with the first two terms, one obtains the following combined law of thermodynamics [97]

$$dG = \gamma_g dA + \sum (\mu_i^{gb} - \mu_i^I) dn_i \qquad \textbf{Eq. 75}$$

where γ_g is the grain boundary energy which is a function of grain boundary composition, μ_i^{gb} and μ_i^I are the chemical potentials of component i in the grain boundary and in the grain interior, respectively, and dn_i denotes the amount of component i migrated from grain interior to grain boundary.

The grain boundary energy, γ, can be defined as follows[97]

$$\gamma = \frac{dG}{dA} = \gamma_g + \sum \left(\mu_i^{gb} - \mu_i^I\right) \frac{\partial n_i}{\partial A} \qquad \textbf{Eq. 76}$$

where $\frac{\partial n_i}{\partial A}$ represents the grain boundary solute excess. When the grain boundary and the grain interior have the same composition, i.e. a fresh grain boundary, there is no migration of components, i.e. $dn_i = 0$ and $\gamma = \gamma_g = \gamma_0$, which can be considered as a constrained equilibrium in terms of redistribution of components, but $\mu_i^{gb} \neq \mu_i^I$ due to their different structures, resulting in a driving force for segregation and the reduction of grain boundary energy. When the equilibrium is reached in terms of $\frac{\partial G}{\partial n_i} = 0$ for a given over-all composition and a given grain size by adjusting the grain boundary composition, i.e. $\mu_i^{gb} = \mu_i^I$, and the grain boundary energy reaches a minimum value, i.e. $\gamma = \gamma_g < \gamma_0$. When this minimum grain boundary energy becomes zero by adjusting the grain size, i.e. $\gamma = \gamma_g = 0$, the polycrystal structure becomes thermodynamically more stable than a single crystal structure.

The thermodynamic modeling of a polycrystal has be carried out in terms of Eq. 76 for the grain boundary energy in binary systems of 44 solvents and 52 solutes[97] or through summation of Gibbs energies of grain boundary and grain interior plus the transitional region between them for various binary alloys.[134] It should be noted that thickness of grain boundary can change with respect to composition and temperature and thus needs to be considered as an internal variable in addition to grain size and grain composition in thermodynamic modeling of grain boundaries at high temperatures. [135]

A surface may be considered as an interface between the condensed phase and its vapor using the formalism discussed in Section 3.6.1, while a phase interface is between two condensed phases. In principle, thermodynamic modeling of surface and phase interfaces can be carried out similarly as described for grain boundary though the segregation to phase interfaces is more difficult to define as two phases usually have difference compositions.[136]

3.7. Tools for thermodynamic modeling

As can be seen in Eq. 38, Eq. 42, Eq. 46, and Eq. 47, the evaluation of model parameters is carried out in a hierarchical structure sequentially from those of pure elements, their lattice stability, binary interaction parameters to ternary and multicomponent interaction parameters. Through the CALPHAD annual conferences, the nonprofit foundation CALPHAD, Inc., and the CALPHAD journal started in 1973, 1975, and 1977, respectively, this hierarchical procedure resulted in several versions of thermodynamic parameters of pure elements and their lattice stability values with the latest one published in 1991 by the Scientific Group Thermodata Europe (SGTE),[137] which significantly enhanced the international collaborations, along with continued development.[138,139] The available computational tools are reported in two special issues of the CALPHAD journal,[140,141] with multicomponent thermodynamic databases of technological important materials available commercially.[142–144] Even though the operational procedures of commercial computational tools are available, the algorithms for Gibbs energy minimization and the database structures in commercial tools and the associated databases are usually proprietary, which significantly hinder the development of new algorithms and new models. Consequently,

there are recent developments of open source codes, such as OpenCalphad,[95,96] PyCalphad,[145,146] and Thermochimica.[147]

It is evident from the hierarchical procedure that modification of a constitutive subsystem has a snowball effect on the description of a multicomponent system in that it affects every Gibbs energy function of every phase in systems that contain that subsystem, *e.g.*, a change in the binary A-B system affects the description of all phases in ternary systems A-B-C, A-B-D, *etc.*, making remodeling of all of these ternaries necessary which is very challenging with the existing computational tools.[148] To address this challenge, the ESPEI software[149] was developed for high throughput CALPHAD modeling. It is built on DFT data and can efficiently re-evaluate the thermodynamic parameters of higher order systems when a sub-system is being updated, and the latest version of ESPEI [150–152] uses PyCalphad [145,146] as the computation engine.

PyCalphad is a free and open-source Python library for designing thermodynamic models, calculating phase diagrams and investigating phase equilibria using the CALPHAD method. It is capable of reading thermodynamic databases and solving the multicomponent, multi-phase Gibbs energy minimization problem. A unique feature of PyCalphad is that the thermodynamic models of individual phases are internally decoupled from the equilibrium solver and the models themselves are represented symbolically. Consequently, the databases can be programmatically manipulated and overridden at run-time without modifying any internal solver or calculation code. The general architecture of PyCalphad software package is shown in Figure 1. The Database object is the fundamental representation of CALPHAD data in PyCalphad and supports reading and writing a large subset of the SGTE thermodynamic database file format (TDB). The

Model is an abstract representation of the molar Gibbs energy function of a phase, built around the computer algebra library SymPy.[153,154] The calculate() function is the core property calculation routine of pycalphad and performs calculations for the case when all independent external and internal variables, i.e., temperature, pressure, sublattice site fractions, are specified, i.e. any nonequilibrium states. Custom models can be specified via the model keyword argument to override the default model for all phases or a specific phase's model. The equilibrium() function is responsible for equilibrium property calculations, and its return value is a multi-dimensional labeled array, including the equilibrium values of the molar Gibbs energy and chemical potentials. Furthermore, it was shown that the combination of random sampling with uniform grid points significantly increases performance in effective sampling to capture key details about the energy surfaces of multicomponent, multisublattice phases.[155]

The complexity of PyCalphad necessities the implementation of strategies to avoid the regression, or accidental breakage. The popular Git source code control (SCC) system [156] is used to manage the source of PyCalphad, allowing its complete history of changes to be recorded for all released and unreleased versions and concurrent work on, e.g., new major features and bug fixes to existing versions through different versions of the software to be stored in separate "branches". PyCalphad has a suite of continuous integration (CI) tests designed to verify that a revision to the code does not cause unintended behavior, which are run automatically every time a new revision is pushed to the Git repository on GitHub. When a bug is reported and fixed a minimal test case is added to the suite whenever possible to prevent the problem from appearing again in future releases. The rigor and current and future impacts of PyCalphad enabled its winning of the runner-up (2nd place) in NASA Software of the Year competition in 2019.[157] It should be

mentioned that the global minimization of Gibbs energy in multicomponent system with complex sublattice models remains a challenging balance between efficiency and robustness of algorithms, which are subject to continuous improvements.[155,158]

Figure 1. General architecture of the PyCalphad software package.[146]

ESPEI implements two steps of model parameter evaluation: generation and Markov Chain Monte Carlo (MCMC) optimization.[150–152] The parameter generation step uses experimental and first-principles data describing the derivatives of the Gibbs energy to parameterize the Gibbs energy of each individual phase, resulting in a complete thermodynamic database based solely on those derivatives, commonly called thermochemical data, along with the reference states described by Eq. 40 and Eq. 41. Experimental thermochemical data for virtually all real alloy systems are too sparse to fully describe the Gibbs energies of the phases and are often unable to access the energetics of metastable configurations defined within the CEF, requiring that available experimental data is augmented with thermochemical data from estimates, empirical models,[159] machine learning models, [160,161] or first-principles calculations,[70] all of which only give approximate energies. For each fitting step, the residual sum of squares between the evaluated parameters and the data are used to score and compare the models within the corrected Akaike information criterion (AICc).[162] The model with the lowest score is the optimal combination of model fitness and complexity. The AICc is a modified version of the AIC that avoids overparameterization when the data is sparse, which is often the case for thermochemical data.

The phase equilibrium data require the Gibbs energies of all phases to be refined, so parameters must be optimized iteratively to be self-consistent by the modeler. Currently, ESPEI uses MCMC to perform a Bayesian optimization of all model parameters simultaneously. Since the parameters for each phase are often correlated to each other because increasing the value one parameter and decreasing another can give the same Gibbs energy for any given set of conditions, ESPEI uses an ensemble sampler, as introduced by Goodman and Weare [163]. Ensemble samplers use an ensemble of Markov chains to form the proposal distribution for the parameters. This allows the proposals to be invariant under affine transformations, solving the problems of scaling proposal length and differing parameter magnitudes in multidimensional parameter space simultaneously. Proposed parameters are accepted or rejected based on the Metropolis criteria. ESPEI uses an ensemble sampler algorithm implemented in the emcee package [164] with parallelizable ensemble samplers. It provides emcee with an initial ensemble of chains as Gaussian distributions centered on the parameters generated by single phase fitting and defines a probability function that calculates point posterior log-probabilities from the prior and likelihood. Prior distributions for the parameters are the main way that modelers input domain knowledge into ESPEI's MCMC optimization.

Three main types of data are considered by the likelihood function defined in ESPEI: single phase thermochemical data of the temperature derivatives of the Gibbs energy, activity data (converted into chemical potential) related to the composition derivatives of the Gibbs energy, and multi-phase equilibria data. For all data types, the error is assumed to follow a normal distribution with default values for the standard deviations of each type of data provided in ESPEI. Users can modify the values by adding a weight for each type of data or for each

individual dataset. The errors for thermochemical data are straightforward, but less so for multi-phase equilibria data. The method implemented in ESPEI is similar to the rough search method implemented in the PanOptimizer software [165] with the residual being the driving force between the target equilibrium and current hyperplanes, obtained by equilibrium calculations at each measured tie-line vertex with all phases active and with only the desired phase active, respectively.

In addition to evaluation of model parameters, another important feature of PyCalphad and ESPEI is the uncertainty quantification in terms of models, model parameters, and model predictions.[166] Parameter uncertainty concerns the distribution of each parameter and is evaluated within the MCMC optimization step of ESPEI by quantifying the distribution of the parameter values that make up each converged Markov chain. The parameter uncertainty enabled the development of a suite of tools to represent uncertainty in forms that surpass previous limitations, including the distribution of phase diagrams and their features, as well as the dependence of phase stability and the distributions of phase fraction, composition, activity and Gibbs energy irrespective of the number of components.[166] Examples are shown in Figure 2 for the model parameters of the liquid phase[151] and the uncertainty intervals of the fcc-Laves–liquid eutectics[166] in the Cu-Mg system.

Figure 2. (a) Corner plot of the parameters in the Cu-Mg liquid phase with the diagonal images for the histogram of each parameter in the Markov chain and the off-diagonal images for the covariance between two parameters; [151] (b) FCC - Laves – liquid eutectics in

Cu-Mg plotted for all 750 sampled parameter sets with 68% and 95% uncertainty intervals.

166

4. Input data for thermodynamic modeling

Input data for thermodynamic modeling can broadly be divided into two categories: thermochemical data and phase equilibrium data as mentioned above, with the former being the first and second derivatives of Gibbs energy and the latter being the amounts and compositions of phases in equilibrium with each other.[70] The data are primarily from three sources: experimental measurements,[167,168] theoretical estimations and predictions,[70,159] and predictions from machine learning,[161,169] with their timespans from weeks to months, days to weeks, and seconds to hours, respectively. The theoretical estimations are not discussed in the present paper.

4.1. Experimental measurements

In the book led by the author,[9] experimental methods for phase equilibrium and thermochemical measurements are discussed and can be grouped into two categories: compositions and energy, including equilibrated materials, diffusion couples/multiples, vapor pressure, and electric/magnetic/high pressure techniques for phase equilibrium data, and solution/heat capacity calorimetry, combustion, direct reaction, and electromotive force techniques for thermochemical data. In general, the uncertainties in measurements of heat are larger than those in compositions. One key promise of experimental measurements is that the material reaches a state of equilibrium when the data are collected, i.e. with respect to small fluctuations of all ξ, the material returns back to its equilibrium state with well-defined values of ξ. Furthermore, one needs to keep in mind that every experimental observation combines the contributions from all

configurations as articulated in Section2.4.2, while theoretical prediction often considers the contributions individually.

4.2. First-principles calculations

It is noted that the limitation of theoretical prediction is at the same time its strength as it can investigate the contributions of individual configuration to the system and provide insights and be complimentary to experimental observations. Particularly, the development of first-principles calculations based on the density functional theory (DFT)[170,171] and a range of efficient computer programs[172] have revolutionized the theoretical predictions in terms of both accuracy and efficiency in the last few decades.[173–175] The fundamental theorem is that there exists a universal functional of the electron density that minimizes the energy of the ground state of a system, and this electron density can then be used to calculated all properties of the ground state. It is thus self-evident that the DFT-based calculations are for individual configurations as discussed in Section 2.4.2. Through constraints on volume and perturbations of atomic positions, the Helmholtz energy of a configuration can be obtained as follows [29,176,177]

$$F(V,T) = E_c(V) + F_{vib}(V,T) + F_{el}(V,T) \qquad Eq.\ 77$$

where E_c is the static total energy at 0 K calculated directly by first-principles,[178] and F_{vib} and F_{el} are the lattice vibrational free energy and the thermal electronic contribution, respectively, related to contributions at finite temperatures. F_{el} is evaluated from the electronic densities of state at different volumes.[29] F_{vib} can be obtained from first-principles phonon calculations for accurate results[29,176,177] or the Debye model for simplicity,[177] using a modified scaling factor.[179]

The results from DFT-based calculations can also be used to develop interatomic potentials or molecular force fields for molecular dynamic (MD) simulations of the physical movements of atoms, molecules and defects,[180] or evaluate the coefficients for effective cluster interaction in the cluster expansion approach which are then used as a Hamiltonian for Monte Carlo simulations (CE-MC). [181,182]

In addition to the crystal structure corresponding to the ground state, DFT-based calculations have also been extensively performed for non-ground state atomic configurations with several online open databases.[183–185] However, the free energy of unstable structures cannot be directly calculated due to the their imaginary vibrational modes.[42] It was shown that for an element with the fcc structure as its ground state, it is unstable in the bcc structure at zero Kelvin, and vice versa.[44] Progresses have been made in terms of *ab initio* molecular dynamics (AIMD) simulations [186,187] and using the limit of stability,[46,47] and these approaches provide useful data in the desired smooth extrapolation behavior between stable, metastable, and unstable regions in the CALPHAD method. However, if one would like to predict the transition between the unstable and stable structures with the change of external fields, i.e. the critical point and associate anomalies, one may need to use the "partition function" approach discussed in Section 2.4.2 and in ref. [10] by considering the statistical competition among various configurations. The author anticipates that this approach is applicable to properties of any phases under conditions that the probabilities of metastable configurations become statistically significant. By the same token, DFT-based calculations can be used to predict properties of phases with those defects discussed in Section 3.6 as demonstrated in the literature.[120,127,128,188–192] For non-stoichiometric phases, in

addition to the MD and EC-MC simulations mentioned above, one can use the coherent potential approximation (CPA) [193] and special quasirandom structures (SQS).[194–197]

The accuracy of DFT-based calculations is often evaluated by comparing the calculated energetics with experimental measurements. Kirklin et al. compared the formation energies in the Open Quantum Materials Database (OQMD) database with 1670 experimental formation energies of compounds with an apparent mean absolute error (MAE) being 0.096 eV/atom (~9.3kJ/mol).[198] They also pointed out that the MAE between different experimental measurements from multiple sources is about 0.082 eV/atom (~7.9kJ/mol). Hautier et al. compared the reaction energies of 135 reactions of the formation of ternary oxides from chemically similar binary oxides and modeled the errors by a normal distribution with a mean close to zero and a standard deviation of 24 meV/atom (~2.3kJ/mol).[199] The experimental tabulated data at 298K were extrapolated to zero K in order to compare with the computed data. In both cases, generalized gradient approximation (GGA) with a Hubbard U parameter were used for some transition metal elements (GGA+U).

4.3. Machine learning

DFT-based calculations significantly reduce the time in obtaining thermochemical data in comparison with experimental measurements, but still take considerable amount of computer resources and time for each calculation. Furthermore, the number of calculations needed for a phase increases exponentially with the numbers of sublattices and components. It is thus desirable to find more efficient procedures to generate input data for thermodynamic modeling.

The current trend points to machine learning as an exciting tool available to materials science.[161,169,200]

There are three key components in machine learning: databases, descriptors, and algorithms. In an effort to predict formation energies of compounds, Ward et al. [161] utilized the OQMD database of 435000 formation energies [184,201], with over 30000 entries from the Inorganic Crystal Structure Database (ICSD) and the remainder derived by replacing elements in known crystal structures with different elements, i.e. various atomic configurations. They created total 271 attributes/descriptors based on the Voronoi tessellation and composition of structures. The random forests algorithm was used due to its superior performance and robustness against overfitting. Through systematic test of training set size, a 72 meV/atom (~ 7kJ/mol) MAE in cross validation was achieved, a significant improvement in comparison with existing approaches. The training and running times are in the order of 3000 and 0.1 seconds, respectively.

Bartel et al. [169] used the SISSO (sure independence screening and sparsifying operator) approach to a massive (~10^{10}) space of mathematical expressions and identify a simple descriptor to predict Gibbs energy for stoichiometric inorganic compounds. They used experimental data for 262 solid compounds to identify the descriptor and tested on a randomly chosen excluded set of 47 compounds and 131 compounds with first-principles computed Gibbs energy. The following descriptor was obtained

$$G - \Delta H_f\left(\frac{eV}{atom}\right) = (-2.48 * 10^{-4} * ln(V) - 8.84 * 10^{-5} mV^{-1})T + 0.181 * ln(T) - 0.882 \qquad \textit{Eq. 78}$$

where ΔH_f is the formation energy of the compound at 298K, V the calculated atomic volume (Å^3/atom), and m the reduced atomic mass (amu). This descriptor was selected by SISSO from a space of ~3×10^{10} candidate three-dimensional descriptors, where the dimensionality is defined as the number of fit coefficients (excluding the intercept). 262 compounds with 2991 data points was randomly selected from 309 inorganic crystalline solid compounds as the training set, and the remaining 47 compounds with 558 data points were for cross validation. The resulted MAE was ~50 meV/atom (~5 kJ/mol) for temperatures ranging from 300–1800 K. The selected three quantities, T, V, and m, are among the key factors affecting the magnitude of vibrational entropy, i.e. the right-hand side of Eq. 78.[202] This descriptor was further applied to 29,525 compounds in ICSD, enabling the prediction of thousands of temperature-dependent phase diagrams of inorganic compounds.

In a recent work, we tested a range of deep neural network (DNN) architectures using the same database and descriptors by Ward et al. [161]. During the DNN design process, around 50 networks belonging to 19 architectures were created and tested with cross-validation on a randomly selected test set comprising 5% of the OQMD database (21,800 test entries). The best network achieved a MAE of ~28 meV/atom (~3kJ/mol).[203,204] Furthermore, the improved prediction speed enabled the screening of the whole databases and identification of entries that do not fit the discovered patterns. This, in turn, combined with more in-depth analysis, allows us to pinpoint entries that are likely to contain poor quality data, as well as those at risk of having a systematic error in the DFT-based calculations. Such DNN models can also be trained for specific benchmarks such as memory constrained applications, improved performance on non-OQMD datasets, and enhanced transfer learning capability.[203,204]

5. Applications

In the spirits of Integrated Computational Materials Engineering (ICME) [205] and Materials Genome Initiative (MGI),[206] computational materials science and engineering plays a central role in the advancement of industrial manufacturing. Manufacturing is a combination of many processes in which external variables are adjusted to induce internal processes, transform materials from one state to another state, and ultimately produce a product that possesses one or multiple functionalities.[207] Such one transformation can be schematically shown in terms of energy profile as a function of one internal variable in Figure 3. More complex energy landscape such as fractal free energy landscapes with simple basins, metabasins and fractal basins in structural glasses [208] can in principle be considered as being composed of many such individual energy profiles shown in Figure 3 at various time and spatial scales. The applications of computational thermodynamics can be schematically articulated by this diagram in terms of derivatives of energy in following aspects:

1. For a given set of internal variables, ξ_j, the first and second derivatives with respect to its extensive natural variables give a range of physical properties of the system as shown in Table 1, including new sets of kinetic coefficients;[9,10]
2. For a given set of natural variables, the first and second derivatives with respect to ξ_j determine

   2.1. whether the system is at equilibrium with the first derivative being zero,

2.2. whether the equilibrium is stable with the second derivative being positive, or unstable with the second derivative being negative, or at the limit of stability with the second derivative being zero,

2.3. which stable equilibrium is the ground state with the lowest energy,

2.4. the driving force for the transformation from the metastable to stable states along with the transformation barrier denoted by the maximum energy difference between the unstable and metastable states,

2.5. For stable, nonequilibrium systems with second derivative being positive, the first derivative with respect to ξ_j gives the driving force for the transformation towards a local equilibrium state;

2.6. For unstable systems with second derivative being negative, self-assembly, dissipative structures form,[16] including the spinodal decompositions in bulk and grain boudaries.[209,210]

3. The usage of third derivative is currently limited to the critical point where all first, second, and third derivatives are zero. At a critical point, all internal variables, ξ_j, become dependent variables because the system is at equilibrium with first derivative being zero. The second and third derivatives being zero add two constraints, resulting in a zero-dimension point in the space defined by two independent potentials. When a third independent potential is introduced, the zero-dimension critical points in three two-dimensional spaces of two independent potentials extends into the three-dimensional space as lines which merger together to form a zero-dimension critical point in the three-dimensional space. These lines denote the instability limit of the system with three independent potentials, and the zero-

dimensional critical point represents an invariant critical point (ICP) which can be extended to multidimensional spaces of potentials.[211] It may be noted that these instability lines were termed as line of critical end points (LCEP) in the literature.[212]

4. From Eq. 11, it can be seen that when the limit of stability is approached from the stable region, D_2 changes from positive to zero, resulting in the following mathematical singularity at the limit of stability

$$\left[\frac{\partial X^b}{\partial Y^b}\right]_{X^a} = +\infty \qquad \textbf{Eq. 79}$$

This indicates that all extensive variables diverge at the limit of stability, including the critical point and LCEP. It is evident that in the vicinity of the critical point, the system will start to change from normal behavior towards the divergency, demonstrating emergent behaviors such as the colossal positive, zero, or negative thermal expansion,[10,22,27] and giant electromechanical response in ferroelectric relaxors.[212,213] The property of thermal expansion is represented in the temperature-pressure space, while the electromechanical response is in the temperature-electric field space, resulting in the divergence of physical properties. [9,17]

Figure 3. Schematic diagram of energy landscape as a function of one internal variable

The above list of applications can be broadly categorized into the groups of stability, metastability, and instability for emergent behaviors in terms of materials discovery, design, processing, and performance that are discussed in the following sections.[10]

5.1. Stability

Knowing the space of stable phases as a function of independent variables is the key for materials design and manufacturing.[207,212,214,215] This space is traditionally represented by phase diagrams, but usually limited to diagrams with two independent variables. With computational thermodynamics, multi-dimensional spaces can be explored numerically more efficiently. There are three types of phase diagrams: potential, mixed, and molar phase diagrams with the axes of the phase diagrams being all potentials, mixture of potentials and molar quantities, and all molar quantities, respectively. Each type of phase diagrams has its own characteristics. The Gibbs phase rule can only be directly applied to potential phase diagrams and may be modified for mixed and molar phases diagrams.[3] In mixed and molar phase diagrams, the concepts of tie-lines that connect the phases in equilibrium and lever rule based on balance of molar quantities are introduced to define the phase compositions and calculate phase fractions.

For visualization purposes, multidimensional phase diagrams are sectioned along one or more axes. When sectioned along potentials, the number of independent potentials, thus the number of independent variables, is reduced by the number of sectioned potentials, and the Gibbs phase rule, tie-lines, and lever rule can apply based on the types of phase diagrams. However, when sectioned along molar quantities, tie-lines are usually not on the resulted phase diagrams, and the lever rule can thus no longer be used. If a mixed phase diagram is sectioned exactly along the tie-line, it is equivalent to section along a potential because the potential remains constant along the tie-line, and the resulted phase diagrams are called pseudo- or quasi-binary and ternary phase diagrams.

5.1.1. One-component systems and phase boundary rule

Four phase diagrams for one-component pure Fe system are shown in Figure 4, and one can easily plot any one of them using the computational tools after calculations.[95,96,142–146] In the $T-P$ potential phase diagram, the Gibbs phase rule dictates the two-dimensional areas, one-dimensional lines, and zero-dimension points for single-, two-, and three-phase regions, respectively. The $T-V_m$, S_m-P and S_m-V_m phase diagrams are less common in the literature, and the tie-lines are plotted in them which can be used to calculate the phase fractions along them using the lever rule for the balances of molar entropy and molar volume. The Gibbs phase rule cannot be used to analyze the dimensionality of phase regions anymore. As it can be seen, the dimensionality of phase regions in the molar phase diagram is the same of that of the phase diagram, which is true for systems with more than two independent potentials, and there is the MPL phase boundary rule as follows [3]

$$D^+ + D^- = r - b \qquad \textbf{Eq. 80}$$

where D^+ and D^- are the numbers of phases that appear and disappear, respectively, as a phase boundary of dimensionality b is crossed, and r is the number of axes in the molar diagram. The MPL phase boundary rule can also be applied to mixed phase diagrams when the dimension of two neighboring phase regions equals to that of the phase diagram.

Figure 4. Four types of phase diagrams of pure Fe: (a) $T-P$; (b) $T-V_m$; (c) S_m-P; (d) S_m-V_m with the green lines being tie-lines.

In thin films, the volume is replaced by two in-plane strains with two in-plane stresses as conjugate potentials, resulting in one more independent variable. Strains can be introduced into thin films through differences in lattice parameters, thermal expansion behavior between the film

and the underlying substrate, or defects formed during film deposition.[215] Furthermore, strain energy in thin films is a function of film thickness, which can be considered as another external variable, and the spatial arrangements of polarization configurations which are internal variables and reduce the total strain energy.

For example, the stability of individual polarization configurations of $PbTiO_3$ on a cubic substrate is shown in Figure 5a with the paraelectric, a, ac, aa, c and r phases considered. Their polarization configurations along the [100], [010], and [001] directions are $P_1 = P_2 = P_3 = 0$; $P_1 \neq 0$ and $P_2 = P_3 = 0$; $P_1 \neq 0, P_2 = 0$ and $P_3 \neq 0$; $P_1 = P_2 \neq 0$ and $P_3 = 0$; $P_1 = P_2 = 0$ and $P_3 \neq 0$; and $P_1 = P_2 \neq 0$ and $P_3 \neq 0$, respectively.[216] The film thickness was over 50nm, much larger than the ferroelectric correlation length. With the stoichiometry of $PbTiO_3$ fixed, the system behaviors as a one-component system with the misfit strain as an external variable. Since the external constrain is that all configurations must have the same misfit strain, the misfit strain represents a potential of the system in place of stress in the Gibbs phase rule equation. As shown in Figure 5a, the transition between c and r is second-order down to near zero K, indicating that the strain and stress in both configurations at the transition strain are the same. While the transition between aa and r is first order at low temperatures and reaches a critical point at high temperature, i.e. becoming second-order and merging with the second order transition between c and r. The second-order transition revert back to first-order transition at higher temperatures between paraelectric and c phases and between paraelectric and aa phases, respectively. However, this change does not represent a critical point because the first- and second-order transitions involve different phases, rather than the same phases as in the aa and r/c case where all of them merger into one phase.

On the other hand, Li et al. [217] used the phase-field method to simulate the three-dimensional arrangements of three possible polarizations orientation variants with the tetragonal axes along the [100], [010], and [001] directions of the cubic paraelectric phase, denoted by a_1, a_2, and c domains, and obtained the phase diagram shown in Figure 5b. The a_1/a_2 and $c/a_1/a_2$ domain configurations are in analogy to the aa and r phases above though not identical, but the stability regions of phases are rather different in Figure 5a and b. Particularly, Figure 5a is asymmetrical with respect to strain, while Figure 5b is symmetrical with the strain energy and domain wall energy taken into account.

Figure 5. Temperature-strain phase diagrams of $(001)_p$-oriented $PbTiO_3$: (a) with each polarization configuration considered separately and the second- and first-order phase transitions shown by thin and thick lines, respectively.;[216] (b) with the strain interactions and interface energy between configurations (domain wall) considered.[217]

One interesting observation is the four-phase equilibrium point of a_1/a_2, $c/a_1/a_2$, c, and paraelectric phases in Figure 5b using the phase-field method, which was also shown for $BaTiO_3$ with individual configurations.[216,218] This is probably related to the mixture of configurations discussed in Section 2.4.2 since the second-order transitions are not determined by free energy comparison of different configurations or phases as in the first-order transition of a one component system, and rather they are determined by the entropy of mixing of various configurations denoted by Eq. 30. This entropy of mixing should be significant because the energy differences between various configurations are in the range of a few meV/atom.[218] This

is further supported by the conclusions that the transitions between c and r and aa and r configurations are smooth even at zero K and second order at high temperatures as shown in Figure 5a [216,218] and the AIMD simulations discussed in Section 5.3.2.

Since the paraelectric cubic phase is unstable at zero Kelvin, its properties cannot be predicted from DFT-based first-principles calculations due to imaginary phonon modes.[219,220] One way to address this issue is to compute the phonon frequencies of a high temperature structure using the force constants calculated for related low-temperature stable structures. This approach was successfully applied to $SrTiO_3$,[221] and $PbTiO_3$,[222] which is in line with the "partition function" framework discussed in Section 2.4.2 and worth of further investigations as it provides an approach to predict the properties of high temperature phases which are unstable at low temperatures. We are actively working on the prediction of ferroelectric to paraelectric transition using the partition function approach discussed in Section 2.4.2.

5.1.2. Binary and ternary systems

Phase diagrams for binary systems are usually presented under fixed total pressure and are geometrically identical to those of one-component systems. For example, the $T - \mu_{Cr}$ and $T - x_{Cr}$ Fe-Cr binary phase diagrams are shown in Figure 6.

Figure 6. (a) $T - \mu_{Cr}$ and (b) $T - x_{Cr}$ phase diagrams of the Fe-Cr binary system under ambient pressure.

The phase diagrams of ternary systems are the same as those of one-component and binary systems when sectioned along two potentials. The common molar phase diagram of ternary systems is the isothermal section under fixed T and P with two compositions plotted in Gibbs triangle so that all three elements are treated symmetrically. When sectioned along the composition of one component, one usually plots a phase diagram between temperature and the composition of another component, i.e. an isopleth. As mentioned before, sectioning along the tie-line results in the reduction of one independent potential, and the isopleth thus behaves like a binary system called pseudo- or quasi-binary systems that are commonly used for ternary oxide systems.

5.1.3. Multicomponent systems

The isopleth is the primary phase diagram for multicomponent systems sectioned through a mixture of potentials and molar quantities. Figure 7 shows the isobaric $T - w_C$ phase diagram for the Fe-1.5Cr-0.4Mn-3.5Ni-0.3Si-C (in weight percent) system calculated using the TCFE6 thermodynamic database.[142] The numbers denote the zero-phase fraction (ZPF) boundaries, depicting that the phase is stable on one-side of the boundary only. The similar isopleth can be plotted with respect to other elements. The single fcc phase region is at the upper left corner of the phase region and critically important for homogenization treatment of materials.

Figure 7. Isopleth of the Fe-1.5Cr-0.4Mn-3.5Ni-0.3Si-C (in weight percent) system

The phase fractions for a given alloy can be plotted with respect to temperature to understand the evolution of phases under equilibrium conditions with an example showing in Figure 8 for the

Fe-25Cr-7Ni-4Mo-0.27N-0.3Si-0.3Mn (in weight percent) duplex stainless steel using the TCFE6 database. [142]

Figure 8. Phase fractions of the Fe-25Cr-7Ni-4Mo-0.27N-0.3Si-0.3Mn (in weight percent) duplex stainless steel as a function of temperature

5.2. Metastability

A metastable system is with $D < 0$ and $D_2 > 0$ in Eq. 8 for a smaller enough $d\xi$, but its energy is higher than those of more stable states with lower energies. Practically majority systems around us are metastable including most pure elements on the chemical periodic table and their alloys because they could be oxidized under ambient conditions to become more stable. Our metal-based civilization is in terms of the extraordinary kinetic stabilities of the reactive metals in oxidizing environments, attributed to the existence of a thin reaction product film on the metal surface that isolates the metal from the corrosive environment.[223]

In addition to this passivity, another main contributor is the high kinetic barrier (see Figure 3) so that the probability for the system to overcome the barrier is negligible, such as both diamond and cementite (Fe_3C) with respect to graphite in its pure form and in the Fe-C binary system. Metastable states can be obtained by removing the more stable phases from the equilibrium calculations of the system. The stability of cementite is particularly interesting. The Gibbs energy of formation of Fe_3C from pure Fe and graphite is negative, e.g. equal to −1620J/mole of formula of Fe_3C at 1169K. So Fe_3C should be stable based on the following reaction

$$3Fe + C = Fe_3C \qquad \textbf{Eq. 81}$$

However, Fe and C can form an interstitial solution to lower its Gibbs energy with respect to pure Fe and C, resulting in the Gibbs energy of Fe_3C above the tie-line between the Fe-C solution and graphite so that Fe_3C becomes metastable as shown in the Gibbs energy diagram in Figure 9.

Figure 9. Gibbs energy diagram of Fe-C binary system at 1169K and 1atm.[3]

The stability of a metastable state is usually discussed in terms of the transformation barrier represented by the maximum energy difference between the metastable and unstable equilibrium states as shown in Figure 3, with contributions from the interfacial energy and strain energy between the two states. However, the system reaches the limit of stability, i.e. the inflection points where $D_2 = 0$ marked by the two red filled circle between the metastable and top of the unstable equilibrium states, before it reaches the top of the unstable equilibrium state marked by the middle red filled circle. In the metastable region, the evolution of a system is usually considered to be deterministic based on physical laws though microscopically the system does not have to cross over the barrier, i.e. reaching the top of the unstable states first unless it is constrained along one given trajectory only such as diffusion. If the system in the unstable region has more than one possible trajectories, its evolution is in principle no longer deterministic and thus becomes stochastic. It is noted that van de Walle *et al.* [46,47] used the limit of stability to represented the lattice stability used in the CALPHAD modeling approach, while the SGTE lattice stability used in the CALPHAD community [137] was obtained by extrapolations

from the stable region to the unstable region, and the results from these two approaches seem agree with each other and will be further discussed in Section 5.3.3.

5.3. Instability

Modeling instability is challenging due to the divergency of the inverse of the 2nd derivative as shown by Eq. 79, i.e. mathematical singularity for the derivative of each extensive variable with respect to its conjugate potential. As discussed in the beginning of Section 5, there are two types of instability: the limit of stability with only the 2nd derivative being zero and the zero-dimension ICP with all derivatives being zero. The limit of instability can be seen in Figure 3 by the two red dots separating the stable and unstable regions, i.e. inflection points, where the system is not at equilibrium because its 1st derivative is not zero. While the ICP is when all the stable/metastable/unstable equilibria merge together into one point, so do the two inflection points, where the system is also at equilibrium because its 1st derivative vanishes.

5.3.1. Theory of critical point and its applications to Ce and Fe_3Pt in relation to Clausius-Clapeyron equation

Let us consider the critical point in the $T-P$ potential phase diagram for one component systems using Ce and Fe_3Pt as two examples as shown in Figure 10. Both have the fcc lattice structure, and their critical points are related to the change of magnetic spin configurations. The ground states of Ce and Fe_3Pt at zero K are non-magnetic (NM) and ferromagnetic (FM), and above the critical point they become ferromagnetic and paramagnetic (PM), respectively. As discussed earlier, if an external magnetic field is added, one can imagine that this critical point will become a line in the $T-P-\mathcal{H}$ space until it ends at an ICP.

It is interesting to see that the signs of the two-phase equilibrium lines are opposite to each other in the two potential phase diagrams, positive for Ce and negative for Fe_3Pt. Based on the Clausius-Clapeyron equation, the slope of a two-phase equilibrium line is related to the differences of their molar volume, ΔV_m, and molar entropy, ΔS_m, as follows

$$\frac{dT}{dP} = \frac{\Delta V_m}{\Delta S_m} \qquad \textbf{Eq. 82}$$

So that the high temperature FM Ce has a larger volume than the low temperature NM Ce, while the high temperature PM Fe_3Pt has a smaller volume than the low temperature FM Fe_3Pt.

Figure 10. $T - P$ potential phase diagrams for (a) Ce,[25] and (b) Fe_3Pt [224]

From the stability criteria shown by Eq. 11, the conjugate variables in a stable system change in the same direction of increase or decrease, i.e. T vs S, and $-P$ and V, so the sign of Eq. 82 depends on the change of V_m vs T and S_m vs $-P$. It is thus evident that at the regions slightly away from the critical point, V_m of Ce and Fe_3Pt would increase and decrease with the increase of temperature, respectively, indicating that the negative thermal expansion in the homogeneous Fe_3Pt phase originates from the negative slope of the two-phase equilibrium line. Consequently, the divergence of extensive variables with respect to their non-conjugate potentials, i.e., V_m vs T and S_m vs $-P$, is $+\infty$ for Ce and $-\infty$ for Fe_3Pt at the critical point, i.e., the non-conjugate variables in a stable system can change in different directions for different systems as discussed in Section 2.1 in relation to Table 1.

The sign of Eq. 82 was used to search for elements and compounds with potential negative thermal expansion through temperature-pressure phase diagrams.[224] It was found that all systems with experimentally observed negative thermal expansion exhibit negative slopes of two-phase equilibrium, i.e. Eq. 82, while there are many systems with negative slopes, but no negative thermal expansion was reported. It is noted that none of systems examined contain critical points in their equilibrium temperature-pressure phase diagrams. This can be understood by considering the two-phase equilibrium line extends into its metastable region at higher temperature, and ultimately becomes unstable at its metastable critical point, resulting in either positive or negative divergence of extensive variables with respect to their non-conjugate potentials.[22] As will be discussed shortly below, whether the anomaly is observed in the stable single-phase region depends on how close the system is to the critical point when the potential diagram is converted to a mixed potential-molar phase diagram for Ce and Fe_3Pt.

As discussed in the literature and in the text above, an ICP is usually presented as the instability of a homogenous system. However, it can be equally viewed as the merger of different phases, of which each is homogenous, into a macroscopically homogeneous system when the ICP is approached from the side of a heterogeneous system. This prompted us to develop a theory that the homogeneous system is a superposition of many possible stable and metastable configurations based on statistical mechanics that results in Eq. 32, which is briefly discussed below.

In statistical mechanics for a system with a number of possible configurations, the partition function of the system equals to the sum of partition function of possible configurations, i.e.

$$Z = \sum Z^k \qquad \textbf{Eq. 83}$$

The assumption is that all configurations are independent with each other, so that their probabilities can be represented by Eq. 31. However, this assumption is not valid when the probability of a metastable configuration in a stable matrix is considered as shown by Eq. 34 and Eq. 33. This is because when a metastable configuration appears statistically in the matrix of a stable configuration, an interface between the metastable and stable configurations is created, which generates elastic deformation due to their volume differences. The resulted interfacial energy and strain energy can not and should not be accounted for by the statistical mechanics, i.e. Eq. 83. These challenges can be approximately resolved by designing important configurations that contain those interfaces and using Helmholtz energy in the statistical mechanics instead of total energy commonly used in the literature.[10,25–27]

The Helmholtz energy of the system is thus obtained as follows

$$F = -k_B T lnZ = \sum p^k F^k - \sum p^k F^k - k_B T lnZ = \sum p^k F^k + k_B T \sum p^k lnZ^k - k_B T lnZ \qquad \textbf{Eq. 84}$$

$$= \sum p^k F^k + k_B T \sum p^k lnp^k$$

$$p^k = \frac{e^{-F^k/k_B T}}{e^{-F/k_B T}} = e^{-(F^k - F)/k_B T} \qquad \textbf{Eq. 85}$$

where F^k is the Helmholtz energy of configuration k that can be computed from Eq. 77 in terms of DFT-based first-principles calculations. It is important to mentioned that Eq. 77 can only be used for stable and metastable configurations and cannot be applied to unstable states because the vibrational entropy of unstable configurations cannot be calculated due to their imaginary vibrational frequencies.

For Ce, three magnetic configurations were considered, i.e. NM, antiferromagnetic (AFM), and FM configurations[25] While for Fe_3Pt, a supercell with 12 atoms was considered, resulting in $2^9 = 512$ magnetic spin flipping configurations (SFC), in which 37 SFCs are unique in terms of symmetry.[26] Their energies as a function of volume at zero K, i.e. $E_c(V)$ in Eq. 77, are plotted in Figure 11, showing the equilibrium between NM and AFM configurations/phases for Ce at negative pressure (common tangent with positive slope), and the equilibrium between FM and SFC configurations/phases at positive pressure (common tangent with negative slope). The increase of p^k for metastable configurations has the potential to result in the increase (for Ce) or decrease (for Fe_3Pt) of the system volume with the increase of temperature. The net change of volume for Fe_3Pt depends on the relative magnitudes of the decrease of volume due to the increase of p^k for metastable configurations with smaller volumes and the increase of volume of individual configurations due to their individual positive thermal expansions. This is demonstrated by the plot of the Helmholtz energy differences, $(F^k - F)/k_BT$ (see Eq. 85), for 37 SFCs of Fe_3Pt in Figure 12.

Figure 11. $E_c(V)$ in Eq. 77 for (a) Ce [25] and (b) Fe_3Pt [26]

Figure 12. $(F^k - F)/k_BT$ as a function of temperature plotted for 37 SFCs of Fe_3Pt.[224]

By replacing P in Figure 10 with its conjugate variable, V or V_m, one obtains the mixed potential-molar quantity phase diagram shown in Figure 13 along with several isobaric volume curves.[27] The anomaly, i.e. the dramatic increase or decrease of volume on each isobaric curves with the

increase of temperature in the single phase region, is marked by the pink open diamonds, and the critical point is denoted by the green open circle. Below the critical point, the homogeneous system with a mixture of various magnetic configurations is no longer stable and decomposes into a two-phase mixture in the area of miscibility gap with both phases being mixtures of various magnetic configurations, but with different proportions.

Figure 13. $T-(V/V_N)$ phase diagrams for (a) Ce, and (b) Fe_3Pt, with V_N being the equilibrium volume at atmospheric pressure and room temperature. [27]

The thermal populations of three configurations for Ce, two major SFCs, and all SFC for Fe_3Pt are plotted in Figure 14. For Ce, the population of the AFM Configuration at high temperatures is way higher than those of both FM and NM configurations, and the overall magnetic spin configuration is FM. For Fe_3Pt, even though the FM configuration has the lowest Helmholtz energy at all temperatures considered, its population is lower than 20% at high temperatures.

Figure 14. (a) Thermal populations of the nonmagnetic (red dot–dashed), antiferromagnetic (green dashed), and ferromagnetic (blue solid) as a function of temperature in Ce at the critical pressure of 2.05 GPa;[25] **(b) Thermal populations of the FMC (black solid line) and that of the sum over all SFCs (black dot-dashed line) with the two major contributions to the PM phase from SFC55 and SFC41, plotted using red dashed and long dashed lines, respectively, for Fe_3Pt at 1atm, respectively.**[26]

The phase diagrams in Figure 13 resemble the miscibility gap commonly seen in binary temperature-composition phase diagrams. Miscibility gap has been routinely modeled in CALPHAD databases, such as the fcc-based three-phase miscibility gap in multicomponent steels.[225] However, it was pointed out that CALPHAD modeling does not really address the instability because the divergency of molar quantities is not considered, and it is not clear how the singularity can be efficiently addressed by a closed mathematical form, and thus more work is needed.[10]

It is natural to think that if there is a technique with higher time and spatial resolutions comparable to the residence times and dimensions of metastable configurations, one would see many different configurations rather than a homogeneous system away from the critical point in the areas marked by the pink open diamonds in Figure 13, which can be far away from the critical point itself as shown. Even though there are no reports in the literature for Ce and Fe_3Pt, there are reports for other materials such as water,[226,227] ferroelectrics, [228–232] and thermoelectrics.[233] The ferroelectric $PbTiO_3$ is particularly interesting as introduced in Section 5.1.1 and discussed below. Of course, it should be noted that the microscopic mechanisms in different materials are different when their critical points are approached due to their intrinsic electronic structures and atomic interactions, demonstrating the importance to find the key configurations for each individual system. But the general statistical approach based on fundamental thermodynamics discussed here should be applicable to all systems.

5.3.2. Configurations in $PbTiO_3$

Under ambient pressure, X-ray measurements indicate a structure transition of $PbTiO_3$ from ferroelectric tetragonal (FE) to paraelectric cubic (PE) at 763K,[234] and the cubic structure is unstable at zero K.[219,235] The volume of the tetragonal FE phase decreases with the increase of temperature and increases in the cubic PE phase.[234] However, when both Pb and Ti edges were measured in XAFS (x-ray-absorption fine structure) analysis with the time and spatial resolutions being $\sim 10^{-16}$ sec (0.1fs) and 1st to 4th nearest neighbor shells, it was found that the displacements of the atoms within the unit cell vary little with temperature below the transition and decrease only slightly above the transition temperature.[228–230] In the PE phase, the Pb and Ti distortions are about 50% and 70% of the corresponding low temperature values, respectively. The presence of this distortion is readily apparent in the high-temperature data as the first ‘‘edge peak’’ above the Fermi energy does not disappear or become small as in centrosymmetric structures.

The local tetragonality is plotted Figure 15 in terms of lattice parameters of $PbTiO_3$ unit cell with the data from the x-ray diffractions[234] and AIMD simulations superimposed.[74] The AIMD simulations were performed with the lattice parameters of the supercell fixed to the values from the x-ray diffractions, i.e. tetragonal and cubic below and above the transition temperature, respectively.[234] In contrast to conventional molecular dynamics analyses where results are averaged over time, the atomic configurations in the AIMD simulations were categorized as a function of time in terms of the individual Ti-O bond lengths in the nearest-neighboring shell.

Figure 15. Temperature dependence of the lattice parameters a, c of $PbTiO_3$ unit cell with data in the open symbols from the XAFS measurements, [228–230] the closed symbols from the x-ray diffraction,[234] and the crossed symbols from AIMD simulations[74]

The AIMD simulations indicate that the cubic configuration exists at temperatures about 300 K even though the time-averaged overall atomic configuration is tetragonal. The quantitative results depict that as the temperature increases, the population of the cubic configuration increases and that of the tetragonal configuration decreases, and both become constant above the transition temperature as shown in Figure 16 with the majority of tetragonal configurations polarized. By following individual Ti atoms, it was observed that the tetragonal configurations with different polarization directions switch between each other with the cubic configuration as the intermediate state (see Figure 17).[17] It is thus concluded that the negative thermal expansion in the tetragonal phase region is due to the increased population of the transitory cubic configuration that has smaller volume and higher entropy than the tetragonal matrix, originated from the more frequent switching of the polarization directions and the longer total residence time at the cubic configurations at high temperatures.

When a group of tetragonal configurations change their polarization directions, the domain walls are created with neighboring tetragonal configurations with the original polarization directions. There are two types of domain walls in $PbTiO_3$, i.e. 90° and 180°.[236] Considering the multiplicities of these two domain walls, we are able to predict the FE-PE transition of $PbTiO_3$ in excellent agreement with experimental data. The details will be reported in a separate paper.

Figure 16. Fractions of the cubic (closed circles) and tetragonal (closed squares) configurations as a function of temperature, obtained from the AIMD simulations.[74] Among the tetragonal configurations, the fractions of the polarized and unpolarized ones in the <001> direction are shown in the open squares and open diamonds, respectively

Figure 17: Instantaneous lattice parameters of $PbTiO_3$ measured in all three directions as a function of AIMD simulation steps, (a) 623K, and (b) 753K. [17]

5.3.3. Limit of instability with $D_2 = 0$, $D \neq 0$ and $D_3 \neq 0$

It is commonly accepted that the system needs to overcome the full barrier in order to transform from a metastable state to a more stable state as shown by Figure 3. This is true when there is only one pathway between the metastable and stable states. One example is atomic diffusion during which the moving atom must cross over the top of the barrier to reach the next vacancy site, and the inflection point with $D_2 = 0$ only indicates that the increasing rate of resistance decreases moving forward. However, when there are more than one states that the system can attend after it crosses the limit of stability, the system can transform into those states spontaneously without barrier because the system is unstable. The spinodal decomposition in binary and multicomponent materials is such an example, in which an unstable homogeneous solution spontaneously separate into two or more states with different compositions and lower total energy without barrier, and the spatial arrangements of those states can be drastically different with small stochastic perturbations,[209,210] resulting in structures similar to those dissipative structures.[5,16] Therefore, the limit of stability alone cannot determine whether the system undergoes spontaneous transformations.

Recently, van de Walle et al. connected the energetics at the limit of stability, i.e. $D_2 = 0, D \neq 0$ and $D_3 \neq 0$, with the SGTE lattice stability obtained through extrapolations in the CALPHAD approach.[47] Their approach is based on three complementary points of view: (1) a topological partitioning of phase space in terms of curvature criterion of potential energy hypersurface; (2) stabilizing the system by constraining the minimum number degrees of freedom by neglecting the few unstable modes at the thermodynamic limit; and (3) smooth extrapolation of free energies from local minima through inflection points to cross the instability. The Ir–Re–W alloy system was selected as a benchmark because it combines elements that each favors a different lattice: Ir in fcc, Re in hcp and W in bcc. Furthermore, the difference of lattice stability for fcc W between CALPHAD modeling and the DFT-based first-principles calculations is about 30kJ/mole-atom, among the largest.[44]

Figure 18 plots the formation energies of bcc/hcp/fcc ideal solutions in the three binary systems in the Ir–Re–W ternary system from three methods: the inflection method and two DFT-base calculations with or without constraints on symmetry.[47] The energies at the inflection point are calculated by finding a path of steepest descent that connects the unrelaxed unstable configuration to the fully relaxed stable configuration in one of two ways: (i) the generalized nudged elastic band method with cell shape variations[237] or (ii) the 'damped' dynamics with the atoms repeatedly displaced in the direction of the force upon on them by a fixed distance. It can be seen that in stable regions, all three methods agree, but the inflection-detection method provides the smoothest extrapolation behavior into the unstable regions and agree with the values in the CALPHAD community (labeled as SGTE).[137] The DFT-based calculations with

symmetry-constrained relaxations, i.e. no change of space group during relaxations, give much higher formation energy, while the calculations for unstable structures without symmetry constrain resulted in full relaxation towards nearby stable phases.

Figure 18. Formation energies of ideal solid solutions in all binary subsystems of the Ir–Re–W alloy system, obtained via various methods. [47]

The work by van de Walle et al.[47] implies that the energy at the limit of stability represents the "apparent" energy of an unstable structure when extrapolated from various stable regions. This approach seems reasonable because after the system crosses the limit of stability, there is no need for the system to increase its energy anymore because the system can spontaneously assembly itself into a dissipative structure [16] with spatially distributed higher and lower energy regions with the summed energy lower than that of the original homogeneous system. Consequently, the higher energy region can venture further into the more unstable territory and can continuously dissipate itself in the same fashion until the high energy region crosses over the barrier and may even develop oscillating patterns,[16] in the same fashion as the spinodal decomposition discussed above [209,210,238] with the formation of self-assembly of complex structures.[239–241]

One can imagine that repetitive impacts from the surroundings to a system can bring the system across its limits of stability cyclically in a multidimensional space and result in more and more complex internal structures in the system. As pointed out by Prigogine, many systems can spontaneously organize themselves if they are forced away from thermodynamic equilibrium into unstable regions.[5,16] This is in analogy to the hypothesis by Oparin[242] that energy from the

Sun, electrical activity like lightning (or possibly impact shocks or ultraviolet light), and Earth's internal heat triggered chemical reactions to produce small organic molecules which were further organized into the complex organic molecules (such as proteins, carbohydrates and nucleic acids) as the basis of life. The key is that the external inputs bring the system across its limit of stability. Various concepts were elaborated in many recent publications,[243–245] demonstrating its extremely complex and controversial characteristics. Hopefully, the thermodynamics of limit of stability can help to enhance our understanding of the formation of dissipative structures and life.[10]

5.4. Materials design

The detailed understanding of stability, metastability, and instability of a system enables the design of materials for specific applications. As Olson articulated, the conceptual design of multilevel-structured materials is possible with a systems approach that integrates processing, structure, property, and performance relations through a hierarchy of computational models to define subsystem design parameters that are integrated through CALPHAD-based computational thermodynamics.[214,246]

5.4.1. Phase stability in alloys

The best example of materials design in terms of phase stability is probably the materials system chart for a high-performance alloy steel schematically shown in Figure 19 with three subsystems: strength, toughness, and embrittlement resistance.[214] The strength of the steel comes from the metastable lath martensite as the matrix of the steel and the nano-scale precipitates. The stable bcc phase is prevented to form due to sluggish diffusion with respect to fast cooling. The

martensitic transition temperature (M_s) is modeled as a function of composition when the Gibbs energies of the high temperature fcc phase (austenite) and the martensite with the same compositions equal to each other. The accurate calculations of M_s temperatures require an improved thermodynamic model of the martensitic phase. For further strengthening, the driving forces for the formations of undesirable carbides and topologically close pack (TCP) phases need to be made negative or minimized, while the driving forces for the MC and M_2C carbides must be enhanced through the optimal combinations of compositions and processing parameters to increase their nucleation rates. The sizes of the precipitates are to be maintained at nanometer scale through the coherent interfaces between the precipitates and matrix with the lowest interfacial energy to minimize the driving force for coarsening.

Figure 19. Materials system chart for high-performance alloy steel.[214]

The toughness is regulated by the lath thickness of martensite, austenite grain size that affects the packet size and lath thickness of martensite, and the amount of retained austenite that is softer than martensite and transforms to martensite under deformation with an increase of volume and at the same time absorb energy, that deflect the crack propagation and improv the toughness. The stability of grain refiner agents must be carefully controlled so they would not dissolve during the high temperature processing and be effective in reducing the grain size of austenite through nucleant particles. The stability of the retained austenite is determined by the alloy concentrations and the enrichment of carbon during the martensite formation.

The embrittlement resistance centers on the control of grain boundary segregation/desegregation to enhance the grain boundary cohesion and avoid the intergranular cracking. The thermodynamic description of intergranular embrittlement is related to the segregation energy difference to the free surface versus a grain boundary. Correlated with experimental embrittlement sensitivity data with the segregation energy difference from DFT-based first-principles calculations, it is possible to predict the embrittlement potency of a segregating solute with or without prior segregation of other solutes. Furthermore, the charge-transfer plots from the DFT-based calculations reveal that embrittling P and S with positive segregation energy differences undergo a nonhybridized electrostatic interaction with Fe and promote the formation a free surface, whereas the cohesion-enhancing B and C exhibit anisotropic hybridized bonding across the grain boundary. The DFT-based calculations also demonstrate that the embrittling effect of Mn is related to the strengthened in-plane bonding and thus the weakened out-plane bonding.

Another example is shown for the design of corrosion-resistant landing gear steel allowing a drop-in replacement for current non-stainless landing-gear steels, eliminating the need for cadmium plating with the strategy similar to that shown in Figure 19,[246] which was also listed as an ICME success example in a recent publication by National Research Council.[247] Another ICME success example in the same publication [247] is on the development of Ni-based superalloy GTD262 at GE to replace tantalum (Ta), a critical refractory element subjected to high risks of supply and price disruptions, in superalloy GTD222. Through integrating CALPHAD-based computational thermodynamic predictions of phase equilibria with GE's internal materials property models and databases, four alloys with niobium (Nb) replacing Ta and with

modifications to the concentrations of other elements to optimize and balance key properties and producibility. The best of the four alloys doubled creep-resistance performance with other properties remained comparable to those of the Ta-bearing GTD222 and successfully passed the industrial-scale production trial and qualifications without any technical hurdles.[248] The new alloy was introduced into GE power generation gas turbines in about 4 years from concept to industrial production at less than 20 percent of the typical alloy development cost. High-confidence CALPHAD-based thermodynamic predictions not only eliminated several of the experimental iterations that are usually needed to obtain the right alloy compositions, but also eliminated the long-term thermal exposure experiments that are generally required to test the propensity to form detrimental phases.

5.4.2. High entropy materials

In last two decades or so, a new group of materials, called high entropy alloys (HEA) or more generally high entropy materials (HEM), with equal atomic ratios of multicomponent elements has been extensively investigated.[249–253] The key argument is that the atomic mixing entropy, denoted by Eq. 37, is maximized for a given number of components in a solution phase when all components have the same mole fraction, i.e. central regions of multicomponent phase diagrams, thus lowering the Gibbs energy of the phase and increasing its stability. The development of HEMs includes single solution phases with one sublattice and compounds with more than one sublattices[254–257] for both structural and functional applications.[258]

Senkov et al. [259,260] used the then available CALPHAD databases developed by CompuTherm[143] to analyze thousands of 3-, 4-, 5-, and 6-component alloys at equiatomic compositions of the

alloying elements with the validity and reliability of the calculated phase diagrams estimated through the comparison with experimental binary and ternary systems. Based on a number of criteria they selected 27 elements from the chemical periodic table, i.e. Ag, Al, Co, Cr, Cu, Dy, Fe, Gd, Hf, Lu, Mg, Mn, Mo, Nb, Ni, Re, Rh, Ru, Sc, Si, Ta, Ti, Tm, V, W, Y, and Zr, with 2925, 17,550, 80,730, and 296,010 alloys in 3-, 4-, 5-, and 6-component systems, respectively. It was found that though most binary systems were modeled comprehensively, many CALPHAD modeling of ternary systems was lacking because databases were usually developed for alloys with one major element and relatively low contents of alloying elements. Nevertheless, their CALPHAD-based thermodynamic calculations predicted that the majority of the equiatomic alloys contain both solid solution, i.e. bcc/hcp/hcp with bcc being the most common one followed by hcp and fcc, and various intermetallic phases at the melting temperature and 600°C. Total 453 different phases were identified. The fraction of the solid-solution alloys decreases significantly with the increase in the number of alloying elements, e.g. from 46% to 10% in 3- and 6-component alloys at the melting temperature as shown in Figure 20, and from 30 to 4% at 600°C (not shown here), respectively. The elements that more often appear in solid solution phases at melting temperatures are Al, Cr, Hf, Mg, Mn, Mo, Nb, Re, Rh, Ru, Ta, Ti, V and W. The elements that appear less frequently in solid solution alloys are Fe, Ni, Sc, Y and Zr with Si completely absent. Further down selection was made by alloy density, Young's modulus, and cost.

Figure 20. Distributions of the N-component equiatomic alloys by the number of phases at the melting temperature with SS for solid solution and IM for intermetallic compounds. **259,260**

The more recent HEA CALPHAD database[261] developed by ThermoCalc included the enthalpy of mixing data for bcc, fcc and hcp solutions from the DFT-based calculations using the SQS approach.[194–197] Since the single solid solution phase regions depend on the Gibbs energies of both the solid solutions and intermetallic compounds, it is important to also improve the modeling of intermetallic compounds in the central regions of multicomponent phase diagrams. Due to the lack of experimental data, the large composition space in HEAs, and the complex structures of intermetallic phases, efficient theoretical predictions such as high-throughput DFT-based calculations and ML approaches are highly critical. As an example, we recently studied the σ phase in the Cr-Fe-Ni ternary system with the unit cell containing 30 atoms on 5 Wycoff positions.[262] The Gibbs energies of the $3^5 = 243$ end-members were calculated using the high-throughput DFT-based first-principles calculations, and the data is publicly accessible online at Citrine Informatics.[263] The site occupancies in various sublattices with ideal mixing in each sublattice are plotted in Figure 21 for the three binary systems in the Cr-Fe-Ni ternary system at 925K. The σ phase is stable in the Cr-Fe binary system, and the agreement between the predicted and experimental site occupancies are reasonable and can be improved by introducing vibrational entropy and interaction parameters in sublattices as shown in Eq. 47. The systematic inclusion of thermochemical data from DFT-based calculations can significantly speed up the development of multicomponent databases for HEMs with enhanced accuracy.[264,265]

Figure 21. Predicted equilibrium site occupancies at 925K for the Cr-Fe, Cr-Ni and Fe-Ni [262,263] in comparison with experimental data.[266,267]

For the entropy-stabilized oxide investigated by Rost et al.,[255], $(Mg, Ni, Co, Cu, Zn)O$ with equiatomic cation elements, i.e. 0.2 each, transforms from the two-phase mixture of rocksalt and tenorite to the single-phase rocksalt solution at temperatures above 875°C. Rocksalt MgO, NiO and CoO oxides are stable, while tenorite CuO and wurtzite ZnO oxides are stable. As the configurational entropy over k_B at equiatomic fractions is 1.609, the maximum theoretically expected configurational entropy difference at the transition temperature 875°C between the single species and the random five-species solid solution results in an energy of ~15 kJ/mole-atom, which is 5 kJ/mole-atom larger than the enthalpy of transition calculated from tenorite CuO and wurtzite ZnO to the rocksalt structure. Rost et al.[255] attributed this 5kJ/mole-atom difference to the enthalpy of mixing at the equiatomic composition. When the mole fraction of one cation changes to 0.10 or 0.30 with equiatomic fractions for other four cation elements, the decomposition temperature increases to 960°C on both sides for MgO, 985°C and 1010°C for NiO, 1000°C and 1050°C for ZnO, 1025°C on both sides for CoO, and 1025°C and 1050°C for CuO, respectively, as shown in Figure 22. The ideal configurational entropy over k_B is the same for all cation elements at 0.10 or 0.30 mole fraction of one cation element, i.e. 1.573 and 1.581, respectively, resulting in the increase of the decomposition temperature by about 20 to 27°C with respect to the 0.2 equiatomic composition. The differences of decomposition temperature of 65°C for 0.1 mole fraction of one cation element and 155°C for 0.3 mole fraction from MgO to CuO, respectively, are due to the enthalpy effect, which can be estimated to be about 850 and 2040 J/mole-atom, respectively. Further DFT-based first-principles calculations can be used to validate the above estimations.

Figure 22. Partial phase diagrams showing the transition temperature to single phase as a function of composition (solvus) in the vicinity of the equimolar composition where maximum configurational entropy is expected. Error bars account for uncertainty between temperature intervals. Each phase diagram varies systematically the concentration of one element. [255]

In an investigation of high-entropy high-hardness metal carbides, Sarker et al. [256] proposed a entropy-forming-ability (EFA) descriptor based on the energy distribution spectrum of randomized calculations as follows

$$\frac{1}{EFA} = \sqrt{\frac{\sum_{k=1}^{n} g^k (H^k - H_{mix})}{(\sum_{k=1}^{n} g^k) - 1}} = \sqrt{\frac{\sum_{i=1}^{n} g^k (H^k - [\sum_{k=1}^{n} g^k H^k] / \sum_{k=1}^{n} g^k)}{(\sum_{k=1}^{n} g^k) - 1}} \quad \textbf{Eq. 86}$$

where H^k and g^k are the enthalpy at zero K and the degeneracy of the configuration k, respectively. The middle portion of Eq. 86 denotes the standard deviation of enthalpy of all n configurations with H_{mix} being the simple average of enthalpy of all configurations. They hypothesized that the larger the *EFA* value, i.e. the smaller the standard deviation of the energy distribution spectrum above the ground state, the higher the configurational disorder capable of accessing equally-sampled states near the ground state and stabilizing high-entropy homogeneous phases. This is in accordance with the configurational entropy represented by Eq. 30 or Eq. 32.

A total of 56 five-metal compositions were generated using the eight refractory metals of interest (Hf, Nb, Mo, Ta, Ti, V, W, and Zr), resulting in a total of 2744 configurations with 10-atom supercells. Nine candidates were chosen for experimental synthesis and investigation with three

candidates of the highest values of EFA, two candidates with the lowest values of EFA, and four chosen at random with intermediate EFA values. It was a great success that the six five-metal carbides with the high EFA values are all single-phase materials after spark plasma sintering at 2200°C. It is noted that Eq. 86 is within the same framework as Eq. 84 and Eq. 85 by considering enthalpy only with the smaller difference representing the higher probability of metastable configurations and thus higher entropy among configurations as denoted by Eq. 30 or Eq. 32 if the entropy of individual configurations including vibrational and thermal electronic contributions (see Eq. 77) is considered.

5.4.3. Energy materials

The energy materials can be broadly defined as materials that convert energy between thermal/mechanical/electrical/magnetic/chemical energies as shown in Table 1 such as chemical/electrical in batteries and fuel cells, solar/chemical in photosynthesis, solar/electrical in photovoltaics, mechanical/electrical in ferroelectrics, electrical/magnetic/mechanical in motors, chemical/thermal/mechanical in engines, and so on. The conversion between chemical and electrical energy in battery fits to the current discussion the most as it involves the change of composition and energy storage in addition to energy conversion, and particularly the rechargeable Li-ion batteries (LIB) have revolutionized the industry in terms of energy conversion and energy storage.

In LIBs, the Li ions migrate through a lithium-containing electrolyte and interclade into cathodes (positive electrodes made of metal oxides such as $LiCoO_2$ and $LiFePO_4$) during charging and into anodes (negative electrodes such as the commonly used graphite) during discharge,

respectively. The chemical potential difference of Li between the cathode and anode gives the voltage through the Nernst equation as follows

$$-\Delta\mu_{Li} = -RTln\frac{a_{Li}^{+}}{a_{Li}^{-}} = zf\varepsilon \qquad \textbf{Eq. 87}$$

where $z = 1$ represents the moles of electrons in the cell reaction, *f* the Faraday constant equal to 96,485 J/V/mole-electron, ε the potential difference, often referred as electromotive force (emf) in the literature and being -3.0 Volts for the Li^{+}/Li electrode, and a_{Li}^{+} and a_{Li}^{-} are the Li activities in cathode and anode, respectively. The negative sign is because the system does work to the surroundings when the chemical potential, thus the Gibbs energy of the system, decreases.

For $LiCoO_2$ batteries, the graphite anode and cathode reactions can be written in simple forms as follows

$$Li_{1-x}C_6 = (1-x)Li^{+} + (1-x)e^{-} + 6C \qquad \textbf{Eq. 88}$$

$$(1-x)Li^{+} + (1-x)e^{-} + Li_xCoO_2 = LiCoO_2 \qquad \textbf{Eq. 89}$$

with the net reaction and electric potential being

$$Li_{1-x}C_6 + Li_xCoO_2 = LiCoO_2 + 6C \qquad \textbf{Eq. 90}$$

$$\varepsilon = -\frac{1}{(1-x)f}\{6{}^{0}G^{C} + {}^{0}G^{LiCoO_2} - G^{Li_{1-x}C_6} - G^{Li_xCoO_2}\} \qquad \textbf{Eq. 91}$$

$$= -\frac{1}{f}\left\{\left(\mu_{Li}^{Li_xCoO_2} - \mu_{Li}^{Li_{1-x}C}\right) - \frac{1}{1-x}\left(\mu_{LiCoO_2}^{Li_xCoO_2} - {}^{0}G^{LiCoO_2}\right)\right\}$$

The electric potential is a function of x. The value in the first parenthesis in Eq. 91 denotes the chemical potential difference of Li between two electrodes, and the value in the second parenthesis represents the chemical potential difference of $LiCoO_2$ between the states in the

solution phase of Li_xCoO_2 and by itself. Gibbs energies of $Li_{1-x}C_6$ and Li_xCoO_2 need to be obtained as a function x in order to calculate the electric potential of the battery.

The phase diagram for Li_xCoO_2 with x from 0 to 1 was predicted by first-principles calculations as shown in Figure 23.[268] The partition function and free energy in terms of Eq. 83 to Eq. 85 were utilized by omitting the electronic and vibrational degrees of freedom, i.e. F_{vib} and F_{el} in Eq. 77 for F^k, and considering only the contributions to the free energy of the configurational degrees of freedom associated with Li and vacancy distributions within different CoO_2hosts, i.e. the last term in Eq. 84 or Eq. 30 multiplied by $-T$. The energies of various configurations were calculated by the CE method with three host structures: O1 with an ABAB oxygen stacking, O3 with an ABC oxygen stacking, and H1-3 with an ABABCACABCBCAB mixed O1/O3 stacking. The finite temperature thermodynamic properties were obtained by MC simulations.[181,182] The three host structures O3, O1, and H1-3 are very similar to each other in that the O-Co-O slabs consist of edge-sharing CoO_6 octahedra and can be derived from the other by a simple gliding of the O-Co-O slabs with respect to each other adjacent to an empty Li plane. The charge density plots showed that although the Li ions are ionized, the electron transfer from Li to the host is very local through a significant increase in the electron density at the oxygen sites immediately surroundings the Li ions. [268]

Figure 23. Calculated Li_xCoO_2 phase diagram with x plotted on the x-axis and the insets showing the in-plane Li ordering predicted to be stable at $x = 1/2$ and 1/3, respectively.[268]

It can be seen in Figure 23 that the O3 host is stable for Li concentrations above $x = 0.3$. For Li concentrations above $x = 0.6$, the Li ions and vacancies remain disordered within the O3 host at all temperatures. The order-disorder transition temperature of the O3 phase is about 160°C, which is 100 °C higher than the experimentally measured value. The authors attributed this overprediction as typical of most first-principles phase diagram calculations within the local-density approximation, and it may also be related to the omission of F_{vib} and F_{el} since both would stabilize the disordered configurations,[224] plus the configurational entropy from various configurations with relatively small energy differences denoted by Eq. 30 or Eq. 32. At $x = 0.3$, a new ordered structure was predicted though not observed experimentally. At even lower Li concentrations centered around $x = 0.15$, the H1-3 configuration was found to be stable in qualitative agreement with experimental observation.

The computed voltage of Li_xCoO_2 as a function of x is plotted in Figure 24 with various functionals used in the DFT-based calculations,[269] showing that the hybrid HSE06 with the mixing parameter of 0.17 gives the best agreement with experimental data.[270] In two-phase regions, the calculated voltage remains constant because the chemical potential of Li does not change though the experimentally measured voltages are not constant as the full equilibrium may not have reached with the finite charging and discharging rates.

Figure 24. Computed voltage profiles of Li_xCoO_2 with various functionals with the experimental data superimposed.[269]

For $LiFePO_4$ batteries with metallic lithium as the anode, the half-cell and net cell reactions are as follows

$$(1-x)Li = (1-x)Li^+ + xe^- \quad \textbf{Eq. 92}$$

$$(1-x)Li^+ + (1-x)e^- + Li_xFePO_4 = LiFePO_4 \quad \textbf{Eq. 93}$$

$$(1-x)Li + Li_xFePO_4 = LiFePO_4 \quad \textbf{Eq. 94}$$

Its electric potential is also a function of x, i.e.

$$\varepsilon = -\frac{1}{(1-x)f}\{{}^0G^{LiFePO_4} - (1-x)\,{}^0G^{Li} - G^{Li_xFePO_4}\} \quad \textbf{Eq. 95}$$

$$= -\frac{1}{f}\left\{\left(\mu_{Li}^{Li_xFePO_4} - {}^0\mu_{Li}\right) - \frac{1}{1-x}\left(\mu_{LiFePO_4}^{Li_xFePO_4} - {}^0G^{LiFePO_4}\right)\right\}$$

The value in the first parenthesis in Eq. 95 denotes the chemical potential difference of Li between two electrodes, and the value in the second parenthesis represents the chemical potential difference of $LiFePO_4$ between the states in the solution phase of Li_xFePO_4 and by itself. Consequently, Gibbs energy of Li_xFePO_4 needs to be obtained as a function x in order to calculate the electric potential of the battery. Through the CE-MC method mentioned above,[271] the predicted phase diagram is shown in Figure 25. In the CE, the dependences of the energy on the arrangements of Li^+/V and Fe^{2+}/Fe^{3+}, i.e., both ionic and electronic degrees of freedom are considered with the generalized gradient approximation + U (GGA+U) calculations for 245 Li_xFePO_4 configurations and ferromagnetic high-spin Fe ions.

Figure 25. Li_xFePO_4 phase diagram. (a) Experimental phase boundary data;[272,273] (b) calculated with both Li and electron degrees of freedom, and (c) with explicit Li only. [271]

The calculated phase diagram shows a miscibility gap between $FePO_4$and $LiFePO_4$ at low temperatures and an unusual eutectoid transition to the solid solution phase around 400K about 20–70 K off from experimental estimations.[272,273] It was also shown that without the consideration of electronic degrees of freedom, i.e. Fe^{2+}/Fe^{3+} ordering, the calculated phase diagram (Figure 25c) shows one typical two-phase miscibility gap only, qualitatively different from experimental observations. The CALPHAD modeling of the Li_xFePO_4 phase diagram is shown in Figure 26 with various models.[274] The calculated voltage shown in Figure 27 is in good agreement with the experiments.[275] It is noted that three-phase miscibility gap has been observed in multicomponent systems such as in high strength low alloying steels,[225] but it is rare in binary or pseudo-binary systems as shown here for the Li_xFePO_4 system due to the internal degree of freedom in terms of the short-range ordering between Fe^{2+} and Fe^{3+} as demonstrated.

Figure 26. Phase diagrams of $FePO_4$and $LiFePO_4$ with various CALPHAD models.[274]

Figure 27. Calculated open-circuit voltage (OCV) curves obtained by: (a) delithiating $LiFePO_4$ via equilibrium phase transformation at various temperatures (298, 448, and 563 K) where the two voltage plateaus at 563 K are marked; and (b) delithiating $LiFePO_4$ and lithiating $FePO_4$ via spinodal decomposition and delithiating/lithiating via solid solution route at 298 K. [274]

Figure 28. Open-circuit voltage curves of LiFePO4 particles: open and solid circles denote the measured values during the discharging and charging process, respectively.[275]

It may be noted that when the electrolyte in an electrochemical system is an aqueous solution, the electric potentials for cathode reduction reactions are usually plotted with respect to $pH = -\log[H^+]$, where $[H^+]$ is the concentration of H^+ in the solution, in a Pourbaix diagram after its inventor to depict the stability relationships of ionic species and solid phases at constant temperature, pressure, and a constant concentration of one metallic element. With the CALPHAD thermodynamic models available, Pourbaix diagrams for complex materials can be calculated with one example shown in Figure 29 for a multicomponent amorphous alloy.[276]

Figure 29. Calculated Pourbaix diagram at 90°C in a solution containing 1000 g of H2O, 0.68 mol of NaCl (4 wt%) and one gram of alloy (Fe-2.5 at.% Mo-19 at.% Cr-4 at.% C-16-at.% B and 1.7 at.% W)[276]

5.4.4. Thermodynamically stable nanograins

Nanocrystalline alloys possess simultaneously superior strength and ductility in comparison with coarse grained alloys. However, they are usually not stable due to the large amount of grain boundary that provides huge driving force for rapid growth of their grains even at low temperatures, preventing their engineering applications. Segregation of alloying elements to grain boundaries and other interfaces has been studied for a long time, including the work by Gibbs.[1] It seems that Weissmüller started to discuss the reduction of the grain boundary energy by grain boundary segregation and articulated the concept for the stabilization of nanocrystalline solids against grain-growth by grain boundary segregation and the possibility of zero grain boundary energy in systems with large heat of segregation.[130,131] Through MD simulations of

bicrystals and a nanocrystalline network in fcc copper with oversized hypothetic dopants, Millett et al. [277] demonstrated theoretically that the grain boundary energy can be reduced to zero with systematically increasing dopant coverage and atomic radius mismatch in bicrystals and determined the critical dopant concentration required to eliminate grain growth in bulk and thin film structures.

Trelewicz and Schuh [278] developed a Gibbs energy function of a binary nanograin system by considering the intergranular bonds within the intergranular region and transitional bonds between the atoms in the intergranular and bulk regions with intergranular region assigned as a shell of finite thickness as shown in the following equation

$$\Delta G_{\mathrm{mix}} = (1 - f_{\mathrm{ig}})\Delta G^{\mathrm{b}}_{\mathrm{mix}} + f_{\mathrm{ig}}\Delta G^{\mathrm{ig}}_{\mathrm{mix}} + z\upsilon f_{\mathrm{ig}}\left\{[X_{\mathrm{ig}}(X_{\mathrm{ig}} - X_{\mathrm{b}}) - (1 - X_{\mathrm{ig}})(X_{\mathrm{ig}} - X_{\mathrm{b}})]\omega_{\mathrm{ig}} - \frac{\Omega}{zt}(X_{\mathrm{ig}} - X_{\mathrm{b}})(\gamma_{\mathrm{B}} - \gamma_{\mathrm{A}})\right\}. \quad (\text{Eq. 96}$$

The key model parameters are the grain boundary energies of the pure solvent and solute (γ_A and γ_B), the regular solution interaction parameters in the grain and intergranular regions included in ΔG^{b}_{mix} and ΔG^{ig}_{mix}, the coordination number (z), and the solvent atomic volume (Ω) along with approximations related to the bond distribution between the grain and intergranular regions (ν). For a given grain size which determines the fraction of intergranular region (f_{ig}), the equilibrium composition in the intergranular region is obtained by letting the derivative of the Gibbs energy with respect to the composition (X_b for grain or X_{ig} for intergranular regions) equal to zero, and the corresponding grain boundary energy is calculated by the derivative of the Gibbs energy with respect to the fraction of the intergranular region. When both derivatives equal to zero, a

thermodynamic stable grain configuration is obtained. Systematic parametric investigations were carried out for a range of model parameters, and qualitatively agreements with the experimental observations for the Ni-W and Ni-P systems were observed. [278]

Chookajorn et al. [132] used the model to predict the nanostructure stability map for tungsten based binary alloys, and the results at 1100°C are shown in Figure 30 with the enthalpy of segregation plotted with respect to the enthalpy of mixing in the bulk. The enthalpy of segregation is related to the differences of the regular solution interaction parameters in the grain and intergranular regions and the atomic volume and grain boundary energies of pure elements. The experimental validations were carried out using the pure W and the binary W-20at.%Ti alloy with the alloys processed by high-energy ball milling and about the same grain size of 20nm. The powders were then equilibrated at 1100°C in an argon atmosphere for one week. The unalloyed nanocrystalline W exhibits the normal grain growth to about 600nm, while the W–20at.% Ti alloy keeps its nanostructure with its nominally average grain size unchanged. This model has been successfully applied to a range of binary and ternary alloys.[279–282] Similar approach has also been developed by Saber et al.[283]

Figure 30. Nanostructure stability map for tungsten based binary alloys at 1100°C. [132]

Darling et al. [97] considered the two independent internal processes in terms of Eq. 65 for nanograins and derived the grain boundary energy similar to Eq. 76 The equations were tested for the Fe-Zr system and compared with available experimental data as shown in Figure 31a with the normalized grain boundary energy versus mole fraction of Zr in the grain boundary for an

alloy of $x_{Zr} = 0.03$ at $T = 550$℃ for several grain sizes. In Figure 31b the stabilized grain size is plotted as a function of temperature for different Zr molar fractions with the experimental XRD data for an $x_{Zr} = 0.04$ alloy superimposed, showing good agreement between predictions and experiments. Systematic calculations were then performed for binary systems of 44 solvents and 52 solutes, and as an example, the stability map for W binary alloys is plotted in Figure 32 with the elastic enthalpy versus the enthalpy of mixing for both the stabilizing (red dots) and non-stabilizing (black dots) solutes. This model has been extended to ternary systems with the normalized grain boundary energy contours plotted for an Fe-Ni-Zr alloys shown in Figure 33.

Figure 31. (a) Normalized grain boundary energy versus mole fraction of Zr in the grain boundary for an alloy with $x_{Zr} = 0.03$ at $T = 550$℃, showing the stabilized grain size of 23.1 nm; (b) Stabilized grain size as a function of temperature for different Zr molar fractions with the experimental XRD data for an $x_{Zr} = 0.04$ alloy superimposed, showing quantitative agreement between predictions and experiments. [97]

Figure 32. Nanocrystalline W stability map for both the stabilizing (red dots) and non-stabilizing (black dots) solutes [97]

Figure 33. Contour plot of iso-grain boundary energy in the bcc Fe-Ni-Zr ternary system.

5.4.5. Strain engineering and molecular beam epitaxial (MBE): TOMBE diagram

The strain engineering and epitaxial growth are often used interchangeably in the literature. The central theme is to manipulate the lattice structure and lattice parameter of thin films through the

constraints from the substrate.[215] Even though it is often termed as metastable phase equilibria for thin films, it is not strictly accurate because the system is internally at a stable equilibrium. The epitaxial constraint that restricts the lattice structure of the thin film, i.e. the coherent interface between the substrate and the thin film, is an external condition placed on the thin film as the substrate is usually not included as part of the system. When the bulk stable phase has the similar lattice structure of the substrate, it is likely that the thin film of this phase will form. When the bulk stable phase cannot have a coherent interface with the substrate, the competition arises between the interfacial energy and strain energy, and the interfacial energy usually dominates due to the very large surface to volume ratio of atoms for thin films. It should be emphasized that due to the strain/stress inhomogeneity in the thin film, the energetics of the system has to be investigated through integration and thus depends on spatial arrangements of domains and phases as illustrated in Figure 5 and the related discussions.[216,217] Nevertheless, computational thermodynamics can give valuable guidance on processing design as shown in some examples below.

For the then newly discovered superconductor MgB_2,[284] the stable region of the gas and MgB_2 two phases can be calculated through the CALPHAD modeling of the Mg-B system,[285] as shown in Figure 34 for a section through $x_{Mg}/x_B \geq 1/2$.[286] It was shown that the phase relations do not change with higher ratios due to the phases being stoichiometric and the gas phase of nearly pure Mg. It is important to realize that the total pressure in the thermodynamic calculations equals to the vapor pressure of Mg due to the near zero vapor pressure of B at the temperature range of interest, representing the activity of Mg. The system pressure is thus not an independent variable anymore in the thermodynamic calculations when the gas phase is involved.

The high pressure of Mg needed to form MgB_2 is impractical for many vacuum deposition techniques and prompted the development of the hybrid physical–chemical vapor deposition (HPCVD) technique,[287] with diborane (B2H6) as the boron precursor gas and heated bulk Mg in the deposition chamber as the Mg source. The (0001)-oriented MgB_2 films form as in-plane epitaxy on (0001) sapphire and (0001) 4H-SiC substrates which have six-fold symmetry characteristic. The dominant in-plane epitaxial relationship is that the hexagonal MgB_2 lattice is rotated by 30° to match the hexagonal lattice of sapphire, but is directly on top of the hexagonal lattice of SiC owing to the close lattice match.

Figure 34. Mg-B pressure-temperature phase diagram with $x_{Mg}/x_B \geq 1/2$. [286]

In many other cases, the lattice structure of the substrate stabilizes the phases that are metastable in unstrained conditions as reflected in our previous publications including $BiFeO_3$,[288] $BiMnO_3$,[289] $LuFe_2O_4$,[290] $PbTiO_3$,[291] $BaSnO_3$,[292] $BaFe_2As_2$,[293] $SrRuO_3$ and $CaRuO_3$,[294] and $\alpha - SnS$.[295] Particularly worth further discussion is the case for $SrRuO_3$ and $CaRuO_3$ with a combined pressure-temperature *potential* phase diagram based on the thermodynamics of MBE (TOMBE) growth shown in Figure 35, sectioned along a given Ru partial pressure evaluated from its flux.[294] It can be seen that this diagram is a combined pressure-temperature *potential* phase diagram with top and bottom parts based on the thermodynamics of MBE growth conditions, thus termed as a TOMBE diagram. The solid lines in the bottom half of Figure 35 are the typical Ellingham diagram applied to the Sr-Ru-O and Ca-Ru-O ternary systems, respectively. They depict the windows under which different members of the $Sr_{n+1}Ru_nO_{3n+1}$

and $Ca_{n+1}Ru_nO_{3n+1}$ Ruddlesden-Popper (RP) series are thermodynamically stable. There are three solid phases in equilibrium on each line, and the Gibbs phase rule for a three-component system from Eq. 29 is as follows.

$$v = c + 2 - p - n_s = 5 - 4 = 1 \qquad \textbf{Eq. 97}$$

where n_s is the number of fixed potentials, the pressure in the present cas. This results in one independent potential, i.e. lines in the bottom half of the phase diagrams in Figure 35. Along those lines, the partial pressures of all species in the system are a function of temperature including the partial pressure of oxygen plotted on the vertical axis of the diagram. It should be noted that the gas phase is not explicitly presented in the calculations, but represented by the sum of partial pressures of all species in the gas phase.

Figure 35. TOMBE diagrams illustrating the adsorption-controlled growth window for (a) $Sr_{n+1}Ru_nO_{3n+1}$ and (b) $Ca_{n+1}Ru_nO_{3n+1}$ phases.[294]

When the oxygen partial pressure is higher enough to vaporize all Ru in the form of RuO_x with RuO_2 and RuO_3 as the primary species, the equilibrium between various RuO_x correlates the partial pressures of Ru and O_2, and the Gibbs phase rule thus becomes

$$v = 3 + 2 - p - 2 = 3 - p = 3 - 2 = 1 \qquad \textbf{Eq. 98}$$

A line in a potential phase diagram, i.e. $v = 1$, thus represents a *two-phase equilibrium*, as shown by the dashed lines in the top half of Figure 35. The light green shaded regions in the figure are the adsorption-controlled growth windows for $SrRuO_3$ and $CaRuO_3$, respectively.

The boundary separating the top and bottom halves in Figure 35, i.e. the thin dashed near-horizontal brown line, is the equilibrium between the solid and gas phases in the O-Ru binary system. With given incoming flux of Ru, i.e. $1.95\times10^{13}\ atoms/cm^2/s$ and $3.2\times10^{13}\ atoms/cm^2/s$ for Figure 35(a) and (b), respectively, the oxygen partial pressure becomes a dependent variable as a function of temperature with the Gibbs phase rule written as

$$v = 2 + 2 - p - 1 = 3 - p = 3 - 2 = 1 \qquad \textbf{Eq. 99}$$

Furthermore, the cyan lines show the equivalent oxidation potential for ozone partial pressures ranging from $10^{-11} - 10^{-5}$ Torr, illustrating the benefit of having ozone as an oxidant while maintaining the long mean free path with low total pressure necessary for MBE.

Another important factor for oxide MBE is the source materials. MBE traditionally utilizes elemental molecular beams as shown above. However, this is challenging when various elements have different vapor pressure and potency for oxidation. Alternatively, one might be tempted to just evaporate the desired oxide directly. In general, such an approach does not work due to two factors: different vapor pressures of elements in the oxide and incongruent evaporation of the oxide, resulting in changing partial pressures of the species from the source over time and making it very difficult for the controlled deposition of thin films. Recently, we conducted a comprehensive thermodynamic analysis of the volatility of 128 binary oxides to evaluate their suitability as source materials for oxide MBE.[296] 16 solid or liquid oxides were identified that evaporate nearly congruently from stable oxide sources to gas species and 24 oxides could provide molecular beams with dominant oxygen-containing gas species. It was also discovered that the two-phase mixtures of a wide range of elements and their oxides can provide stable sources of dominant oxygen-containing gas species with very high flux, which can be

further oxidized to form desired oxides with high growth rates, easy control of dopants, and low defects in comparison with the existing, state-of-the-art techniques. It is termed as suboxide MBE or S-MBE because the dominant oxygen-containing gas species, called suboxides, needs to be further oxidized to form the desired oxides. [296]

5.4.6. Additive manufacturing and functionally graded materials

Additive Manufacturing (AM), also known as three-dimensional printing or layer manufacturing, is a freeform fabrication process by which an object is built up, layer by layer, via selective deposition of material.[297] The AM process is unique compared with other manufacturing technologies because a component can be built without the removal of material. Polymer AM has been well established over the last decades, and AM of metallic alloys is more recent due to higher melting temperatures needed and lower viscosity of molten metal. Debroy et al. recently presented a critical assessment of process, structure and properties of metallic components by AM,[298] and Reichardt et al. reviewed the advances in metal-based functionally graded materials (FMG) by AM in which the compositions are varied spatially to tailor the location specific properties.[299] One of the important features of the AM process is the fast and repeated heating and cooling in the consolidated layers, including partial remelting, when new layers are continuously added.

Keller et al. [300] combined thermal modeling by finite element analysis to simulate the thermal profile of the laser melt pool. They used the Scheil-Gulliver solidification model and DICTRA and TC-Prisma simulation tools [142] to predict microsegregation between dendrite arms during solidification of the melt pool, and the phase-field simulations to calculate the primary

cellular/dendritic arm spacings, using Ni-Nb as a binary analogue to Inconel 625. The CALPHAD thermodynamic and atomic mobility databases were used in the simulations involving atomic diffusion.[100] In the Scheil-Gulliver solidification model,[301,302] the diffusion in the liquid phase is assumed to be infinite, thus a perfect atomic mixing, while the diffusion in solid phases is assumed to be zero. It represents a scenario of solidification when the cooling rate is fast enough to prevent the diffusion in sloid phases and slow enough for rapid diffusion in the liquid phase due to the large difference in their diffusion rates. It is self-evident that the other scenario is to assume that the diffusion is also infinite in the solid phases, i.e. the equilibrium calculations. The reality is then between these two scenarios such as the one-dimensional simulations using DICTRA[303] or two- and three-dimensional simulations using phase-field[304] or other methods such as the Kampmann-Wagner numerical (KWN) method [305,306] implemented in ThermoCalc[307] and Pandat[308].

A Scheil-Gulliver solidification simulation starts when the temperature reaches the liquidus of an alloy. An equilibrium calculation is then performed at a lower temperature, usually one or several degrees lower than the liquidus, to obtain the compositions and fractions of liquid and solid phases. The composition of the liquid phase is subsequently used as the over-all composition for the equilibrium calculation at the next lower temperature. This process continues until the amount of liquid becomes practically zero or the composition reaches a multicomponent invariant eutectic point. The simulation results in Inconel 625 showed significant microsegregation for all elements. The temperature profile from the FEM analysis by Keller et al. [300] was validated by the surface temperatures from the *in situ* thermographic measurements. The alloy was re-melted during the second scan temperature peak, and the

DICTRA simulation using the simulated temperature file was thus carried out for the second and third laser scans and show very minor homogenization of the segregated profiles. The fcc phase fraction as a function of temperature from the DICTRA simulation is very close to those from the Scheil-Gulliver model.

For the parameters chosen for the phase-field simulations in the Ni-4%Nb binary alloy, cellular domains were observed with much less microsegregation than that predicted by a Scheil-Gulliver analysis and DICTRA simulations of the same binary alloy, and the simulated primary cellular arm spacings is in agreement with experimentally measured spacings in observed microstructures. Since the precipitates of other solid phases were not considered, the driving forces for precipitates were calculated using the fcc phase composition when 1% liquid remains. It was found that the MC carbide is with the largest driving force to form, in qualitative agreement with the carbides of 50-200nm near cell/dendrite boundaries observed after the stress-relief treatment. [300]

The FGMs by AM add another layer of complexity with the spatial change of compositions.[309] We have studied a series of FGMs in recent years, including Ti-6Al-4V (Ti64) to V (Ti64/V),[309] stainless steel (SS) 304L to Invar (SS304L/Invar),[309] SS304L to Inconel 625 (SS304L/IN625),[310] Ti64 to Invar (Ti64/Invar),[311] Ti64 to SS304L (Ti64/SS304l),[312] V to Invar (V/Invar),[313] and SS420 to V to Ti64 (SS420/V/Ti64), Ti64 to V to SS304 L (Ti64/V/SS304L), and SS420 to V (SS420/V)[314] through experimental and computational investigations. The formation of detrimental phases in most FGMs calls for more sophisticated design of the composition paths between the ending alloys. One approach is through equilibrium calculations in one temperature

below which solid phase transformations are kinetically precluded through simple calculations [310–314] or a temperature range to circumscribe the phase regions of the undesirable phases through systematical explorations of composition and temperature spaces.[315,316]

Scheil-Gulliver analysis can be performed along the composition path of a FGM.[317–319] To facilitate the Scheil-Gulliver analysis of FGMs of multicomponent alloys, a simulation tool based on PyCalphad[145,146], called "*scheil*" and distributed on the Python Package Index (PyPI) [320], was developed.[318,321] It provides simulation results in a user-friendly data structure that can be post processed and combined into higher level analysis. The s*cheil* code enables high-throughput simulations in multicomponent composition space and can thus be used as a design tool for screening predictions of solidification products and viable FGM compositional paths.[318] Simulation results for both Scheil-Gulliver and equilibrium solidification are stored in a *SolidificationResult* data structure that provides access to the phase fractions and phase compositions of all the phases in the system throughout the simulation.

To ensure global minimization during the simulation, additional candidate grid points are adaptively added to the point grid for starting point generation and global minimization.[155] They correspond to the site fractions of the equilibrium phases found at a particular temperature. Since the site fractions of the stable phases at T_i are likely close to those at T_{i+1} both the performance and accuracy of the energy minimization in PyCalphad are improved by starting near the global minimum solution. One of the key features of the *scheil* code is the ability to distinguish and treat separately ordered and disordered configurations of phases that are modeled using a partitioned order-disorder model.[322,323] It allows the solidified phase fractions of the

ordered and disordered configurations to accumulate separately, even if they both form at the same temperature step. The *scheil* code can perform multiple simulations by looping over a series of compositions. The composition pathways may correspond to a linear or non-linear gradient path, or a grid in multicomponent composition space as part of a more complex data-driven path planning simulation.

As an example, the *scheil* simulations were performed for a commercial pure Ti to Invar (CPTi/Invar) and Ti64/Invar[311] FGMs using experimentally measured composition paths and a temperature step size of 10˚C until the fraction of material solidified reached 0.9999.[318] It was tested that the results are insensitive to the temperature step size in the range of 1-10 ˚C. All the results in this publication were created using *scheil* version 0.1.2 [321] and PyCalphad version 0.8.1[146] with a Jupyter notebook containing all of the code. [324] The liquidus project of the Fe-Ni-Ti system is shown in Figure 36, which is used to approximate the Ti64/Invar FGM with the measured compositions normalized to the ternary system. The compositions are marked by layer number and colored in red (closed circles) for the Ti64/Invar and blue (open circles) for CPTi/Invar FGMs, respectively. It is interesting to note that the region with the Laves phase as the primary crystalline product is divided into three regions separated by dashed lines which correspond to the three eutectic points where the Scheil-Gulliver simulations end. The regions and corresponding eutectics are labeled E1, E2, and E3, respectively.

Figure 36. Liquidus projection of the Fe-Ni-Ti system based on the CALPHAD modeling [325] with other information in the text. [318]

The Scheil-Gulliver and equilibrium solidification calculations are presented in Figure 37 for the linear gradient between Ti and Invar, respectively. Both figures have deconvoluted the disordered bcc phase from the ordered B2 phase, which were modeled as the same phase in the thermodynamic database.[325] In addition to the difference in phase fractions between the Scheil-Gulliver and equilibrium solidification calculations, the Ni_3Ti phase is only predicted by the Scheil-Gulliver solidification calculations, which were observed in several Ti64/Invar layers.[318] This demonstrates the usefulness of the Scheil-Gulliver model in predicting the solidification phases during the AM process and design the FGMs to control the formation of phases along the composition pathways.

Figure 37. Phase fractions of the as-solidified phases predicted along the linear gradient path from Ti to Invar using the Scheil-Gulliver model (a) and the equilibrium solidification (b). [318]

5.5. Extension to kinetics and mechanics

In addition to applications discussed above, computational thermodynamics can be used to predict other properties as shown in Table 1, such as elastic properties[82,326–328] and thermal expansion[27,329–331], with many more to be explored. In this section, two applications to kinetic properties are discussed, i.e. the diffusion and Seebeck coefficients in relation to the transition states between two stable states and the second derivatives in Table 1, respectively, followed by brief discussions on general off-diagonal transport coefficients and calculations of mechanical properties.

5.5.1. Diffusion coefficient

Diffusion coefficients are usually calculated through molecular dynamic simulations.[332,333] The main challenge to predict diffusion coefficients directly from DFT-based calculations is because the vibrational properties at the unstable transition state cannot be defined due to imaginary vibrational frequencies. Fortunately, this issue was already addressed in the absolute rate theory of reaction by Eyring[334,335] and in the transition state theory (TST) by Vineyard,[336] both giving the successful jumping rate of diffusion as follows

$$\Gamma = \frac{k_B T}{h} e^{\Delta S_{mi}/T} e^{-\Delta H_{mi}/k_B T} \qquad \textbf{Eq. 100}$$

where h is Planck's constant, and ΔH_{mi} and ΔS_{mi} are the migration enthalpy and entropy, respectively, denoting the differences between the transition and ground/equilibrium states. The free translational degree of freedom in the transition state is moved to the $\frac{k_B T}{h}$ so the enthalpy and entropy at the transition state are evaluated with the imaginary vibrational frequency removed. Consequently, the diffusion coefficients for vacancy-mediate self-diffusion in Al [337] and the interstitial diffusion of interstitial hydrogen (H), deuterium (D), and tritium (T) in Ni [338] were successfully predicted completely from the DFT-based first-principles calculations as shown in Figure 38 along with the Gibbs energy of formation of vacancy in Al. The intermediate states between the ground and transition states, i.e. various ξ in Eq. 8, are obtained by the nudged elastic band method.[339] The same approaches were subsequently applied to self-diffusion coefficients in bcc and in hcp with diffusion in the basal plan and perpendicular to the basal plan, respectively.[340]

Figure 38. Predicted vacancy concentration (a) and self-diffusion coefficient (b) in fcc Al [337] and interstitial diffusion coefficients of interstitial hydrogen (H), deuterium (D), and tritium (T) in Ni (c) [338]

For dilute solute diffusion, the jump of the solute atom into a neighboring vacant site is complicated by the neighboring jumps. In the presence of a solute the jump frequencies of solvent atoms around the solute are different compared with that in the pure element system. Each of these distinct atomic jumps contributes to solute diffusion. Le Claire and Lidiard [341] established the five jump frequency model for diffusion in dilute fcc alloys with dilute vacancy concentration. All of them can be predicted in terms of Eq. 100 by the DFT-based first-principles calculations as shown above based on the absolute rate theory of reaction [334,335] and TST.[336] The solute diffusion correlation factor is related to the probability of the impurity atom making a reverse jump back to its previous position and can be calculated from various jump frequencies.[342] The predictions were made for solute diffusion coefficients in fcc Al,[342–344] fcc-Ni,[98,345,346] bcc-Fe,[99,347,348] bcc Mo,[340] and the high-throughput dilute diffusivity database.[349]

The prediction of dilute solute diffusion coefficients in hcp proved to be more challenging with less satisfactory agreements with experimental data in calculations using the local density approximation (LDA) in the DFT-based calculations.[340,350,351] In a more recent work,[352] the improved generalized gradient approximation (GGA) of PBEsol [353] exchange-correlation functionals were used, resulted in better vacancy formation energies and vibrational properties and thus more accurate quantitative predictions of diffusion coefficients, including the self-diffusion coefficient shown in Figure 39 and the dilute diffusion coefficients of 47 substitutional

solutes in hcp Mg.[352] It was also found that correlation effects are not negligible for solutes Ca, Na, Se, Sr, Te, and Y, in which the direct solute migration barriers are significantly smaller than the solvent migration barriers. This indicates that the larger solute atoms can move faster while the smaller ones move slower, with the exception of Se. However, it should be kept in mind that the diffusion coefficients depend on both the vacancy formation and migration free energies.

Figure 39. Predicted self-diffusion coefficients in Mg from LDA,[350] GGA,[350] and PBEsol[352] compared with experimental data (see references in [352]).

Diffusion in phases with short- and long-range ordering is much more complicated because the migration barriers of individual jumps are affected by the local atomic environments that can result in strong correlations between successive jumps and ultimately diffusion coefficients. Van der Ven et al. [354–356] used the cluster expansion to describe both the equilibrium and transition states by considering all relevant jumps with their barriers and jump frequencies (Eq. 100) obtained from DFT-based first-principles calculations. Since migration barriers depend on the direction of the jump in a concentrated alloy, a kinetically resolved activation (KRA) is defined by the energy difference between the transition state and the average of two equilibrium states before and after the jump to separate the direction dependence of the migration barrier from the environmental dependence. Once cluster expansions for the equilibrium states of the jump and the KRA barrier for each of the jump types are parametrized using first-principles training data, the migration barrier for any local environments can be calculated efficiently. Atomic trajectories through stochastic atom-vacancy exchanges can then be sampled with kinetic Monte Carlo simulations as shown for the Ni-rich Ni-Al alloys in Figure 40 including disordered fcc

and ordered $L1_2$ phases.[356] The calculated tracer coefficients are an order of magnitude smaller in comparison with experimental data with possible sources of errors from neglected vibrational contributions in the determination of the equilibrium vacancy concentration and the thermal expansion, and both of them become more important at high temperatures and tend to reduce migration barriers and increase the diffusion coefficients.

Figure 40. Tracer diffusion coefficients of Al and Ni at 1300K as a function of concentration in disordered fcc and ordered $L1_2$ phases.[356]

5.5.2. Seebeck coefficient

Thermoelectric effects, measured by Seebeck coefficients, refer to phenomena in which a temperature gradient across a thermoelectric material induces an electrical potential gradient, and vice versa, enabling the direct conversion between thermal and electric energies.[357–359] According to classical mechanics, the net force felt by a charge carrier (q) equals to the negative gradient of its potential, $-\nabla\mu_q$. This force can be expressed as an effective electric field, $-\nabla\mu_q/Q_q$, where Q_q represents the q's charge. Hence, the electrical current, J_q, can be written as

$$J_q = -\frac{1}{Q_q}\sigma\cdot\nabla\mu_q \qquad \textbf{Eq. 101}$$

where σ is the electrical conductivity. It is important to realize that the number of charge carrier is an additional natural variable to be added to the combined law of thermodynamics. In the case of Gibbs energy in terms of Eq. 14, the potential of the charge carrier is a function of all the natural variables, i.e. $\mu_q(T, P, N_i, n_q)$, where n_q is the number of moles of charge carrier.

In formulating thermoelectric effects, the current is usually expressed as follows[359]

$$J_q = \sigma \cdot (-\nabla V_e - S_e \cdot \nabla T) \qquad \textbf{Eq. 102}$$

where ∇V_e is the local electric field induced by the charge carrier gradient, ∇n_q, S_e the Seebeck coefficient, and ∇T the temperature gradient. In the literature, S_e has been determined from the kinetic Boltzmann transport theory.[360–362] As we demonstrated recently, S_e is a thermodynamic quantity shown in Table 1, and by Eq. 21 [363,364] as derived below.

Comparing Eq. 101 and Eq. 102, one obtains[363,364]

$$\nabla \mu_q = q\nabla V_e + qS_e \cdot \nabla T \qquad \textbf{Eq. 103}$$

$$\nabla V_e = \frac{1}{q}\frac{\partial \mu_q}{\partial n_q}\nabla n_q \qquad \textbf{Eq. 104}$$

$$S_e = \frac{1}{q}\frac{\partial \mu_q}{\partial T} = -\frac{1}{q}\frac{\partial S}{\partial n_q} = -\frac{1}{q}S_q \qquad \textbf{Eq. 105}$$

The last part of Eq. 105 is taken from Table 1, or Eq. 21 with S_q being the partial entropy of charge carrier. μ_q is related to the electronic density of states (e-DOS) which can be calculated from Mermin's finite temperature density functional theory [365,366] as demonstrated in previous work [363] and is also used to calculate the thermal electronic contribution to free energy, F_{el}, in Eq. 77. The reference state of μ_q is conventionally set to the Fermi energy at 0K. Since electrons are explicitly treated in the current implementation [367,368] of first-principles calculations, μ_q obeys the Fermi-Dirac distribution as follows

$$f = \frac{1}{\exp\left[\frac{\varepsilon - \mu_q}{k_B T}\right] + 1} \qquad \textbf{Eq. 106}$$

where ε is the band energy using the Fermi energy as the reference. In such a way, μ_q is determined by the conservation equation

$$\int n(\varepsilon, V) f d\varepsilon = N_e \qquad \textbf{Eq. 107}$$

where $n(\varepsilon, V)$ is e-DOS, and N_e the number of electrons included in the DFT-based first-principles calculations.

The e-DOS of PbTe calculated using WIEN2k package [369] is shown in Figure 41 in the full range at zero K and near the Fermi energy for p- and n-doping at zero K and 610K, respectively.[363] PbTe is an intrinsic semiconductor as indicated by its 0K e-DOS shown in Figure 41a with the conduction band unoccupied and separated by an energy gap from the completely filled valence band. When the e-DOS curve has a negative slope at the 0 K Fermi energy with respect to the band energy as in the present case of p-type PbTe, the chemical potential of electrons increases with increasing temperature as shown in Figure 41b. On the other hand, when the e-DOS curve has a positive slope with increasing energy at the 0 K Fermi energy with respect to the band energy as in the case of n-type PbTe in Figure 41a, the chemical potential of electrons will decrease with increasing temperature as shown in Figure 41c.

Figure 41. Calculated results for PbTe, a) e-DOS (black curve); b) e-DOS near the Fermi energy for p-doping; c) e-DOS near the Fermi energy for n-doping; with the areas shaded by gray (partially overlapped by the blue semitransparent shaded areas) for the electron occupation at 0 K and the blue semitransparent shaded areas for the electron occupation at a finite temperature 610 K described by the Fermi distribution. [363]

The calculated Seebeck coefficients are compared with experimental data in Figure 42 for p-type and n-type PbTe with various doping levels, showing remarkable agreement with experimental measurements.[363] The comparison was also made for p-type SnSe with both experimental data and data calculated from the Boltzmann transport theory as shown in Figure 43, demonstrating much better agreement from the present thermodynamic approach. The comparison between the thermodynamic and Boltzmann transport theory approaches were also compared for p- and n-type PbTe, showing better agreement from the present thermodynamic approach with respect to the experimental data. [363] The calculations were made for the mobile charge carrier concentrations for p-type SnSe with reasonable agreement with experiments.[363] Further comparison were made for La_3Te_4, $La_{2.75}Te_4$, and $La_{2.67}Te_4$ showing excellent agreement with experiments.[364]

Figure 42. Calculated Seebeck coefficients for PbTe for various p- and n-type doping levels (lines) [363] in comparison with the experimental data for p-type PbTe by Heremans and coauthors [370,371] and n-type PbTe by LaLonde et al. [372] (symbols with same colors and sequences as the lines).

Figure 43. Calculated Seebeck coefficients for p-type SnSe[363] compared with results from experiments[373–376] and kinetic Boltzmann transport theory using the BoltzTrap package.[362]

5.5.3. General discussion on off-diagonal transport coefficients

One can further generalize Eq. 101 based on the conjugate variables in the combined law of thermodynamics Eq. 18 as follows

$$J_{X^a} = -L_{X^a} \nabla Y^a \qquad \textbf{Eq. 108}$$

where J_{X^a} is the flux of extensive variable X^a with a unit of X^a per area per second, L_{X^a} the kinetic coefficients of X^a with a unit of X^a/Y^a per length per second, and ∇Y^a the gradient of Y^a with a unite of Y^a per length. The entropy production rate per volume due to the transport of X^a is usually defined by the product of its flux and the gradient, i.e.

$$T\frac{d_{ip}S_{X^a}}{dt} = J_{X^a}\nabla Y^a = -L_{X^a}(\nabla Y^a)^2 \qquad \textbf{Eq. 109}$$

The potential Y^a is a function of X^a and other extensive variables X^b and potentials Y^c, i.e. $Y^a(X^a, X^b, Y^c)$, with the combined law and characteristic function generalized from Eq. 27 as follows

$$d\Phi(X^a, X^b, Y^c) = d\left(U - \sum X^c Y^c\right) = Y^a dX^a + Y^b dX^b - \sum X^c dY^c \qquad \textbf{Eq. 110}$$

It should be noted that the Gibbs-Duhem equation among potentials, Eq. 25, is applicable to equilibrium systems only and cannot be applied to nonequilibrium systems. In nonequilibrium systems, all potentials can be independently controlled. ∇Y^a can thus be expanded in terms of independent variables as follows

$$\nabla Y^a = \frac{\partial Y^a}{\partial X^a}\nabla X^a + \sum \frac{\partial Y^a}{\partial X^b}\nabla X^b + \sum \frac{\partial Y^a}{\partial Y^c}\nabla Y^c \qquad \textbf{Eq. 111}$$

where the two summations are for independent extensive variables and independent potentials, respectively. The partial derivative $\frac{\partial Y^a}{\partial X^a}$ denotes the diagonal terms in Table 1 and is always positive for a stable system depicted by Eq. 11. The partial derivative $\frac{\partial Y^a}{\partial X^b}$ denotes the off-

diagonal terms in Table 1 and can be either positive or negative such as the thermal expansion discussed above for Ce and Fe_3Pt. The partial derivative $\frac{\partial Y^a}{\partial Y^c}$ denotes the last row in Table 1 with $Y^a = \mu_i$ as one example and general quantities by Eq. 21, which is used in the calculation of Seebeck coefficient above in terms of $\frac{\partial \mu_q}{\partial T}$ and can be written as follows based on Eq. 110

$$\frac{\partial Y^a}{\partial Y^c} = \frac{\partial^2 \Phi}{\partial Y^c \partial X^a} = \frac{\partial^2 \Phi}{\partial X^a \partial Y^c} = -\frac{\partial X^c}{\partial X^a} \quad \textbf{Eq. 112}$$

Combining Eq. 108 and Eq. 111, one gets

$$J_{X^a} = -L_{X^a}\left(\frac{\partial Y^a}{\partial X^a}\nabla X^a + \sum \frac{\partial Y^a}{\partial X^b}\nabla X^b + \sum \frac{\partial Y^a}{\partial Y^c}\nabla Y^c\right) \quad \textbf{Eq. 113}$$

Applying Eq. 113 to a thermoelectric system, one obtains both electric and thermal fluxes as follows

$$J_q = -\sigma\nabla\mu_q = -\sigma(\frac{\partial \mu_q}{\partial n_q}\nabla n_q + \frac{\partial \mu_q}{\partial T}\nabla T) \quad \textbf{Eq. 114}$$

$$J_Q = -L_Q\nabla T = -L_Q(\frac{\partial T}{\partial \mu_q}\nabla \mu_q + \frac{\partial T}{\partial S}\nabla S) \quad \textbf{Eq. 115}$$

where L_Q is the thermal conductivity. The first parts of Eq. 114 and Eq. 115 fulfil the Onsager reciprocal relationships as a diagonal matrix. While the second parts have both the gradients of potentials and molar quantities as the driving forces, and the discussion whether the matrix fulfils the Onsager reciprocal relationships is out of the scope of the present paper and worth of further investigation.

5.5.4. Mechanical properties

Mechanical properties can be denoted by the energy of a system as a function of the state of the system as demonstrated by the ideal pure shear strength of aluminum and copper with the energy as a function of shear deformation.[377] By the same token, the elastic coefficients can be calculated by the elastic energy as a function of deformation strain.[70,296–29] However, the plastic deformation is more difficult to deal with due to the long-range elastic fields around dislocations, which is actually also an issure related to the calculation of elastic coefficients in the DFT-based first-principles calculations. This issue was discussed in the calculations of energetics of charged defects in terms of different relaxation schemes of supercells.[378]

Nevertheless, the DFT-based first-principles calculations can provide valuable insights on deformation mechanisms and mechanical behaviors. In our recent work, it was demonstrated that better understanding of dislocation characteristics in Ni_3Al can be achieved by the predicted stacking fault energy and ideal shear strength.[379] The results include direct evidence for the splitting of a $1/2[\bar{1}10]$ dislocation into two Shockley partials on the $\{111\}$ plane, which is further supported by the equivalence of the complex stacking fault (CSF) energy and the antiphase boundary (APB) energy. The estimated Peierls stresses at 0 K using ideal shear strength and elastic properties for edge (e) and screw (s) dislocations with elastic factors for isotropic (iso) and anisotropic (aniso) crystals are compared with experimental critical resolved shear stress (CRSS) values at room temperature for Ni_3Al and Ni as shown in Figure 44, with quantitative agreement observed.

Figure 44. Calculated Peierls stresses at 0 K for edge (e) and screw (s) dislocations for isotropic (iso) and anisotropic (aniso) crystals in comparison with experimental CRSS values at room temperature for Ni_3Al and Ni.[379]

In another work, a multiscale approach combines first-principles calculations and crystal plasticity finite element method (CPFEM) to predict the strain hardening behavior of pure Ni single crystal.[380] The first-principles calculations include the ideal shear strength and elastic properties to predict the Peierls stress for pure edge and pure screw dislocations for a CPFEM framework in the same fashion as in the above case.[379] It is commonly accepted that the plastic deformation of pure Ni initially involves edge dislocations, and eventually also the interactions of edge dislocations that result in junctions with complex screw dislocation characteristics. [118,119] The strain hardening thus includes contributions from both edge and screw dislocations. It was found that CPFEM predictions based solely on edge dislocations agreed well with experiments at small strains (< 0.06), while the predictions adopting the proposed edge-screw model fully capture experimental data at large deformations, as shown in Figure 45 for various orientations of Ni single crystals. It is anticipated that more mechanical properties can be predicted in terms of the energetics of a system as a function of internal variables such as grain size, twin boundary, and stacking faults.

Figure 45. Strain hardening behavior of pure Ni single crystal:[380] left a) Peierls stresses (symbols), $\tau_c^{\alpha,es}$, on slip system α that combine contributions from both edge and screw dislocations as a function of shear strain on slip system β with the corresponding CPFEM fits (lines); (middle b) CPFEM simulated engineering stress-strain curves (lines) with

experimental data by Yao et al. (symbols) [381]; (right a, b) CPFEM simulated engineering stress-strain curves (lines) with experimental data by Haasen (symbols).[382]

5.6. Information

At a first glance, information may seem far away from the contents discussed so far. However, if one looks at how information is stored today, it becomes evident that thermodynamics and information are closely related through entropy and the configurations of the system. As a matter of fact, the discussion of information started with the mathematical solution to communication and message transmission problems by Shannon [383,384] who defined the information entropy as a macrostate (a source) with the number of possible microstates (ensembles of possible messages) that could be sent by that source. Thus, information in the communication begins with a set of messages, each with a probability, and the average information content per message is defined in analogy to Eq. 30. Szilard [385,386] demonstrated that a "biological phenomenon" of a nonliving device generates the same quantity of entropy required by thermodynamics, a critical link in the integration of physical and cognitive concepts that later became the foundation of information theory and a key idea in complex systems. Their works were followed by Brillouin, Landauer, Bennett and others both theoretically and experimentally.[387–394]

Therefore, considering that information is stored in physical materials, it is written and extracted in the same scale of the configurational features of the physical materials, such as books with words, telegraphs with coded pulses, the magnetic storages with magnetic spin configurations, a range of digital storages with two distinct states arranged in space, future quantum systems based

on quantum states of quantum materials, and of cause deoxyribonucleic acid (DNA, a long polymer) with a huge array of chemical pairs in various genes. On the other hand, in the scale of a society, Huntington [395] argued that the increased distribution of age groups between the ages of 15 and 30 in a society increases its instability with increased unemployment ratio. While for the scale of Earth's critical zone defined as the heterogeneous, near surface environment, Quijano and Lin [396] made a comprehensive review on the extensive applications of thermodynamic and information entropy in different fields related to the Critical Zone, such as hydrology, ecology, pedology, and geomorphology.

In collaboration with Lin who co-authored the above publication,[396] we considered the information generation or loss as part of an internal process with the entropy production as follows,[10] similar to Eq. 3

$$d_{ip}S = \frac{d_{ip}Q}{T} - \sum S_i^n dN_i^n + \sum S_j^w dN_j^w - d_{ip}I \qquad \textbf{Eq. 116}$$

where S_i^n and S_j^w are the entropies of incoming component (nutrient) i (dN_i^n) and outgoing component (waste) j $\left(dN_j^w\right)$, respectively, and the internal process re-organizes the configurations to produce certain amount of information $\left(d_{ip}I\right)$ and generate or absorb the amount of heat $(d_{ip}Q)$. Various thought experiments of spontaneous IP, i.e. $d_{ip}S > 0$, were discussed in ref. [10] in terms of relative magnitudes of quantities in Eq. 116.

Eq. 116 can be re-organized for the information change for an irreversible internal process ($d_{ip}S$ >0) as follows

$$d_{ip}I < \frac{d_{ip}Q}{T} - \sum S_i^n dN_i^n + \sum S_j^w dN_j^w \qquad \textbf{Eq. 117}$$

which gives the bound of information that can be produced (positive $d_{ip}I$) or lost (negative $d_{ip}I$) by an internal process. It is shown that the information generation (loss) can be increased (decreases) with higher heat production, lower entropy of nutrient inputs, and higher entropy of waste outputs. It should be pointed out that even though the entropy change due to internal processes is only part of total entropy change of the system, the information change of the system is fully dictated by the internal processes in the system which are regulated by the heat and exchanges of nutrients and wastes between the system and its surroundings, as shown by Eq. 3 and Eq. 116.

The total information change of a system would be the sum of information changes by individual internal processes. Following the discussions by Shannon [383,384] and Brillouin[388,397–400], we can re-write Eq. 32 as follows

$$S = -I^k + \sum_{k=1}^{m} p^k S^k \qquad \textbf{Eq. 118}$$

$$I^k = -S^{conf} = k_B \sum_{k=1}^{m} p^k ln p^k \qquad \textbf{Eq. 119}$$

where I^k denote the information at the scale k. The sub-scale information makes its contribution to the probability p^k as shown by F^k in Eq. 34 or Eq. 85. As all spontaneous internal processes produce entropy, one may tend to think that the information of the universe has been decreasing from the beginning of time if the beginning of time and the boundary of the universe could be defined such as by the Big Bang. However, certain sub-systems may experience an increase of their information as discussed in the thought experiments,[10] when the sub-systems are brought across their limits of stability through the interactions with their surroundings, resulting in self-

organized structures in local subsystems. This is what discussed by Kondepudi and Prigogine,[16] who concluded that instability in a system enables the generation of dissipative structures, thus more distinct configurations and more information, as also demonstrated in three examples in Section 5.3. Therefore, the fundamentals of thermodynamics and information discussed in the present paper may provide a framework for investigations of complex systems such as quantum systems,[401–403] nano devices,[404] and ecosystems,[396,405] along with new sciences and specfic characteristics of individual systems to be discovered.

6. Summary and conclusion

In this overview, the fundamentals of thermodynamics are reviewed in terms of the first law of thermodynamics for open systems and the second law of thermodynamics for internal processes. By doing so, the chemical potentials are defined naturally. It is shown that the combined law of thermodynamics is applicable to stable, metastable, and unstable states of a system. The first and second derivatives of internal energy, Gibbs energy, and other characteristic functions with respect to their natural variables are defined, and their importance is articulated. The first derivatives with respect to extensive variables give the conjugate potentials which are homogenous for an equilibrium system, and first derivatives with respect to potentials give the conjugate extensive variable. The second derivatives with respect to the same natural extensive variable determine the stability of an equilibrium system, i.e. positive for a stable system, zero for the limit of stability, and negative for an unstable system. While the second derivatives with respect to two different natural variables give various physical and kinetic properties. The third derivatives should be explored further. For a nonequilibrium system, the difference of a

potential between two states acts as the driving force for the transport of the corresponding conjugate molar quantity.

The computational thermodynamics is presented in terms of the commonly used modeling approach, i.e. the CALPHAD method which covers various states in the system though more works are needed for unstable states. With the available CALPHAD thermodynamic databases, some successful examples of materials design in terms of chemistry, processing, and properties are presented. It is evident that much more modeling is needed for more properties, particularly physical and mechanical properties and kinetic coefficients.

It is pointed out that the critical point can be considered as a mixture of competing configurations with the metastable configurations having higher entropies than the stable one. The property anomalies associated with a critical point can be predicted by statistical mixture of individual configurations. The entropies of individual configurations play an essential role in determining their statistical probabilities and thus the configurational entropy among individual configurations, and ultimately the emergent behaviors and the information of systems. It is shown that further discussions of information and Onsager reciprocal relationships are warranted.

7. Acknowledgements

The author feels privileged to work with all his current and previous students and numerous collaborators over the years at Penn State and around the world as reflected in the references cited in this overview paper. He would like to particularly thank Long-Qing Chen and Darrell Schlom for long-term collaborations of more than 20 years, Yi Wang, Shun-Li Shang, Yond Du,

and Xidong Hui for many stimulating interactions over 15 years, and Suveen Mathaudhu, William Yi Wang, Laszlo Kecskes, and Kris Darling for continued partnerships over 10 years. The author is grateful for financial supports from many funding agencies in the United States as listed in the cited references, including the National Science Foundation (NSF, with the latest grant 1825538), the Department of Energy (with the latest grants being DE-FE0031553 and DE-NE0008757), Army Research Lab (with the latest grant W911NF-14-2-0084), Office of Naval Research (with the latest grant N00014-17-1-2567), Wright Patterson AirForce Base, NASA Jet Propulsion Laboratory, and the National Institute of Standards and Technology, plus a number of national laboratories and companies that supported the NSF Center for Computational Materials Design (NSF, 0433033, 0541674/8, 1034965/8), the LION clusters at the Pennsylvania State University, the resources of NERSC supported by the Office of Science of the U.S. Department of Energy under contract No. DE-AC02-05CH11231, and the resources of XSEDE supported by NSF with Grant ACI-1053575.

8. References

1. Gibbs, J. W. *The collected works of J. Willard Gibbs: Vol. I Thermodynamics*. (Yale University Press, 1948).
2. Gibbs, J. W. Graphical methods in the thermodynamics of fluids. *Trans. Connect. Acad. II* **April-May,** 309–342 (1873).
3. Hillert, M. *Phase equilibria, phase diagrams and phase transformations: Their thermodynamic basis*. (Cambridge University Press, 2008).
4. Onsager, L. Reciprocal Relations in Irreversible Processes, I. *Phys. Rev.* **37,** 405–426 (1931).
5. Prigogine, I. *Thermodynamics of Irreversible Processes*. (New York: Interscience, 1961).
6. de Groot, S. R. *Thermodynamics of irreversible processes.* (North-Holland pub. co., 1961).
7. Muller, I. & Ruggeri, T. *Rational Extended Thermodynamics*. (Springer, 2002). doi:10.1007/978-3-662-05056-9_8
8. Jou, D., Casas-Vázquez, J. & Lebon, G. *Extended irreversible thermodynamics*. (Springer Netherlands, 2010). doi:10.1007/978-90-481-3074-0
9. Liu, Z. K. & Wang, Y. *Computational Thermodynamics of Materials*. (Cambridge University Press, 2016).
10. Liu, Z. K., Li, B. & Lin, H. Multiscale Entropy and Its Implications to Critical Phenomena, Emergent Behaviors, and Information. *J. Phase Equilibria Diffus.* **40,** 508–521 (2019).
11. Guggenheim, E. A. The Thermodynamics of Magnetization. *Proc. R. Soc. London. Ser. A - Math. Phys. Sci.* **155,** 70–101 (1936).
12. Koenig, F. O. The Thermodynamics of the Electric Field with Special Reference to Equilibrium. *J. Phys. Chem.* **41,** 597–620 (1937).

13. Nye, J. F. *Physical Properties of Crystals: Their Representation by Tensors and Matrices*. (Clarendon Press, 1985).

14. Zimmels, Y. Thermodynamics in the presence of electromagnetic fields. *Phys. Rev. E* **52,** 1452–1464 (1995).

15. Abdel-Hady, S. A Fundamental Equation of Thermodynamics that Embraces Electrical and Magnetic Potentials. *J. Electromagn. Anal. Appl.* **2,** 162–168 (2010).

16. Kondepudi, D. & Prigogine, I. *Modern Thermodynamics: From Heat Engines to Dissipative Structures*. (John Wiley & Sons Ltd., 1998).

17. Liu, Z. K. Ocean of Data: Integrating first-principles calculations and CALPHAD modeling with machine learning. *J. Phase Equilibria Diffus.* **39,** 635–649 (2018).

18. Patel, S., Chauhan, A. & Vaish, R. Elastocaloric and Piezocaloric Effects in Lead Zirconate Titanate Ceramics. *Energy Technol.* **4,** 647–652 (2016).

19. Bai, G., Xie, Q., Xu, J. & Gao, C. Large negative piezocaloric effect: Uniaxial stress effect. *Solid State Commun.* **291,** 11–14 (2019).

20. Del Mar Olaya, M., Reyes-Labarta, J. A., Serrano, M. D. & Marcilla, A. Vapor-liquid equilibria: Using the gibbs energy and the common tangent plane criterion. *Chem. Eng. Educ.* **44,** 236–244 (2010).

21. Liu, Z. K. Perspective on materials genome®. *Chinese Sci. Bull.* **59,** 1619–1623 (2014).

22. Liu, Z. K., Shang, S. L. & Wang, Y. Fundamentals of Thermal Expansion and Thermal Contraction. *Materials (Basel).* **10,** 410 (2017).

23. Gibbs, J. W. *The collected works of J. Willard Gibbs: Vol. II Statistical Mechanics*. (Yale University Press, 1948).

24. Wang, Y., Hector, L. G., Zhang, H., Shang, S. L., Chen, L. Q. & Liu, Z. K.

Thermodynamics of the Ce gamma-alpha transition: Density-functional study. *Phys. Rev. B* **78,** 104113 (2008).

25. Wang, Y., Hector, L. G., Zhang, H., Shang, S. L., Chen, L. Q. & Liu, Z. K. A thermodynamic framework for a system with itinerant-electron magnetism. *J. Physics-Condensed Matter* **21,** 326003 (2009).

26. Wang, Y., Shang, S. L. L., Zhang, H., Chen, L.-Q. Q. & Liu, Z.-K. K. Thermodynamic fluctuations in magnetic states: Fe3Pt as a prototype. *Philos. Mag. Lett.* **90,** 851–859 (2010).

27. Liu, Z. K., Wang, Y. & Shang, S. L. Thermal expansion anomaly regulated by entropy. *Sci. Rep.* **4,** 7043 (2014).

28. van de Walle, A., Ceder, G. & Waghmare, U. V. First-principles computation of the vibrational entropy of ordered and disordered Ni3Al. *Phys. Rev. Lett.* **80,** 4911 (1998).

29. Wang, Y., Liu, Z. K. & Chen, L. Q. Thermodynamic properties of Al, Ni, NiAl, and Ni3Al from first-principles calculations. *Acta Mater.* **52,** 2665–2671 (2004).

30. Kaufman, L. & Cohen, M. The martensitic transformation in the iron-nickel system-Reply. *Trans. Am. Inst. Min. Metall. Eng.* **209,** 1315 (1957).

31. Kaufman, L. & Bernstein, H. *Computer Calculation of Phase Diagram*. (Academic Press Inc., 1970).

32. Saunders, N. & Miodownik, A. P. *CALPHAD (Calculation of Phase Diagrams): A Comprehensive Guide*. (Pergamon, 1998).

33. Lukas, H. L., Fries, S. G. & Sundman, B. *Computational Thermodynamics: The CALPHAD Method*. (Cambridge University Press, 2007).

34. Hillert, M. & Stafansson, L. I. Regular Solution Model for Stoichiometric Phases and

Ionic Melts. *Acta Chem. Scand.* **24,** 3618–3826 (1970).

35. Hillert, M. The compound energy formalism. *J. Alloys Compd.* **320,** 161–176 (2001).

36. Muggianu, Y. M., Gambino, M. & Bros, J. P. Enthalpies Of Formation Of Liquid Alloys Bismuth-Gallium-Tin At 723 k - Choice Of An Analytical Representation Of Integral And Partial Thermodynamic Functions Of Mixing For This Ternary- System. *J Chim Phys-Chim Biol* **72,** 83–88 (1975).

37. Redlich, O. & Kister, A. T. Algebraic Representations of Thermodynamic Properties and the Classification of Solutions. *Ind. Eng. Chem.* **40,** 345–348 (1948).

38. Pelton, A. D. & Chartrand, P. The modified quasi-chemical model: Part II. Multicomponent solutions. *Metall. Mater. Trans. a-Physical Metall. Mater. Sci.* **32,** 1355–1360 (2001).

39. Sommer, F. Determination of Thermodynamic Activities of Liquid Alloys in the Systems Mg--Sr and Ba--Mg. *Z. Met.* **71,** 120–123 (1980).

40. Kaufman, L. The Lattice Stability of Metals .1. Titanium and Zirconium. *Acta Met.* **7,** 575–587 (1959).

41. Kaufman, L. in *Phase Stability in Metals and Alloys* (eds. Rudman, P. S., Stringer, J. S. & Jaffee, R. I.) 125–150 (McGraw-Hill, 1967).

42. Skriver, H. L. Crystal structure from one-electron theory. *Phys. Rev. B* **31,** 1909–1923 (1985).

43. Grimvall, G. Reconciling ab initio and semiempirical approaches to lattice stabilities. *Berichte Der Bunsen-Gesellschaft-Physical Chem. Chem. Phys.* **102,** 1083–1087 (1998).

44. Wang, Y., Curtarolo, S., Jiang, C., Arroyave, R., Wang, T., Ceder, G., Chen, L. Q. & Liu, Z. K. Ab initio lattice stability in comparison with CALPHAD lattice stability. *CALPHAD*

28, 79–90 (2004).

45. Grimvall, G., Magyari-Koepe, B., Ozolins, V. & Persson, K. A. Lattice instabilities in metallic elements. *Rev. Mod. Phys.* **84,** 945–986 (2012).

46. van de Walle, A. Invited paper: Reconciling SGTE and ab initio enthalpies of the elements. *CALPHAD* **60,** 1–6 (2018).

47. van de Walle, A., Hong, Q., Kadkhodaei, S. & Sun, R. The free energy of mechanically unstable phases. *Nat. Commun.* **6,** 7559 (2015).

48. Abe, T. & Sundman, B. A description of the effect of short range ordering in the compound energy formalism. *CALPHAD* **27,** 403–408 (2003).

49. Hillert, M., Jansson, B., Sundman, B. & Agren, J. A 2-Sublattice Model for Molten Solutions with Different Tendency for Ionization. *Metall. Trans. a-Physical Metall. Mater. Sci.* **16,** 261–266 (1985).

50. Hallstedt, B. Thermodynamic Assessment of the System MgO-Al2O3. *J. Am. Ceram. Soc.* **75,** 1497–1507 (1992).

51. Mao, H., Selleby, M. & Fabrichnaya, O. Thermodynamic reassessment of the Y2O3–Al2O3–SiO2 system and its subsystems. *CALPHAD* **32,** 399–412 (2008).

52. Lee, S. H., Manga, V. R., Carolan, M. F. & Liu, Z. K. Defect Chemistry and Phase Equilibria of (La1-xCax)FeO3-delta Thermodynamic Modeling. *J. Electrochem. Soc.* **160,** F1103–F1108 (2013).

53. Chang, K., Hallstedt, B. & Music, D. Thermodynamic and Electrochemical Properties of the Li–Co–O and Li–Ni–O Systems. *Chem. Mater.* **24,** 97–105 (2011).

54. Inden, G. Determination of chemical and magnetic interchange energies in BCC alloys .1. General treatment. *Zeitschrift fur Met.* **66,** 577–582 (1975).

55. Inden, G. Determination of chemical and magnetic interchange energies in BCC alloys .3. Application to ferromagnetic-alloys. *Zeitschrift fur Met.* **68,** 529–534 (1977).

56. Hillert, M. & Jarl, M. A Model for Alloying Effects in Ferromagnetic Metals. *CALPHAD* **2,** 227–238 (1978).

57. Hertzman, S. & Sundman, B. A thermodynamic analysis of the Fe-Cr system. *CALPHAD* **6,** 67–80 (1982).

58. Chen, Q. & Sundman, B. Modeling of thermodynamic properties for Bcc, Fcc, liquid, and amorphous iron. *J. Phase Equilibria* **22,** 631–644 (2001).

59. Xiong, W., Chen, Q., Korzhavyi, P. A. & Selleby, M. An improved magnetic model for thermodynamic modeling. *CALPHAD* **39,** 11–20 (2012).

60. Vinokurova, L. I., Vlaso, A. V., Ivanov, V. Y., Pardavi-Horvath, M. & Schwab, E. in *The magnetic and electron structures of transition metals and alloys* (eds. Veselago, V. G. & Vinokurova, L. I.) 1–43 (1988).

61. Kudrnovský, J., Drchal, V. & Turek, I. Physical properties of FeRh alloys: The antiferromagnetic to ferromagnetic transition. *Phys. Rev. B - Condens. Matter Mater. Phys.* **91,** 1–11 (2015).

62. Koermann, F., Dick, A., Grabowski, B., Hallstedt, B., Hickel, T. & Neugebauer, J. Free energy of bcc iron: Integrated ab initio derivation of vibrational, electronic, and magnetic contributions. *Phys. Rev. B* **78,** 33102 (2008).

63. Körmann, F., Dick, A., Hickel, T. & Neugebauer, J. Rescaled Monte Carlo approach for magnetic systems: Ab initio thermodynamics of bcc iron. *Phys. Rev. B - Condens. Matter Mater. Phys.* **81,** 1–9 (2010).

64. Körmann, F., Grabowski, B., Dutta, B., Hickel, T., Mauger, L., Fultz, B. & Neugebauer, J.

Temperature dependent magnon-phonon coupling in bcc Fe from theory and experiment. *Phys. Rev. Lett.* **113,** 1–5 (2014).

65. Shang, S. L., Saal, J. E., Mei, Z. G., Wang, Y. & Liu, Z. K. Magnetic thermodynamics of fcc Ni from first-principles partition function approach. *J. Appl. Phys.* **108,** 123514 (2010).

66. Shang, S. L., Wang, Y. & Liu, Z. K. Thermodynamic fluctuations between magnetic states from first-principles phonon calculations: The case of bcc Fe. *Phys. Rev. B* **82,** 14425 (2010).

67. Lavrentiev, M. Y., Nguyen-Manh, D. & Dudarev, S. L. Magnetic cluster expansion model for bcc-fcc transitions in Fe and Fe-Cr alloys. *Phys. Rev. B* **81,** 184202 (2010).

68. Lavrentiev, M. Y., Wrobel, J. S., Nguyen-Manh, D. & Dudarev, S. L. Magnetic and thermodynamic properties of face-centered cubic Fe-Ni alloys. *Phys. Chem. Chem. Phys.* **16,** 16049–16059 (2014).

69. Lavrentiev, M. Y., Wróbel, J. S., Nguyen-Manh, D., Dudarev, S. L. & Ganchenkova, M. G. Magnetic cluster expansion model for random and ordered magnetic face-centered cubic Fe-Ni-Cr alloys. *J. Appl. Phys.* **120,** 1–10 (2016).

70. Liu, Z. K. First-Principles calculations and CALPHAD modeling of thermodynamics. *J. Phase Equilibria Diffus.* **30,** 517–534 (2009).

71. Shirane, G., Hoshino, S. & Suzuki, K. X-ray study of the phase transition in lead titanate. *Phys. Rev.* **80,** 1105–1106 (1950).

72. Noheda, B., Cereceda, N., Iglesias, T., Lifante, G., Gonzalo, J. A., Chen, H. T. & Wang, Y. L. Composition dependence of the ferroelectric-paraelectric transition in the mixed system PbZr1-xTixO3. *Phys. Rev. B* **51,** 16388–16391 (1995).

73. Liu, Z. K., Mei, Z. G., Wang, Y. & Shang, S. L. Nature of ferroelectric-paraelectric

transition. *Philos. Mag. Lett.* **92,** 399–407 (2012).

74. Fang, H. Z., Wang, Y., Shang, S. L. & Liu, Z. K. Nature of ferroelectric-paraelectric phase transition and origin of negative thermal expansion in PbTiO3. *Phys. Rev. B* **91,** 24104 (2015).

75. Haun, M. J., Furman, E., Jang, S. J., McKinstry, H. A. & Cross, L. E. Thermodynamic theory of PbTiO3. *J. Appl. Phys.* **62,** 3331–3338 (1987).

76. Haun, M. J., Furman, E., Jang, S. J. & Cross, L. E. Thermodynamic theory of the lead zirconate-titanatesolid solution system, part I: Phenomenology. *Ferroelectrics* **99,** 13–25 (1989).

77. Haun, M. J., Furman, E., Jang, S. J. & Cross, L. E. Thermodynamic theory of the lead zirconate-titanate solid solution system, part v: Theoretical calculations. *Ferroelectrics* **99,** 63–86 (1989).

78. Devonshire, A. F. Theory of barium titanate 1. *Philos. Mag.* **40,** 1040–1063 (1949).

79. Jona, F. & Shirane, G. *Ferroelectric crystals*. (Macmillan, New York, 1962).

80. Chen, L. Q. in *Physics of Ferroelectrics: a Modern Perspective* (eds. Rabe, K. M., Ahn, C. H. & Triscone, J.) 396 (Springer, 2007).

81. Pohlmann, H., Wang, J. J., Wang, B. & Chen, L. Q. A thermodynamic potential and the temperature-composition phase diagram for single-crystalline K 1-x Na x NbO 3 ($0 \leq x \leq 0.5$). *Appl. Phys. Lett.* **110,** 102906 (2017).

82. Liu, Z. K., Zhang, H., Ganeshan, S., Wang, Y. & Mathaudhu, S. N. Computational modeling of effects of alloying elements on elastic coefficients. *Scr. Mater.* **63,** 686–691 (2010).

83. Zhong, W., Vanderbilt, D. & Rabe, K. M. Phase-Transitions in BaTiO3 From First

Principles. *Phys. Rev. Lett.* **73,** 1861 (1994).

84. Zhong, W., Vanderbilt, D. & Rabe, K. M. First-Principles Theory of Ferroelectric Phase-Transitions for Perovskites - The Case of BaTiO3. *Phys. Rev. B* **52,** 6301–6312 (1995).

85. Bellaiche, L., García, A. & Vanderbilt, D. Finite-Temperature Properties of PbZr1-xTi xO3 Alloys from First Principles. *Phys. Rev. Lett.* **84,** 5427–5430 (2000).

86. Akbarzadeh, A. R., Prosandeev, S., Walter, E. J., Al-Barakaty, A. & Bellaiche, L. Finite-temperature properties of Ba(Zr,Ti)O3 relaxors from first principles. *Phys. Rev. Lett.* **108,** 1–5 (2012).

87. Ponomareva, I., Tagantsev, A. K. & Bellaiche, L. Finite-temperature flexoelectricity in ferroelectric thin films from first principles. *Phys. Rev. B* **85,** 104101 (2012).

88. Flory, P. J. Themodynamics of high polymer solutions. *J. Chem. Phys.* **10,** 51–61 (1942).

89. Huggins, M. L. Some properties of solutions of long-chain compounds. *J. Phys. Chem.* **46,** 151–158 (1942).

90. Abrams, D. S. & Prausnitz, J. M. Statistical thermodynamics of liquid mixtures: A new expression for the excess Gibbs energy of partly or completely miscible systems. *AIChE J.* **21,** 116–128 (1975).

91. Wilson, G. M. Vapor-Liquid Equilibrium. XI. A New Expression for the Excess Free Energy of Mixing. *J. Am. Chem. Soc.* **86,** 127–130 (1964).

92. Renon, H. & Prausnitz, J. M. Local compositions in thermodynamic excess functions for liquid mixtures. *AIChE J.* **14,** 135–144 (1968).

93. Staverman, A. J. The entropy of high polymer solutions. Generalization of formulae. *Recl. des Trav. Chim. des Pays-Bas* **69,** 163–174 (1950).

94. Li, J., Sundman, B., Winkelman, J. G. M., Vakis, A. I. & Picchioni, F. Implementation of

the UNIQUAC model in the OpenCalphad software. *Fluid Phase Equilib.* **507,** 112398 (2020).

95. Sundman, B., Kattner, U. R., Palumbo, M. & Fries, S. G. OpenCalphad-a free thermodynamic software. *Integr. Mater. Manuf. Innov.* **4,** 1–15 (2015).

96. Open CALPHAD. Available at: http://www.opencalphad.com.

97. Darling, K. A., Tschopp, M. A., VanLeeuwen, B. K., Atwater, M. A. & Liu, Z. K. Mitigating grain growth in binary nanocrystalline alloys through solute selection based on thermodynamic stability maps. *Comput. Mater. Sci.* **84,** 255–266 (2014).

98. Fang, H. Z., Shang, S. L., Wang, Y., Liu, Z. K., Alfonso, D., Alman, D. E., Shin, Y. K., Zou, C. Y., van Duin, A. C. T., Lei, K. & Wang, G. F. First-principles studies on vacancy-modified interstitial diffusion mechanism of oxygen in nickel, associated with large-scale atomic simulation techniques. *J. Appl. Phys.* **115,** 43501 (2014).

99. Shang, S. L., Fang, H. Z., Wang, J., Guo, C. P., Wang, Y., Jablonski, P. D., Du, Y. & Liu, Z. K. Vacancy mechanism of oxygen diffusivity in bcc Fe: A first-principles study. *Corros. Sci.* **83,** 94–102 (2014).

100. Andersson, J. O. & Agren, J. Models for Numerical Treatment of Multicomponent Diffusion in Simple Phases. *J. Appl. Phys.* **72,** 1350–1355 (1992).

101. Oates, W. A., Chen, S. L., Cao, W., Zhang, F., Chang, Y. A., Bencze, L., Doernberg, E. & Schmid-Fetzer, R. Vacancy thermodynamics for intermediate phases using the compound energy formalism. *Acta Mater.* **56,** 5255–5262 (2008).

102. Dupin, N., Ansara, I. & Sundman, B. Thermodynamic Re-Assessment of the Ternary System Al-Cr-Ni. *CALPHAD* **25,** 279–298 (2001).

103. Peçanha, R. M., Ferreira, F., Coelho, G. C., Nunes, C. A. & Sundman, B. Thermodynamic

modeling of the Nb–B system. *Intermetallics* **15,** 999–1005 (2007).

104. Xiong, W., Xu, H. & Du, Y. Thermodynamic investigation of the galvanizing systems, II: Thermodynamic evaluation of the Ni–Zn system. *CALPHAD* **35,** 276–283 (2011).

105. Rogal, J., Divinski, S. V, Finnis, M. W., Glensk, A., Neugebauer, J., Perepezko, J. H., Schuwalow, S., Sluiter, M. H. F. & Sundman, B. Perspectives on point defect thermodynamics. *Phys. Status Solidi B-Basic Solid State Phys.* **251,** 97–129 (2014).

106. Connetable, D., Lacaze, J., Maugis, P. & Sundman, B. A Calphad assessment of Al–C–Fe system with the κ carbide modelled as an ordered form of the fcc phase. *CALPHAD* **32,** 361–370 (2008).

107. Dinsdale, A. T., Khvan, A. V. & Watson, A. Critical Assessment 5: Thermodynamic data for vacancies. *Mater. Sci. Technol.* **30,** 1715–1718 (2014).

108. Franke, P. Modeling of Thermal Vacancies in Metals within the Framework of the Compound Energy Formalism. *J. Phase Equilibria Diffus.* **35,** 780–787 (2014).

109. Ågren, J. & Hillert, M. Thermodynamic modelling of vacancies as a constituent. *Calphad Comput. Coupling Phase Diagrams Thermochem.* **67,** 101666 (2019).

110. Guan, P.-W. & Liu, Z.-K. A physical model of thermal vacancies within the CALPHAD approach. *Scr. Mater.* **133,** 5–8 (2017).

111. Cottrell, A. H. *Dislocations and plastic flow in crystals*. (Oxford University Press, 1953).

112. Hirth, J. P. & Lothe, J. *Theory of dislocations*. (McGraw-Hill, 1968).

113. Nabarro, F. R. N. (Frank R. N. & Duesbery, M. S. *Dislocations in solids. Volume 11*. (Elsevier Science, 2002).

114. Langer, J. S., Bouchbinder, E. & Lookman, T. Thermodynamic theory of dislocation-mediated plasticity. *Acta Mater.* **58,** 3718–3732 (2010).

115. Wilson, W. E. The effective temperature of the sun. *Proc. R. Soc. London* **69,** 312–320 (1902).

116. Alonso, A., Arribas, S. & Martínez-Roger, C. The effective temperature scale of giant stars (F0-K5) II. Empirical calibration of T eff versus colours and [Fe/H]. *Astron. Astrophys. Suppl. Ser.* **140,** 261–277 (1999).

117. Bouchbinder, E. & Langer, J. S. Nonequilibrium thermodynamics of driven amorphous materials. II. Effective-temperature theory. *Phys. Rev. E* **80,** 031132 (2009).

118. Bulatov, V. V, Hsiung, L. L., Tang, M., Arsenlis, A., Bartelt, M. C., Cai, W., Florando, J. N., Hiratani, M., Rhee, M., Hommes, G., Pierce, T. G. & Diaz De La Rubia, T. Dislocation multi-junctions and strain hardening. *Nature* **440,** 1174–1178 (2006).

119. Kocks, U. F. & Mecking, H. Physics and phenomenology of strain hardening: the FCC case. *Prog. Mater. Sci.* **48,** 171–273 (2003).

120. Hu, Y.-J., Fellinger, M. R., Bulter, B. G., Wang, Y., Darling, K. A., Kecskes, L. J., Trinkle, D. R. & Liu, Z. K. Solute-induced solid-solution softening and hardening in bcc tungsten. *Acta Mater.* **141,** 304–316 (2017).

121. Cottrell, A. H. & Bilby, B. A. Dislocation Theory of Yielding and Strain Ageing of Iron. *Proc. Phys. Soc. Sect. A* **62,** 49–62 (1949).

122. Blavette, D., Cadel, E., Fraczkiewicz, A. & Menand, A. Three-dimensional atomic-scale imaging of impurity segregation to line defects. *Science* **286,** 2317–2319 (1999).

123. Calcagnotto, M., Adachi, Y., Ponge, D. & Raabe, D. Deformation and fracture mechanisms in fine- and ultrafine-grained ferrite/martensite dual-phase steels and the effect of aging. *Acta Mater.* **59,** 658–670 (2011).

124. Sato, H., Toth, R. S. & Honjo, G. Long period stacking order in close packed structures of

metals. *J. Phys. Chem. Solids* **28,** 137–160 (1967).

125. Zhu, Y. M., Morton, A. J. & Nie, J. F. The 18R and 14H long-period stacking ordered structures in Mg–Y–Zn alloys. *Acta Mater.* **58,** 2936–2947 (2010).

126. Saal, J. E. & Wolverton, C. Thermodynamic stability of Mg-based ternary long-period stacking ordered structures. *Acta Mater.* **68,** 325–338 (2014).

127. Wang, W. Y., Shang, S. L., Wang, Y., Darling, K. A., Kecskes, L. J., Mathaudhu, S. N., Hui, X. D. & Liu, Z.-K. Electronic structures of long periodic stacking order structures in Mg: A first-principles study. *J. Alloys Compd.* **586,** 656–662 (2014).

128. Kim, H., Ross, A. J., Shang, S.-L., Wang, Y., Kecskes, L. J. & Liu, Z.-K. First-principles calculations and thermodynamic modelling of long periodic stacking ordered (LPSO) phases in Mg-Al-Gd. *Materialia* **4,** 192–202 (2018).

129. Wang, W. Y., Wang, Y., Shang, S. L., Darling, K. A., Kim, H., Tang, B., Kou, H. C., Mathaudhu, S. N., Hui, X. D., Li, J. S., Kecskes, L. J. & Liu, Z. K. Strengthening Mg by self-dispersed nano-lamellar faults. *Mater. Res. Lett.* **5,** 415–425 (2017).

130. Weissmüller, J. Alloy effects in nanostructures. *Nanostructured Mater.* **3,** 261–272 (1993).

131. Weissmüller, J. Alloy thermodynamics in nanostructures. *J. Mater. Res.* **9,** 4–7 (1994).

132. Chookajorn, T., Murdoch, H. A. & Schuh, C. A. Design of stable nanocrystalline alloys. *Science* **337,** 951–954 (2012).

133. Wagih, M. & Schuh, C. A. Spectrum of grain boundary segregation energies in a polycrystal. *Acta Mater.* **181,** 228–237 (2019).

134. Murdoch, H. A. & Schuh, C. A. Stability of binary nanocrystalline alloys against grain growth and phase separation. *Acta Mater.* **61,** 2121–2132 (2013).

135. Cantwell, P. R., Tang, M., Dillon, S. J., Luo, J., Rohrer, G. S. & Harmer, M. P. Grain

boundary complexions. *Acta Mater.* **62,** 1–48 (2014).

136. Liu, Z. K., Agren, J. & Suehiro, M. Thermodynamics of interfacial segregation in solute drag. *Mater. Sci. Eng. a-Structural Mater. Prop. Microstruct. Process.* **247,** 222–228 (1998).

137. Dinsdale, A. T. SGTE Data for Pure Elements. *CALPHAD* **15,** 317–425 (1991).

138. Bigdeli, S., Mao, H. & Selleby, M. On the third-generation Calphad databases: An updated description of Mn. *Phys. Status Solidi Basic Res.* **252,** 2199–2208 (2015).

139. Roslyakova, I., Sundman, B., Dette, H., Zhang, L. & Steinbach, I. Modeling of Gibbs energies of pure elements down to 0 K using segmented regression. *Calphad Comput. Coupling Phase Diagrams Thermochem.* **55,** 165–180 (2016).

140. CALPHAD. Special issue on CALPHAD software tools. *CALPHAD* **33,** 141–312 (2002).

141. Hallstedt, B. & Liu, Z. K. Software for thermodynamic and kinetic calculation and modelling Foreword. *CALPHAD* **33,** 265 (2009).

142. Thermo-Calc Software and Databases. Available at: http://www.thermocalc.com/.

143. CompuTherm Software and Databases. Available at: http://www.computherm.com/.

144. FactSage. Available at: http://www.factsage.com/.

145. PyCalphad: CALPHAD-based computational thermodynamics in Python. (2020). Available at: http://pycalphad.org.

146. Otis, R. A. & Liu, Z. K. pycalphad: CALPHAD-based computational thermodynamics in Python. *J. Open Res. Softw.* **5,** 1 (2017).

147. Thermochimica. Available at: https://nuclear.ontariotechu.ca/piro/thermochimica/index.php; https://github.com/ORNL-CEES/thermochimica.

148. Campbell, C. E., Kattner, U. R. & Liu, Z. K. The development of phase-based property data using the CALPHAD method and infrastructure needs. *Integr. Mater. Manuf. Innov.* **3,** 158–180 (2014).

149. Shang, S.-L., Wang, Y. & Liu, Z.-K. ESPEI: Extensible, Self-optimizing Phase Equilibrium Infrastructure for magnesium alloys. in *Magnesium Technology 2010* (eds. Agnew, S. R., Neelameggham, N. R., Nyberg, E. A. & Sillekens, W. H.) 617–622 (The Minerals, Metals and Materials Society (TMS), Pittsburgh, PA, 2010).

150. Otis, R. A. & Liu, Z.-K. High-throughput thermodynamic modeling and uncertainty quantification for ICME. *JOM* **69,** 886–892 (2017).

151. Bocklund, B., Otis, R., Egorov, A., Obaied, A., Roslyakova, I. & Liu, Z. K. ESPEI for efficient thermodynamic database development, modification, and uncertainty quantification: application to Cu–Mg. *MRS Commun.* **9,** 618–627 (2019).

152. ESPEI: Extensible Self-optimizing Phase Equilibria Infrastructure. Available at: http://espei.org.

153. Meurer, A., Smith, C. P., Paprocki, M., Čertík, O., Kirpichev, S. B., Rocklin, M., Kumar, Am. T., Ivanov, S., Moore, J. K., Singh, S., Rathnayake, T., Vig, S., Granger, B. E., Muller, R. P., Bonazzi, F., Gupta, H., Vats, S., Johansson, F., Pedregosa, F., Curry, M. J., Terrel, A. R., Roučka, Š., Saboo, A., Fernando, I., Kulal, S., Cimrman, R. & Scopatz, A. SymPy: Symbolic computing in python. *PeerJ Comput. Sci.* **2017,** e103 (2017).

154. SymPy. (2016). Available at: http://www.sympy.org.

155. Otis, R., Emelianenko, M. & Liu, Z.-K. An improved sampling strategy for global energy minimization of multi-component systems. *Comput. Mater. Sci.* **130,** 282–291 (2017).

156. Chacon, S. & Straub, B. *Pro Git*. *Pro Git* (Apress, 2014). doi:10.1007/978-1-4842-0076-6

157. NASA Software of the Year. Available at: https://icb.nasa.gov/software-of-the-year.

158. Emelianenko, M., Liu, Z. K. & Du, Q. A new algorithm for the automation of phase diagram calculation. *Comput. Mater. Sci.* **35,** 61–74 (2006).

159. de Boer, F. R., Boom, R., Matten, W. C. M., Miedema, A. R. & Niessen, A. K. *Cohesion in Metals: Transition Metal Alloys*. (North Holland, Amsterdam, 1988).

160. Hautier, G., Fischer, C. C., Jain, A., Mueller, T. & Ceder, G. Finding natures missing ternary oxide compounds using machine learning and density functional theory. *Chem. Mater.* **22,** 3762–3767 (2010).

161. Ward, L., Liu, R., Krishna, A., Hegde, V. I., Agrawal, A., Choudhary, A. & Wolverton, C. Including crystal structure attributes in machine learning models of formation energies via Voronoi tessellations. *Phys. Rev. B* **96,** 024104 (2017).

162. Cavanaugh, J. E. Unifying the derivations for the Akaike and corrected Akaike information criteria. *Stat. Probab. Lett.* **33,** 201–208 (1997).

163. Goodman, J. & Weare, J. Ensemble samplers with affine invariance. *Commun. Appl. Math. Comput. Sci.* **5,** 65–80 (2010).

164. Foreman-Mackey, D., Hogg, D. W., Lang, D. & Goodman, J. emcee : The MCMC Hammer. *Publ. Astron. Soc. Pacific* **125,** 306–312 (2013).

165. Cao, W., Chen, S.-L., Zhang, F., Wu, K., Yang, Y., Chang, Y. A., Schmid-Fetzer, R. & Oates, W. A. PANDAT software with PanEngine, PanOptimizer and PanPrecipitation for multi-component phase diagram calculation and materials property simulation. *CALPHAD* **33,** 328–342 (2009).

166. Paulson, N. H., Bocklund, B. J., Otis, R. A., Liu, Z.-K. & Stan, M. Quantified uncertainty in thermodynamic modeling for materials design. *Acta Mater.* **174,** 9–15 (2019).

167. Zhao, J. C. *Methods for Phase Diagram Determination*. *Elsevier* (Elsevier, 2007).

168. Meschel, S. V. A brief history of heat measurements by calorimetry with emphasis on the thermochemistry of metallic and metal-nonmetal compounds. *CALPHAD* **68,** 101714 (2020).

169. Bartel, C. J., Millican, S. L., Deml, A. M., Rumptz, J. R., Tumas, W., Weimer, A. W., Lany, S., Stevanović, V., Musgrave, C. B. & Holder, A. M. Physical descriptor for the Gibbs energy of inorganic crystalline solids and temperature-dependent materials chemistry. *Nat. Commun.* **9,** 4168 (2018).

170. Hohenberg, P. & Kohn, W. Inhomogeneous electron gas. *Phys. Rev. B* **136,** B864- (1964).

171. Kohn, W. & Sham, L. J. Self-consisten equations including exchange and correlation effects. *Phys. Rev.* **140,** A1133–A1138 (1965).

172. Quantum chemistry and solid-state physics software. (2020). Available at: https://en.wikipedia.org/wiki/List_of_quantum_chemistry_and_solid-state_physics_software.

173. Grimme, S., Antony, J., Ehrlich, S. & Krieg, H. A consistent and accurate ab initio parametrization of density functional dispersion correction (DFT-D) for the 94 elements H-Pu. *J. Chem. Phys.* **132,** 154104 (2010).

174. Medvedev, M. G., Bushmarinov, I. S., Sun, J., Perdew, J. P. & Lyssenko, K. A. Density functional theory is straying from the path toward the exact functional. *Science* **355,** 49–52 (2017).

175. Mardirossian, N. & Head-Gordon, M. Thirty years of density functional theory in computational chemistry: An overview and extensive assessment of 200 density functionals. *Molecular Physics* **115,** 2315–2372 (2017).

176. van de Walle, A. & Ceder, G. The effect of lattice vibrations on substitutional alloy thermodynamics. *Rev. Mod. Phys.* **74,** 11–45 (2002).

177. Shang, S.-L., Wang, Y., Kim, D. & Liu, Z.-K. First-principles thermodynamics from phonon and Debye model: Application to Ni and Ni3Al. *Comput. Mater. Sci.* **47,** 1040–1048 (2010).

178. Kresse, G., Furthmuller, J., Furthmüller, J., Furthmueller, J., Furthmuller, J. & Furthmüller, J. Efficient iterative schemes for ab initio total-energy calculations using a plane-wave basis set. *Phys. Rev. B* **54,** 11169 (1996).

179. Liu, X. L., VanLeeuwen, B. K., Shang, S.-L., Du, Y. & Liu, Z.-K. On the scaling factor in Debye–Grüneisen model: A case study of the Mg–Zn binary system. *Comput. Mater. Sci.* **98,** 34–41 (2015).

180. van Duin, A. C. T., Dasgupta, S., Lorant, F. & Goddard, W. A. ReaxFF: A Reactive Force Field for Hydrocarbons. *J. Phys. Chem. A* **105,** 9396–9409 (2001).

181. Sanchez, J. M. Cluster Expansion and the Configurational Energy of Alloys. *Phys. Rev. B Condens. Matter* **48,** R14013–R14015 (1993).

182. van de Walle, A. Multicomponent multisublattice alloys, nonconfigurational entropy and other additions to the Alloy Theoretic Automated Toolkit. *CALPHAD* **33,** 266–278 (2009).

183. Materials Project. Available at: http://materialsproject.org/.

184. OQMD: An Open Quantum Materials Database. Available at: http://oqmd.org.

185. AFLOW: Automatic Flow for Materials Discovery. Available at: http://www.aflowlib.org.

186. Ozolins, V. First-Principles Calculations of Free Energies of Unstable Phases: The Case of fcc W. *Phys. Rev. Lett.* **102,** 65702 (2009).

187. Mei, Z. G. First-principles Thermodynamics of Phase Transition: from Metal to Oxide.

PhD, (The Pennsylvania State University, 2011).

188. Freysoldt, C., Grabowski, B., Hickel, T., Neugebauer, J., Kresse, G., Janotti, A. & Van De Walle, C. G. First-principles calculations for point defects in solids. *Rev. Mod. Phys.* **86,** 253–305 (2014).

189. Shang, S.-L., Zhou, B.-C., Wang, W. Y., Ross, A. J., Liu, X. L., Hu, Y.-J., Fang, H.-Z., Wang, Y. & Liu, Z.-K. A comprehensive first-principles study of pure elements: Vacancy formation and migration energies and self-diffusion coefficients. *ACTA Mater.* **109,** 128–141 (2016).

190. Wang, Y., Chen, L. Q., Liu, Z. K. & Mathaudhu, S. N. First-principles calculations of twin-boundary and stacking-fault energies in magnesium. *Scr. Mater.* **62,** 646–649 (2010).

191. Shang, S. L., Wang, W. Y., Zhou, B. C., Wang, Y., Darling, K. A., Kecskes, L. J., Mathaudhu, S. N. & Liu, Z. K. Generalized stacking fault energy, ideal strength and twinnability of dilute Mg-based alloys: A first-principles study of shear deformation. *Acta Mater.* **67,** 168–180 (2014).

192. Hu, Y. J., Wang, Y., Wang, W. Y., Darling, K. A., Kecskes, L. J. & Liu, Z. K. Solute effects on the Σ3 111[11-0] tilt grain boundary in BCC Fe: Grain boundary segregation, stability, and embrittlement. *Comput. Mater. Sci.* **171,** 109271 (2020).

193. Vitos, L., Abrikosov, I. A. & Johansson, B. Anisotropic Lattice Distortions in Random Alloys from First-Principles Theory. *Phys. Rev. l* **87,** 156401 (2001).

194. Zunger, A., Wei, S. H., Ferreira, L. G. & Bernard, J. E. Special Quasirandom Structures. *Phys. Rev. Lett.* **65,** 353–356 (1990).

195. Jiang, C., Wolverton, C., Sofo, J., Chen, L. Q. & Liu, Z. K. First-principles study of binary bcc alloys using special quasirandom structures. *Phys. Rev. B* **69,** 214202 (2004).

196. Shin, D., van de Walle, A., Wang, Y. & Liu, Z. K. First-principles study of ternary fcc solution phases from special quasirandom structures. *Phys. Rev. B* **76,** 144204 (2007).

197. van de Walle, A., Tiwary, P., de Jong, M., Olmsted, D. L., Asta, M., Dick, A., Shin, D., Wang, Y., Chen, L.-Q. & Liu, Z.-K. Efficient stochastic generation of special quasirandom structures. *CALPHAD* **42,** 13–18 (2013).

198. Kirklin, S., Saal, J. E., Meredig, B., Thompson, A., Doak, J. W., Aykol, M., Rühl, S. & Wolverton, C. The Open Quantum Materials Database (OQMD): assessing the accuracy of DFT formation energies. *npj Comput. Mater.* **1,** 15010 (2015).

199. Hautier, G., Ong, S. P., Jain, A., Moore, C. J. & Ceder, G. Accuracy of density functional theory in predicting formation energies of ternary oxides from binary oxides and its implication on phase stability. *Phys. Rev. B* **85,** 155208 (2012).

200. Schmidt, J., Marques, M. R. G., Botti, S. & Marques, M. A. L. Recent advances and applications of machine learning in solid-state materials science. *npj Comput. Mater.* **5,** 83 (2019).

201. Saal, J. E., Kirklin, S., Aykol, M., Meredig, B. & Wolverton, C. Materials Design and Discovery with High-Throughput Density Functional Theory: The Open Quantum Materials Database (OQMD). *JOM* **65,** 1501–1509 (2013).

202. Fultz, B. Vibrational thermodynamics of materials. *Prog. Mater. Sci.* **55,** 247–352 (2010).

203. Krajewski, A. M., Siegel, J., Liu, Z., Xu, J. C. & Liu, Z. K. SIPFENN: Tool for Structure-Informed Prediction of Formation Energy using Neural Networks and DFT Data. *in-preparation* (2020).

204. SIPFENN: Structure-Informed Prediction of Formation Energy using Neural Networks. (2020). Available at: https://phaseslab.com/sipfenn.

205. National Research Council. *Integrated Computational Materials Engineering: A Transformational Discipline for Improved Competitiveness and National Security*. (2008).

206. National Science and Technology Council. Materials Genome Initiative for Global Competitiveness. (2011). Available at: https://www.mgi.gov/sites/default/files/documents/materials_genome_initiative-final.pdf.

207. Lee, J., Lapira, E., Bagheri, B. & Kao, H.-A. Recent advances and trends in predictive manufacturing systems in big data environment. *Manuf. Lett.* **1,** 38–41 (2013).

208. Charbonneau, P., Kurchan, J., Parisi, G., Urbani, P. & Zamponi, F. Fractal free energy landscapes in structural glasses. *Nat. Commun.* **5,** 3725 (2014).

209. Cahn, J. W. On spinodal decomposition. *Acta Metall.* **9,** 795–801 (1961).

210. Li, L., Li, Z., Kwiatkowski da Silva, A., Peng, Z., Zhao, H., Gault, B. & Raabe, D. Segregation-driven grain boundary spinodal decomposition as a pathway for phase nucleation in a high-entropy alloy. *Acta Mater.* **178,** 1–9 (2019).

211. Liu, Z. K., Li, X. Y. & Zhang, Q. M. Maximizing the number of coexisting phases near invariant critical points for giant electrocaloric and electromechanical responses in ferroelectrics. *Appl. Phys. Lett.* **101,** 82904 (2012).

212. Kutnjak, Z., Petzelt, J. & Blinc, R. The giant electromechanical response in ferroelectric relaxors as a critical phenomenon. *Nature* **441,** 956–959 (2006).

213. Weyland, F., Acosta, M., Koruza, J., Breckner, P., Rödel, J. & Novak, N. Criticality: Concept to Enhance the Piezoelectric and Electrocaloric Properties of Ferroelectrics. *Adv. Funct. Mater.* **26,** 7326–7333 (2016).

214. Olson, G. B. Computational Design of Hierarchically Structured Materials. *Science* **277,** 1237–1242 (1997).

215. Schlom, D. G., Chen, L.-Q., Eom, C.-B., Rabe, K. M., Streiffer, S. K. & Triscone, J.-M. Strain Tuning of Ferroelectric Thin Films. *Annu. Rev. Mater. Res.* **37,** 589–626 (2007).

216. Pertsev, N. A., Zembilgotov, A. G. & Tagantsev, A. K. Effect of Mechanical Boundary Conditions on Phase Diagrams of Epitaxial Ferroelectric Thin Films. *Phys. Rev. Lett.* **80,** 1988–1991 (1998).

217. Li, Y. L., Hu, S. Y., Liu, Z. K. & Chen, L. Q. Effect of substrate constraint on the stability and evolution of ferroelectric domain structures in thin films. *Acta Mater.* **50,** 395–411 (2002).

218. Diéguez, O., Tinte, S., Antons, A., Bungaro, C., Neaton, J. B., Rabe, K. M. & Vanderbilt, D. Ab initio study of the phase diagram of epitaxial BaTiO3. *Phys. Rev. B* **69,** 212101 (2004).

219. Cohen, R. E. Origin of ferroelectricity in perovskite oxides. *Nature* **358,** 136–138 (1992).

220. Garcia, A. & Vanderbilt, D. First-principles study of stability and vibrational properties of tetragonal PbTiO3. *Phys. Rev. B* **54,** 3817–3824 (1996).

221. Wang, Y., Saal, J. E., Mei, Z. G., Wu, P. P., Wang, J. J., Shang, S. L., Liu, Z. K. & Chen, L. Q. A first-principles scheme to phonons of high temperature phase: No imaginary modes for cubic SrTiO3. *Appl. Phys. Lett.* **97,** 162907 (2010).

222. Zhou, M. J., Wang, Y., Ji, Y., Liu, Z. K., Chen, L. Q. & Nan, C. W. First-principles lattice dynamics and thermodynamic properties of pre-perovskite PbTiO 3. *Acta Mater.* **171,** 146–153 (2019).

223. Macdonald, D. D. Passivity - the key to our metals-based civilization. *Pure Appl. Chem.* **71,** 951–978 (1999).

224. Liu, Z. K., Wang, Y. & Shang, S. L. Origin of negative thermal expansion phenomenon in

solids. *Scr. Mater.* **66,** 130 (2011).

225. Liu, Z. K. Thermodynamic calculations of carbonitrides in microalloyed steels. *Scr. Mater.* **50,** 601–606 (2004).

226. Huang, C., Wikfeldt, K. T., Tokushima, T., Nordlund, D., Harada, Y., Bergmann, U., Niebuhr, M., Weiss, T. M., Horikawa, Y., Leetmaa, M., Ljungberg, M. P., Takahashi, O., Lenz, A., Ojamae, L., Lyubartsev, A. P., Shin, S., Pettersson, L. G. M. & Nilsson, A. The inhomogeneous structure of water at ambient conditions. *Proc. Natl. Acad. Sci. U. S. A.* **106,** 15214–15218 (2009).

227. Nilsson, A. & Pettersson, L. G. M. The structural origin of anomalous properties of liquid water. *Nat. Commun.* **6,** 8998 (2015).

228. Sicron, N., Ravel, B., Yacoby, Y., Stern, E. A., Dogan, F. & Rehr, J. J. Nature of the ferroelectric phase-transition in PbTiO3. *Phys. Rev. B* **50,** 13168–13180 (1994).

229. Sicron, N., Ravel, B., Yacoby, Y., Stern, E. A., Dogan, F. & Rehr, J. J. The ferroelectric phase transition in PbTiO3 from a local perspective. *Phys. B Condens. Matter* **208–209,** 319–320 (1995).

230. Ravel, B., Sicron, N., Yacoby, Y., Stern, E. A., Dogan, F. & Rehr, J. J. Order-disorder behavior in the phase transition of pbti03. *Ferroelectrics* **164,** 265–277 (1995).

231. Manley, M. E., Yethiraj, M., Sinn, H., Volz, H. M., Alatas, A., Lashley, J. C., Hults, W. L., Lander, G. H. & Smith, J. L. Formation of a new dynamical mode in alpha-uranium observed by inelastic x-ray and neutron scattering. *Phys. Rev. Lett.* **96,** 125501 (2006).

232. Manley, M. E., Lynn, J. W., Abernathy, D. L., Specht, E. D., Delaire, O., Bishop, A. R., Sahul, R. & Budai, J. D. Phonon localization drives polar nanoregions in a relaxor ferroelectric. *Nat Commun* **5,** 3683 (2014).

233. Manley, M. E., Hellman, O., Shulumba, N., May, A. F., Stonaha, P. J., Lynn, J. W., Garlea, V. O., Alatas, A., Hermann, R. P., Budai, J. D., Wang, H., Sales, B. C. & Minnich, A. J. Intrinsic anharmonic localization in thermoelectric PbSe. *Nat. Commun.* **10,** 1928 (2019).

234. Shirane, G. & Hoshino, S. On the phase transition in lead titanate. *J. Phys. Soc. Japan* **6,** 265–270 (1951).

235. Fu, H. X. & Cohen, R. E. Polarization rotation mechanism for ultrahigh electromechanical response in single-crystal piezoelectrics. *Nature* **403,** 281–283 (2000).

236. Meyer, B. & Vanderbilt, D. Ab initio study of BaTiO 3 and PbTiO 3 surfaces in external electric fields. *Phys. Rev. B* **63,** 205426 (2001).

237. Sheppard, D., Xiao, P., Chemelewski, W., Johnson, D. D. & Henkelman, G. A generalized solid-state nudged elastic band method. *J. Chem. Phys.* **136,** 1–8 (2012).

238. Chen, L.-Q. *Computer simulation of spinodal decomposition in ternary systems*. *Acta metal mater* **42,** (1994).

239. Whitesides, G. M. & Grzybowski, B. Self-assembly at all scales. *Science* **295,** 2418–2421 (2002).

240. Yu, H. C. & Lu, W. Dynamics of the self-assembly of nanovoids and nanobubbles in solids. *Acta Mater.* **53,** 1799–1807 (2005).

241. Stephanopoulos, N., Ortony, J. H. & Stupp, S. I. Self-assembly for the synthesis of functional biomaterials. *Acta Mater.* **61,** 912–930 (2013).

242. Oparin, A. I. *Origin of life*. (Dover Publications, 1965).

243. Martin, W., Baross, J., Kelley, D. & Russell, M. J. Hydrothermal vents and the origin of life. *Nat. Rev. Microbiol.* **6,** 805–814 (2008).

244. Sutherland, J. D. The Origin of Life - Out of the Blue. *Angew. Chemie - Int. Ed.* **55,** 104–121 (2016).

245. Maruyama, S., Kurokawa, K., Ebisuzaki, T., Sawaki, Y., Suda, K. & Santosh, M. Nine requirements for the origin of Earth's life: Not at the hydrothermal vent, but in a nuclear geyser system. *Geosci. Front.* **10,** 1337–1357 (2019).

246. Olson, G. B. & Kuehmann, C. J. Materials genomics: From CALPHAD to flight. *Scr. Mater.* **70,** 25–30 (2014).

247. National Research Council. *Application of lightweighting technology to military aircraft, vessels, and vehicles*. (National Academies Press, 2012).

248. Jiang, L., Zhao, J.-C. & Feng, G. *Nickel-Containing Alloys, Method of Manufacture Thereof*. (World Patent Application WO2005056852, 2005; U.S. Patent Application 20100135847, 2009).

249. Yeh, J.-W., Chen, S.-K., Lin, S.-J., Gan, J.-Y., Chin, T.-S., Shun, T.-T., Tsau, C.-H. & Chang, S.-Y. Nanostructured High-Entropy Alloys with Multiple Principal Elements: Novel Alloy Design Concepts and Outcomes. *Adv. Eng. Mater.* **6,** 299–303 (2004).

250. Cantor, B., Chang, I. T. H., Knight, P. & Vincent, A. J. B. Microstructural development in equiatomic multicomponent alloys. *Mater. Sci. Eng. A* **375–377,** 213–218 (2004).

251. Tsai, M.-H. & Yeh, J.-W. High-Entropy Alloys: A Critical Review. *Mater. Res. Lett.* **2,** 107–123 (2014).

252. Miracle, D. B. & Senkov, O. N. A critical review of high entropy alloys and related concepts. *Acta Mater.* **122,** 448–511 (2017).

253. Miracle, D. B. High entropy alloys as a bold step forward in alloy development. *Nat. Commun.* **10,** 1805 (2019).

254. Hsieh, M. H., Tsai, M. H., Shen, W. J. & Yeh, J. W. Structure and properties of two Al-Cr-Nb-Si-Ti high-entropy nitride coatings. *Surf. Coatings Technol.* **221,** 118–123 (2013).

255. Rost, C. M., Sachet, E., Borman, T., Moballegh, A., Dickey, E. C., Hou, D., Jones, J. L., Curtarolo, S. & Maria, J.-P. P. Entropy-stabilized oxides. *Nat. Commun.* **6,** 1–8 (2015).

256. Sarker, P., Harrington, T., Toher, C., Oses, C., Samiee, M., Maria, J. P., Brenner, D. W., Vecchio, K. S. & Curtarolo, S. High-entropy high-hardness metal carbides discovered by entropy descriptors. *Nat. Commun.* **9,** 1–10 (2018).

257. Harrington, T. J., Gild, J., Sarker, P., Toher, C., Rost, C. M., Dippo, O. F., McElfresh, C., Kaufmann, K., Marin, E., Borowski, L., Hopkins, P. E., Luo, J., Curtarolo, S., Brenner, D. W. & Vecchio, K. S. Phase stability and mechanical properties of novel high entropy transition metal carbides. *Acta Mater.* **166,** 271–280 (2019).

258. Gao, M. C., Miracle, D. B., Maurice, D., Yan, X., Zhang, Y. & Hawk, J. A. High-entropy functional materials. *Journal of Materials Research* **33,** 3138–3155 (2018).

259. Senkov, O. N., Miller, J. D., Miracle, D. B. & Woodward, C. Accelerated exploration of multi-principal element alloys with solid solution phases. *Nat. Commun.* **6,** 1–10 (2015).

260. Senkov, O. N., Miller, J. D., Miracle, D. B. & Woodward, C. Accelerated exploration of multi-principal element alloys for structural applications. *CALPHAD* **50,** 32–48 (2015).

261. TCHEA3: TCS High Entropy Alloy Database. Available at: https://www.thermocalc.com/media/83722/TCHEA3_extended_info.pdf.

262. Feurer, M. Updated sublattice models of topologically close packed phases with a revised phase description of σ phase. (2019). Available at: https://etda.libraries.psu.edu/catalog/17378mxf469.

263. Feurer, M., Liu, Z. K., Beese, A. M., Shang, S. L. & Bocklund, B. Sigma Phase Finite

Temperature Calculations. (2019). Available at: https://doi.org/10.25920/YJRC-ZJ59.

264. Qiu, Y., Hu, Y. J., Taylor, A., Styles, M. J., Marceau, R. K. W., Ceguerra, A. V., Gibson, M. A., Liu, Z. K., Fraser, H. L. & Birbilis, N. A lightweight single-phase AlTiVCr compositionally complex alloy. *Acta Mater.* **123,** 115–124 (2017).

265. Wang, Y., Yan, M., Zhu, Q., Wang, W. Y., Wu, Y., Hui, X. D., Otis, R., Shang, S. L., Liu, Z. K. & Chen, L. Q. Computation of entropies and phase equilibria in refractory V-Nb-Mo-Ta-W high-entropy alloys. *Acta Mater.* **143,** 88–101 (2018).

266. Yakel, H. L. Atom distributions in sigma phases. I. Fe and Cr atom distributions in a binary sigma phase equilibrated at 1063, 1013 and 923 K. *Acta Crystallogr. Sect. B Struct. Sci.* **39,** 20–28 (1983).

267. Cieślak, J., Reissner, M., Dubiel, S. M., Wernisch, J. & Steiner, W. Influence of composition and annealing conditions on the site-occupation in the σ-phase of Fe–Cr and Fe–V systems. *J. Alloys Compd.* **460,** 20–25 (2008).

268. van der Ven, A., Aydinol, M. K., Ceder, G., Kresse, G. & Hafner, J. First-Principles Investigation of Phase Stability in LixCoO2. *Phys. Rev. B* **58,** 2975 (1998).

269. Seo, D. H., Urban, A. & Ceder, G. Calibrating transition-metal energy levels and oxygen bands in first-principles calculations: Accurate prediction of redox potentials and charge transfer in lithium transition-metal oxides. *Phys. Rev. B* **92,** 115118 (2015).

270. Okumura, T., Yamaguchi, Y., Shikano, M. & Kobayashi, H. Correlation of lithium ion distribution and X-ray absorption near-edge structure in O3- and O2-lithium cobalt oxides from first-principle calculation. *J. Mater. Chem.* **22,** 17340–17348 (2012).

271. Zhou, F., Maxisch, T. & Ceder, G. Configurational Electronic Entropy and the Phase Diagram of Mixed-Valence Oxides: The Case of Li x FePO 4. *Phys. Rev. Lett.* **97,** 155704

(2006).

272. Delacourt, C., Poizot, P., Tarascon, J. & Masquelier, C. The existence of a temperature-driven solid solution in LixFePO 4 for 0 ≤ x ≤ 1. *Nat. Mater.* **4,** 254–260 (2005).

273. Dodd, J. L., Yazami, R. & Fultz, B. Phase Diagram of LixFePO 4. *Electrochem. Solid State Lett.* **9,** A151–A155 (2006).

274. Phan, A. T., Gheribi, A. E. & Chartrand, P. Modelling of phase equilibria of LiFePO4 - FePO4 olivine join for cathode material. *Can. J. Chem. Eng.* **97,** 2224–2233 (2019).

275. Matsui, H., Nakamura, T., Kobayashi, Y., Tabuchi, M. & Yamada, Y. Open-circuit voltage study on LiFePO 4 olivine cathode. *J. Power Sources* **195,** 6879–6883 (2010).

276. Kaufman, L., Perepezko, J. H., Hildal, K., Farmer, J., Day, D., Yang, N. & Branagan, D. Transformation, stability and Pourbaix diagrams of high performance corrosion resistant (HPCRM) alloys. *CALPHAD* **33,** 89–99 (2009).

277. Millett, P. C., Selvam, R. P. & Saxena, A. Stabilizing nanocrystalline materials with dopants. *Acta Mater.* **55,** 2329–2336 (2007).

278. Trelewicz, J. R. & Schuh, C. A. Grain boundary segregation and thermodynamically stable binary nanocrystalline alloys. *Phys. Rev. B* **79,** 94112 (2009).

279. Park, M., Chookajorn, T. & Schuh, C. A. Nano-phase separation sintering in nanostructure-stable vs. bulk-stable alloys. *Acta Mater.* **145,** 123–133 (2018).

280. Huang, T. Y., Kalidindi, A. R. & Schuh, C. A. Grain growth and second-phase precipitation in nanocrystalline aluminum–manganese electrodeposits. *J. Mater. Sci.* **53,** 3709–3719 (2018).

281. Amram, D. & Schuh, C. A. Higher Temperatures Yield Smaller Grains in a Thermally Stable Phase-Transforming Nanocrystalline Alloy. *Phys. Rev. Lett.* **121,** 145503 (2018).

282. Xing, W., Kalidindi, A. R., Amram, D. & Schuh, C. A. Solute interaction effects on grain boundary segregation in ternary alloys. *Acta Mater.* **161,** 285–294 (2018).

283. Saber, M., Kotan, H., Koch, C. C. & Scattergood, R. O. Thermodynamic stabilization of nanocrystalline binary alloys. *J. Appl. Phys.* **113,** 063515 (2013).

284. Nagamatsu, J., Nakagawa, N., Muranaka, T., Zenitani, Y. & Akimitsu, J. Superconductivity at 39 K in magnesium diboride. *Nature* **410,** 63–64 (2001).

285. Liu, Z. K., Zhong, Y., Schlom, D. G., Xi, X. X. & Li, Q. Computational thermodynamic modeling of the Mg-B system. *CALPHAD* **25,** 299–303 (2001).

286. Liu, Z. K., Schlom, D. G., Li, Q. & Xi, X. X. Thermodynamics of the Mg–B system: Implications for the deposition of MgB2 thin films. *Appl. Phys. Lett.* **78,** 3678 (2001).

287. Zeng, X. H., Pogrebnyakov, A. V, Kotcharov, A., Jones, J. E., Xi, X. X., Lysczek, E. M., Redwing, J. M., Xu, S. Y., Lettieri, J., Schlom, D. G., Tian, W., Pan, X. Q. & Liu, Z. K. In situ epitaxial MgB2 thin films for superconducting electronics. *Nat. Mater.* **1,** 35–38 (2002).

288. Ihlefeld, J. F., Podraza, N. J., Liu, Z. K., Rai, R. C., Xu, X., Heeg, T., Chen, Y. B., Li, J., Collins, R. W., Musfeldt, J. L., Pan, X. Q., Schubert, J., Ramesh, R. & Schlom, D. G. Optical band gap of BiFeO[sub 3] grown by molecular-beam epitaxy. *Appl. Phys. Lett.* **92,** 142908 (2008).

289. Lee, J. H., Ke, X., Misra, R., Ihlefeld, J. F., Xu, X. S., Mei, Z. G., Heeg, T., Roeckerath, M., Schubert, J., Liu, Z. K., Musfeldt, J. L., Schiffer, P. & Schlom, D. G. Adsorption-controlled growth of BiMnO3 films by molecular-beam epitaxy. *Appl. Phys. Lett.* **96,** 262905 (2010).

290. Brooks, C. M., Misra, R., Mundy, J. A., Zhang, L. A., Holinsworth, B. S., O'Neal, K. R.,

Heeg, T., Zander, W., Schubert, J., Musfeldt, J. L., Liu, Z.-K., Muller, D. A., Schiffer, P. & Schlom, D. G. The adsorption-controlled growth of LuFe 2 O 4 by molecular-beam epitaxy. *Appl. Phys. Lett.* **101,** 132907 (2012).

291. Smith, E. H., Ihlefeld, J. F., Heikes, C. A., Paik, H., Nie, Y., Adamo, C., Heeg, T., Liu, Z. K. & Schlom, D. G. Exploiting kinetics and thermodynamics to grow phase-pure complex oxides by molecular-beam epitaxy under continuous codeposition. *Phys. Rev. Mater.* **1,** 023403 (2017).

292. Paik, H., Chen, Z., Lochocki, E., Seidner H., A., Verma, A., Tanen, N., Park, J., Uchida, M., Shang, S., Zhou, B.-C., Brützam, M., Uecker, R., Liu, Z.-K., Jena, D., Shen, K. M., Muller, D. A. & Schlom, D. G. Adsorption-controlled growth of La-doped BaSnO 3 by molecular-beam epitaxy. *APL Mater.* **5,** 116107 (2017).

293. Kang, J.-H., Xie, L., Wang, Y., Lee, H., Campbell, N., Jiang, J., Ryan, P. J., Keavney, D. J., Lee, J.-W., Kim, T. H., Pan, X., Chen, L.-Q., Hellstrom, E. E., Rzchowski, M. S., Liu, Z.-K. & Eom, C.-B. Control of Epitaxial BaFe2As2 Atomic Configurations with Substrate Surface Terminations. *Nano Lett.* **18,** 6347–6352 (2018).

294. Nair, H. P., Liu, Y., Ruf, J. P., Schreiber, N. J., Shang, S.-L., Baek, D. J., Goodge, B. H., Kourkoutis, L. F., Liu, Z. K., Shen, K. M. & Schlom, D. G. Synthesis science of SrRuO3and CaRuO3epitaxial films with high residual resistivity ratios. *APL Mater.* **6,** 046101 (2018).

295. Lindwall, G., Shang, S., Kelly, N. R. N. R., Anderson, T. & Liu, Z.-K. Thermodynamics of the S-Sn system: Implication for synthesis of earth abundant photovoltaic absorber materials. *Sol. Energy* **125,** 314–323 (2016).

296. Adkison, K. M., Shang, S.-L., Bocklund, B. J., Klimm, D., Schlom, D. G. & Liu, Z. K.

Suitability of Binary Oxides for Molecular-Beam Epitaxy Source Materials: A Comprehensive Thermodynamic Analysis. *Appl. Phys. Lett. Mater.* **under revi,** (2020).

297. Hopkinson, N., Hague, R. & Dickens, P. *Rapid Manufacturing: An Industrial Revolution for the Digital Age - Neil Hopkinson, Richard Hague, Philip Dickens*. (Wiley-Blackwell, Berlin, 2005).

298. DebRoy, T., Wei, H. L., Zuback, J. S., Mukherjee, T., Elmer, J. W., Milewski, J. O., Beese, A. M., Wilson-Heid, A., De, A. & Zhang, W. Additive manufacturing of metallic components – Process, structure and properties. *Prog. Mater. Sci.* **92,** 112–224 (2018).

299. Reichardt, A., Shapiro, A. A., Otis, R., Dillon, R. P., Borgonia, J. P., McEnerney, B. W., Hosemann, P. & Beese, A. M. Advances in additive manufacturing of metal-based functionally graded materials. *Int. Mater. Rev.* 1–29 (2020). doi:10.1080/09506608.2019.1709354

300. Keller, T., Lindwall, G., Ghosh, S., Ma, L., Lane, B. M., Zhang, F., Kattner, U. R., Lass, E. A., Heigel, J. C., Idell, Y., Williams, M. E., Allen, A. J., Guyer, J. E. & Levine, L. E. Application of finite element, phase-field, and CALPHAD-based methods to additive manufacturing of Ni-based superalloys. *Acta Mater.* **139,** 244–253 (2017).

301. Scheil, E. Bemerkungen zur Schichtkristallbildung. *Zeitschrift Fur Met.* **34,** 70–72 (1942).

302. Gulliver, G. H. The quantitative effect of rapid cooling upon the constitution of binary alloys. *J. Inst. Met* **9,** 120–157 (1913).

303. Andersson, J. O., Helander, T., Höglund, L., Shi, P. F., Sundman, B., Hoglund, L. H., Shi, P. F., Sundman, B., Höglund, L., Shi, P. F. & Sundman, B. THERMO-CALC & DICTRA, computational tools for materials science. *CALPHAD* **26,** 273–312 (2002).

304. Chen, L.-Q. Phase-field models for microstructure evolution. *Annu. Rev. Mater. Res.* **32,**

113–140 (2002).

305. Wagner, R., Kampmann, R. & Voorhees, P. W. in *Phase Transformations in Materials* (ed. Kostorz, G.) (Weinheim, Wiley-VCH, 2001).

306. Langer, J. S. & Schwartz, A. J. Kinetics of nucleation in near-critical fluids. *Phys. Rev. A* **21,** 948–958 (1980).

307. TC-PRISMA. Available at: http://www.thermocalc.com/products-services/software/precipitation-module-(tc-prisma).

308. PanPrecipitation: https://computherm.com/?docs=documentations/software-manual/panprecipitation. (2020).

309. Hofmann, D. C., Roberts, S., Otis, R., Kolodziejska, J., Dillon, R. P., Suh, J. O., Shapiro, A. A., Liu, Z. K. & Borgonia, J. P. Developing gradient metal alloys through radial deposition additive manufacturing. *Sci. Rep.* **4,** 5357 (2014).

310. Carroll, B. E., Otis, R. A., Borgonia, J. P., Suh, J. O., Dillon, P. R., Shapiro, A. A., Hofmann, D. C., Liu, Z.-K. & Beese, A. M. Functionally graded material of 304L stainless steel and Inconel 625 fabricated by directed energy deposition: Characterization and thermodynamic modeling. *Acta Mater.* **108,** 46–54 (2016).

311. Bobbio, L. D., Otis, R. A., Borgonia, J. P., Dillon, R. P., Shapiro, A. A., Liu, Z.-K. & Beese, A. M. Additive manufacturing of a functionally graded material from Ti-6Al-4V to Invar: Experimental characterization and thermodynamic calculations. *Acta Mater.* **127,** 133–142 (2017).

312. Bobbio, L. D., Bocklund, B., Otis, R., Borgonia, J. P., Dillon, R. P., Shapiro, A. A., McEnerney, B., Liu, Z.-K. & Beese, A. M. Characterization of a functionally graded material of Ti-6Al-4V to 304L stainless steel with an intermediate V section. *J. Alloys*

Compd. **742,** 1031–1036 (2018).

313. Bobbio, L. D., Bocklund, B., Otis, R., Borgonia, J. P., Dillon, R. P., Shapiro, A. A. A., McEnerney, B., Liu, Z.-K. & Beese, A. M. Experimental analysis and thermodynamic calculations of an additively manufactured functionally graded material of V to Invar 36. *J. Mater. Res.* **33,** 1642–1649 (2018).

314. Bobbio, L. D., Bocklund, B., Reichardt, A., Otis, R., Borgonia, J. P., Dillon, R. P., Shapiro, A. A., McEnerney, B. W., Hosemann, P., Liu, Z. K. & Beese, A. M. Analysis of formation and growth of the σ phase in additively manufactured functionally graded materials. *J. Alloys Compd.* **814,** 151729 (2020).

315. Kirk, T., Galvan, E., Malak, R. & Arroyave, R. Computational design of gradient paths in additively manufactured functionally graded materials. *J. Mech. Des. Trans. ASME* **140,** (2018).

316. Eliseeva, O. V., Kirk, T., Samimi, P., Malak, R., Arróyave, R., Elwany, A. & Karaman, I. Functionally Graded Materials through robotics-inspired path planning. *Mater. Des.* **182,** 107975 (2019).

317. Moustafa, A. R., Durga, A., Lindwall, G. & Cordero, Z. C. Scheil ternary projection (STeP) diagrams for designing additively manufactured functionally graded metals. *Addit. Manuf.* **32,** 101008 (2019).

318. Bocklund, B., Bobbio, L. D., Otis, R. A., Beese, A. M. & Liu, Z.-K. Experimental validation of Scheil–Gulliver simulations for gradient path planning in additively manufactured functionally graded materials. *Materialia* **11,** 100689 (2020).

319. Liu, Y., Wang, Y., Wu, X. & Shi, J. Nonequilibrium thermodynamic calculation and experimental investigation of an additively manufactured functionally graded material. *J.*

Alloys Compd. **838,** 155322 (2020).

320. Python Software Foundation. Python Package Index (PyPI). (2019).

321. Bocklund, B., Bobbio, L. D., Otis, R. A., Beese, A. M. & Liu, Z.-K. pycalphad-scheil: 0.1.2. (2020). doi:10.5281/zenodo.3630657

322. Sundman, B., Chen, Q. & Du, Y. A Review of Calphad Modeling of Ordered Phases. *J. Phase Equilibria Diffus.* **39,** 678–693 (2018).

323. Ansara, I., Sundman, B. & Willemin, P. Thermodynamic modeling of ordered phases in the Ni-Al system. *Acta Metall.* **36,** 977–982 (1988).

324. Bocklund, B., Bobbio, L. D., Otis, R. A., Beese, A. M. & Liu, Z.-K. PhasesResearchLab/scheil-solidification- ti64-invar: 1.0. (2020). doi:10.5281/zenodo.3630600

325. De Keyzer, J., Cacciamani, G., Dupin, N. & Wollants, P. Thermodynamic modeling and optimization of the Fe–Ni–Ti system. *CALPHAD* **33,** 109–123 (2009).

326. Shang, S. L., Wang, Y. & Liu, Z. K. First-principles elastic constants of α- and θ- Al2O3. *Appl. Phys. Lett.* **90,** 101909 (2007).

327. Shang, S.-L., Zhang, H., Wang, Y. & Liu, Z.-K. Temperature-dependent elastic stiffness constants of α- and θ-Al 2 O 3 from first-principles calculations. *J. Phys. Condens. Matter* **22,** 375403 (2010).

328. Zhang, H., Shang, S. L., Wang, Y., Saengdeejing, A., Chen, L. Q. & Liu, Z. K. First-principles calculations of the elastic, phonon and thermodynamic properties of Al12Mg17. *Acta Mater.* **58,** 4012–4018 (2010).

329. Lu, X. G., Selleby, M. & Sundman, B. Theoretical modeling of molar volume and thermal expansion. *Acta Mater.* **53,** 2259–2272 (2005).

330. Lu, X. G., Selleby, M. & Sundman, B. Assessments of molar volume and thermal expansion for selected bcc, fcc and hcp metallic elements. *Calphad Comput. Coupling Phase Diagrams Thermochem.* **29,** 68–89 (2005).

331. Brosh, E., Makov, G. & Shneck, R. Z. Application of CALPHAD to high pressures. *Calphad Comput. Coupling Phase Diagrams Thermochem.* **31,** 173–185 (2007).

332. Sandberg, N., Magyari-Köpe, B. & Mattsson, T. R. Self-Diffusion Rates in Al from Combined First-Principles and Model-Potential Calculations. *Phys. Rev. Lett.* **89,** 065901 (2002).

333. Fang, H. Z., Wang, W. Y., Jablonski, P. D. & Liu, Z. K. Effects of reactive elements on the structure and diffusivity of liquid chromia: An ab initio molecular dynamics study. *Phys. Rev. B* **85,** 014207 (2012).

334. Eyring, H. The Activated Complex in Chemical Reactions. *J. Chem. Phys.* **3,** 107–115 (1935).

335. Wynne-Jones, W. F. K. & Eyring, H. The absolute rate of reactions in condensed phases. *J. Chem. Phys.* **3,** 492–502 (1935).

336. Vineyard, G. H. & Dienes, G. J. The theory of defect concentration in crystals. *Phys. Rev.* **93,** 265–268 (1954).

337. Mantina, M., Wang, Y., Arroyave, R., Chen, L. Q., Liu, Z. K. & Wolverton, C. First-principles calculation of self-diffusion coefficients. *Phys. Rev. Lett.* **100,** 215901 (2008).

338. Wimmer, E., Wolf, W., Sticht, J., Saxe, P., Geller, C. B., Najafabadi, R. & Young, G. A. Temperature-dependent diffusion coefficients from ab initio computations: Hydrogen, deuterium, and tritium in nickel. *Phys. Rev. B* **77,** 134305 (2008).

339. Henkelman, G. & Jónsson, H. Improved tangent estimate in the nudged elastic band

method for finding minimum energy paths and saddle points. *J. Chem. Phys.* **113,** 9978 (2000).

340. Mantina, M., Chen, L. Q. Q. & Liu, Z. K. K. Predicting Diffusion Coefficients from First-principles via Eyring's Reaction Rate Theory. *Defect Diffus. Forum* **294,** 1–13 (2009).

341. Leclaire, A. D. & Lidiard, A. B. LIII. Correlation effects in diffusion in crystals. *Philos. Mag.* **1,** 518–527 (1956).

342. Mantina, M., Wang, Y., Chen, L. Q., Liu, Z. K. & Wolverton, C. First principles impurity diffusion coefficients. *Acta Mater.* **57,** 4102–4108 (2009).

343. Mantina, M., Shang, S. L., Wang, Y., Chen, L. Q. & Liu, Z. K. 3d transition metal impurities in aluminum: A first-principles study. *Phys. Rev. B* **80,** 184111 (2009).

344. Ross, A. J., Fang, H. Z., Shang, S. L., Lindwall, G. & Liu, Z. K. A curved pathway for oxygen interstitial diffusion in aluminum. *Comput. Mater. Sci.* **140,** 47–54 (2017).

345. Hargather, C. Z., Shang, S. L., Liu, Z. K. & Du, Y. A first-principles study of self-diffusion coefficients of fcc Ni. *Comput. Mater. Sci.* **86,** 17–23 (2014).

346. Hargather, C. Z., Shang, S. L. & Liu, Z. K. A comprehensive first-principles study of solute elements in dilute Ni alloys: Diffusion coefficients and their implications to tailor creep rate. *Acta Mater.* **157,** 126–141 (2018).

347. Huang, S., Worthington, D. L., Asta, M., Ozolins, V., Ghosh, G. & Liaw, P. K. Calculation of impurity diffusivities in α-Fe using first-principles methods. *Acta Mater.* **58,** 1982–1993 (2010).

348. Ding, H., Huang, S., Ghosh, G., Liaw, P. K. & Asta, M. A computational study of impurity diffusivities for 5d transition metal solutes in α-Fe. *Scr. Mater.* **67,** 732–735 (2012).

349. Wu, H., Mayeshiba, T. & Morgan, D. High-throughput ab-initio dilute solute diffusion database. *Sci. Data* **3,** 160054 (2016).

350. Ganeshan, S., Hector, L. G. & Liu, Z. K. First-principles study of self-diffusion in hcp Mg and Zn. *Comput. Mater. Sci.* **50,** 301–307 (2010).

351. Ganeshan, S., Shang, S. L., Wang, Y. & Liu, Z. K. Effect of alloying elements on the elastic properties of Mg from first-principles calculations. *Acta Mater.* **57,** 3876–3884 (2009).

352. Zhou, B.-C., Shang, S.-L., Wang, Y. & Liu, Z.-K. Diffusion coefficients of alloying elements in dilute Mg alloys: A comprehensive first-principles study. *Acta Mater.* **103,** 573–586 (2016).

353. Perdew, J. P., Ruzsinszky, A., Csonka, G. I., Vydrov, O. A., Scuseria, G. E., Constantin, L. A., Zhou, X. L. & Burke, K. Restoring the density-gradient expansion for exchange in solids and surfaces. *Phys. Rev. Lett.* **100,** 136406 (2008).

354. Van der Ven, A., Ceder, G., Asta, M. & Tepesch, P. D. First-principles theory of ionic diffusion with nondilute carriers. *Phys. Rev. B* **64,** 184307 (2001).

355. Van der Ven, A. & Ceder, G. First principles calculation of the interdiffusion coefficient in binary alloys. *Phys. Rev. Lett.* **94,** 45901 (2005).

356. Gabriel Goiri, J., Krishna Kolli, S. & Van der Ven, A. Role of short- and long-range ordering on diffusion in Ni-Al alloys. *Phys. Rev. Mater.* **3,** 93402 (2019).

357. Mahan, G. D. & Sofo, J. O. The best thermoelectric. *Proc. Natl. Acad. Sci.* **93,** 7436–7439 (1996).

358. Snyder, G. J. & Toberer, E. S. Complex thermoelectric materials. *Nat. Mater.* **7,** 105–114 (2008).

359. Dávila Pineda, D. & Rezania, A. *Thermoelectric Energy Conversion: Basic Concepts and Device Applications*. (Wiley, 2017).

360. Cutler, M. & Mott, N. F. Observation of Anderson localization in an electron gas. *Phys. Rev.* **181,** 1336 (1969).

361. Scheidemantel, T. J., Ambrosch-Draxl, C., Thonhauser, T., Badding, J. V. & Sofo, J. O. Transport coefficients from first-principles calculations. *Phys. Rev. B* **68,** 125210 (2003).

362. Madsen, G. K. H. & Singh, D. J. BoltzTraP. A code for calculating band-structure dependent quantities. *Comput. Phys. Commun.* **175,** 67–71 (2006).

363. Wang, Y., Hu, Y.-J., Bocklund, B., Shang, S.-L., Zhou, B.-C., Liu, Z.-K. & Chen, L.-Q. First-principles thermodynamic theory of Seebeck coefficients. *Phys. Rev. B* **98,** 224101 (2018).

364. Wang, Y., Chong, X., Hu, Y. J., Shang, S. L., Drymiotis, F. R., Firdosy, S. A., Star, K. E., Fleurial, J. P., Ravi, V. A., Chen, L. Q. & Liu, Z. K. An alternative approach to predict Seebeck coefficients: Application to La 3−x Te 4. *Scr. Mater.* **169,** 87–91 (2019).

365. McMahan, A. K. & Ross, M. High-temperature electron-band calculations. *Phys. Rev. B* **15,** 718 (1977).

366. Mermin, N. D. Thermal Properties of the Inhomogeneous Electron Gas. *Phys. Rev.* **137,** A1441–A1443 (1965).

367. Kresse, G. & Furthmüller, J. Efficiency of ab-initio total energy calculations for metals and semiconductors using a plane-wave basis set. *Comput. Mater. Sci.* **6,** 15–50 (1996).

368. Kresse, G., Joubert, D., Kresse, D. & Joubert, G. From ultrasoft pseudopotentials to the projector augmented-wave method. *Phys. Rev. B Condens. Matter* **59,** 1758–1775 (1999).

369. Blaha, P., Schwarz, K., Madsen, G., Kvasnicka, D. & Luitz, J. WIEN2k: An Augmented

Plane Wave + Local Orbitals Program for Calculating Crystal Properties. (2003). Available at: http://www.wien2k.at/.

370. Heremans, J. P., Thrush, C. M. & Morelli, D. T. Thermopower enhancement in lead telluride nanostructures. *Phys. Rev. B* **70,** 115334 (2004).

371. Heremans, J. P., Jovovic, V., Toberer, E. S., Saramat, A., Kurosaki, K., Charoenphakdee, A., Yamanaka, S. & Snyder, G. J. Enhancement of thermoelectric efficiency in PbTe by distortion of the electronic density of states. *Science* **321,** 554–557 (2008).

372. LaLonde, A. D., Pei, Y., Snyder, G. J., Zhang, J., Ren, B., Wang, Z., Kanatzidis, M. G., Kanatzidis, M. G., Paraskevopoulos, K. M. & Kanatzidis, M. G. Reevaluation of PbTe1−xIx as high performance n-type thermoelectric material. *Energy Environ. Sci.* **4,** 2090 (2011).

373. Zhao, L.-D., Lo, S.-H., Zhang, Y., Sun, H., Tan, G., Uher, C., Wolverton, C., Dravid, V. P. & Kanatzidis, M. G. Ultralow thermal conductivity and high thermoelectric figure of merit in SnSe crystals. *Nature* **508,** 373–377 (2014).

374. Zhao, L.-D., Tan, G., Hao, S., He, J., Pei, Y., Chi, H., Wang, H., Gong, S., Xu, H. & Dravid, V. P. Ultrahigh power factor and thermoelectric performance in hole-doped single-crystal SnSe. *Science* **351,** 141–144 (2016).

375. Sassi, S., Candolfi, C., Vaney, J.-B., Ohorodniichuk, V., Masschelein, P., Dauscher, A. & Lenoir, B. Assessment of the thermoelectric performance of polycrystalline *p* -type SnSe. *Appl. Phys. Lett.* **104,** 212105 (2014).

376. Serrano-Sánchez, F., Gharsallah, M., Nemes, N. M., Mompean, F. J., Martínez, J. L. & Alonso, J. A. Record Seebeck coefficient and extremely low thermal conductivity in nanostructured SnSe. *Appl. Phys. Lett.* **106,** 083902 (2015).

377. Ogata, S. Ideal Pure Shear Strength of Aluminum and Copper. *Science* **298,** 807–811 (2002).

378. Kohan, A. F., Ceder, G., Morgan, D. & de Walle, C. G. Van. First-principles study of native point defects in ZnO. *Phys. Rev. B* **61,** 15019 (2000).

379. Shang, S.-L., Shimanek, J., Qin, S., Wang, Y., Beese, A. M. & Liu, Z.-K. Unveiling dislocation characteristics in Ni3Al from stacking fault energy and ideal strength: A first-principles study via pure alias shear deformation. *Phys. Rev. B* **101,** 24102 (2020).

380. Qin, S., Shang, S. L., Shimanek, J., Liu, Z. K. & Beese, A. M. Macroscopic plastic deformation through an integrated first-principles calculations and finite element simulations: Application to nickel single crystal. *http://arxiv.org/abs/2002.08552* (2020).

381. Yao, Z., Schäublin, R. & Victoria, M. Irradiation induced behavior of pure Ni single crystal irradiated with high energy protons. *J. Nucl. Mater.* **323,** 388–393 (2003).

382. Haasen, P. Plastic deformation of nickel single crystals at low temperatures. *Philos. Mag.* **3,** 384–418 (1958).

383. Shannon, C. E. A Mathematical Theory of Communication. *Bell Syst. Tech. J.* **27,** 623–656 (1948).

384. Shannon, C. E. Prediction and Entropy of Printed English. *Bell Syst. Tech. J.* **30,** 50–64 (1951).

385. Szilard, L. Uber die Entropieverminderung in einem thermodynamischen System bei Eingriffen intelligenter Wesen. *Zeitschrift fur Phys.* **53,** 840–856 (1929).

386. Szilard, L. On the Decrease of Entropy in a Thermodynamic System by the Intervention of Intelligent Beings. *Behav. Sci.* **9,** 301–310 (1964).

387. Brillouin, L. Maxwell's Demon Cannot Operate: Information and Entropy. I. *J. Appl. Phys.*

22, 334–337 (1951).

388. Brillouin, L. *Science and information theory*. (Academic Press, 1962).

389. Maruyama, K., Nori, F. & Vedral, V. Colloquium : The physics of Maxwell's demon and information. *Rev. Mod. Phys.* **81,** 1–23 (2009).

390. Landauer, R. Irreversibility and Heat Generation in the Computing Process. *IBM J. Res. Dev.* **5,** 183–191 (1961).

391. Landauer, R. Dissipation and noise immunity in computation and communication. *Nature* **335,** 779–784 (1988).

392. Bennett, C. H. The thermodynamics of computation—a review. *Int. J. Theor. Phys.* **21,** 905–940 (1982).

393. Toyabe, S., Sagawa, T., Ueda, M., Muneyuki, E. & Sano, M. Experimental demonstration of information-to-energy conversion and validation of the generalized Jarzynski equality. *Nat. Phys.* **6,** 988–992 (2010).

394. Bérut, A., Arakelyan, A., Petrosyan, A., Ciliberto, S., Dillenschneider, R. & Lutz, E. Experimental verification of Landauer's principle linking information and thermodynamics. *Nature* **483,** 187–189 (2012).

395. Huntington, S. P. *The clash of civilizations and the remaking of world order*. (Simon & Schuster, 2011).

396. Quijano, J. & Lin, H. Entropy in the Critical Zone: A Comprehensive Review. *Entropy* **16,** 3482–3536 (2014).

397. Brillouin, L. Physical Entropy and Information. II. *J. Appl. Phys.* **22,** 338–343 (1951).

398. Brillouin, L. The Negentropy Principle of Information. *J. Appl. Phys.* **24,** 1152–1163 (1953).

399. Brillouin, L. Information Theory and its Applications to Fundamental Problems in Physics. *Nature* **183,** 501–502 (1959).

400. Brillouin, L. Thermodynamics, Statistics, and Information. *Am. J. Phys.* **29,** 318–328 (1961).

401. Strasberg, P., Schaller, G., Brandes, T. & Esposito, M. Quantum and Information Thermodynamics: A Unifying Framework Based on Repeated Interactions. *Phys. Rev. X* **7,** 021003 (2017).

402. Vinjanampathy, S. & Anders, J. Quantum thermodynamics. *Contemp. Phys.* **57,** 545–579 (2016).

403. James, M. & André, X. Perspective on quantum thermodynamics. *New J. Phys.* **18,** 11002 (2016).

404. Pop, E. Energy Dissipation and Transport in Nanoscale Devices. *Nano Res* **3,** 147–169 (2010).

405. Jørgensen, S. E. *A new ecology : systems perspective*. (Elsevier, 2007).

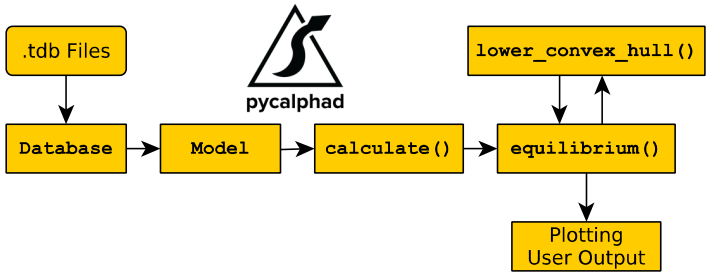

Figure 1. General architecture of the PyCalphad software package.[146]

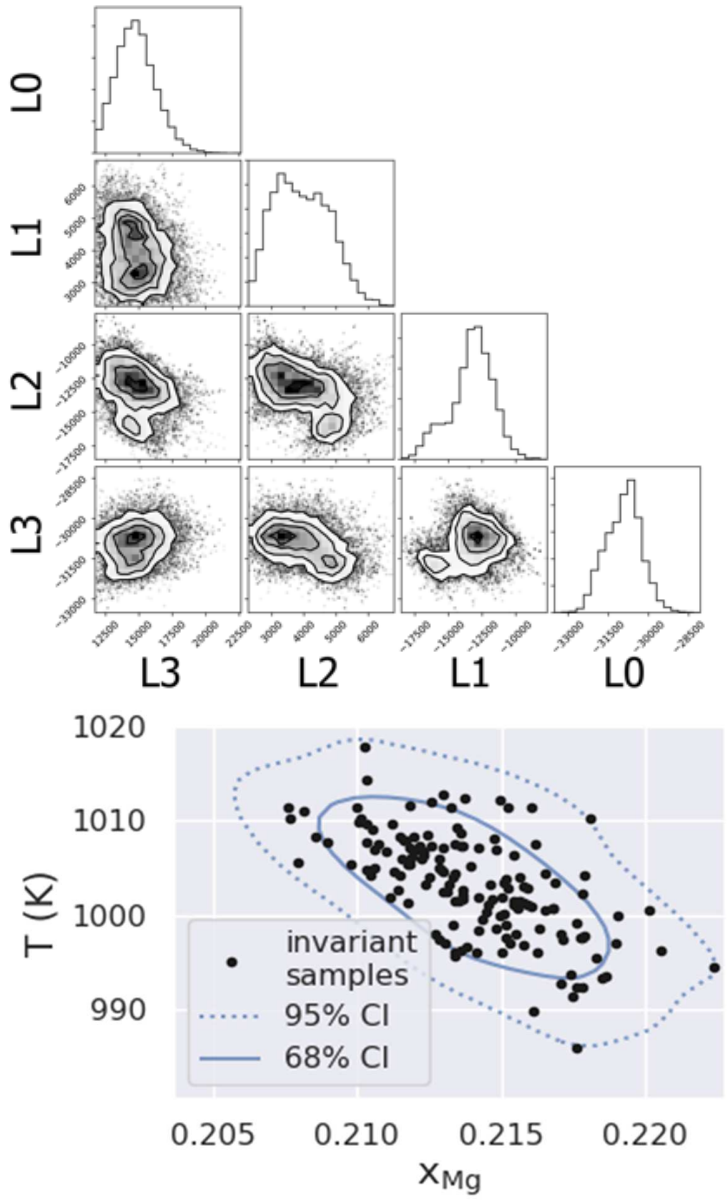

Figure 2. (a) Corner plot of the parameters in the Cu-Mg liquid phase with the diagonal images for the histogram of each parameter in the Markov chain and the off-diagonal images for the covariance between two parameters; [151] (b) FCC - Laves – liquid eutectics in Cu-Mg plotted for all 750 sampled parameter sets with 68% and 95% uncertainty intervals.

166

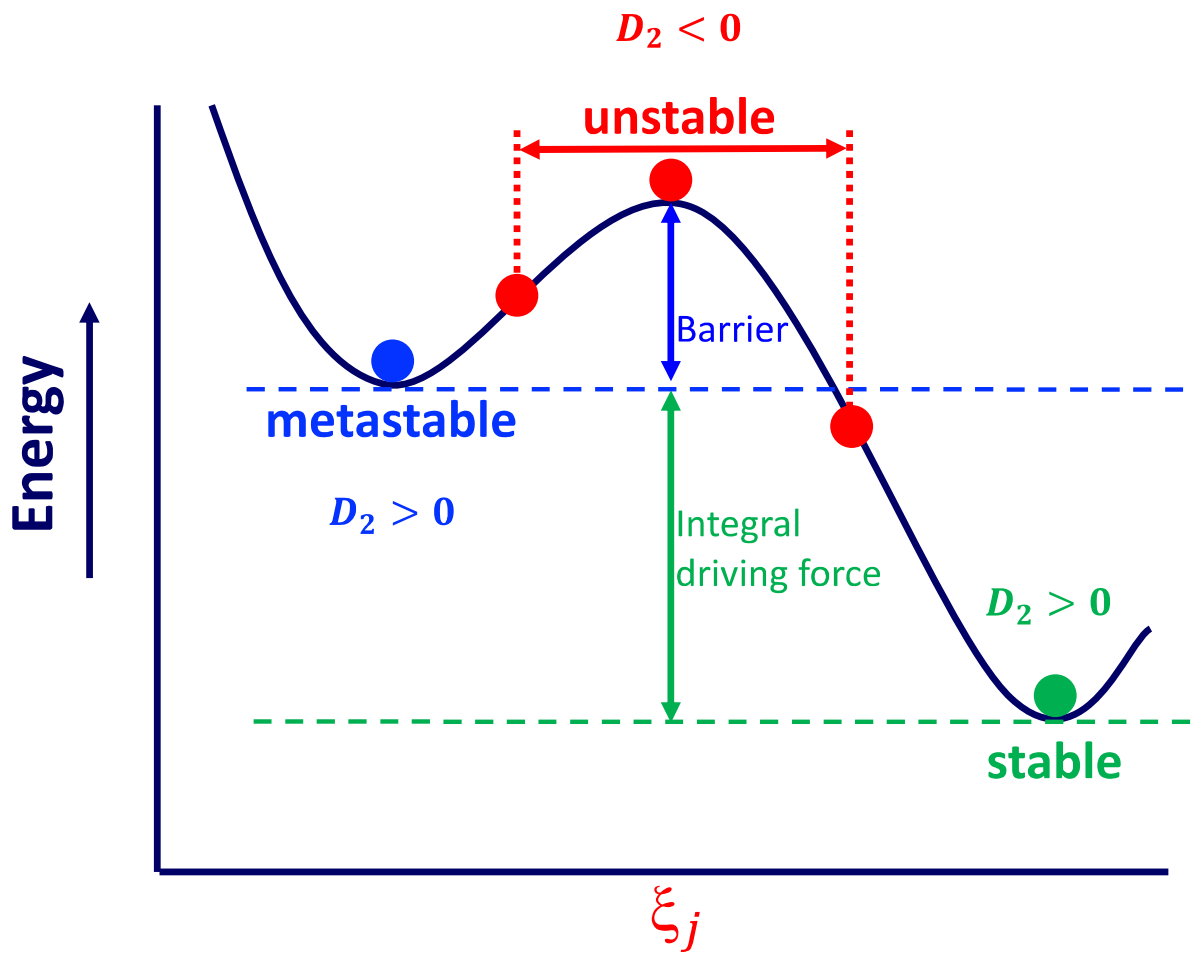

Figure 3. Schematic diagram of energy landscape as a function of one internal variable

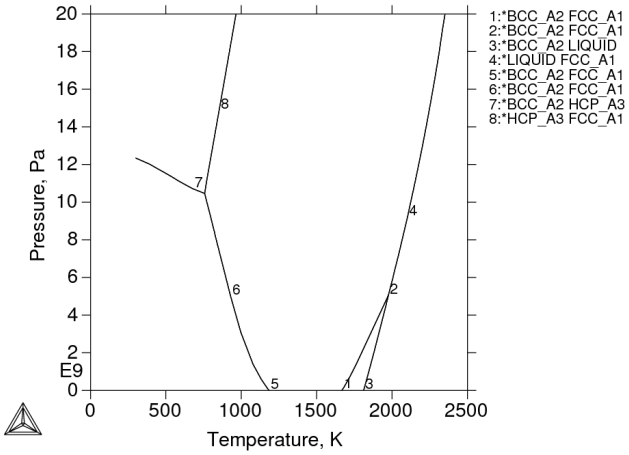
Pressure, Pa
E9
Temperature, K
1:*BCC_A2 FCC_A1
2:*BCC_A2 FCC_A1
3:*BCC_A2 LIQUID
4:*LIQUID FCC_A1
5:*BCC_A2 FCC_A1
6:*BCC_A2 FCC_A1
7:*BCC_A2 HCP_A3
8:*HCP_A3 FCC_A1

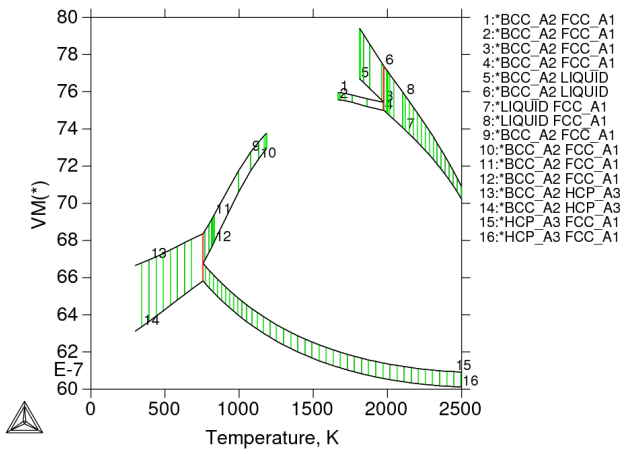
VM(*)
E-7
Temperature, K
1:*BCC_A2 FCC_A1
2:*BCC_A2 FCC_A1
3:*BCC_A2 FCC_A1
4:*BCC_A2 FCC_A1
5:*BCC_A2 LIQUID
6:*BCC_A2 LIQUID
7:*LIQUID FCC_A1
8:*LIQUID FCC_A1
9:*BCC_A2 FCC_A1
10:*BCC_A2 FCC_A1
11:*BCC_A2 FCC_A1
12:*BCC_A2 FCC_A1
13:*BCC_A2 HCP_A3
14:*BCC_A2 HCP_A3
15:*HCP_A3 FCC_A1
16:*HCP_A3 FCC_A1

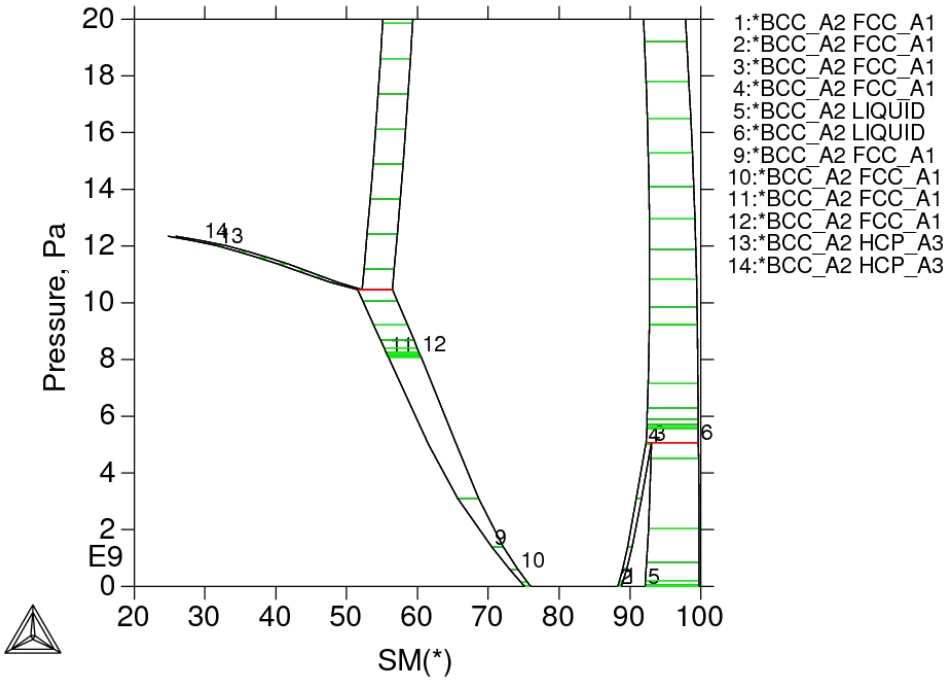
Pressure, Pa
E9
SM(*)
1:*BCC_A2 FCC_A1
2:*BCC_A2 FCC_A1
3:*BCC_A2 FCC_A1
4:*BCC_A2 FCC_A1
5:*BCC_A2 LIQUID
6:*BCC_A2 LIQUID
9:*BCC_A2 FCC_A1
10:*BCC_A2 FCC_A1
11:*BCC_A2 FCC_A1
12:*BCC_A2 FCC_A1
13:*BCC_A2 HCP_A3
14:*BCC_A2 HCP_A3

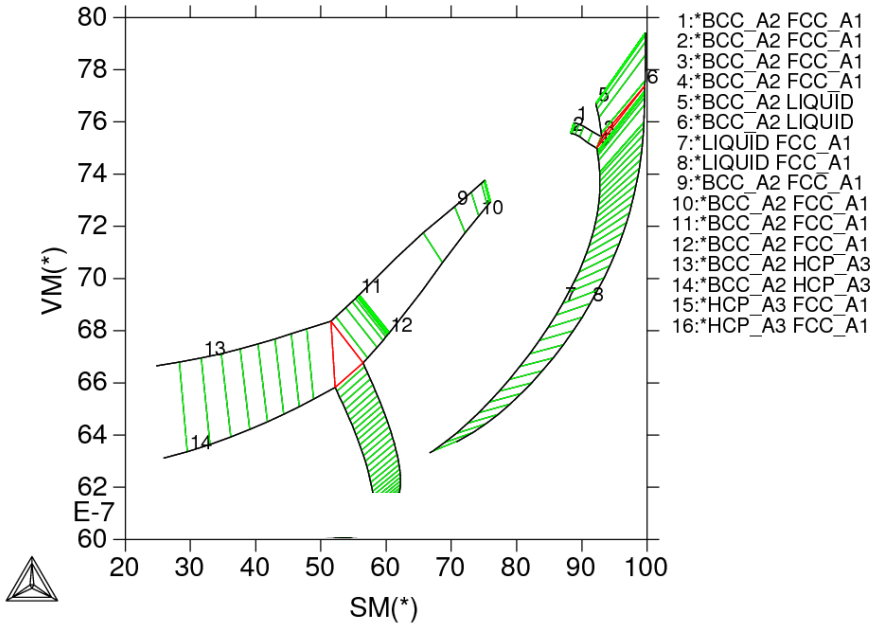

Figure 4. Four types of phase diagrams of pure Fe: (a) T–*P*; (b) T − V_m; (c) S_m − P; (d) S *m*–V *m* with the green lines being tie-lines.

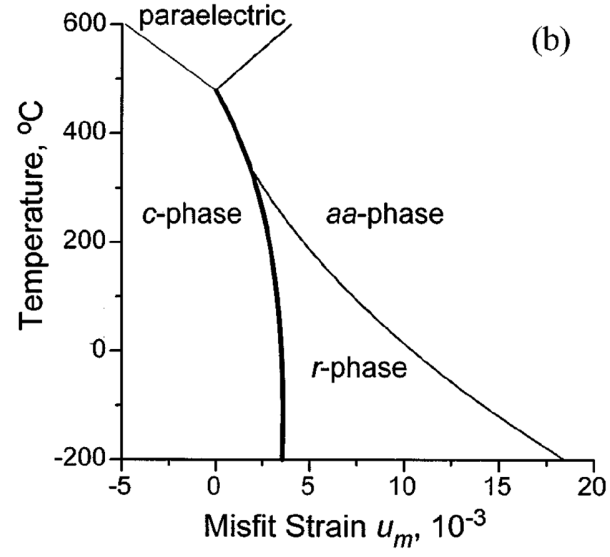

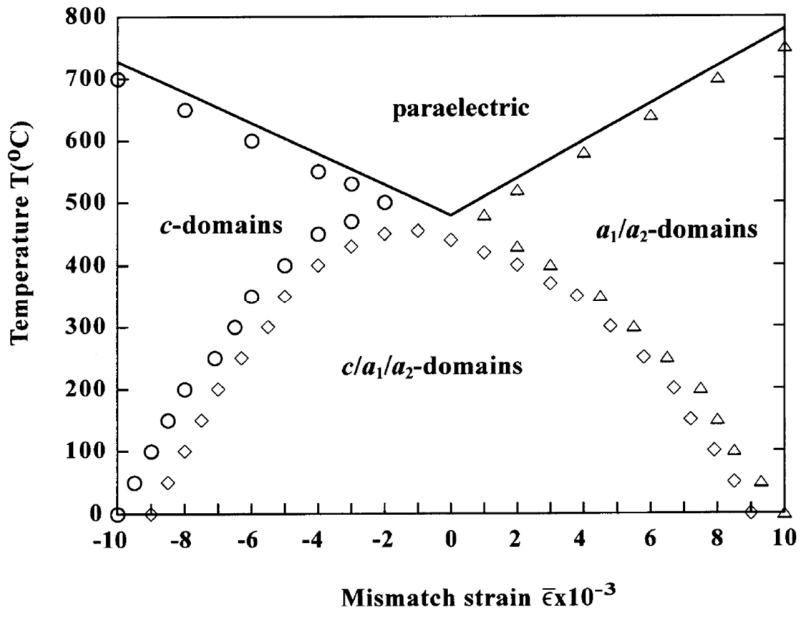

Figure 5. Temperature-strain phase diagrams of $(001)_p$-oriented $PbTiO_3$: (a) with each polarization configuration considered separately and the second- and first-order phase transitions shown by thin and thick lines, respectively.;[216] (b) with the strain interactions and interface energy between configurations (domain wall) considered.[217]

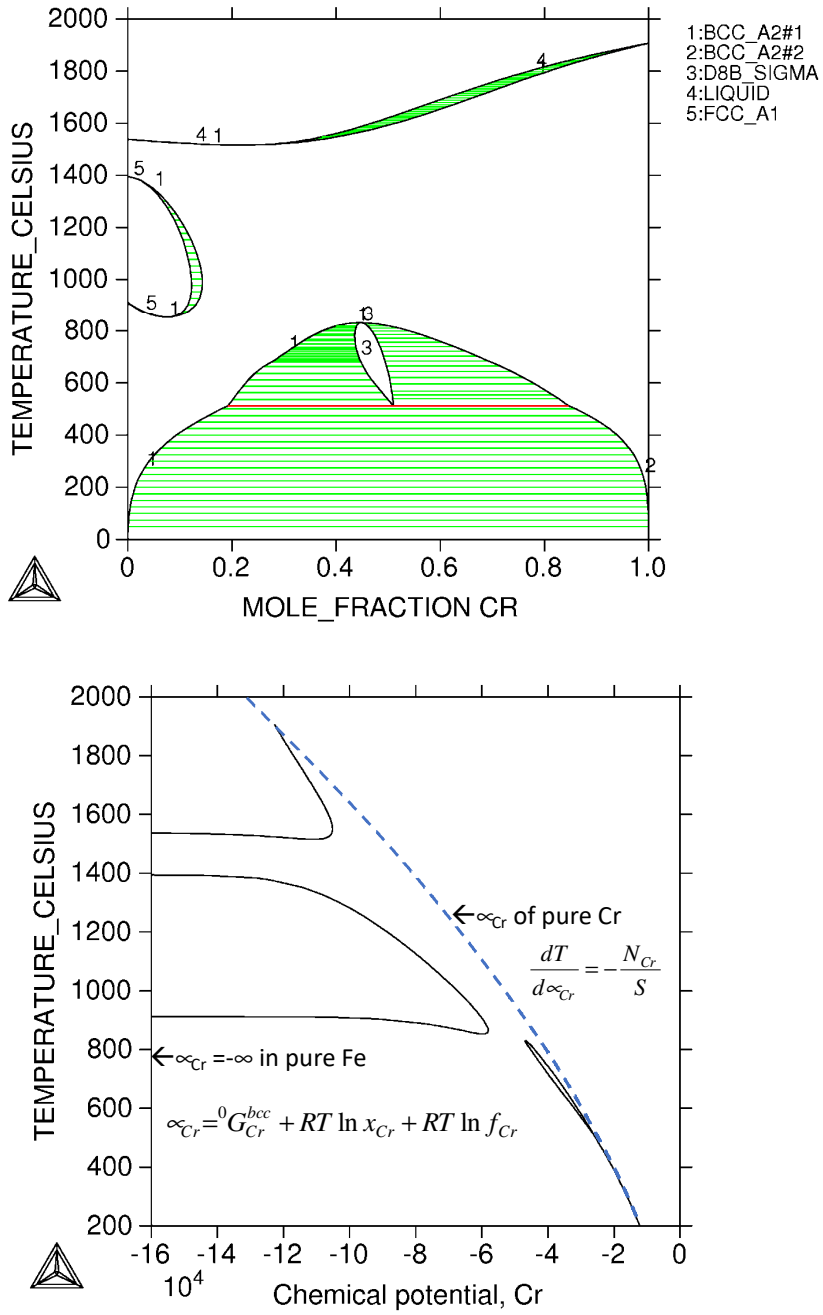

Figure 6. (a) $T - \mu_{Cr}$ and (b) $T - x_{Cr}$ phase diagrams of the Fe-Cr binary system under ambient pressure.

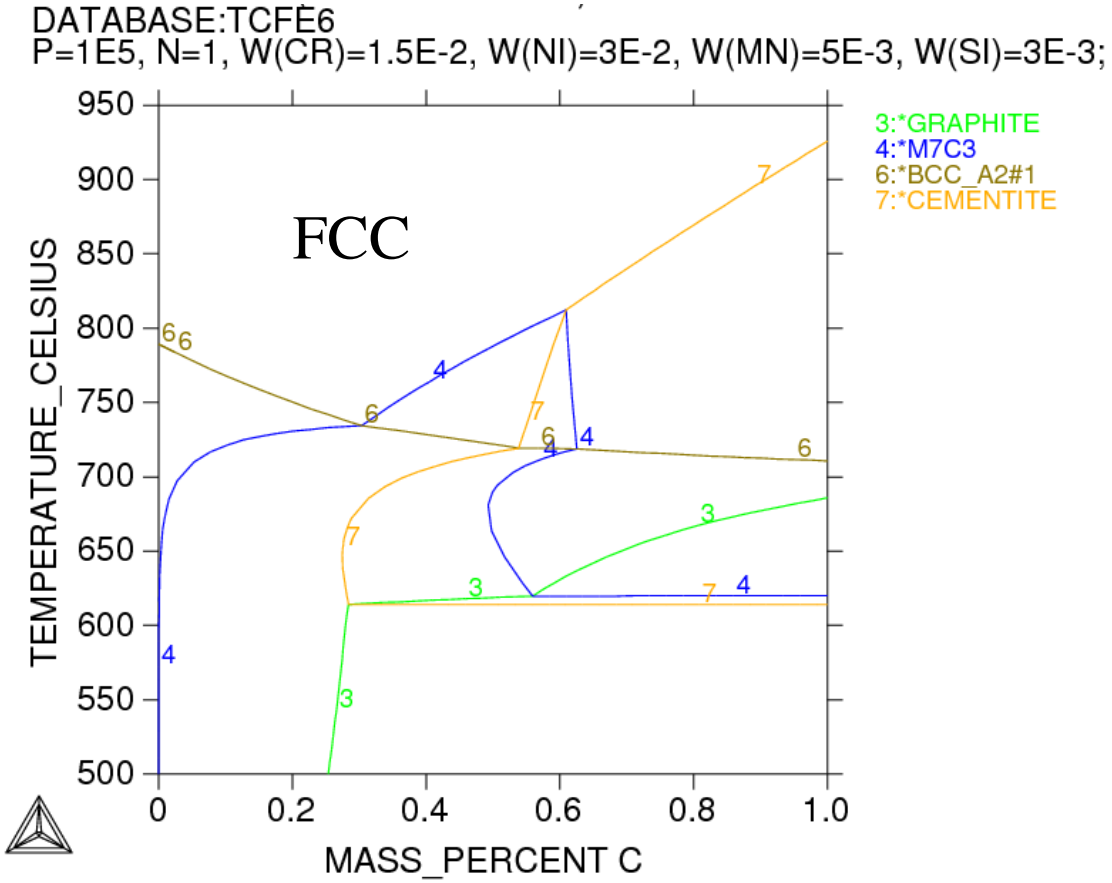

Figure 7. Isopleth of the Fe-1.5Cr-0.4Mn-3.5Ni-0.3Si-C (in weight percent) system

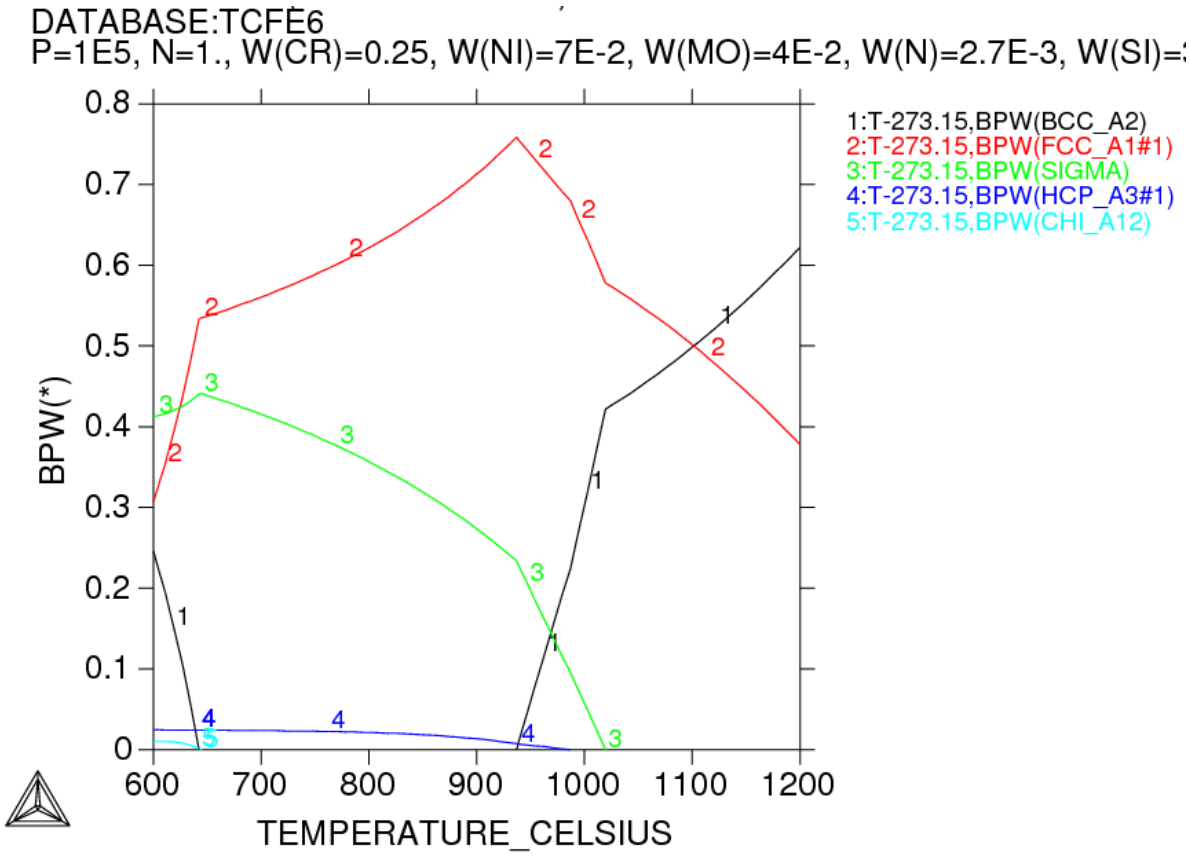

Figure 8. Phase fractions of the Fe-25Cr-7Ni-4Mo-0.27N-0.3Si-0.3Mn (in weight percent) duplex stainless steel as a function of temperature

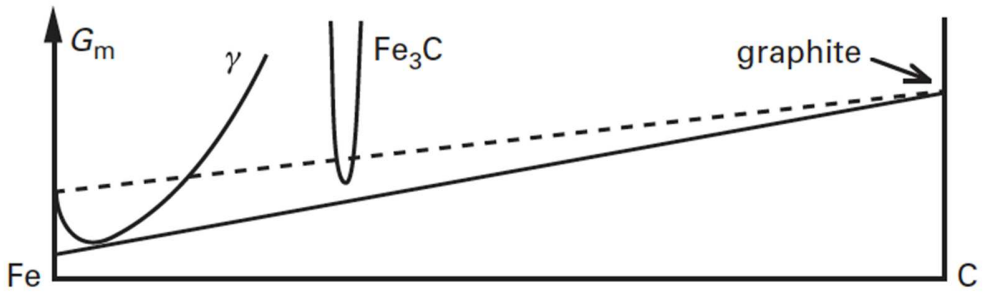

Figure 9. Gibbs energy diagram of Fe-C binary system at 1169K and 1atm.[3]

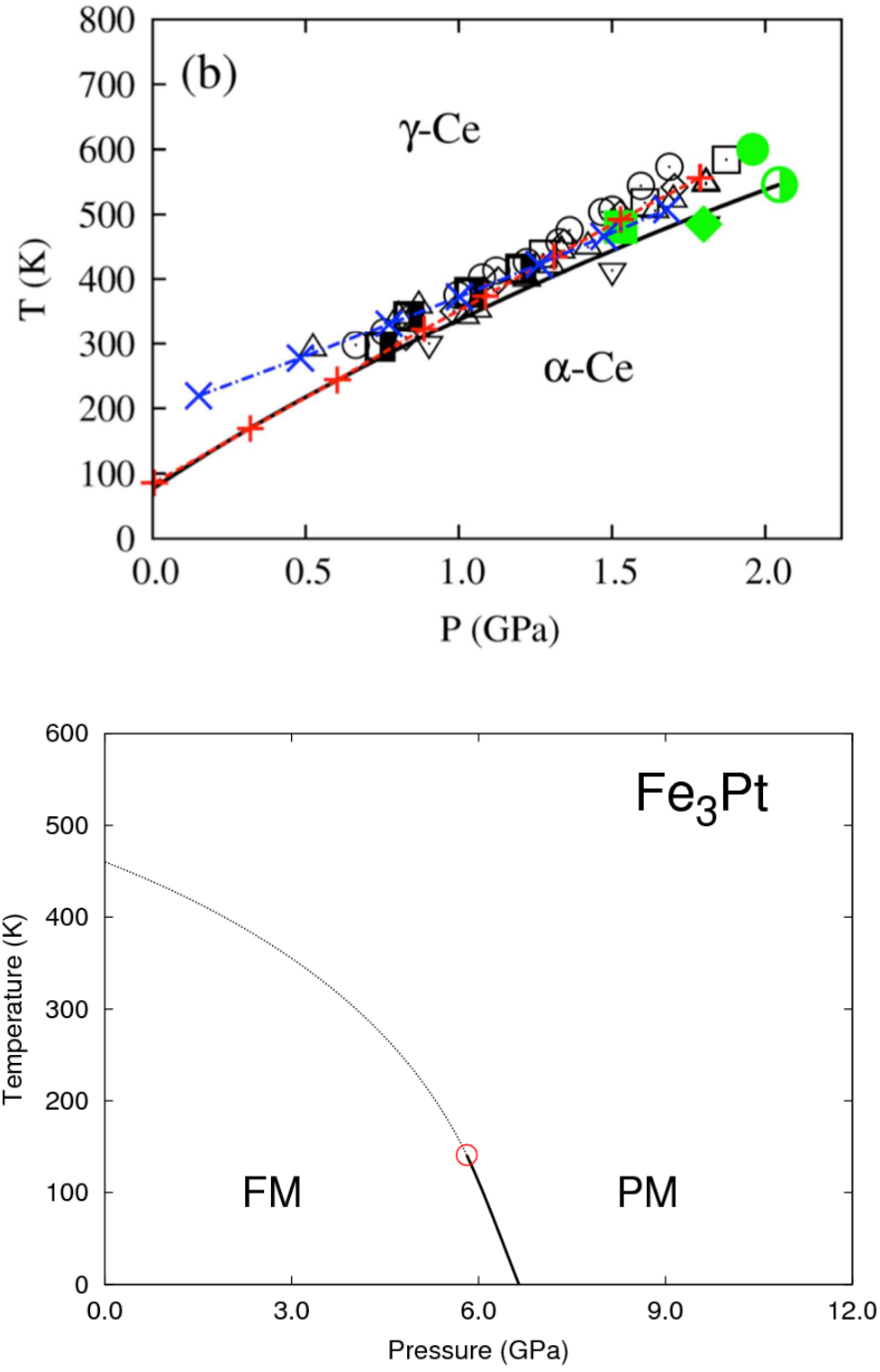

Figure 10. T – P potential phase diagrams for (a) Ce,[25] and (b) Fe_3Pt [224]

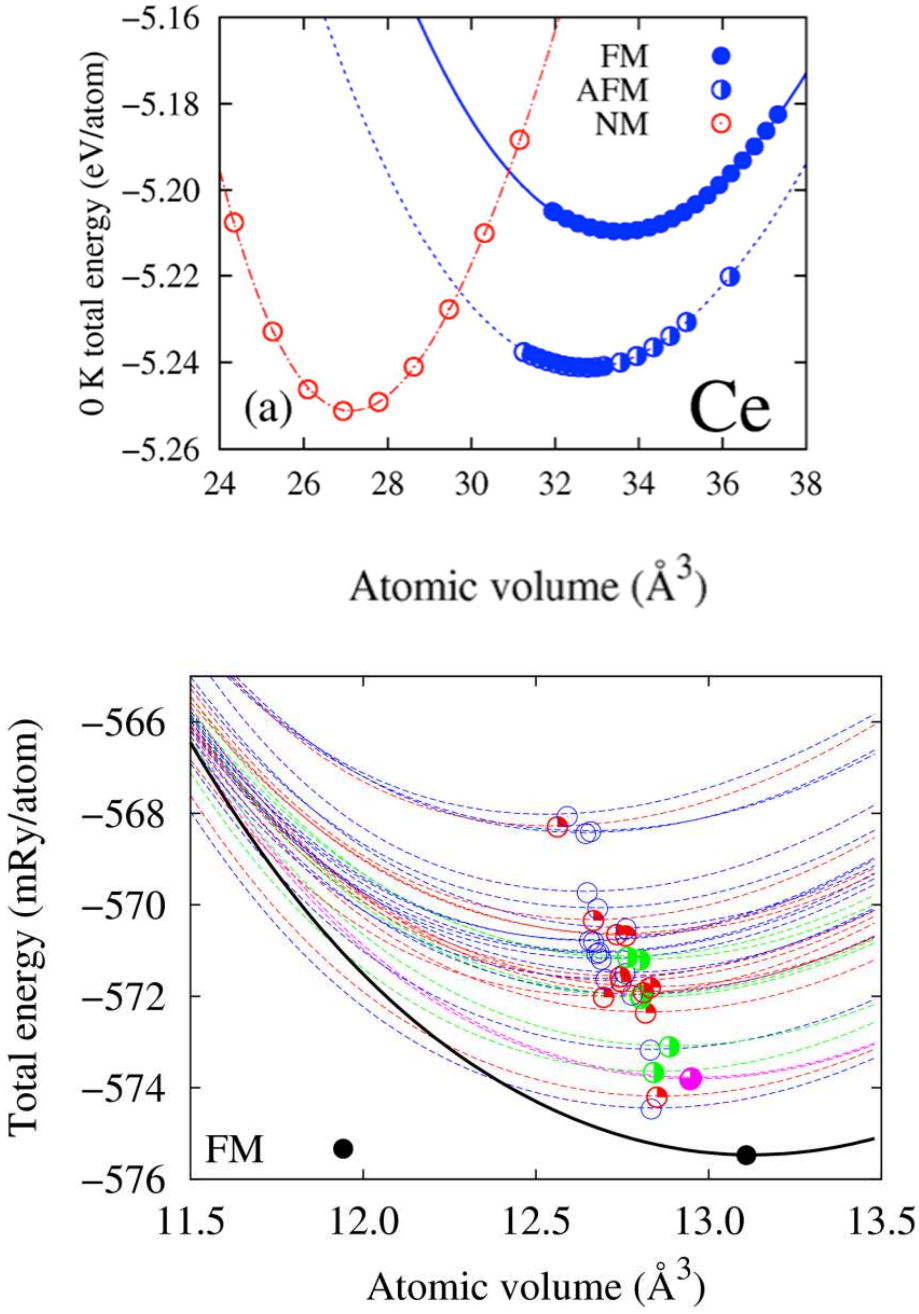

Figure 11. $E_c(V)$ in Eq. 77 for (a) Ce [25] and (b) Fe_3Pt [26]

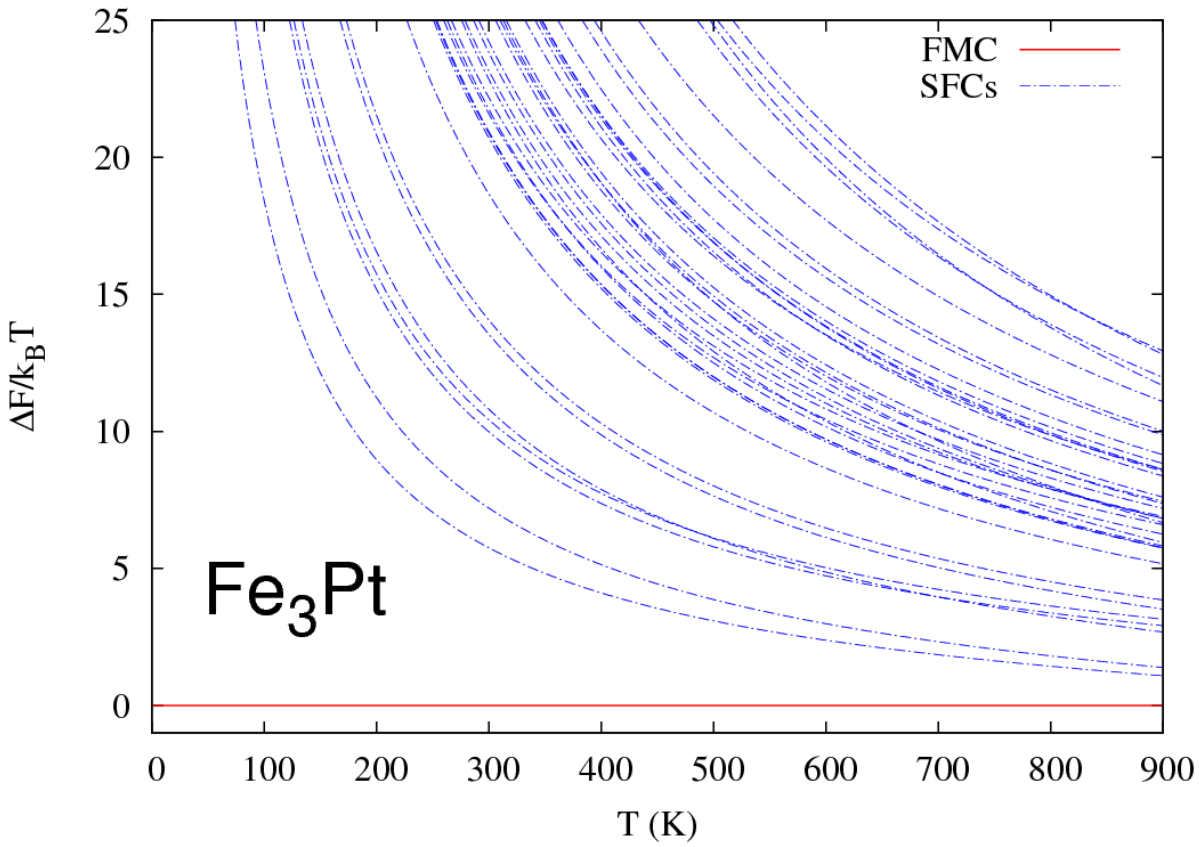

Figure 12. $(F^k - F)/k_B T$ as a function of temperature plotted for 37 SFCs of Fe_3Pt.[224]

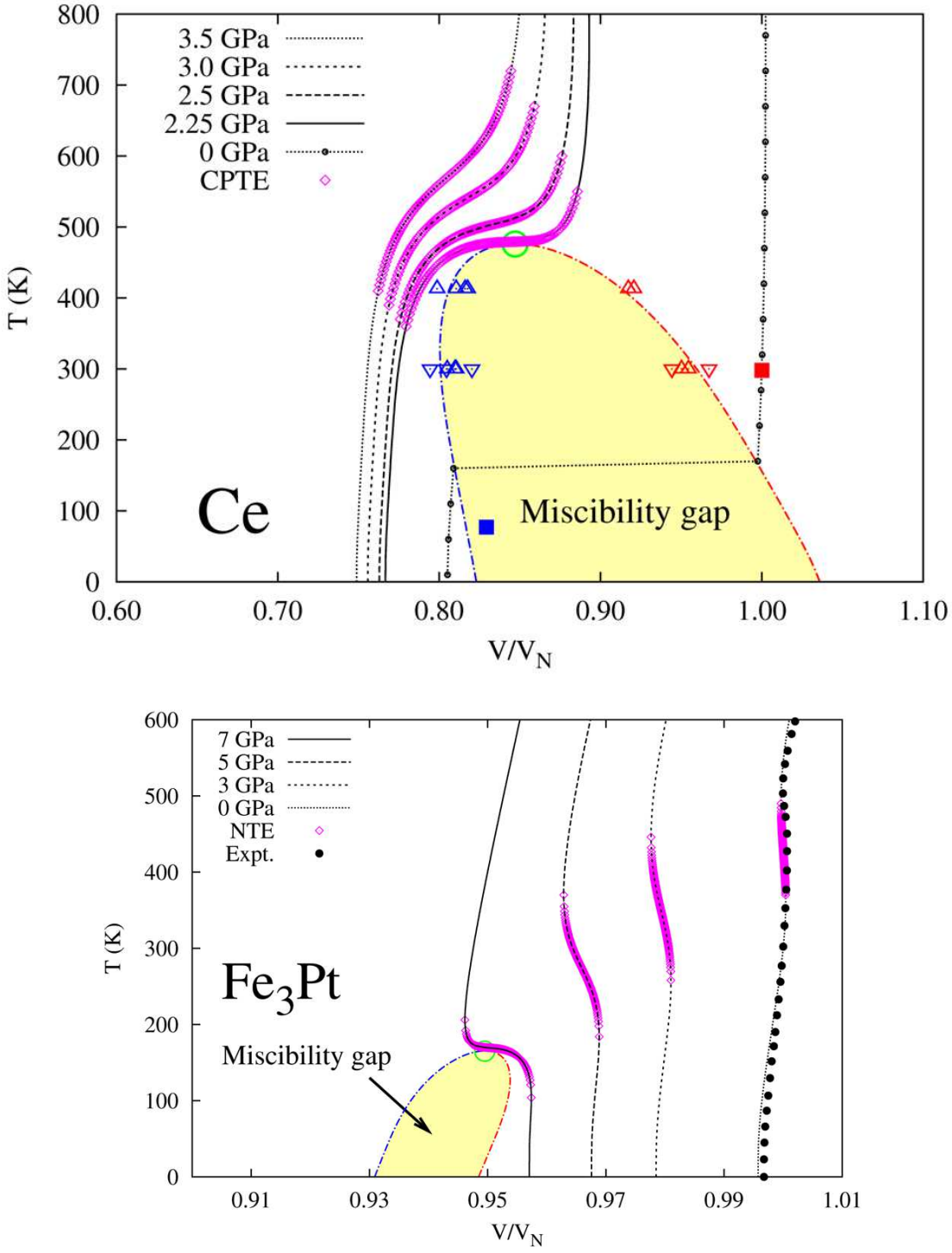

Figure 13. $T-(V/V_N)$ phase diagrams for (a) Ce, and (b) Fe_3Pt, with V_N being the equilibrium volume at atmospheric pressure and room temperature. [27]

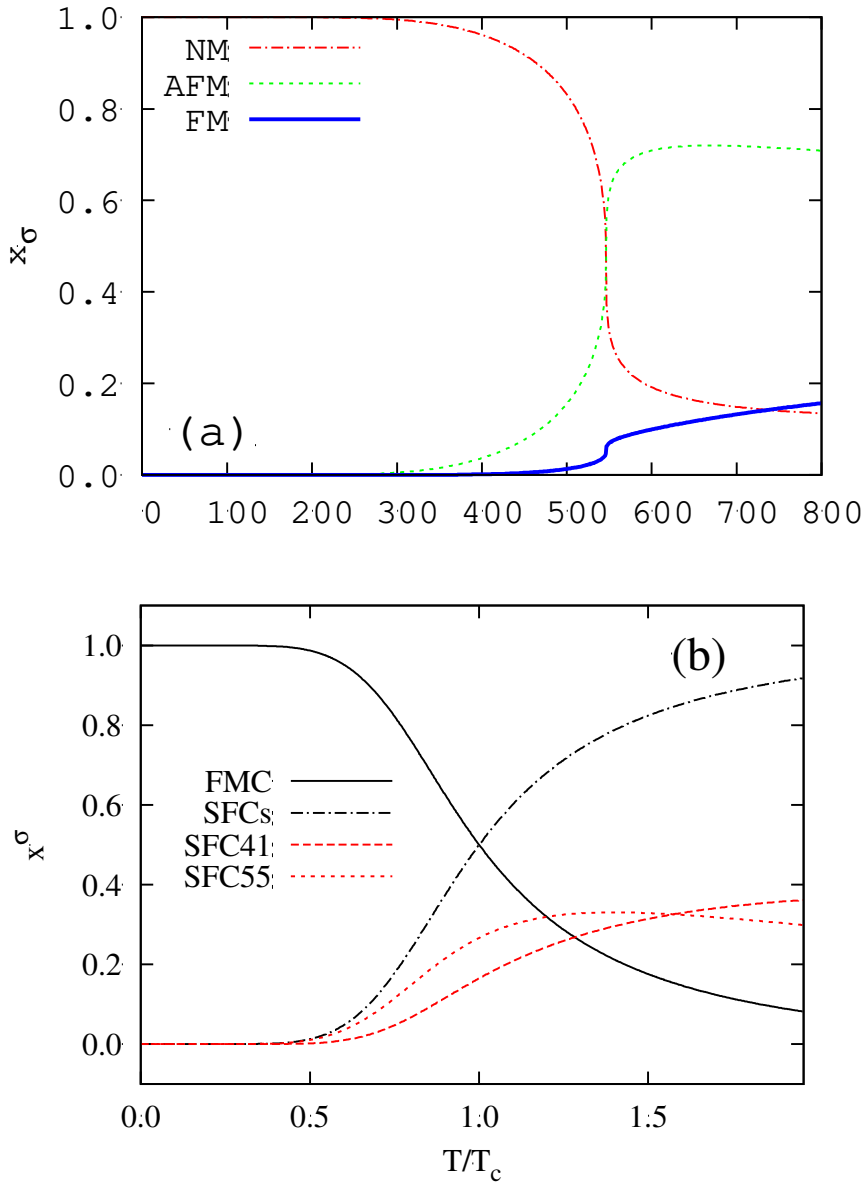

Figure 14. (a) Thermal populations of the nonmagnetic (red dot–dashed), antiferromagnetic (green dashed), and ferromagnetic (blue solid) as a function of temperature in Ce at the critical pressure of 2.05 GPa;[25] (b) Thermal populations of the FMC (black solid line) and that of the sum over all SFCs (black dot-dashed line) with the two major contributions to the PM phase from SFC55 and SFC41, plotted using red dashed and long dashed lines, respectively, for Fe_3Pt at 1atm, respectively.[26]

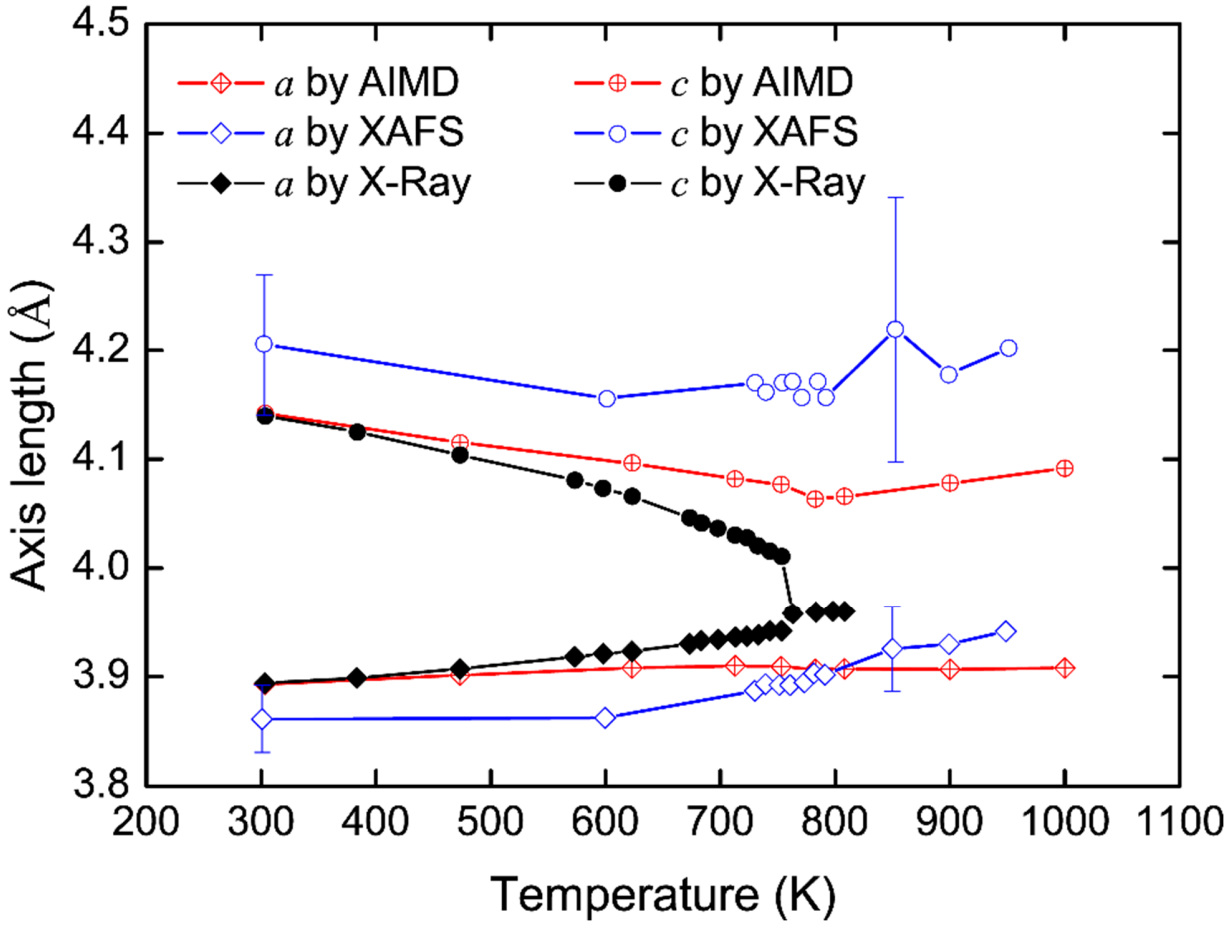

Figure 15. Temperature dependence of the lattice parameters a, c of $PbTiO_3$ unit cell with data in the open symbols from the XAFS measurements, [228–230] the closed symbols from the x-ray diffraction,[234] and the crossed symbols from AIMD simulations[74]

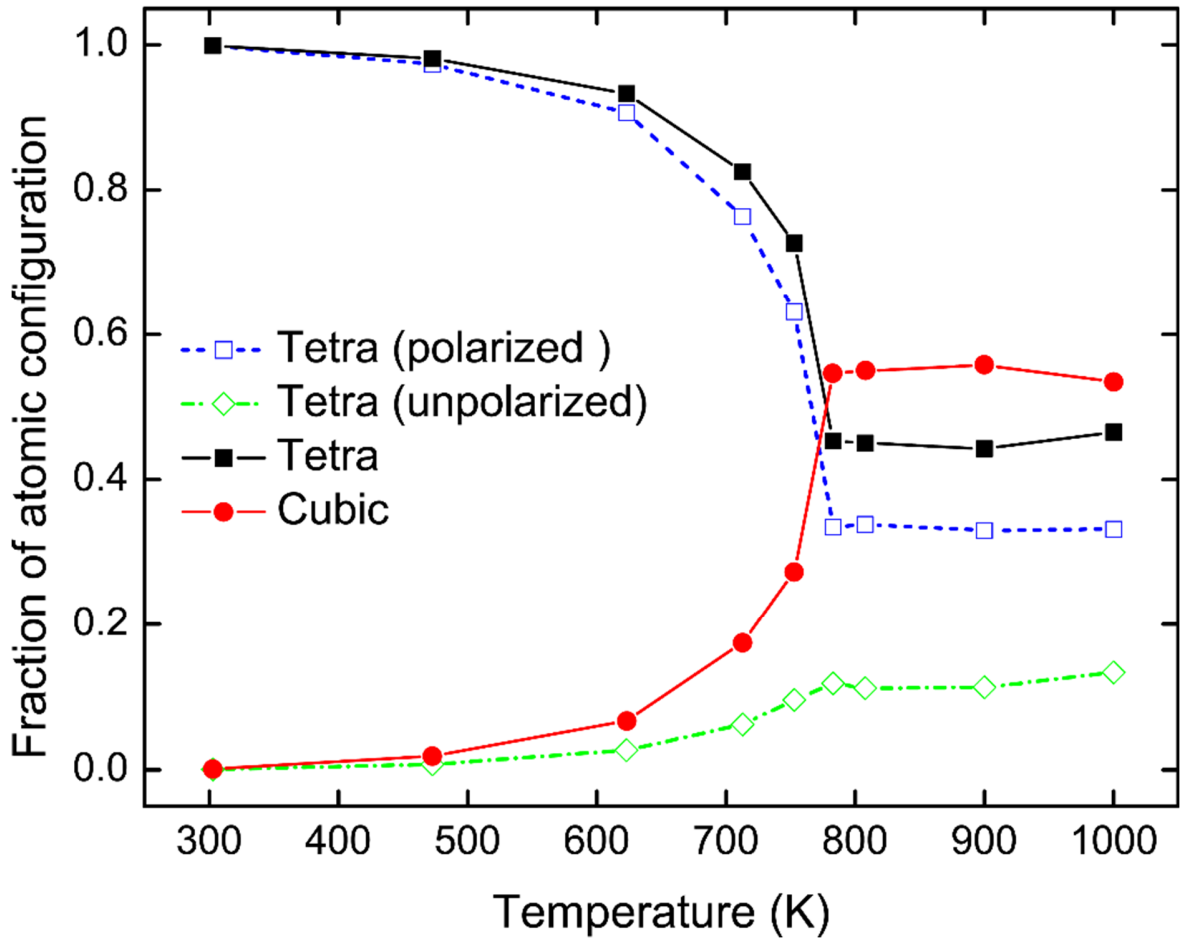

Figure 16. Fractions of the cubic (closed circles) and tetragonal (closed squares) configurations as a function of temperature, obtained from the AIMD simulations.[74] Among the tetragonal configurations, the fractions of the polarized and unpolarized ones in the <001> direction are shown in the open squares and open diamonds, respectively

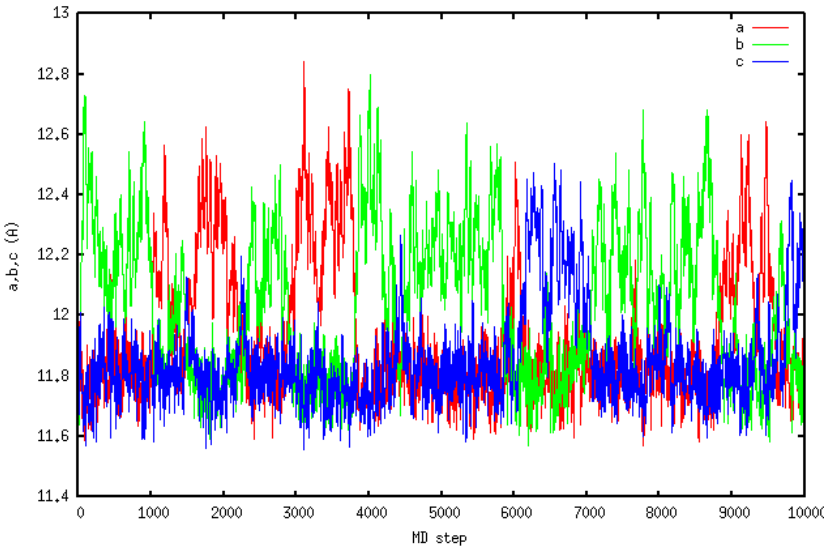

(a)

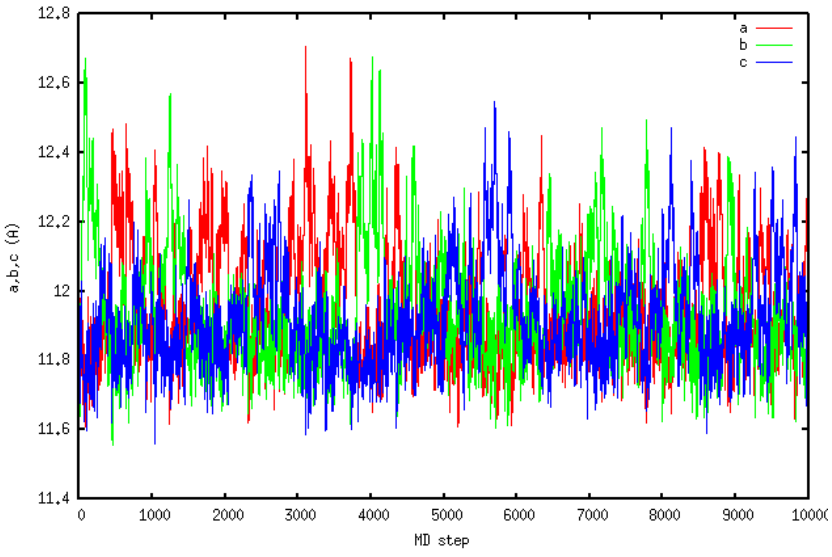

(b)

Figure 17: Instantaneous lattice parameters of $PbTiO_3$ measured in all three directions as a function of AIMD simulation steps, (a) 623K, and (b) 753K. [17]

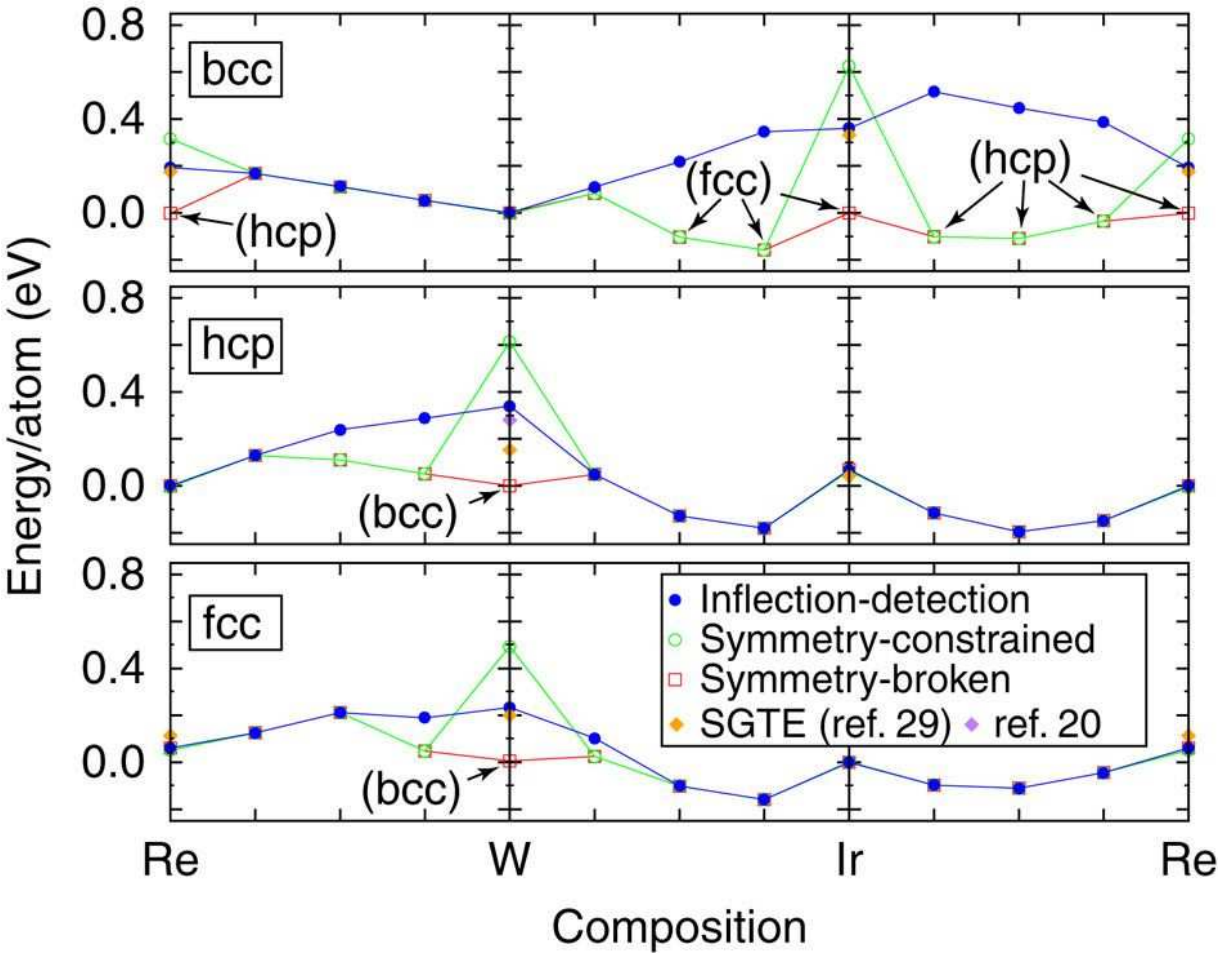

Figure 18. Formation energies of ideal solid solutions in all binary subsystems of the Ir–Re–W alloy system, obtained via various methods. [47]

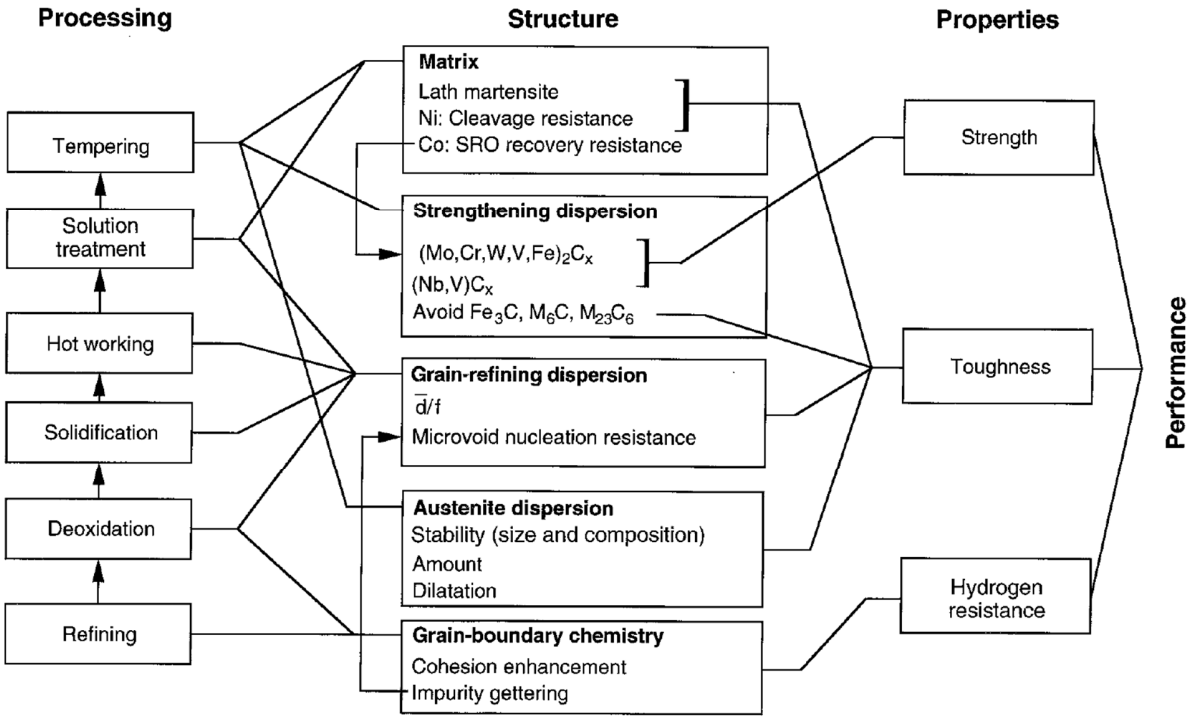

Figure 19. Materials system chart for high-performance alloy steel.[214]

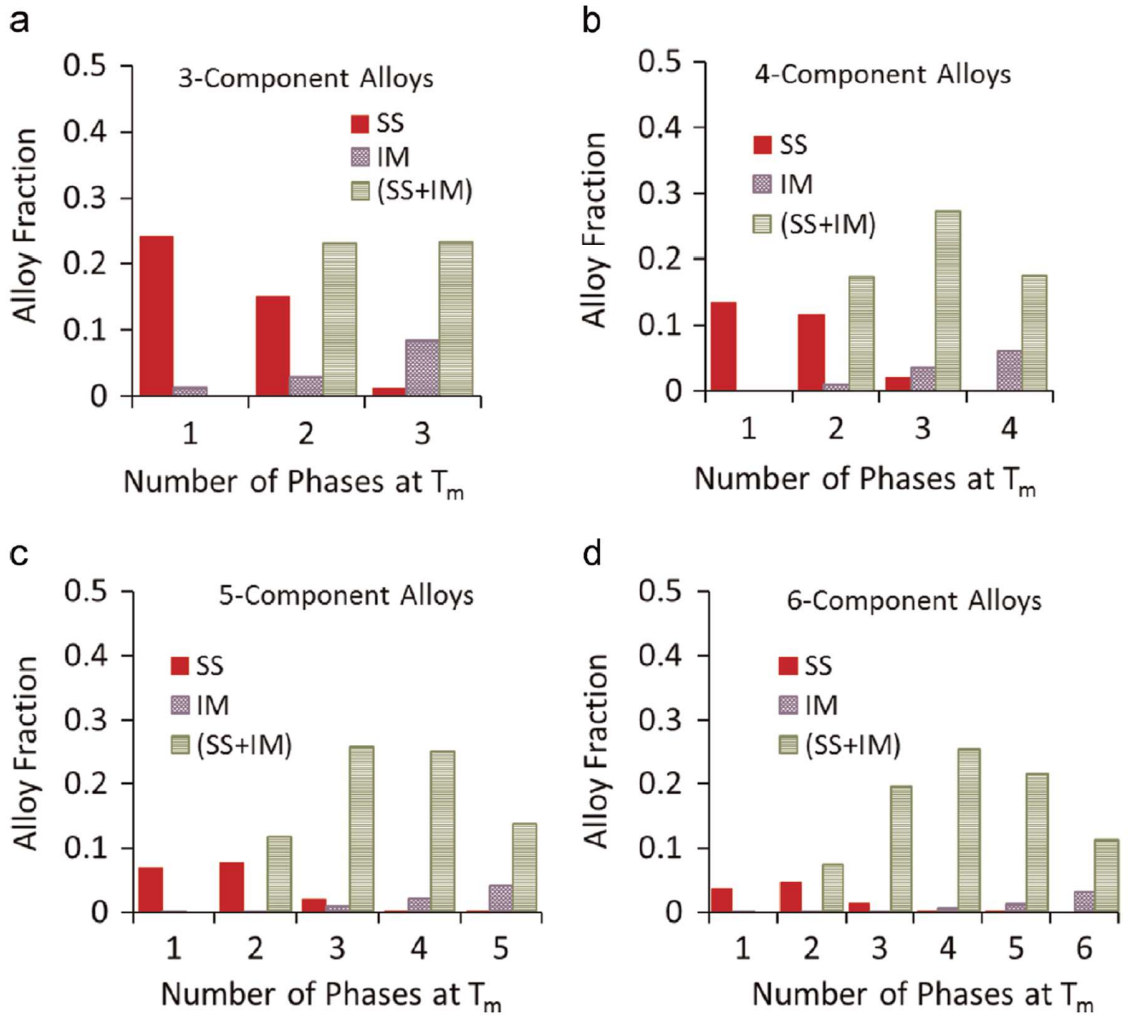

Figure 20. Distributions of the N-component equiatomic alloys by the number of phases at the melting temperature with SS for solid solution and IM for intermetallic compounds.

259,260

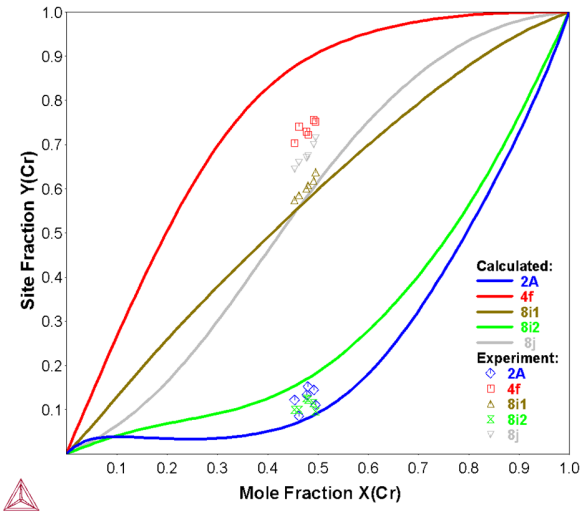

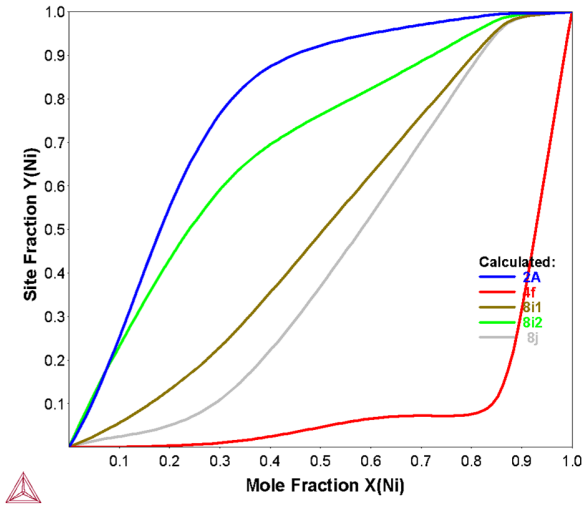

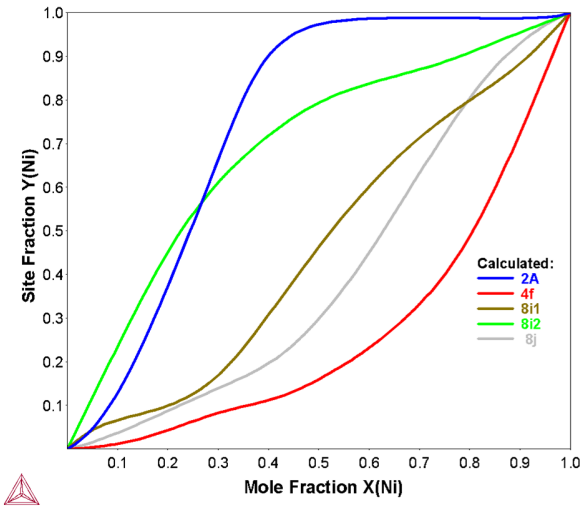

Figure 21. Predicted equilibrium site occupancies at 925K for the Cr-Fe, Cr-Ni and Fe-Ni [262,263] in comparison with experimental data.[266,267]

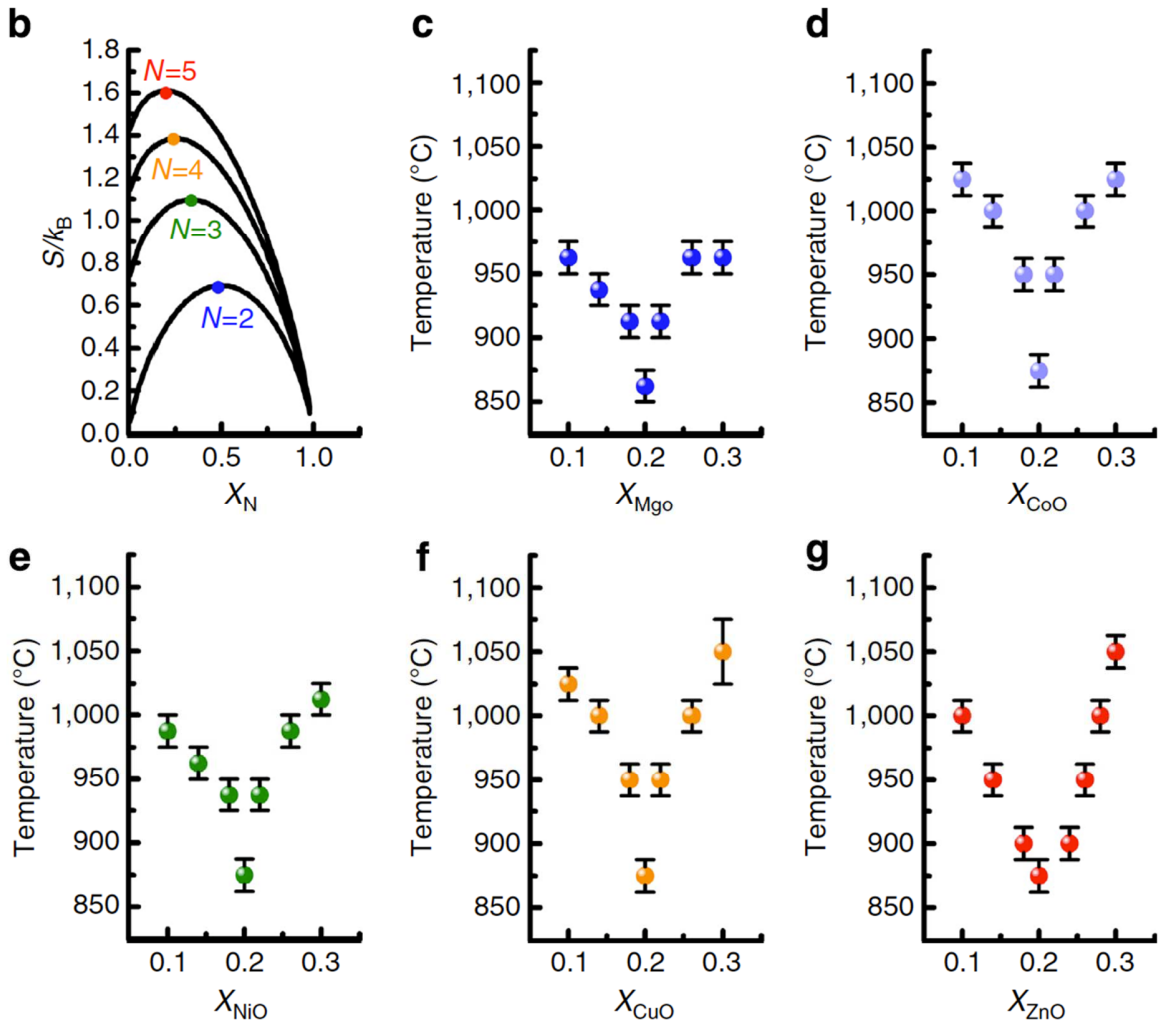

Figure 22. Partial phase diagrams showing the transition temperature to single phase as a function of composition (solvus) in the vicinity of the equimolar composition where maximum configurational entropy is expected. Error bars account for uncertainty between

temperature intervals. Each phase diagram varies systematically the concentration of one element. [255]

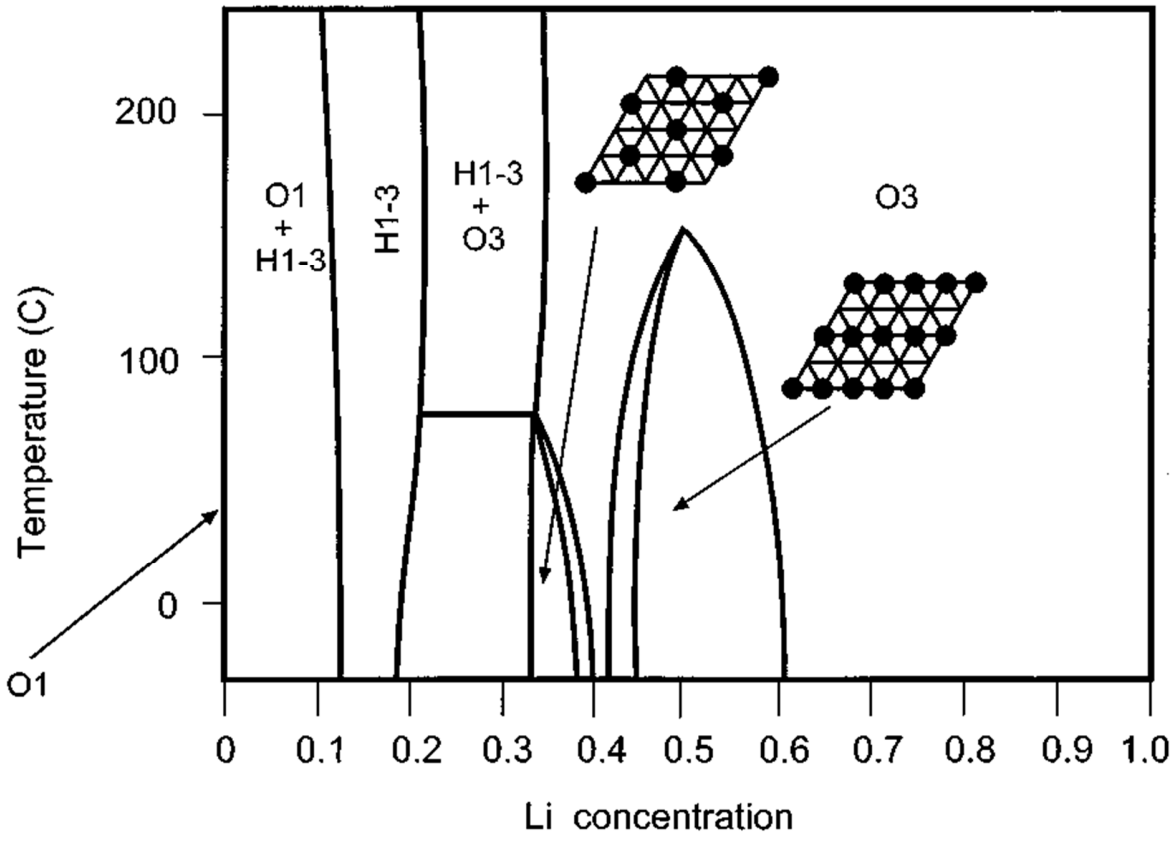

Figure 23. Calculated Li_xCoO_2 phase diagram with x plotted on the x-axis and the insets showing the in-plane Li ordering predicted to be stable at $x = 1/2$ and 1/3, respectively.[268]

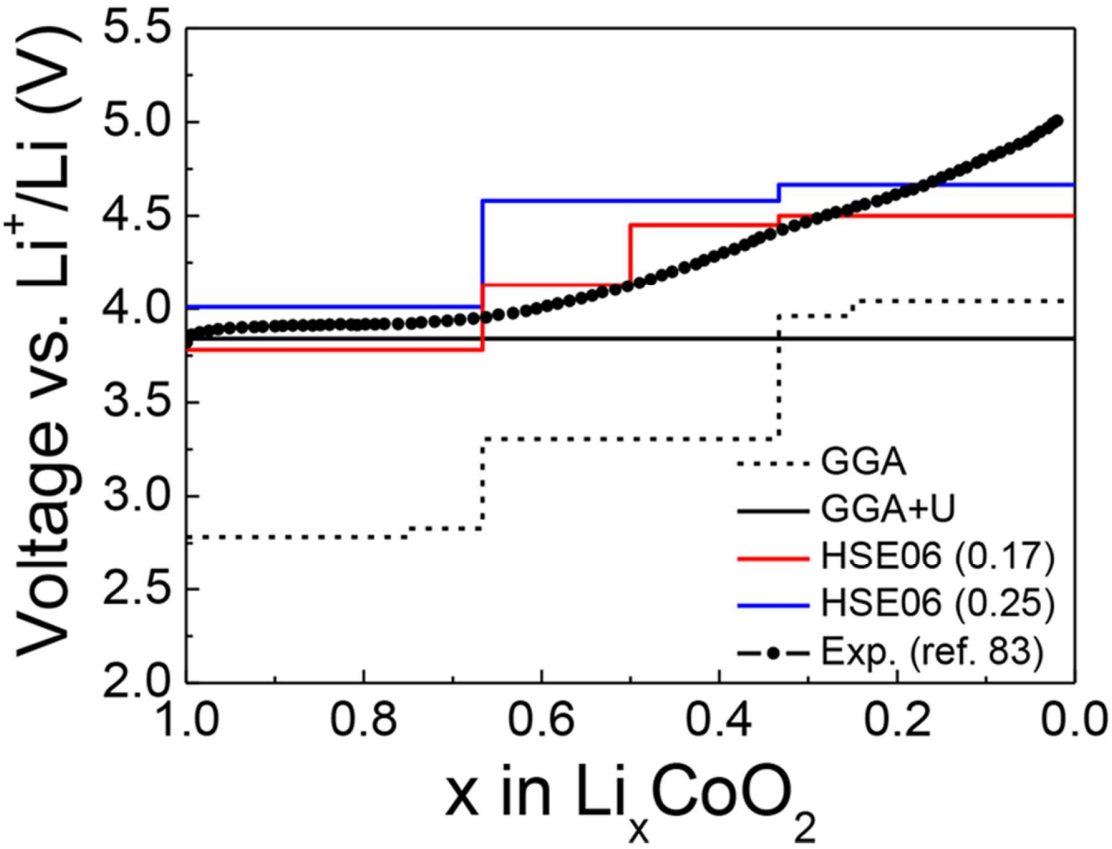

Figure 24. Computed voltage profiles of Li_xCoO_2 with various functionals with the experimental data superimposed.[269]

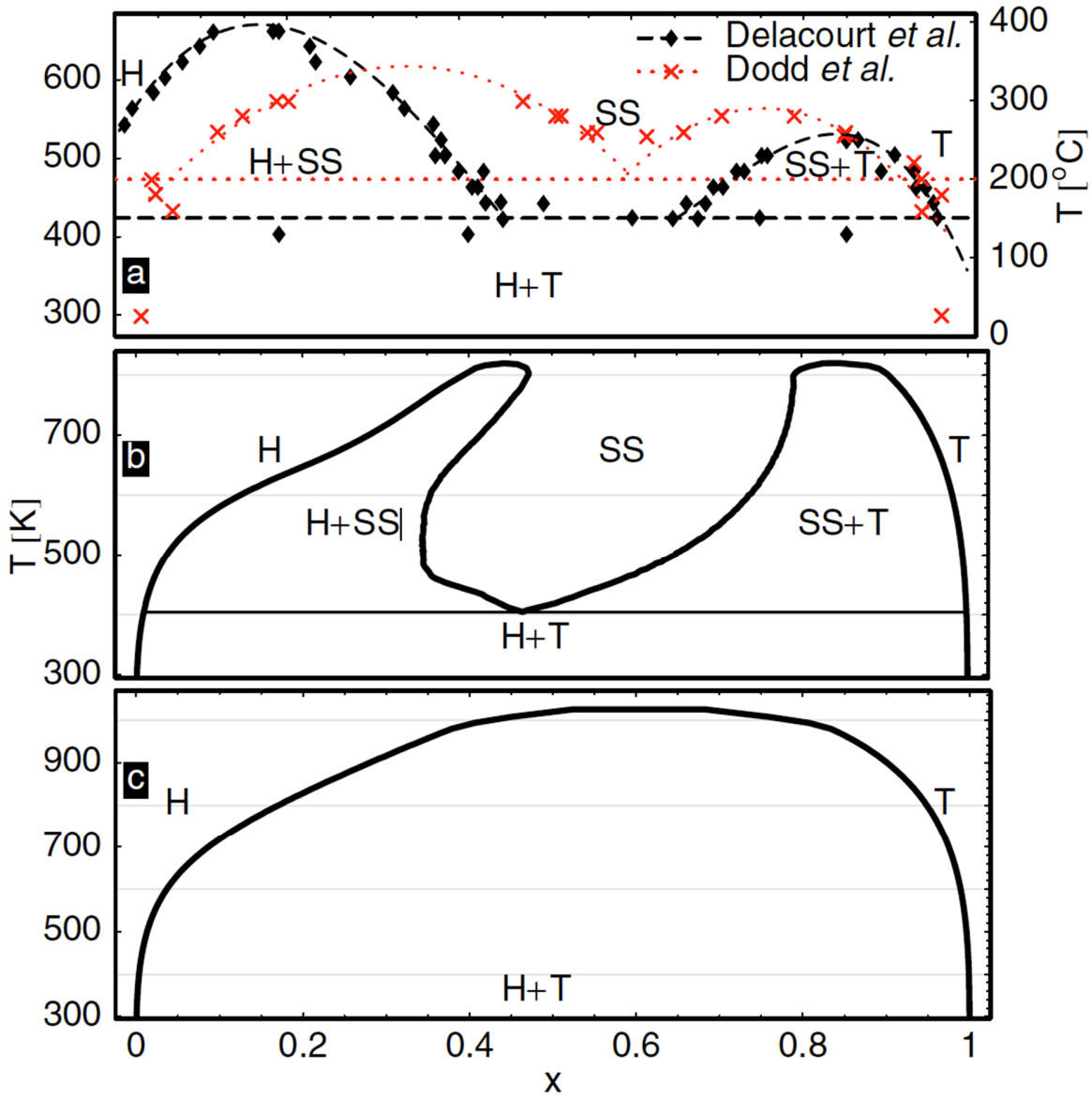

Figure 25. Li_xFePO_4 phase diagram. (a) Experimental phase boundary data;[272,273] (b) calculated with both Li and electron degrees of freedom, and (c) with explicit Li only. [271]

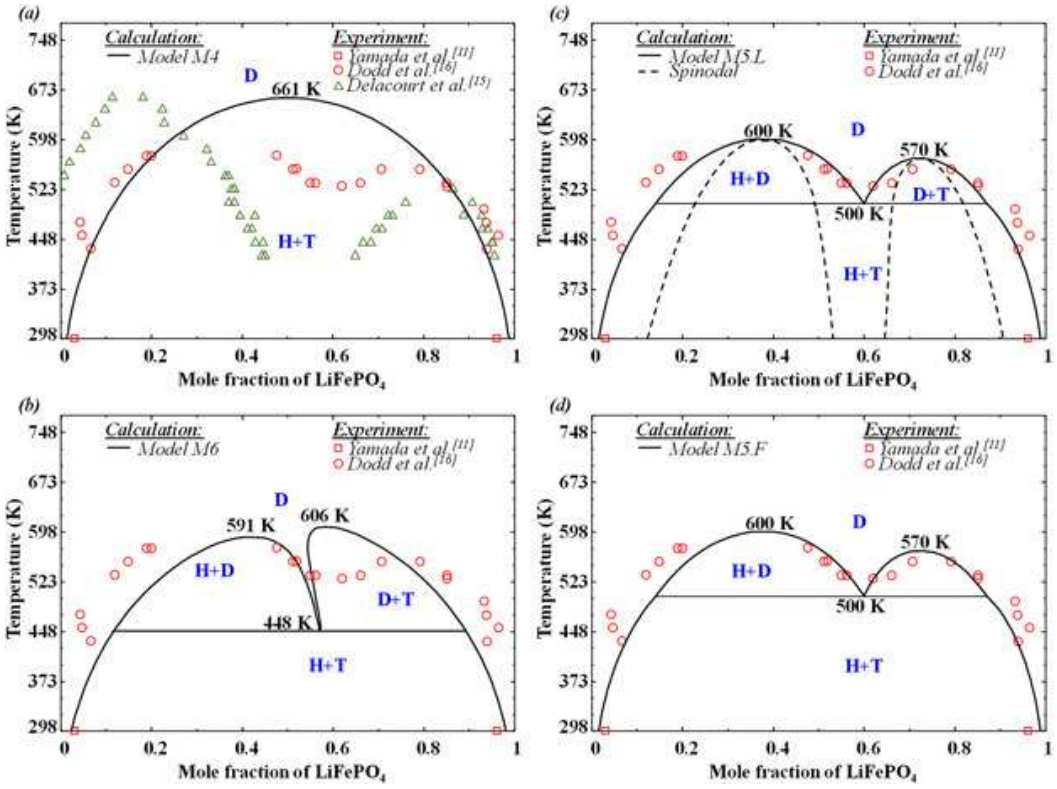

Figure 26. Phase diagrams of $FePO_4$and $LiFePO_4$ with various CALPHAD models.[274]

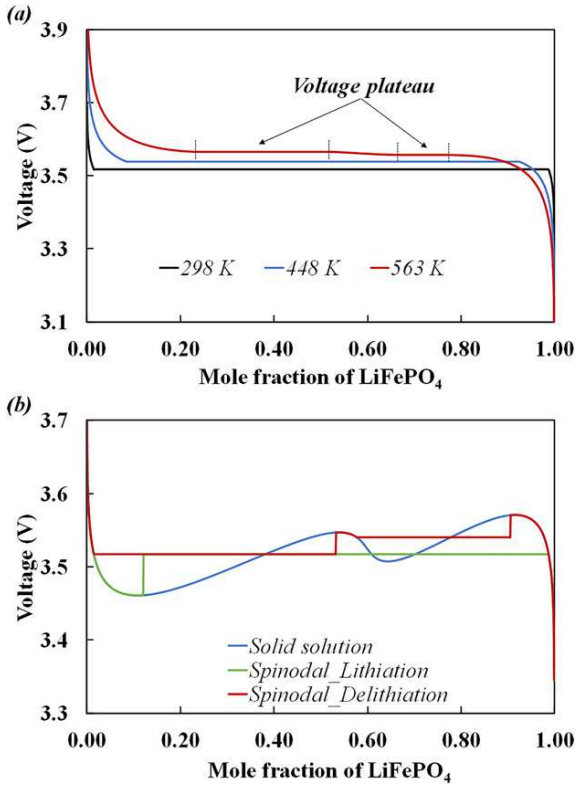

Figure 27. Calculated open-circuit voltage (OCV) curves obtained by: (a) delithiating $LiFePO_4$ via equilibrium phase transformation at various temperatures (298, 448, and 563 K) where the two voltage plateaus at 563 K are marked; and (b) delithiating $LiFePO_4$ and lithiating $FePO_4$ via spinodal decomposition and delithiating/lithiating via solid solution route at 298 K. [274]

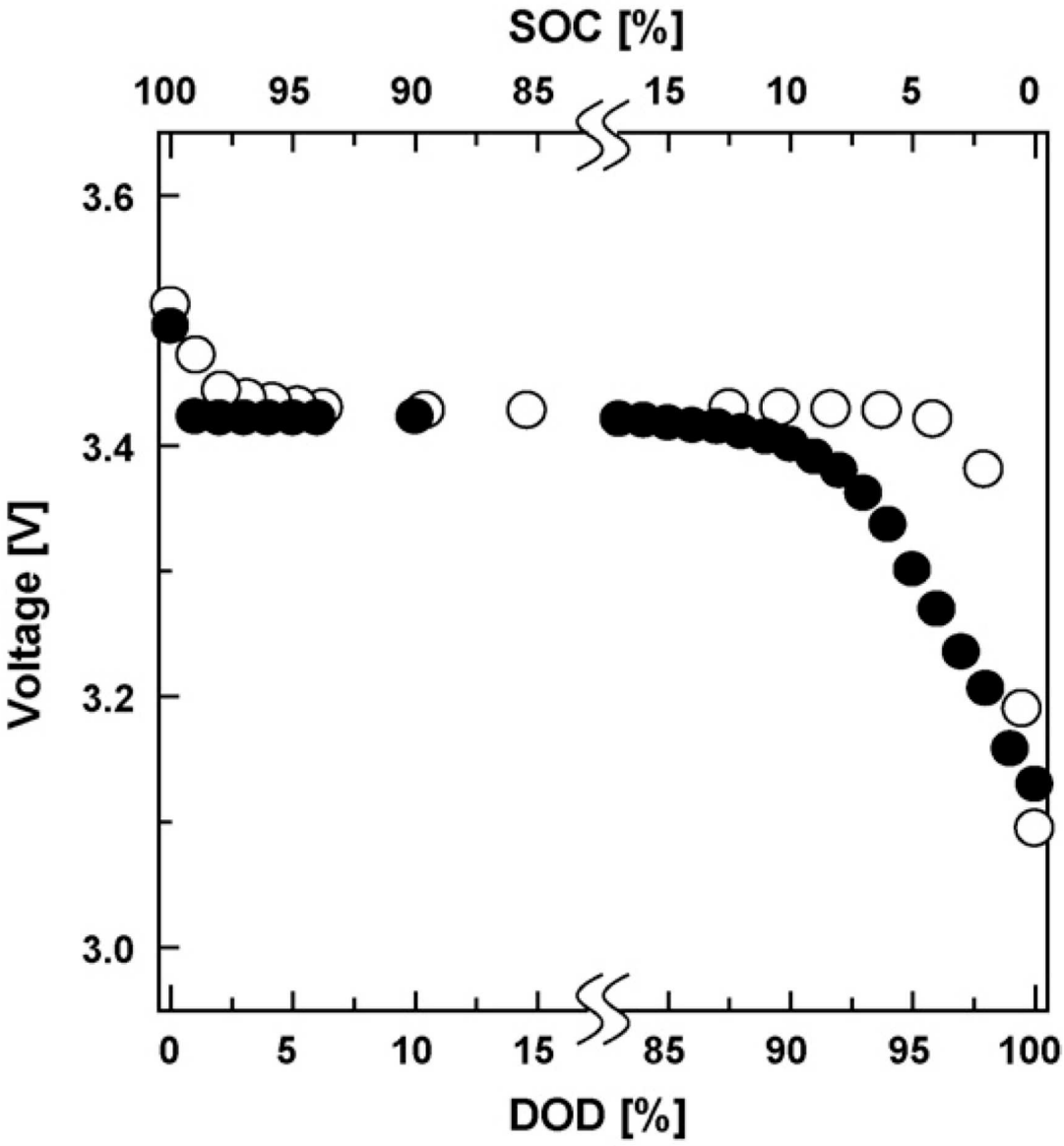

Figure 28. Open-circuit voltage curves of LiFePO4 particles: open and solid circles denote the measured values during the discharging and charging process, respectively.[275]

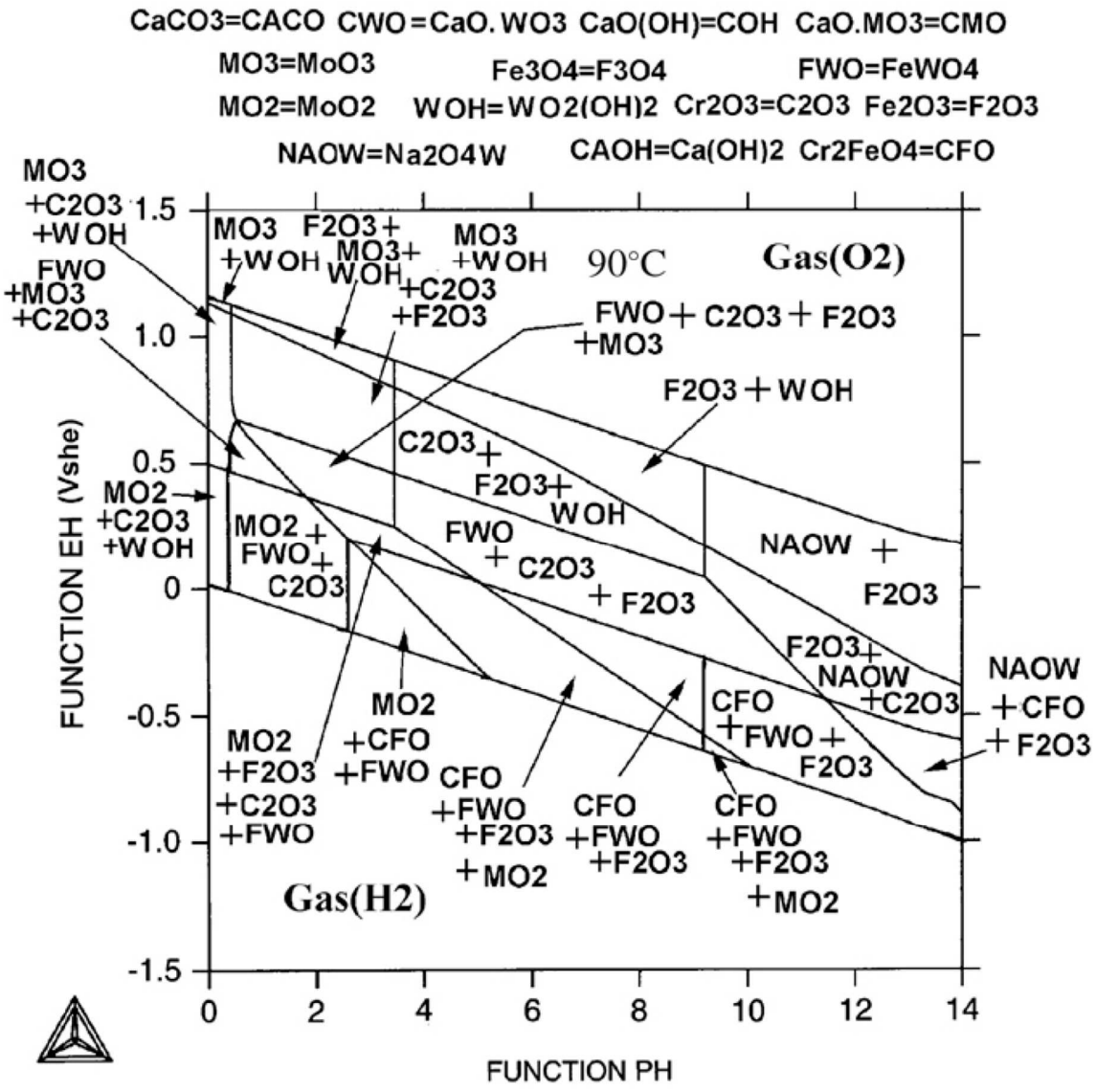

Figure 29. Calculated Pourbaix diagram at 90°C in a solution containing 1000 g of H2O, 0.68 mol of NaCl (4 wt%) and one gram of alloy (Fe-2.5 at.% Mo-19 at.% Cr-4 at.% C-16-at.% B and 1.7 at.% W)[276]

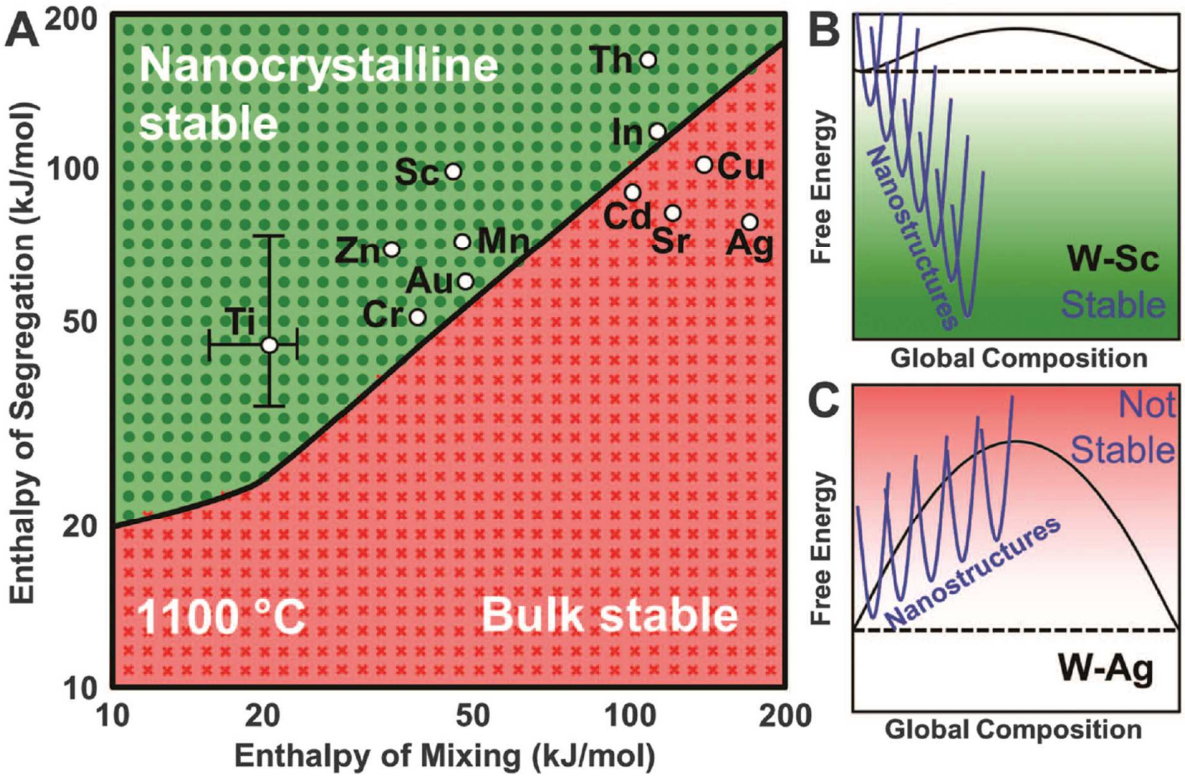

Figure 30. Nanostructure stability map for tungsten based binary alloys at 1100°C. [132]

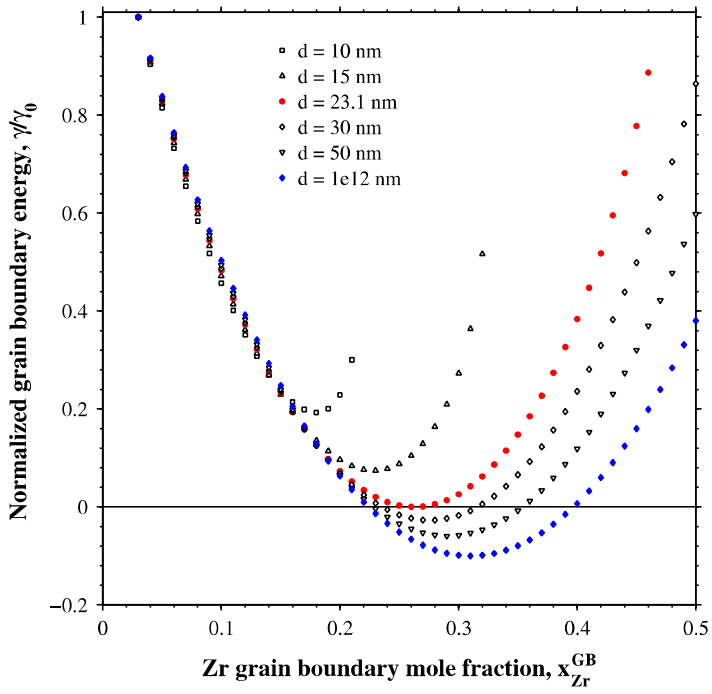

Figure 31. (a) Normalized grain boundary energy versus mole fraction of Zr in the grain boundary for an alloy with $x_{Zr} = 0.03$ at T = 550℃, showing the stabilized grain size of 23.1 nm; (b) Stabilized grain size as a function of temperature for different Zr molar fractions with the experimental XRD data for an $x_{Zr} = 0.04$ alloy superimposed, showing quantitative agreement between predictions and experiments. [97]

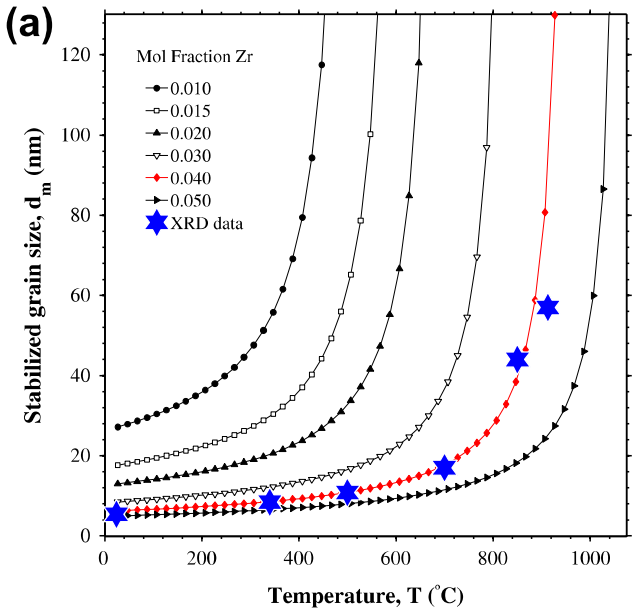

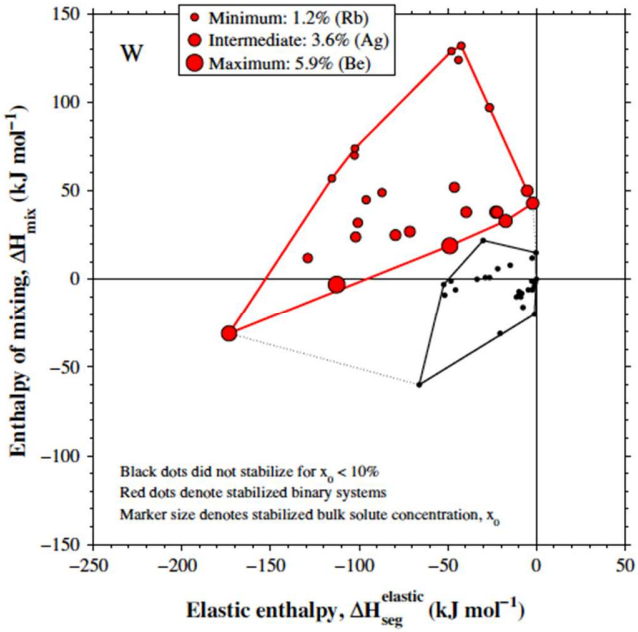

Figure 32. Nanocrystalline W stability map for both the stabilizing (red dots) and non-stabilizing (black dots) solutes [97]

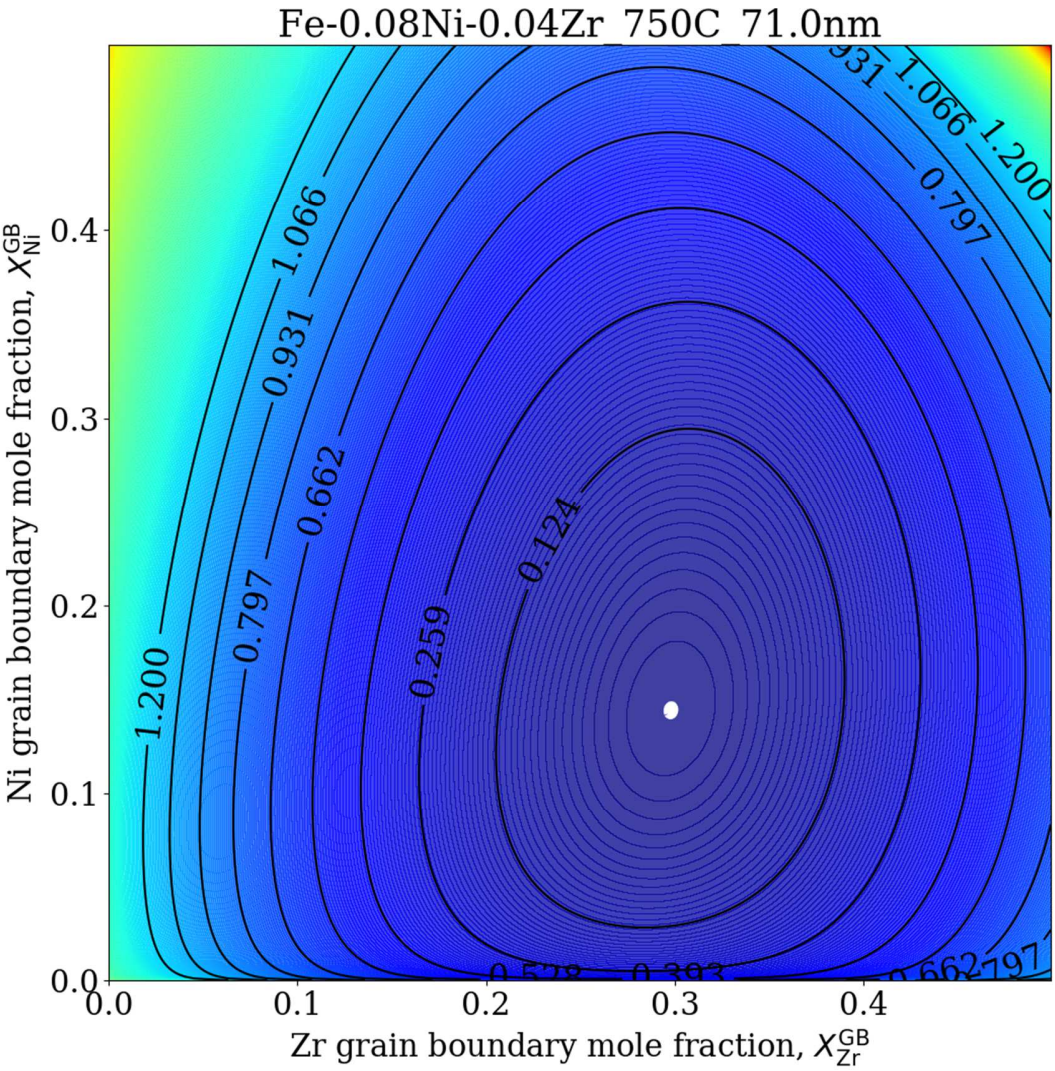

Figure 33. Contour plot of iso-grain boundary energy in the bcc Fe-Ni-Zr

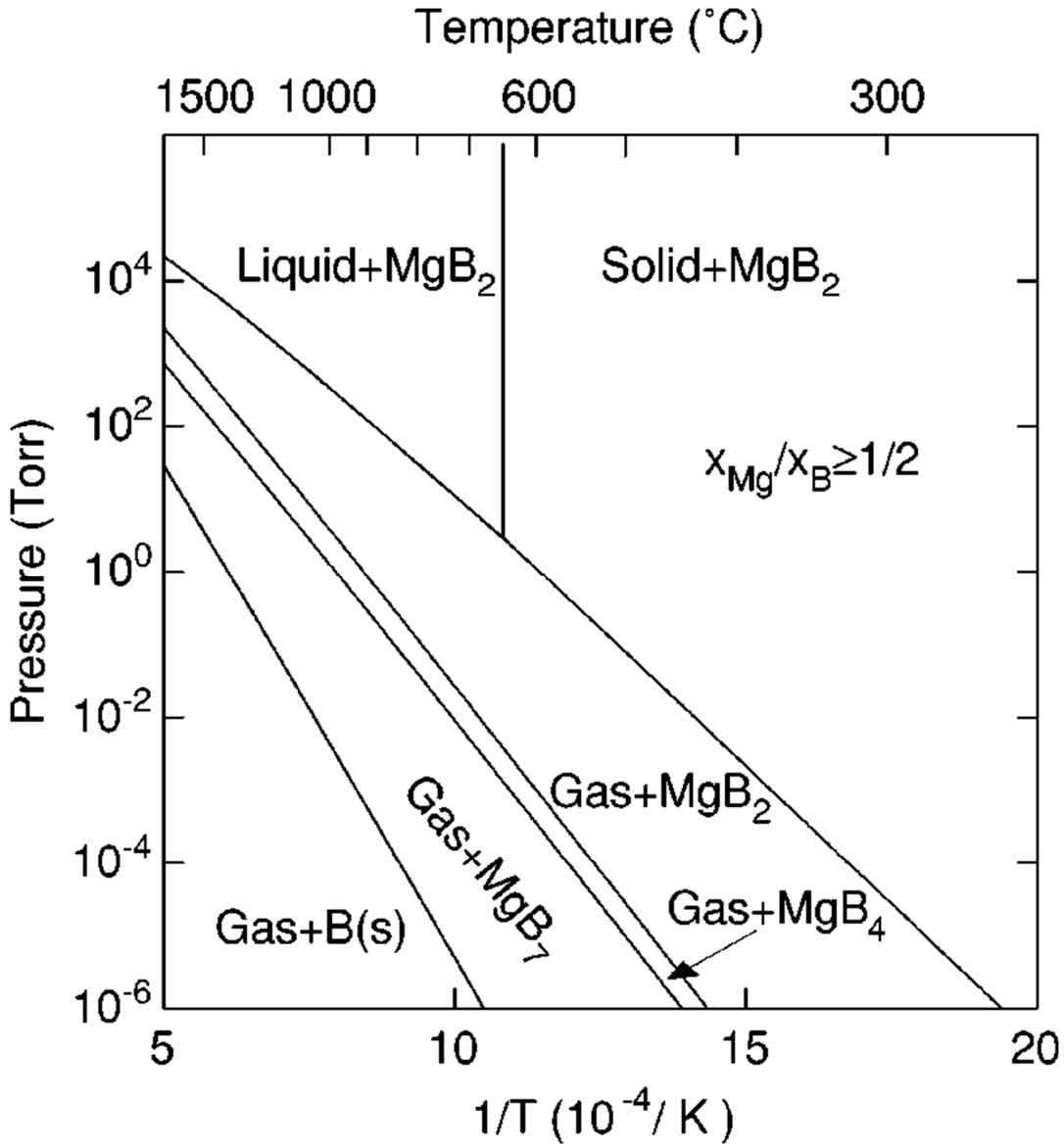

Figure 34. Mg-B pressure-temperature phase diagram with $x_{Mg}/x_B \geq 1/2$. [286]

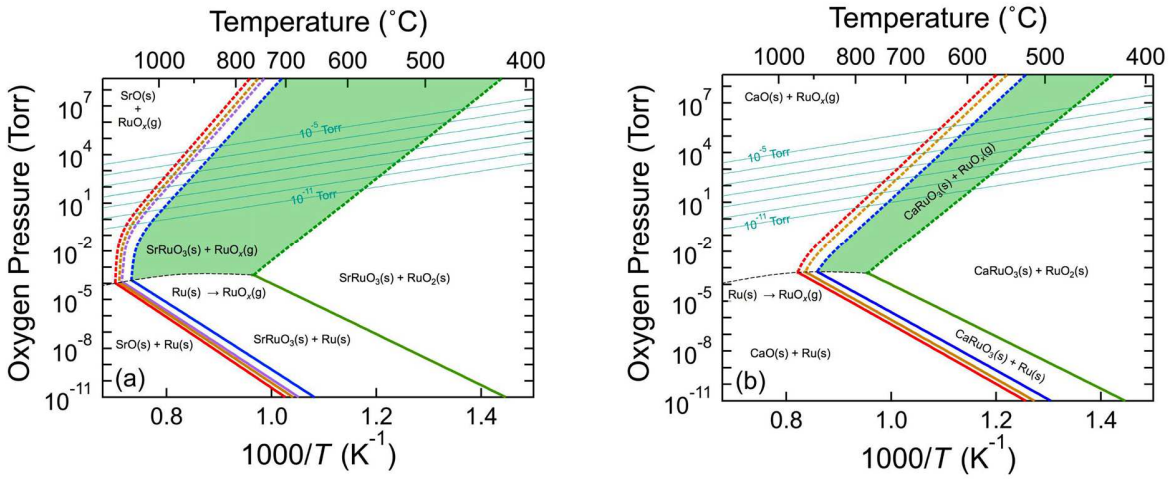

Figure 35. TOMBE diagrams illustrating the adsorption-controlled growth window for (a) $Sr_{n+1}Ru_nO_{3n+1}$ and (b) $Ca_{n+1}Ru_nO_{3n+1}$ phases.[294]

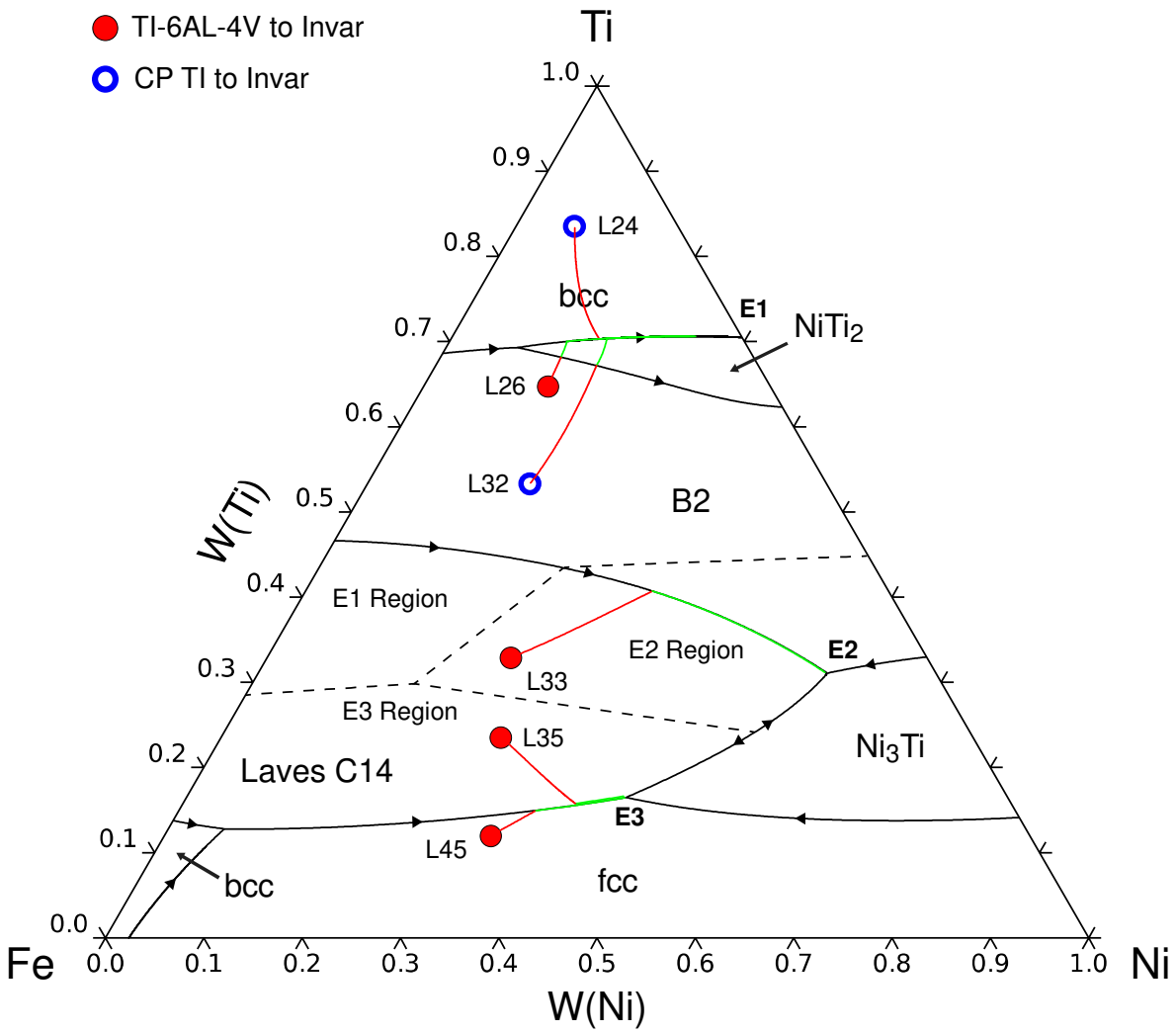

Figure 36. Liquidus projection of the Fe-Ni-Ti system based on the CALPHAD modeling [325] with other information in the text. [318]

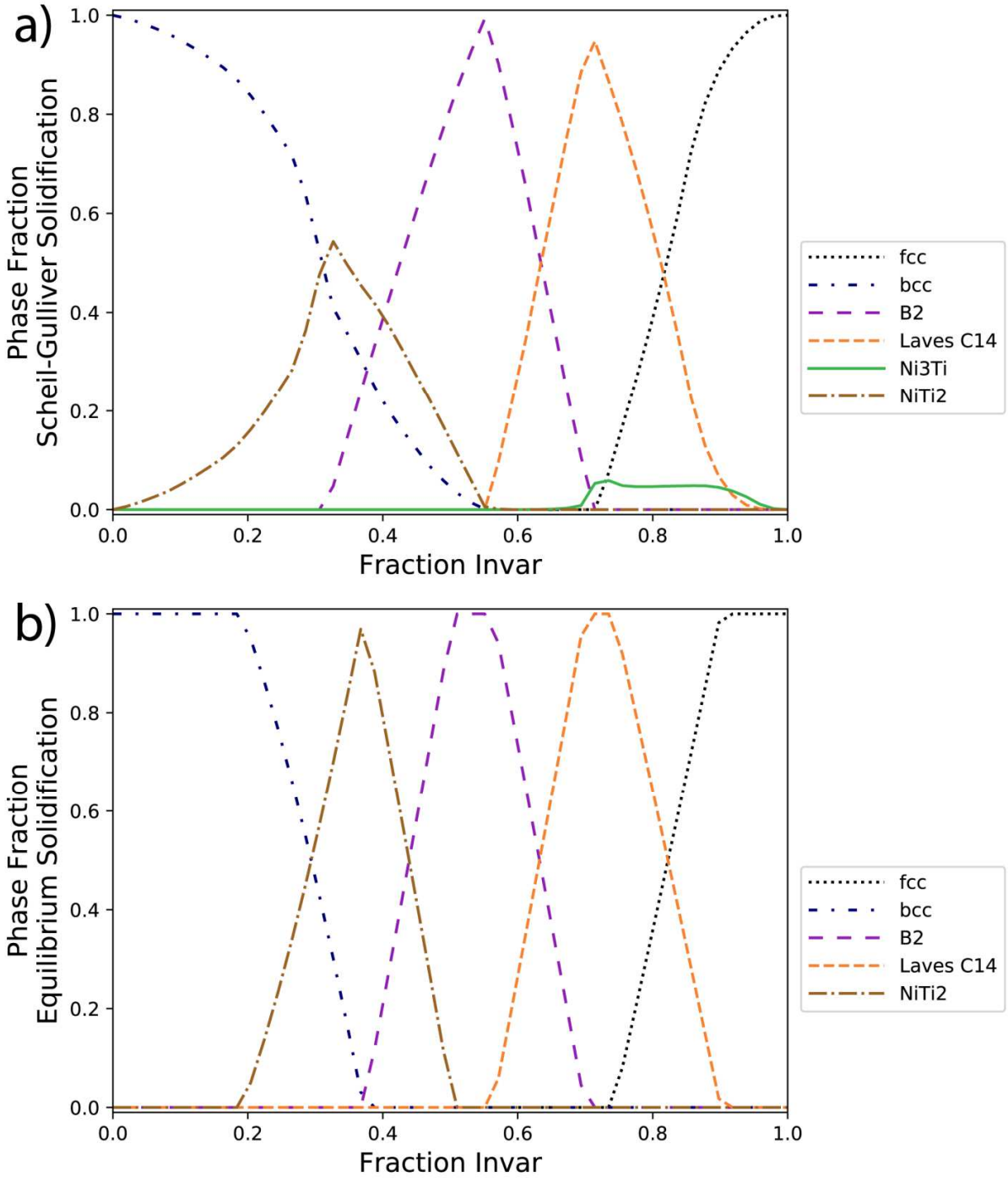

Figure 37. Phase fractions of the as-solidified phases predicted along the linear gradient path from Ti to Invar using the Scheil-Gulliver model (a) and the equilibrium solidification (b).

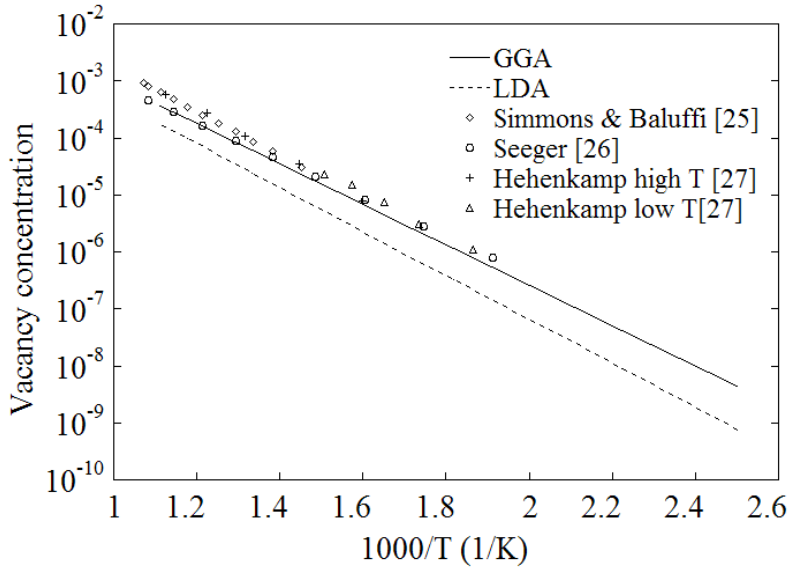
Vacancy concentration
1000/T (1/K)
GGA
LDA
Simmons & Baluffi [25]
Seeger [26]
Hehenkamp high T [27]
Hehenkamp low T[27]

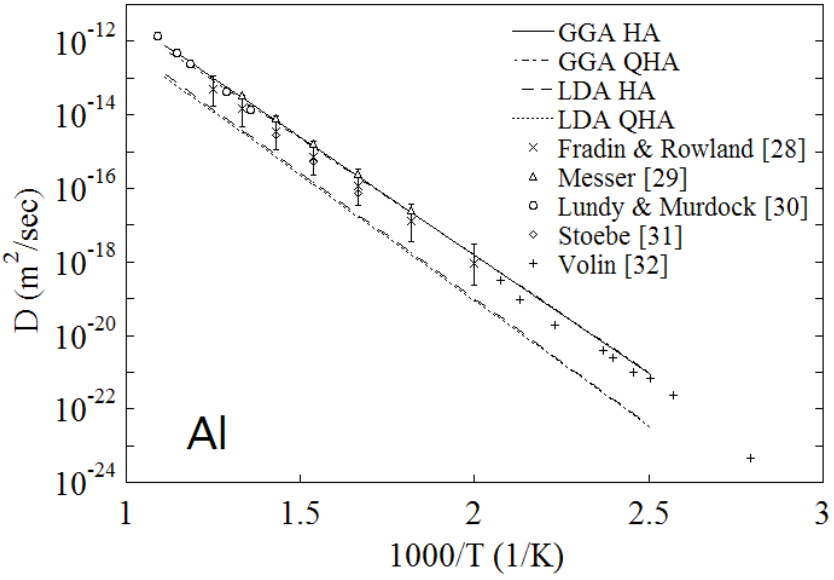
D (m2/sec)
1000/T (1/K)
GGA HA
GGA QHA
LDA HA
LDA QHA
Fradin & Rowland [28]
Messer [29]
Lundy & Murdock [30]
Stoebe [31]
Volin [32]
Al

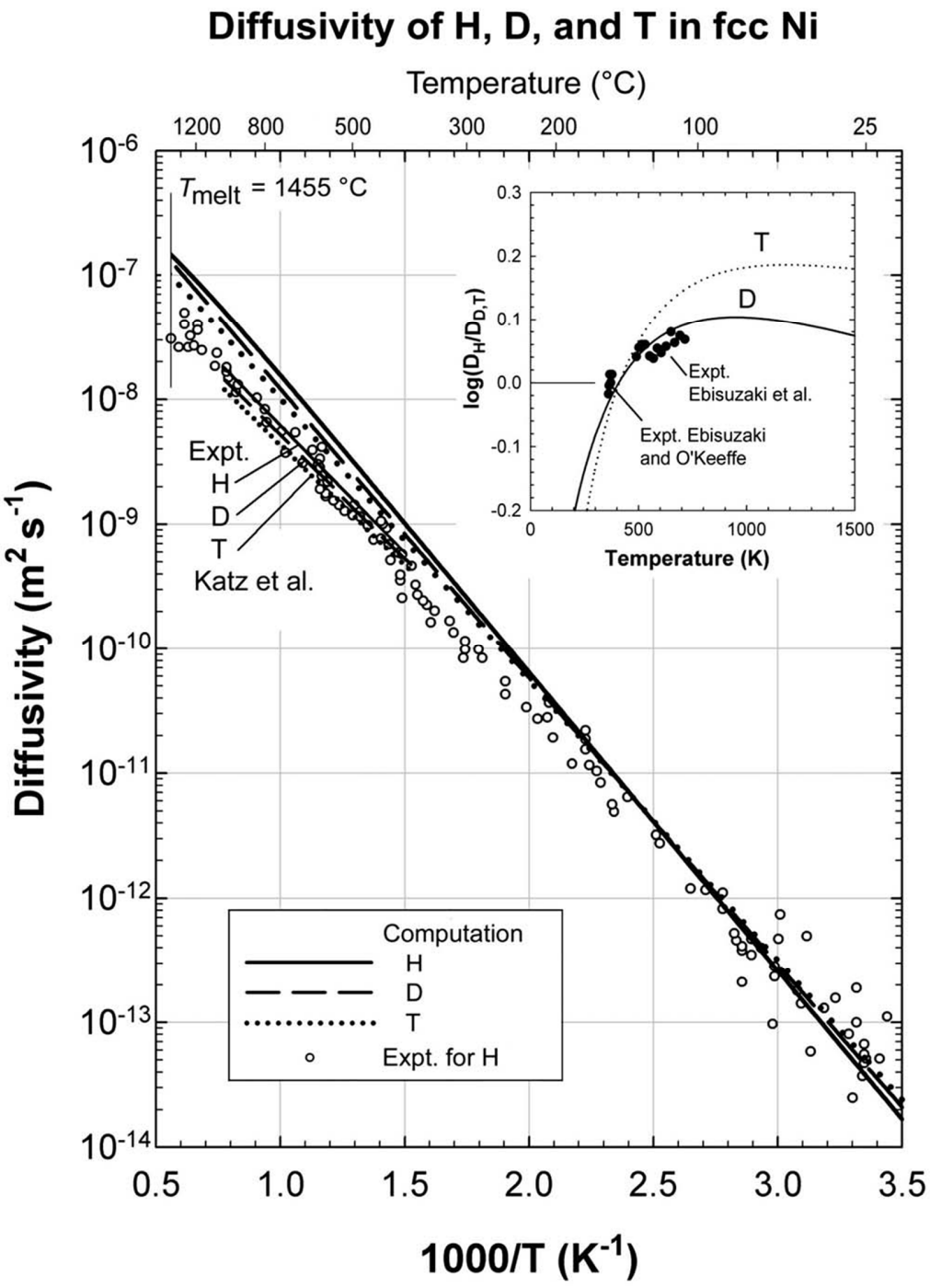

Figure 38. Predicted vacancy concentration (a) and self-diffusion coefficient (b) in fcc Al [337] and interstitial diffusion coefficients of interstitial hydrogen (H), deuterium (D), and tritium (T) in Ni (c) [338]

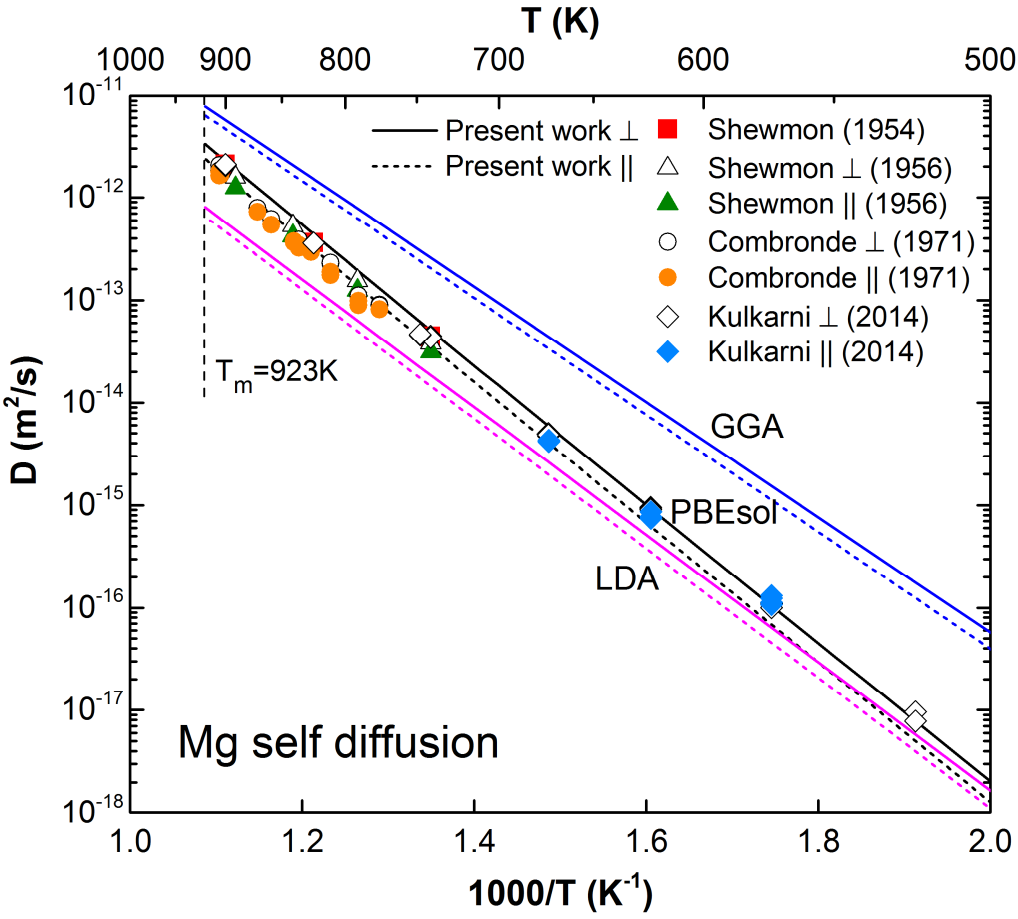

Figure 39. Predicted self-diffusion coefficients in Mg from LDA,[350] GGA,[350] and PBEsol[352] compared with experimental data (see references in [352]).

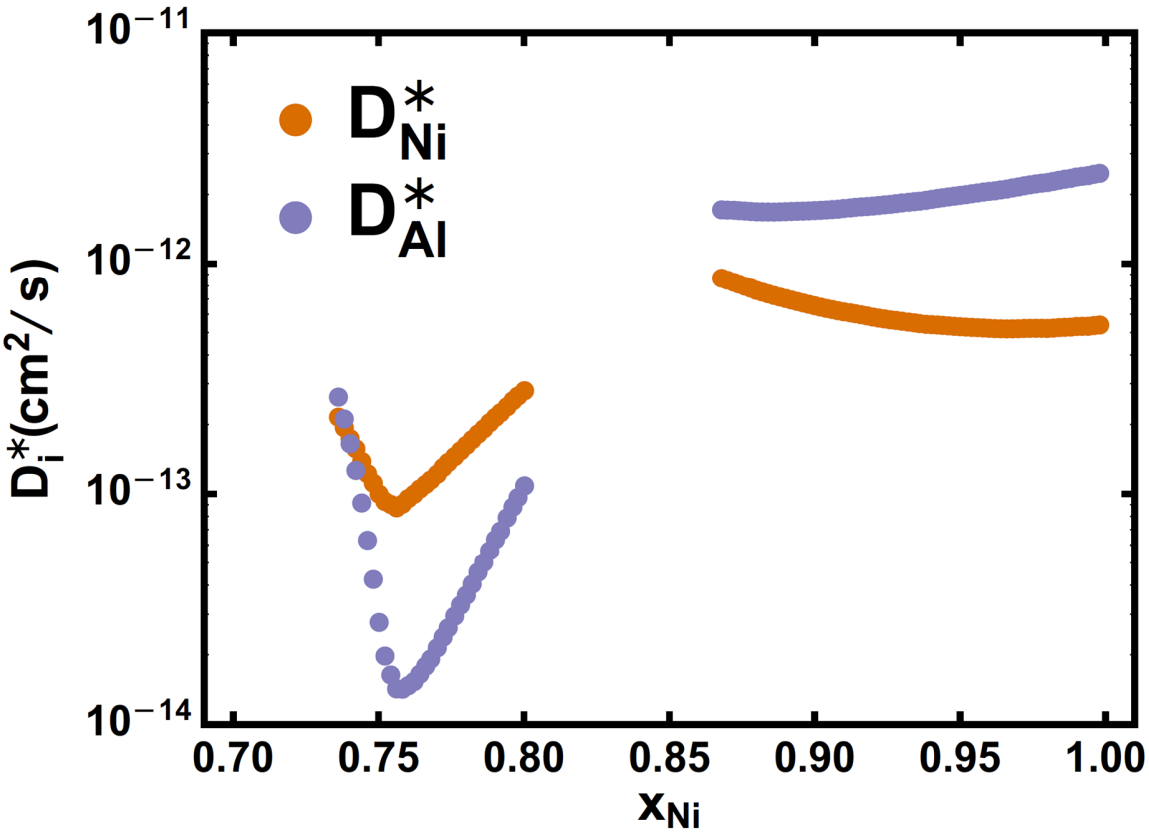

Figure 40. Tracer diffusion coefficients of Al and Ni at 1300K as a function of concentration in disordered fcc and ordered $L1_2$ phases.[356]

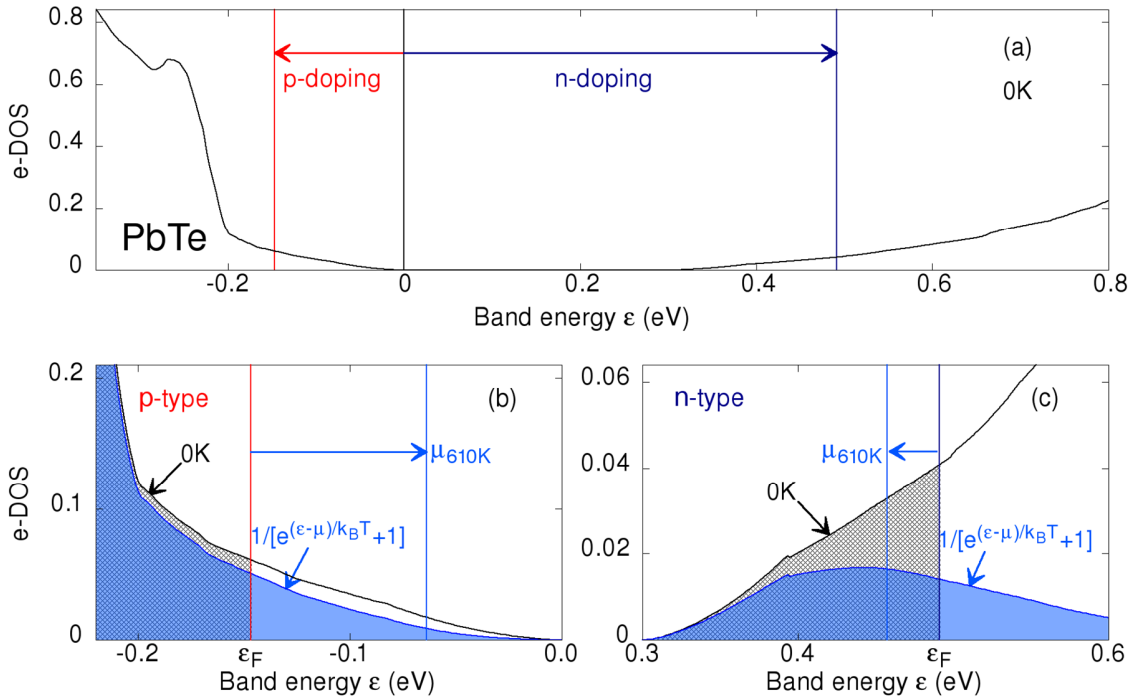

Figure 41. Calculated results for PbTe, a) e-DOS (black curve); b) e-DOS near the Fermi energy for p-doping; c) e-DOS near the Fermi energy for n-doping; with the areas shaded by gray (partially overlapped by the blue semitransparent shaded areas) for the electron occupation at 0 K and the blue semitransparent shaded areas for the electron occupation at a finite temperature 610 K described by the Fermi distribution. [363]

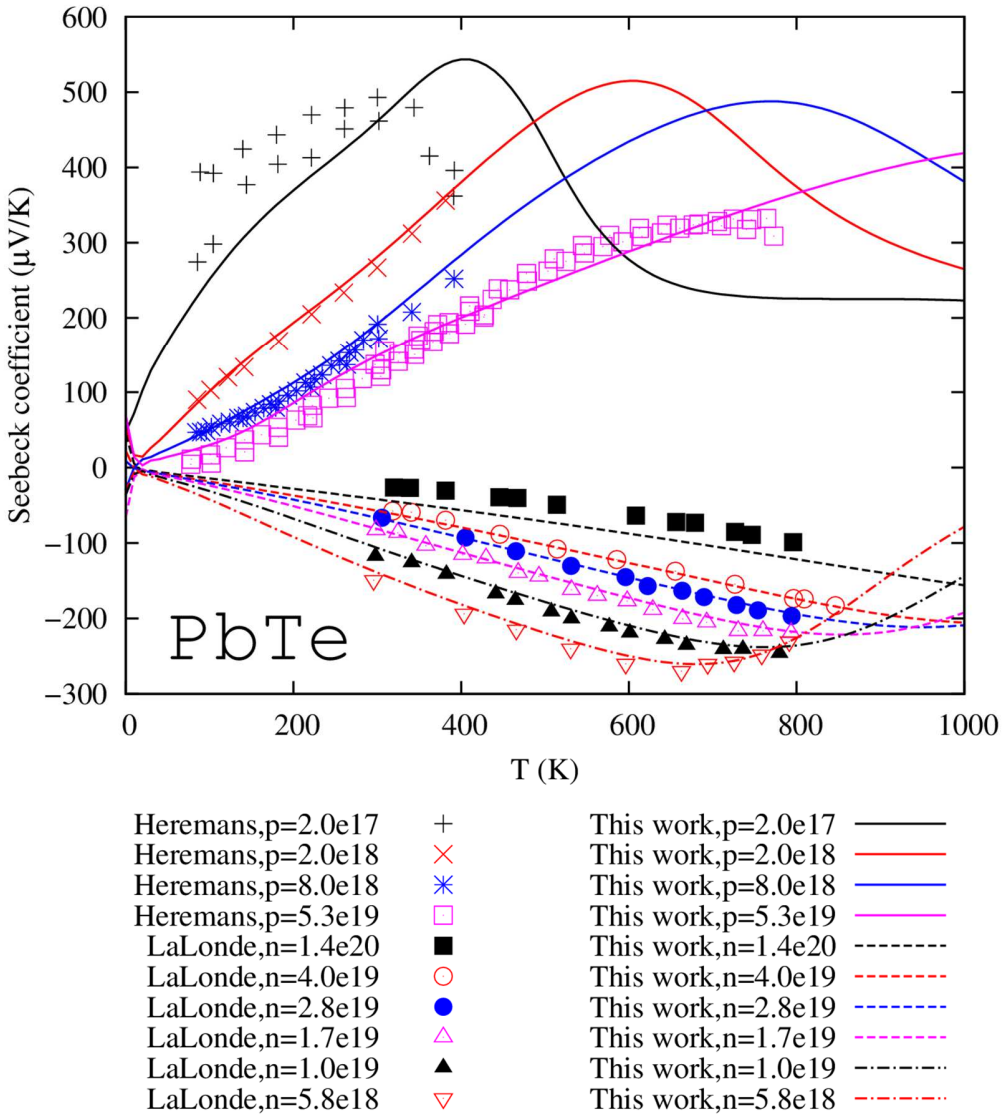

Figure 42. Calculated Seebeck coefficients for PbTe for various p- and n-type doping levels (lines) [363] in comparison with the experimental data for p-type PbTe by Heremans and coauthors [370,371] and n-type PbTe by LaLonde et al. [372] (symbols with same colors and sequences as the lines).

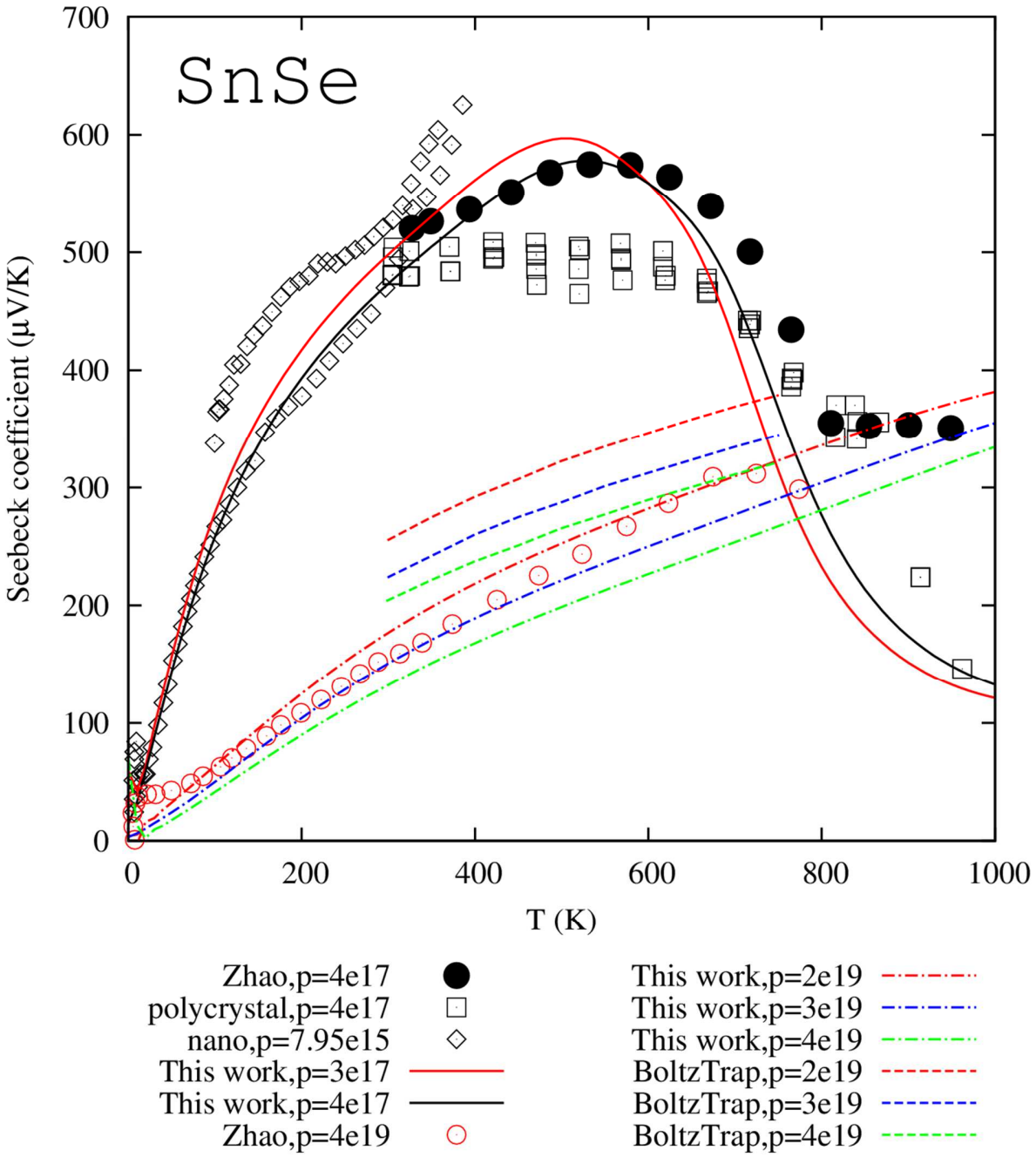

Figure 43. Calculated Seebeck coefficients for p-type SnSe[363] compared with results from experiments[373–376] and kinetic Boltzmann transport theory using the BoltzTrap package.[362]

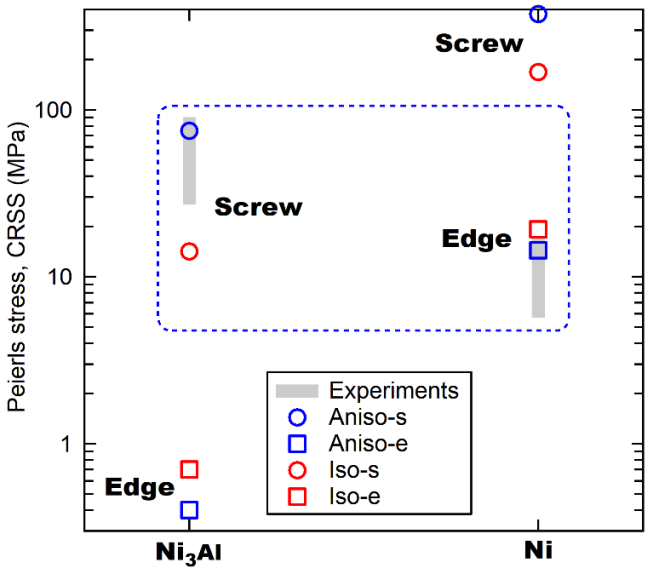

Figure 44. Calculated Peierls stresses at 0 K for edge (e) and screw (s) dislocations for isotropic (iso) and anisotropic (aniso) crystals in comparison with experimental CRSS values at room temperature for Ni_3Al and Ni.[379]

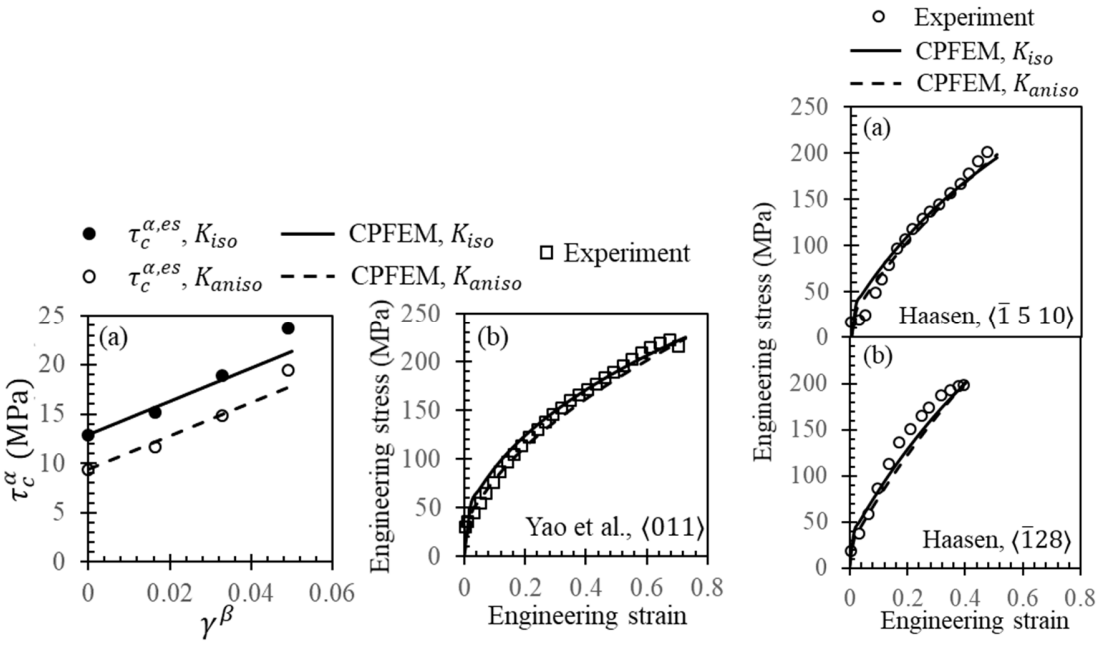

Figure 45. Strain hardening behavior of pure Ni single crystal:[380] left a) Peierls stresses (symbols), $\tau_c^{\alpha,es}$, on slip system α that combine contributions from both edge and screw dislocations as a function of shear strain on slip system β with the corresponding CPFEM fits (lines); (middle b) CPFEM simulated engineering stress-strain curves (lines) with experimental data by Yao et al. (symbols) [381]; (right a, b) CPFEM simulated engineering stress-strain curves (lines) with experimental data by Haasen (symbols).[382]